Doctoral Thesis

University of Trento

Doctoral school in Materials, Mechatronics and Systems Engineering

Applications of Intelligent Manufacturing and of Numerical/Analytical Modeling Techniques to Milling Processes

Kateryna Skrypka

Supervisor: Paolo Bosetti (Università degli Studi di Trento)

Referees: Aldo Attanasio (Università degli Studi di Brescia)

Giovanni Lucchetta (Università degli Studi di Padova)

June 2017

Acknowledgements

I would like to express my gratitude to my advisor *Paolo Bosetti*. I appreciate all your contributions, your support, and the fact that I had the possibility to work under your supervision during my PhD program.

Besides my advisor, I would like to continue by thanking the professors of the Doctoral school in Materials, Mechatronics and Systems Engineering of the University of Trento for their encouragement and attention.

I gratefully acknowledge *Gaetano Pittalà* and *Giovanna Malagnino* from Sandvik Coromant (Rovereto, Italy) for providing me the opportunity to collaborate with their team, and to have access to the laboratory and research facilities.

I thank my PhD colleagues for the great time we spent together, for their help, and for all the fun we have had in the last three years.

I would especially like to thank my dearest friends *Carlos Maximiliano Giorgio Bort*, *Julia Kavko*, *Francine Gonçalves Kraisch*, *Alina Yaruchik*, *Veronica Pedrolli* and *Antonio Di Dino* for their support, their involvement, and their patience.

And the last but not the least, I would like to thank my family: to my mother *Elena*, to my grandparents *Nikolay*, *Vyacheslav* and *Tatyana* for having supported the distance between us, for having supported me spiritually and emotionally not only throughout writing this thesis, but especially during my life.

To the memory of my grandmother Nina.

Contents

List of Tables

List of Figures

Abstract

Milling is one of the most important and common processes widely used in manufacturing industry, which is a very competitive environment. For this reason, manufacturing companies are facing many different challenges. The offering of a variety of high quality products, the restriction of production time and costs, the increase of productivity, and the need for flexibility of production are the goals that manufacturers have to consider and achieve in order to succeed in their field. These aspects relate to the process study, optimization and control, and in recent years many attempts to find possible solutions and techniques to manage these steps in a proper way have been done. The first solution that a lot of enterprises were motivated to research and utilize relates to the application of the finite element modeling (FEM) techniques to study manufacturing processes or to highlight behaviour of products, for example of cutting tools, during the design phase. The second technique deals with the manufacturing process control, and is aimed at the increasing of automation level of modern production systems by evolving them towards the paradigm of *Intelligent Manufacturing*. The present work is focused on the study and evaluation of the effectiveness of both techniques.

The first part of the research presented in this thesis is dedicated to the study of the application of *Intelligent Manufacturing Systems* to milling processes. In particular, in the Chapter 1 it is discussed the improvement of the artificial operator called *Evaluation and Perception Controller* (EPC) built by the Mechatronics group of the University of Trento within the national project Michelangelo in 2013. In this thesis it is proposed to improve the performance characteristics of the EPC system in terms of the process quality,

described by the surface roughness value. In particular, it is proposed to associate the surface roughness term to the scallop height value, and to include a model that describes the mechanism of scallop height formation into the *Optimal Control Problem* formulation.

Chapter 2 of this work is related to the application of FEM techniques to study milling processes. In particular, in this section the influence of CAD cutting tool models (STEP and STL) on 3D FEM AdvantEdge prediction accuracy in terms of the average and maximum cutting forces, and deformed chip thickness and curvature radius values are studied. In addition, this part of the thesis includes also the discussion of the problems related to the application of 2D FEM modeling techniques to study the influence of cutting tools geometries on the feed and tangential cutting forces that act in three-dimensional cutting processes.

Chapter 3 of this thesis is dedicated to the development of a model suitable for prediction of cutting forces that act in non-tilted and tilted side down-milling processes performed with end mills. The development of this model has two purposes. First of all, it can be included into the EPC controller, thus extending the field of the possible applications of this system. The second purpose relates to the fact that in case the side down-milling process simulations are performed by using cutting forces coefficients identified based on 2D FEM cutting forces data, the proposed model allows to overcome the mismatches between real processes and 2D FEM, and to simulate two cutting forces, feed and normal, arising in three-dimensional processes.

Chapter 1

Adaptive control of milling process: roughness minimization

In this chapter the paradigm of *Intelligent Manufacturing* applied to milling processes, and such topics as *Intelligent Manufacturing Systems* (IMS), adaptive control, monitoring systems for cutting forces, tool conditions, chatter detection etc. are briefly discussed.

The main purpose of this chapter is to introduce the control system called *Evaluation and Perception Controller*, which was built within the national project Michelangelo, and to report the results of the improvement of this system performed in terms of the process quality, associated to the scallop height value.

In particular, this study proposes to control the surface roughness value used as the process quality parameter by introducing a theoretical model of the scallop height formation, set as one of the constraints in the *Optimal Control Problem* formulation. The development of this model, its experimental validation, and results of the evaluation of the efficiency of the proposed modified system are discussed in this chapter.

1.1 INTELLIGENT MANUFACTURING SYSTEMS

Milling is one of the manufacturing processes widely used in industry, and in the last 20 years it has become very competitive field. The rapid changing of users needs, evolution of products and production systems had forced companies to change their strategic prerogatives, and to redesign manufacturing taking into account the tendencies to reduce production costs, to increase productivity, and to maintain product quality at the same time. In this scenario, *Computer Numerical Controlled* (CNC) machine tools have become popular, such increasing notably production capabilities and competitiveness of the enterprises. Nevertheless, despite the continuous performance enhancements, the automation level of CNC machines has not been improved significantly. The process set-up, i.e. the selection of the optimal cutting parameters in order to create a competitive market-desired product, remained dependent on operators and their skills. Today, operators of machine tools have to program tool movements, to calculate a set of cutting parameters according to machined material properties and tool. Moreover, during the machining, they often have to adjust or handle machining parameters in order to minimize errors caused by wrong choice of process parameters when designing part-programs, or errors caused by tool deflection, tool wear, vibrations etc.

As a consequence, the increase of automation level has become desirable, and nowadays it plays the key role in the development of the next generation machines - *Intelligent Manufacturing Systems* (IMS), that must provide the improvement of flexibility level, reconfigurability and intelligence to allow them to correspond to the highly dynamic market demands [96].

An IMS is a system that is able to acquire knowledge of the process, to establish the process controls with respect to the production needs (low cost, high productivity etc.), to monitor the process performance, and if some unexpected changes during the process are detected, to self regulate, i.e. to adapt controls. In addition, the IMS system has to be flexible and reconfigurable in order to be able to follow market requirements.

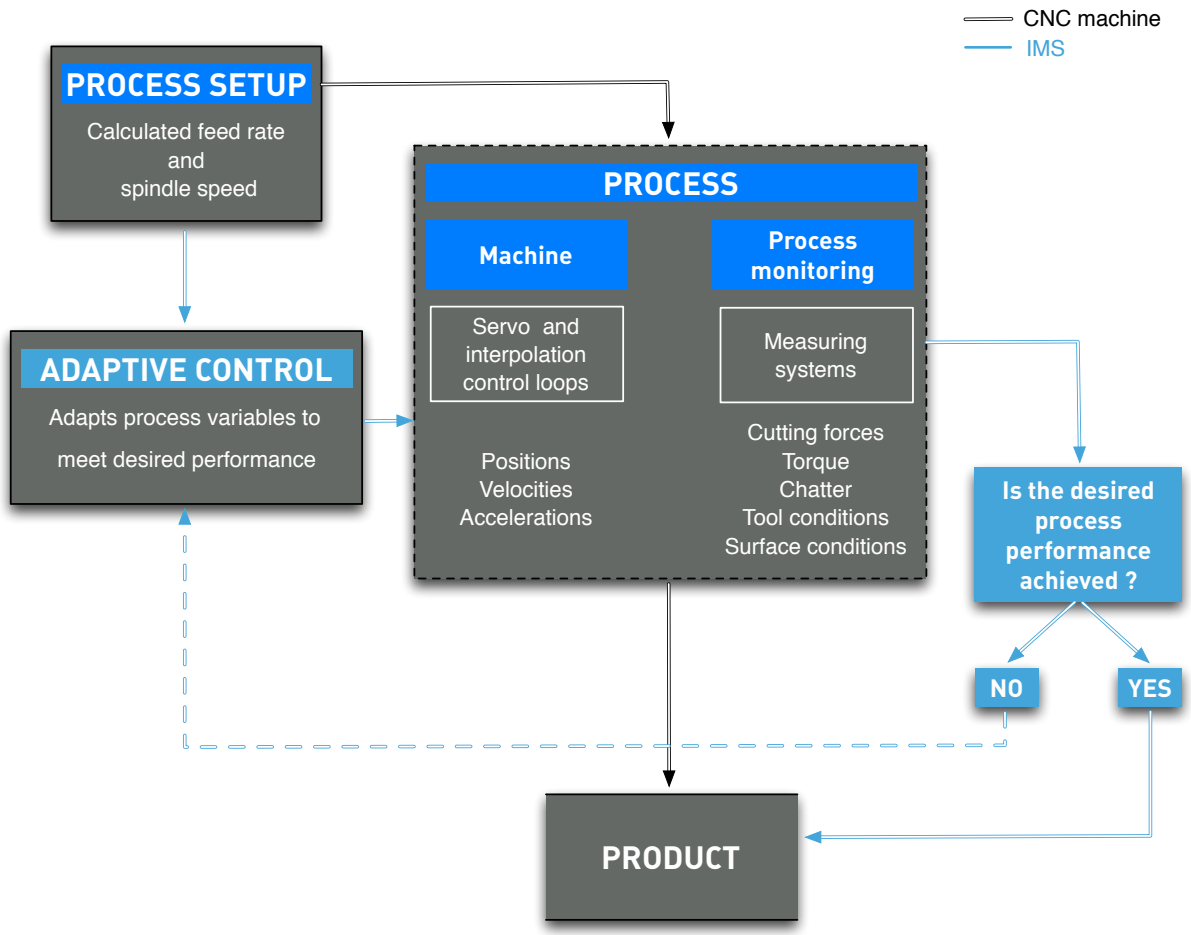

Figure 1.1: General manufacturing process controller scheme with different control levels

Such improvement of the existing CNC systems requires the development and application of the new robust techniques and strategies to study, plan, and control processes, and application of different optimization techniques essential for the multi-objective goals achievement.

1.2 MONITORING AND CONTROL OF MACHINING

Since the 1970's, when the first CNC machines have been introduced, their control architectures have been improved a lot. The general scheme of a simplified machining controller with different control levels is shown in the Fig.1.1.

The general classification of the control systems can be represented based on the tasks they have to perform:

1. Machine control loop
2. Monitoring control loop
3. Adaptive control loop

Machine tool control is applied to monitor the cutting tool motion with respect to the workpiece, and it includes two levels: servo and interpolating control loops. The general purpose of the servo control loop is to regulate machine axes movements, while the interpolating control loops are used to generate coordinated axes movements in order to achieve a programmed tool path [78]. In recent years these two areas have been improved significantly.

Process monitoring and adaptive control loops are very important tasks that IMS systems have to able to perform. In general, monitoring of the process is aimed at the process state identification, and it is based on the application of different measurement systems, i.e. sensors, to monitor such process parameters as forces, temperatures, tool conditions etc. Adaptive control loop, instead, is aimed at the manipulation of the process parameters, such as feed rate, spindle speed and depth of cut, in order to regulate the process, and to achieve desirable performance. Since most part of the CNC machine tools available today have closed controllers, which are very difficult to modify, they don't include adaptive control as a standard component. Only some commercial CNC manufacturers can provide such type of the control as an optional function.

1.2.1 Monitoring Systems

The process control implementation requires the instantaneous information about the key process parameters, and as result, the control systems must include technical devices that are able to measure, transfer, save and process acquired information. Dependently on the type of controlled parameter, these devices can be divided into the following categories: cutting forces and torque measurement systems, chatter detection systems, surface texture and dimensional accuracy measurement systems, and tool condition sensors.

Cutting forces and torque monitoring

In milling process cutting forces are generated by the tool/workpiece interaction. As result, a torque, associated to the power, is produced on the spindle and drive motors. The excessive forces cause some undesired phenomenons as tool failure, structural deflections, tool wear and breakage.

Cutting forces can be monitored by using commercially available load cells or dynamometers, or can be predicted from the current of electric drives. Cutting torque monitoring can be done with strain gauge devices placed on the spindle or with dynamometers. Power from the spindle and axis motors is typically monitored using Hall effect sensors [141].

Chatter monitoring

As mentioned previously, cutting forces cause structural deflections, i.e. unstable tool/workpiece interaction, thus producing chatter, and influencing tool conditions and surface characteristics.

In case the process is monitored by operator, chatter can be detected due to the loud and noise, or by inspecting the surface since 'chatter marks' are usually left on the workpiece. Automatic detection can be performed by using accelerometers.

Tool conditions monitoring

Tool wear occurs due to the contact between cutting tool and workpiece, and leads to eventual tool failure - tool breakage, when a significant portion of the tool breaks off. The information about tool characteristics, such as tool wear and tool breakage, is also very important in process monitoring.

The following methods and systems can be used for the detection of these two types of tool conditions: vision based measurement systems, lasers, acoustic emission, sound and vibrations data.

Surface texture and dimensional accuracy monitoring

The following characteristics can be used to describe surface texture: defects, directionality, waviness, integrity, surface roughness etc. Surface roughness is one of the most important parameters since it influences product quality and performance characteristics. The monitoring of these parameters can be performed by using profilometers and vision systems. The surface integrity monitoring includes measurements of the reflected light intensity variations. The dimensional accuracy monitoring is also an important element of the process control, and can be performed by involving lasers and vision systems.

1.2.2 Adaptive Control Systems

As mentioned previously, adaptive control (AC) is aimed at the process parameters (feed rate and spindle speed) manipulation in order to regulate the process, and to achieve desirable, i.e. optimal, or near-optimal process performance. The authors Groover and Zimmers [53] defined the following functions of adaptive control:

1. Identification
2. Decision
3. Modification

Before being able to perform the listed functions, AC system has to get knowledge of the process to be controlled (Fig.1.2). The main purpose of the knowledge acquiring is to provide the controller with the models that describe process character and behaviour. The models have to be representative and accurate enough in order to provide precise representation of the system, and simple in order to avoid complexity and high computational time. On this basis, it is possible to create the control algorithms. It has to be taken into account the fact that the optimal, i.e. desired, system behaviour has to be real and achievable.

The identification function is aimed at the determining the current state of the process by using the feedback data from the monitoring systems (forces, motor current etc.).

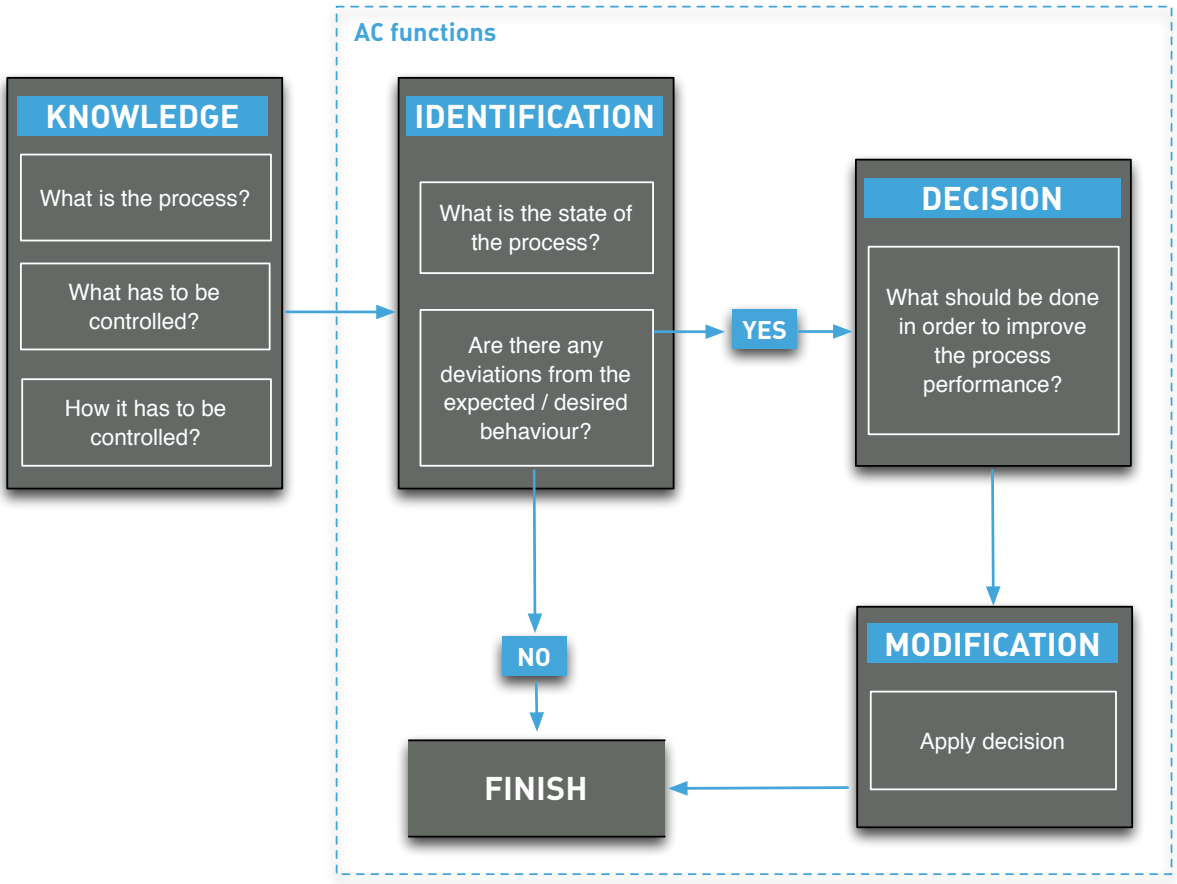

Figure 1.2: Simplified scheme to represent functions of adaptive control

When AC system has information about the process state, it performs the comparison of the measured data against the expected values. If any deviations from the desired (optimal) behaviour are detected, AC system has to perform the next step, decision-making. The system has to decide how the controlled parameters should be adjusted in order to achieve optimal or near–optimal process performance by using the provided set of rules or algorithms.

Modification function is aimed at the applying decision that was made in order to obtain physical or mechanical changes in the system, such providing the required process performance.

The sources [78], [132] and [142] distinguish the following adaptive control techniques:

1. Adaptive control systems with optimization (ACO)

2. Adaptive control systems with constraints (ACC)

3. Geometric adaptive compensation systems (GAC)

The idea of the adaptive control with optimization (ACO) is to find a performance index, usually in the form of a cost or performance function, which is then optimized subjected to the machining constraints (maximum torque, temperature, maximum and minimum spindle speed, surface roughness, power consumption etc.) [101]. ACO system adjusts, i.e. optimizes, the machining parameters such as feed rate, spindle speed or depth of cut in order to maximize the process performance: to maximize material removal rate, to reduce vibrations, or to obtain better quality or lower costs of the product etc.

Adaptive control systems with constraints (ACC) are the systems typically aimed at the material removal rate maximization through the maintenance of the cutting forces at the highest possible limits imposed by the maximum stress that the tool can tolerate without breakage [26], [144]. The field of the application of such type of the systems are roughing operations, where the quality of the process is not important.

The geometric adaptive compensation (GAC) systems are used for finishing operations with the objective of a specific part quality being maintained, despite structural deflections and tool wear [144], [58]. The following two categories of GAC systems can be distinguished: systems that change machine parameters such that the tool deflection remains at a certain level, and systems that can perform tool path compensation by taking into account such inaccuracies of the machine tool as spindle or guideway errors [101].

Literature overview

The first efforts to develop AC systems were done in the late 1960's and 1970's [149], [111], [110], [91], [56], [4]. A lot of the performed studies showed that the adaptive control systems can provide the increase of the material removal rate by 20.0–80.0%, and achievement of other benefits [67], [92], [13], [31].

The first ACO system for cutting processes was proposed by Centner and Idelsohn in 1964 [33]. In their work the authors discussed the primary performance factors, and introduced the figure of merit that can be used to describe quantitatively milling operation performance. The proposed system was used to optimize cost function by applying constraints on such factors as surface finish, and machine horse power. The authors also highlighted that the conditions required to achieve minimum cost and those required to achieve minimum time are not identical, and that some compromise between these two performance factors is needed.

In the work [81] the authors Liu and Wang used the backpropagation neural network (BP NN) and augmented Lagrange multiplier (ALM) algorithm to design an adaptive controller with optimization. The BP NN model was developed for cutting forces modeling, and it uses milling feed rate as an input. The ALM was used to develop the optimal control algorithm aimed at the improvement of milling process efficiency described by material removal rate. As the constraints the authors selected maximum and minimum cutting speed, and maximum cutting force. According to the results of the experimental campaign, the efficiency of the adaptive milling system was improved by about 15.0% compared with that of the traditional CNC milling system.

The source [50] discusses the development of a sensor-based system for on-line adjustment of cutting conditions in a turning operation. The proposed system takes into account tool wear by using monitoring data. The neural network (NN) technique was used in this system for tool life estimation under varying cutting conditions. The objective of the performed work was to maximize chip removal, and at the same time to control wear rate in order to achieve desired tool life. A set of cutting tests performed under conditions optimized for the preset tool life (30 min) and flank wear (0.3 mm) confirmed the efficiency of the proposed system.

In the work [82] the authors Liu et al. discussed the development of the intelligent ACO (IACO) system based on the neural network (NN) and genetic algorithm (GA). The NN technique, the multilayer neural network (MBPNN), was used for milling system modeling. The input of the MBPNN is feed rate value, and the output is cutting force. The GA technique was used to develop optimal control of milling process. The authors selected feed rate as optimized variable. The experimental part to prove the robustness and stability of the proposed system was performed by using the following constraints: machine tool power $P = 4.5$ kW, maximum cutting force $F = 320.0$ N, and cutting speed 7.5 mm/min $\leq$ v $\leq$ 180.0 mm/min. The obtained results showed that the efficiency of the IACO milling system was improved by 20.0% compared with the traditional CNC milling system.

The authors Kim and Jeon [71] designed the fuzzy-logic controller (FLC) that automatically adjusts feed rate parameter in order to regulate cutting force in milling processes. The developed system includes a cutting forces analytical model, and FLC system that modifies feed rate parameter to follow a desired cutting force value. The cutting forces prediction model is based on cutting force coefficients, cut geometry (rotational angle of the flute tip), and length of cut. The performance of the FLC is based on the difference between measured and desired cutting forces, and it determines an appropriate increase or decrease of the feed rate value. A set of machining experiments was performed in order to verify the efficiency of the proposed system. The collected data showed that cutting forces control and regulation were executed successfully when the FLC was used.

The authors Liu et al. in the source [80] presented the dynamic characteristic-based fuzzy adaptive control algorithm (DCbFACA) that can be used to avoid the influence of rapidly changing cutting force on machining process. The authors proposed a system in which spindle motor current, instead of cutting force, is obtained in real time, and is used by the fuzzy algorithm to adjust online feed rate value. The developed system uses two inputs (spindle current error and spindle current change), and has one output - feed speed change - to maintain cutting force constant during machining. The proposed dynamic characteristic-based fuzzy adaptive control algorithm was validated by means

of several cutting tests, and it was confirmed that when the proposed control system is applied, the cutting force is maintained constant, thus improving the machining process stability and quality.

Another work concluded in [57] deals with a cutting force control strategy with a focus on tool life regulation. The authors presented the control scheme ACO, which executes cutting force monitoring only at 'check points' along tool path, thus allowing to reduce amount of the information needed to update the cutting force prediction model, and to re-calculate feed rate profile. The cutting force prediction model that was implemented into the proposed system is the one discussed in [64]. In this work, the authors also presented a scheme to estimate tool wear progress from cutting force. The effectiveness of the proposed control scheme was confirmed by several simple cutting experiments.

In the source [36] the authors Chiang et al. presented the neural network based adaptive control with optimization (NNBACO) based on two neural network models. The first model is used for optimal cutting parameters selection (feed rate, axial and radial depths of cut) for such outputs as upper bounds of cutting forces, power, and surface finish. The second network, instead, is used to find corresponding optimal cutting conditions based on cost function and material removal rate (MRR), subjected to certain constraints. After having performed several cutting operations, it was confirmed that by applying the NNBACO system, the MMR of the studying process was increased.

Another ACO system used for selection of optimal cutting conditions for grinding process was introduced in [52]. The proposed system is based on the regression models of surface roughness R_a and surface damage, and genetic algorithm optimization aimed at MRR maximization (cutting depth, cutting speed are optimized), subjected to the surface roughness and damage constraints. The results of the ACO application showed that MRR maximization is influenced more by the constraint on surface roughness than by surface damage. As instance, in case when the surface roughness and surface damage constraints were selected equal to 0.4 μm and 2.0% respectively, the MRR was increased by almost 10 times. Instead, in case when these constraints were selected equal to 0.25μm and 3.0%, the MRR was increased by only 2.5 times.

In the work [8] Altintas presented the development of the ACC algorithm for milling operations. The following arguments were discussed in this work: dynamics of feed motion and cutting process that were modeled as a third order system, and parametric expressions that can be used to identify maximum cutting force and maximum chip load. As reported by the author, the proposed system allows to control the normal cutting force, maximum resultant cutting force, and maximum torque or power in any machining operation, and it is spindle speed and drive dynamics independent.

Another authors Prasad et al. in their work [112] presented an adaptive control constraint system that controls surface roughness and cutting forces in turning. The main purpose of the system that was developed based on feedback control is to regulate process parameters (feed rate, spindle speed and cutting depth) in order to maintain vibration and disturbances of the machine constant, thus allowing surface finish to remain stable. The experimental campaign consisted of 25 cutting tests performed under different conditions confirmed the adequacy and stability of the proposed control system.

In the work [29] the authors Budak and Kops worked on the improvement of productivity of flank milling process. They proposed an adaptive controller (ACC) able to determine feed rate value to keep constant a desired cutting force value, identified as peak resultant milling force value calculated by using the model proposed in [10], which takes into account tangential and radial force coefficients, tool geometry, and feed per tooth. According to the results of the performed experimental part (roughing operations), during which the controller was interfaced with a CNC unit of a 5-axis machining center, the adaptive controller was able to keep the peak milling force at a constant level (3000.0 N) by varying feed rate.

In the work [43] the authors discussed the development of an adaptive control system with constraints (ACC) for milling process. The proposed system deals with constant force, and the main purpose is to hold force acting on tool at a certain level, thus avoiding conditions that lead to cutter breakage. The controlled parameter is feed rate. The other two constrains, chatter and overload of cutting edge, were also considered. After having carried out the experimental part to evaluate the proposed system, the effectiveness and robustness of it were confirmed.

The authors Župerl et al. in the work [163] discussed the application of the adaptive fuzzy control (AFC) strategy to the problem of cutting force control in high speed end-milling operations. The main purpose of the developed system, and of the fuzzy control in particular, is to keep metal removal rate value as high as possible, and to maintain cutting force as close as possible to a desired value by adjusting feed rate value. The desired cutting force value is found by using a BPNN model with four inputs: feed rate, cutting speed, axial and radial depths of cut. The robustness of the proposed AFC system was verified experimentally by performing controlled and traditional cutting operations. According to the obtained results, when the proposed controller was applied, process productivity was improved by 27.0% compared to the traditional cutting operation.

The authors Župerl et al. in the work [166] discussed the development of an adaptive control system (ACC) suitable to control cutting force and maintain constant surface roughness. The proposed system is able to compensate disturbances that occur during cutting process, such as tool wear, vibrations, chatter, non-homogeneity of workpiece material etc. The cutting force prediction is done by using the neural model based on cutting conditions and cut geometry as discussed in [162] and [95]. The optimization algorithm is based on the artificial neural network (ANN) model with eight neurons (inputs): feed rate, cutting speed, radial and axial depths of cut, workpiece material and its hardness, cutting tool diameter, and tool geometry. According to the reported results the stability and robustness of the proposed control strategy were confirmed.

The authors Xu and Shin [151] dedicated their work to the development of the multi-level fuzzy controller (MLFC). The main purpose of the presented system is to control online cutting forces, and to generate and update control rules for feed rate adjustment without any mathematical model of milling processes like it was proposed in [150] in order to increase machining productivity and improve quality. The process performance is constrained by maximum allowable cutting force value that has to be maintained despite changes in milling process parameters, such as tool wear, workpiece geometry, and material properties. After the MLFC system implementation, the experimental part was performed in order to estimate the efficiency of the system. According to the obtained data, the cycle time was reduced by up to 34.0% over the case without any force controller.

In the source [165] the authors discussed the development of a combined control system ACC aimed at feed rate adjustment in order to maintain cutting force constant in spite of variations in cutting conditions to prevent excessive tool wear, tool breakage, and to maintain high chip removal rate. First, cutting forces are predicted by using the adaptive neuro-fuzzy inference system proposed in [162]. Second, optimal feed rate is calculated by applying the Particle Swarm Optimization algorithm proposed in [164]. While performing cutting process operation, measured cutting forces are sent to the neural control scheme implemented into controller, which estimates the error between measured and desired (predicted) cutting forces. If needed, the neural control scheme adjusts optimal feed rate, and sends new value to machine. The stability and robustness of the proposed control strategy were verified by means of an experimental part. The results showed that when the proposed control strategy is applied, material removal rate can be improved by 27.0%. The time saving of 24.0% was reached in comparison with constant feed rate operation.

The authors Nojedeh et al. in their work [100] discussed the development of a tool path modification strategy (GAC) in order to improve accuracy of machining, and development of the NC program editor to generate compensated part-programs. As reported in this work, the proposed compensation technique includes the following steps: nominal tool path analysis and fragmentation, translation of nominal positions into real positions by applying kinematic error model based on tool and workpiece carrying axis, identification of compensated positions by applying error compensation algorithm, conversion of generated information into new tool paths, and editing of nominal part-program by using the NC code editor that eliminates the identified path deviations. The compensation strategy is based on the estimation of volumetric errors in target positions performed by applying the kinematic transformation concepts, and it is used to calculate a volumetric error vector - spatial deviation between nominal and real tool positions. The experimental verification of the efficiency of the proposed system showed a significant error reduction, about 50.0%.

Another geometric adaptive system for tool deflection error compensation for precision machining of blade was proposed in the work [156], and it includes three different modules: on-machine measurement (OMM), adaptive process geometric modeling, and numerical control (NC) machining. The purpose of the first module is to measure data (change of the

part position and shape distortion), which is then used to calculate the error displacement field and error compensation with curve fairing. The error displacement field is described by deformation error distribution of blade, and it is defined by using statistical analysis. The adaptive process geometric modeling is constructed through cross-section curves with fairing, and new tool paths used for NC machining process are then adaptively generated to implement error compensation. According to the experimental data it was observed that the maximum machining error in case of the error compensation was decreased by 39.5% compared to the traditional machining without using the compensation technique.

The authors Wan et al. in the source [146] discussed the development of a GAC system - the nominal tool path modification strategy with a purpose to minimize machining errors caused by contact deformation and surface entire deformation, which together contribute to rigid displacements of the workpiece. As specified by the authors, the proposed technique does not directly compensate machine tool control commands, but makes changes in cutter location source file (CLSF) through the proposed modification model based on the prediction of cutting tool deviations with respect to workpiece. Thus, nominal tool path scheme is adjusted based on predicted deviation values. The results of the performed experimental part indicated that by using the proposed control strategy it is possible to avoid undercutting and overcutting, and to reduce dimension errors, parallelism and profile errors.

In the work [25] the authors presented a compensation system - composite sensor Direct Deformation Sensor (SDD) - able to detect deformed shapes of structural parts of large CNC machine tools, and to compensate errors deriving from these deformations. As specified by the authors, the proposed sensor performs the real-time, instantaneous detection of deformations sources, and provides deformed position of any given point of structure by interpolation of deformed position of SDD nodes. Another benefit of the proposed system is that it can easily compensate temperature effect. According to the experimental data, the high sensor accuracy was achieved. While measuring the deflection of the attached beam structure over a span of 1.3 m, the sensor accuracy resulted to be order of 1.0 μm.

Another types of the GAC systems have also been developed in recent years. In literature are presented a lot of works related to detection and compensation of different types of errors, such as: thermal errors [153], [108], [159], [152], [158], tool positioning errors [75], [135], [118], [161], and errors caused by tool deflection [137], [119], [41]. The detailed description of the mentioned systems was not included into this chapter since this type of the control systems is not of interest to the presented work.

1.3 STATEMENT OF ORIGINALITY

Despite many different developed AC systems are presented in the literature, the main part of them result to be no flexible and no practical since they were designed based on such techniques as neural networks, fuzzy logic, regression models etc. used for the process model development. The application of such techniques is a quite challenging and time-consuming task. In general, the models based on the mentioned algorithms are suitable for process behaviour prediction only for a specific tool-workpiece combination, and their accuracy is directly proportional to the amount of training data. As was also shown in the state-of-the-art review, not all of the mentioned AC systems create process control strategies by taking into account tool/workpiece engagement geometry, and consequently cutting forces and dynamics of the system.

A successful attempt to overcome these issues was done by the Mechatronics group of the University of Trento within the national project Michelangelo, lasted five years and finished in 2013. The developed ACO system - *Evaluation and Perception Controller* - is a process supervised controller capable to simulate, optimize, monitor and learn milling process performance. In this system, the authors used theoretical models for process description, accurate enough to represent main phenomenons that occur in milling. The control strategy identification to achieve desired targets is performed by using the *Optimal Control Problem* optimization technique, based on the system of *Differential Algebraic Equations* (DAE) that describes machine performance state (feed rate and spindle speed), and its dynamic characteristics (acceleration of axes and spindle speed). The developed system includes also the monitoring and learning layers.

The purpose of this chapter is related to the improvement of the EPC, in particular to the improvement of process quality characteristics, associated to the surface roughness R_z value, and below such arguments as the architecture of the studying system, surface roughness and scallop height phenomenons are discussed.

1.4 EVALUATION AND PERCEPTION CONTROLLER

The architecture of the EPC is build based on the following three components: process simulator, *Optimal Control Problem* (OCP) solver, and perception layer that performs state reconstruction with state learning (Fig.1.3).

When executing the first step, process simulation, a simulator implemented into the EPC performs a tool path analysis, and calculates the material removal rate (MRR), cutting force vector, and stability lobes diagrams (SLD). In detail, the tool path, an ISO G-code part program, is analyzed by a custom - developed interpreter, a simplified Ruby Numerical Control (RNC), that calculates the feed velocity (tool tangent velocity) profiles for each G01, G02, and G03 blocks [27]. These profiles are generated by taking into account the maximum available accelerations of the axes and nominal feed rate specified in the part program. After that, the resulting toolpath, together with a definition of the tool and workpiece geometries, are used to compute the tool/workpiece engagement section, cutting force vector, and SLD as functions of the curvilinear abscissa along the toolpath. Simulation of the milling process is the most time consuming task since it depends on the tool path length, and requires the continuous model updating at each instantaneous tool position. This part can be done offline because it doesn't depend on the manufacturing targets, i.e. parameters to be optimized. More detailed information about the process simulator and RNC was reported in the works [26] and [27].

The second task performed by the EPC is the process offline optimization, during which the optimal feed rate and spindle speed profiles are computed as the continuous functions of the curvilinear abscissa by solving the *Optimal Control Problem* according to the set targets, which can be to maximize productivity, to minimize costs, and to maximize quality. The process optimization is done by using the optimization library

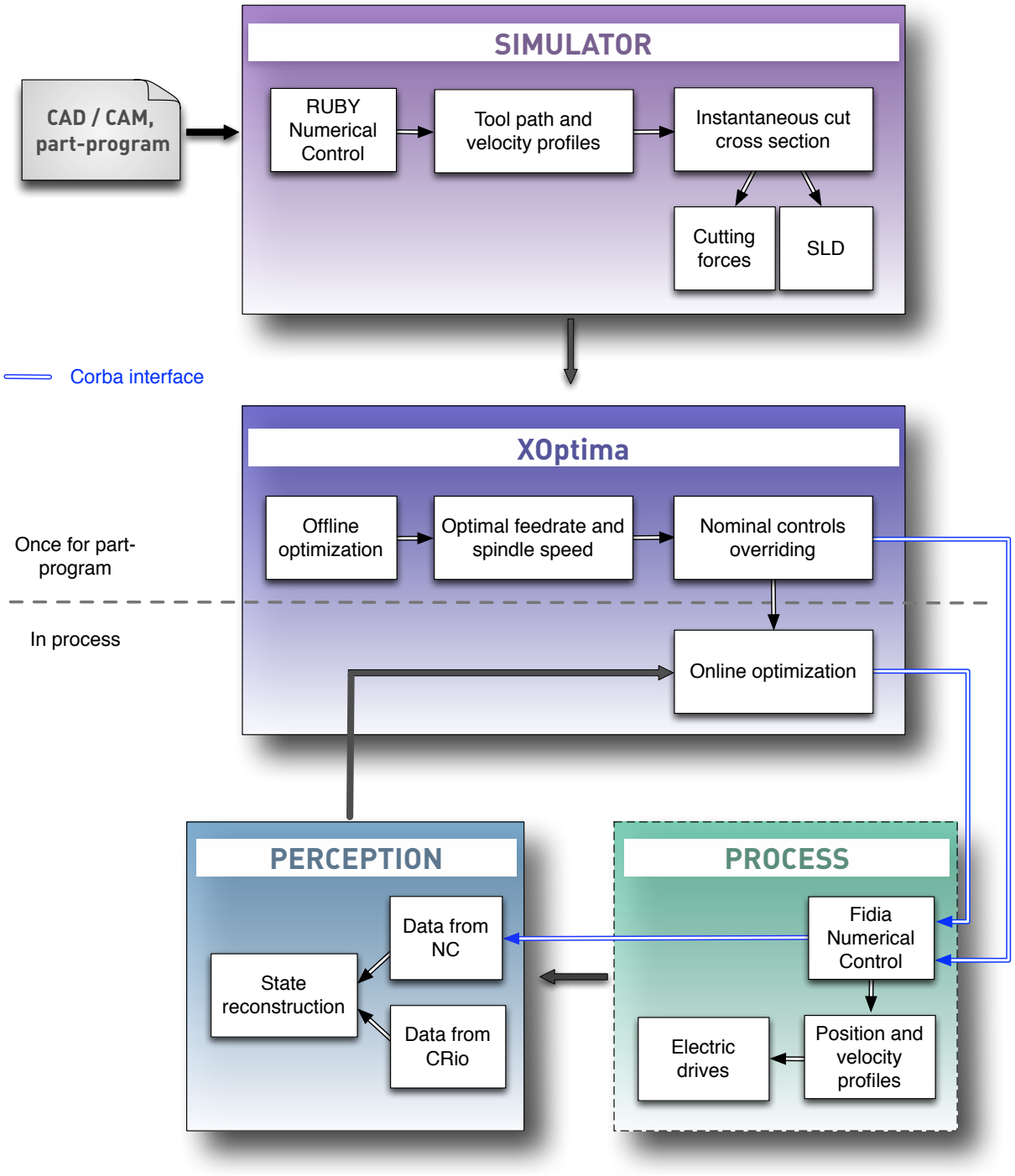

Figure 1.3: Architecture of the EPC

called *XOptima*, which also was developed by the Mechatronics group of the University of Trento. The detailed information about the developed solver can be found in the works [26] and [28], and in one of the sections presented below in this chapter.

After having found the solution of the *Optimal Control Problem*, the nominal controls specified in the G-code are overridden with the optimized ones, and the milling process is performed. During the execution, the CNC of the machine tool continuously communicates the current curvilinear abscissa to the supervising controller EPC, which replies with the instant, optimal values of the feed rate and spindle speed controls. Also, during the cutting operation the system data (absorbed torques, positions, accelerations, vibration levels) are recorded. These data are eventually used by the perception layer, the last element of the EPC, to reconstruct and learn the state of the process. Through this loop, the deviations of the cutting process from the behaviour, i.e. state, predicted during the offline process optimization can be identified and compensated. As instance, it is possible to correct the controls profiles by estimating online the specific energy of the cut material, whenever a workpiece is harder (or even softer) than expected [26].

The purpose of the improvement of the *Evaluation and Perception Controller* relates to the final quality of the product, and it consists in including the scallop height term, which is one of the surface roughness characteristics in milling, into the *XOptima* library, thus allowing to control the surface roughness value according to the technical requests.

1.5 SURFACE ROUGHNESS IN MILLING

The scallop is a volume of uncut material left on a machined surface. Its height is used to determine the surface roughness value - a component of the surface texture, and an indicator of the technological quality. During the manufacturing process the dynamic characteristics of the system may change, and different machining factors, such as tool deflection, tool inclination, tool wear and chatter can influence chip formation mechanism or power consumption, thus affecting the surface roughness formation and scallop height value [126]. The solution of these problems require different prediction, analysis and control techniques, and some interesting works have already been presented in literature.

In this chapter, the state-of-the-art of the prediction techniques will be discussed for both scallop height and surface roughness characteristics, since both of them can be used as the indicators of the machining process quality.

1.5.1 Literature Overview

According to the information reported in the found sources, there are several types of the surface roughness prediction models available nowadays. Some of these models are parameter-based, and they study the effect of cutting parameters, such as cutting depth, cutting speed, feed per tooth, tool wear, lubrication conditions etc. on the scallop height value [23]. Other available models comprise the problem of the tool run-out, tool setting error, and tool deflection induced by cutting forces when studying the scallop formation mechanism. Finally, exist some techniques like tool-path generation strategies and feed rate optimization approaches aimed at the maintaining scallop height close to the desired value during the process.

As instance, the authors in the work [42] presented different theoretical feed-interval scallop height prediction models suitable for the processes performed with torus and ball cutters. In this work, the authors studied the effect of tool radius, feed per tooth, tool inclination angle values, and workpiece surface shapes (horizontal, concave, inclined and convex) on the feed-interval scallop height. The results of the experimental campaign performed to identify the most influencing factors indicated that scallop height is influenced a lot by such factors as step over, cutting tool direction, cutter shape and tool axis inclination angle.

In the source [34] the authors reported the study of the influence of tool radius, feed/pick ratio, initial cutting edge angle, and tool inclination angle on the mechanism of path-interval and feed-interval scallop formation for ball-nosed end milling processes. The authors presented the theoretical model suitable for the scallop formation prediction. The experimental verification of the proposed model showed that it can accurately predict path-interval scallop and feed-interval scallop. It was also found that the feed-interval scallop height is more important for the surface roughness, and that it is very sensitive to the tool-axis inclination.

The authors Sahin and Motorcu in their work [121] presented a study of the development of the surface roughness model for milling operations with coated carbide tools. By applying the response surface methodology, the prediction model was built based on such terms as cutting speed, feed rate and depth of cut. By carrying out an experimental campaign, the authors stabilized that feed rate is the most important factor that influences surface roughness. The experimental data also showed that the increase of the surface roughness value is directly proportional to the increase of feed rate, and is inversely proportional to the increase of cutting speed and depth.

In the paper [35] the authors Chen et al. investigated the effects of tilt and lead angles on the scallop height, surface roughness, surface topography, and surface damages in five-axis ball-end milling process. Based on the results of the performed experimental tests, the authors identified a set of the optimized tool inclination angles that allow to improve surface characteristics. As instance, it was identified that the surface roughness value was relatively small at lead angles equal to -20.0°, -25.0°, and -35.0°. The tilt angle values for the surface roughness improvement varied from -40.0° to -10.0°, and from 10.0° to 40.0°.

The authors Mikó et al. in their work [94] worked on the development of a geometrical model of the cusp, i.e. scallop height, suitable for 3D milling processes of rounded surfaces. The influence of the following factors was investigated: tool inclination angle, feed rate value, and tool edge shape (ball-end mill). According to the obtained experimental results, the better surface finish, i.e. the lower surface roughness, was achieved at the greater leading angles and by increasing the feed rate values.

The authors Baek et al. [17] presented the dynamic surface roughness model for face-milling operations. The proposed model considers the static and dynamic components of cutting process, and it is based on the relative displacement between workpiece and cutting tool because of the impact load, as well as insert runout error, insert edge profile, and cutting conditions. As reported by the authors, the developed model can predict the average and maximum surface roughness values, and it can be used to estimate the texture of the surface to be machined during face milling processes.

In the source [131] the development of a mathematical model for the cusp height prediction was discussed by taking into account such terms as axial and radial depths of cut, surface curvature, and tool diameter. The results of the experimental campaign illustrated that the width of cut, i.e. step over or radial depth of cut, affects the cusp height value. It was also identified that when the step over is increased and cutter diameter is selected to be smaller, such combination produces the larger cusp height.

The work concluded in [22] deals with the study of a mechanism of the surface roughness formation in different feed directions during face-milling operation performed with toroidal ball nose and flat bottom end mills. The authors also worked on a study of the influence of different tool types on the scallop height value. According to the obtained experimental data, toroidal cutters provide smaller scallop height values compared to ball-end mills, and generate smaller surface roughness along the feed direction compared to flat bottom end mills.

The authors Zhang et al. in the source [155] studied the application of the Taguchi design for the surface quality optimization in CNC face milling operations. The proposed model includes such parameters as feed rate, spindle speed, and cutting depth. With the obtained experimental data, the authors identified a set of the optimal levels of selected parameters that provide the surface roughness optimization. The experimental results indicated that spindle speed and feed rate have greater influence on the surface than depth of cut.

In the work [47] another model for surface roughness prediction based on such parameters as cutting speed, feed, depth of cut, tool nose radius and flank width was presented. The experimental campaign carried out to verify the accuracy of the proposed model showed that cutting speed and cutting depth do not affect significantly the surface roughness. Nevertheless, the authors specified that if cutting depth is too large, chatter will occur thus increasing the surface roughness value. It was identified that the surface roughness value is affected by tool nose radius and feed rate values. Despite the large surface roughness can be produced by large feed values, this phenomenon does not occur when feed and tool nose are considered at the same time.

Another work presented by Luo et al. [84] reports the results of the development of a theoretical model of the scallop height formation mechanism used for the prediction of machined surface topography in ultra-precision milling process. By applying the proposed method it is possible to detect the topography value of any point on machined surface through discretizing cutting edge and meshing workpiece. The experimental verification of the developed model showed that increase of the scallop height value is directly proportional to the increase of feed per tooth value. As instance, the authors found that when the feed per tooth value is above 0.01 mm, the scallop height value increases greatly.

The authors Wang and Chang in their work [147] discussed the development of the regression models for the surface roughness prediction in dry and lubricated slot end milling operations. The proposed models are based on such parameters as cutting speed, feed rate, cutting depth, concavity, and axial relief angles of end mill cutting edge. The experimental verification of the proposed models illustrated that the most significant factors that affect surface roughness during dry and lubricated milling are different. For the dry-cut model it was stabilized that the most significant factors are cutting speed, feed, concavity and axial relief angles, while for the lubricated milling model the most significant factors are feed and concavity angle. The authors also specified that since the application of cutting fluid reduces the friction between tool and workpiece, the roughness in coolant (lubricated) conditions results greater than that in dry cutting conditions.

In the work [148] the authors Wang and Li presented a theoretical model for the scallop height prediction suitable for curvature surfaces machining. The proposed model is based on such parameters tool radius and local radius of the surface curvature. After having carried out the experimental campaign, the accuracy of the proposed model was confirmed.

Kim and Chu in the work [70] presented a method for the surface roughness estimation called *texture superposition method*. In the developed model the maximum roughness value is described as a function of feed per tooth, path interval, depth of cut, and geometries of tool and workpiece. In order to allow estimation of the surface

roughness for different milling processes, such as ball end milling, torus-shaped end milling, and flat end milling, the geometry of tool was represented by including a fillet radius term. In addition, in the model the surface roughness is determined by the maximum height of effective scallop including cutter runout effects caused by its geometric inaccuracy. As reported by the authors, from machining experiments with a three-axis machining center, the validity of the developed method was confirmed.

In the work [109] the authors presented a surface roughness prediction model based on the artificial neural network technique. The proposed model establishes the relationship between the surface roughness and such cutting parameters as spindle speed, feed and depth of cut. The model was trained based on the 58 experimental datasets, verified based on the 13 and tested on the 13 different datasets respectively. According to the collected experimental data, the average and maximum prediction errors of the developed model are found to be equal 3.5% and 8.7% respectively.

In the source [60] are reported the results of the development of a regression model for surface roughness prediction and Genetic Algorithm based optimization technique. In this work, the influence of such parameters as cutting speed, feed rate and depth of cut on the surface roughness was investigated for ball nose end milling process. Based on the experimental data of the performed 30 cutting tests, the authors built a second order mathematical model for surface roughness prediction, and applied the Genetic Algorithm with a purpose to optimize this model. The experimental validation of the optimized prediction model confirmed its accuracy, and showed that the observed difference between the predicted and measured surface roughness values amounts 8.9%.

Another authors Baptista and Simões worked on the analysis of the influence of milling parameters, such as stepover, feed per tooth, lead/lag angle and feed direction on the surface finish, and reported the obtained results in the source [20]. Based on the experimental data, a mathematical-statistic model for the surface roughness prediction that relates the roughness with stepover and feed per tooth values was developed. As specified by the authors, the results of the surface roughness measurements performed in

three directions (feed direction, 45.0° relative to the feed direction, and perpendicular to the feed direction) showed that the feed direction has no relevant influence on the surface roughness value, but influences machining time and dimensions of the part-program. Another important phenomenon highlighted by the authors illustrates that by replacing a ball nose mill with an end mill inclined along the feed direction, the scallop height dimensions result reduced, thus allowing to improve the surface roughness.

Despite the fact that a big amount of the works related to the development of the scallop height and surface roughness models have been performed and presented, any of them result suitable for the main purpose of this work. Due to this, in this chapter the development of the scallop height prediction model based on the mechanism of its formation during face milling processes will be discussed.

1.5.2 Scallop Height Model

The scallop height estimation model proposed in this chapter is based on the tool geometry, and takes into account the tool tip engagement angle, thus allowing to estimate the scallop height value in any region of the tool/workpiece engagement area. Figure 1.4 schematically shows the face milling process performed by a flat mill. In the scheme, h represents the maximum scallop height value, which can occur on the surface after using the tool with a tool tip radius, R_f, rotating in the direction ω. It can be observed that the scallop height value depends on the tool tip engagement angle, δ, and on the parameter k - the distance between the studying 'cutting line' and tool center track along the x axis.

The tool tip engagement angle, and consequently the distance k, depend on the tool tip angular position ϕ. In fact, when the angle δ is equal to *zero*, the scallop height has maximum value. Instead, when this angle is equal to $\pi/2$, there is no intersection between the tool tip and workpiece, such that the point P, which lies on the 'cutting line', is outside of the cutting zone, and the scallop height has a minimum value of *zero*.

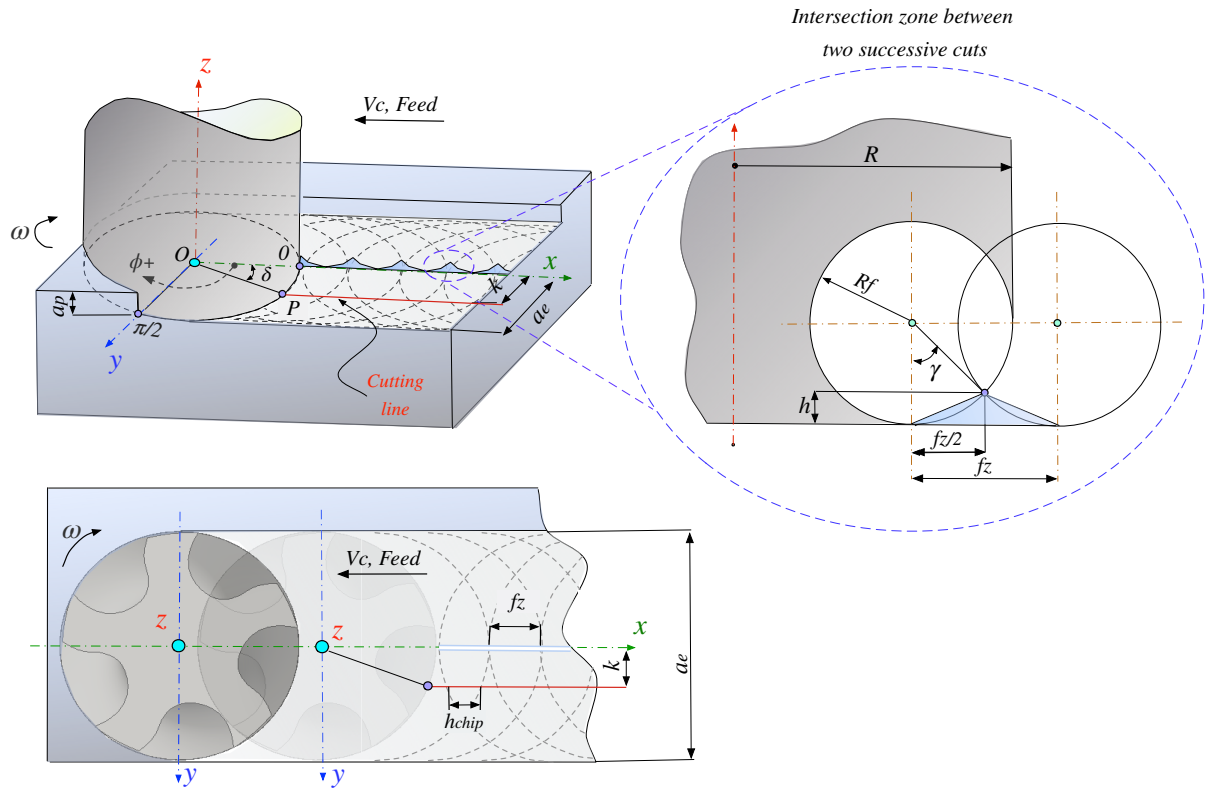

Figure 1.4: Scallop height formation mechanism and tool/workpiece intersection zone: h - scallop height; R_f - tool tip radius; R - tool radius; f_z - feed per tooth; h_{chip} - chip thickness that can be measured at the k distance from the center plane of the tool to the 'cutting line'; δ - tool tip engagement angle: P - point on the 'cutting line'; ϕ - tool angular position; a_p - cutting depth; a_e - cutting width; ω - tool rotation direction

To define the scallop height value at any tool tip angular position, i.e. along any 'cutting line', its length can be assumed as a chip thickness, h_{chip}, measured at the distance k from the center plane of the tool. Thus, the theoretical model for the scallop height value h calculation, the scallop length value h_{chip}, and the angle δ can be expressed by the following formulas:

$$h = R_f\Big[1 - \cos\ \Big[\sin^{-1}\ \Big(\frac{h_{chip}}{2R_f}\Big)\Big]\Big] \tag{1.1}$$

$$h_{chip} = f_z \cos(\delta) \tag{1.2}$$

$$\delta = \sin^{-1}\Big[\frac{k}{R}\Big] \tag{1.3}$$

1.6 EXPERIMENTAL VALIDATION OF THE PROPOSED MODEL

The validation of the proposed model was performed by means of an experimental campaign, which will be described below. The main purpose of this part is to confirm or to reject the dependence of the scallop height value on such parameters as feed per tooth, tool tip engagement angle, tool tip radius, and distance k.

The experimental campaign was designed as a fractional factorial plane consisted of $2^{4-1} = 8$ cutting tests. As the influencing factors were chosen four cutting parameters, such as f_z - feed per tooth (A), V_c - cutting speed (B), a_e - width (C) and a_p - depth (D) of cut. Each of 8 cutting tests was repeated four times, thus the total number of the performed cutting tests amounted 32. The levels of the factors, their values, and information about all tests are listed in the Table 1.1 and Table 1.2 respectively.

The whole experimental campaign was carried out on the Alesamonti MB63 five-axis machining center. As the cutting tool was used a WIDIA M680 series end-mill with 63.0 mm diameter and 5 cutting inserts WIDIA THM XPHT-AL 160408 with TiN coating. The radius of the tool tip, R_f, amounted 0.8 mm. As the workpiece was used the aluminum AA 6082-T6 block. The experimental set-up is presented in the Fig.1.5.

After each cutting test, the surface roughness R_z measurements were performed repeated three times for each test (96 measurements), and the average values of these three measurements of the surface roughness were recorded, and then used as the response values in the *Analysis of Variances* (ANOVA). All the measurements were performed at the distance $k = 4.0$ mm by using surftest SJ-210 series by Mitutoyo with a spherical-conical tip probe with a radius of 2.0 μm (Fig.1.5). The average measured surface roughness values are also reported in the Table 1.2.

To define an appropriate prediction model, the ANOVA was performed with the commercial software R by using the experimental data reported in the Table 1.2. The normality of the residuals was also checked. According to the obtained results, all four machining parameters, feed per tooth, cutting speed, width and depth of cut are correlated. The minimum response is achieved by using the following relation:

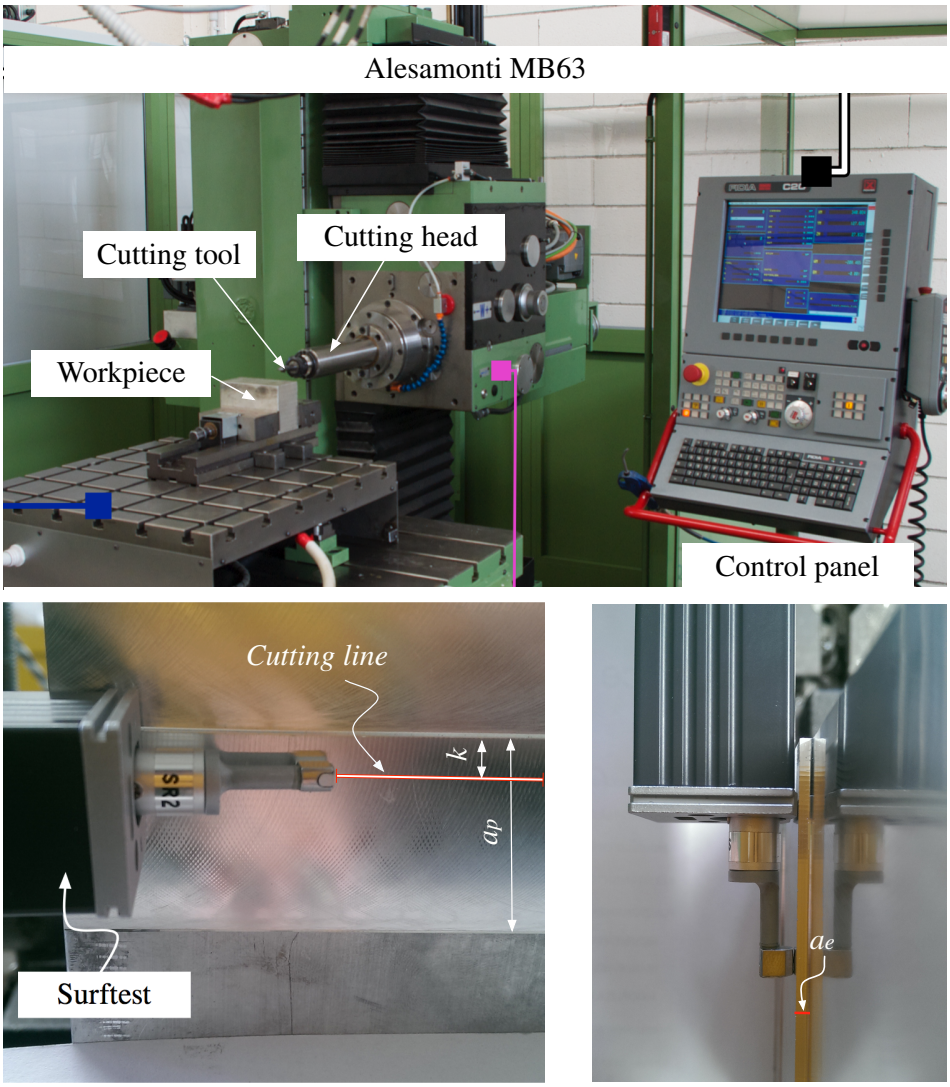

Figure 1.5: Experimental set-up: Alesamonti MB63 five-axis machining center; 63.0 mm diameter WIDIA M680 series end-mill; Mitutoyo profilometer SJ-210 series; a_p - axial cutting depth; a_e - radial cutting depth; k - distance at which a measuring line was selected

Table 1.1: Factors and levels

Level	A, mm/tooth	B, mm/min	C, mm	D, mm
Low	0.15	150.0	31.5	0.5
High	2.0	250.0	63.0	2.0

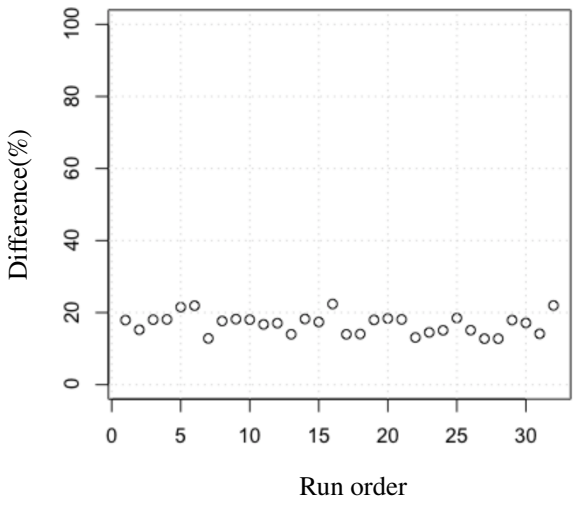

Figure 1.6: Theoretical model validation

$$log(R_z) = -12.1 + 0.2751A - 2.296 \cdot 10^{-2}B + 1.535 \cdot 10^{-3}C + \\ + 1.717 \cdot 10^{-2}D - 7.341 \cdot 10^{-3}BC \tag{1.4}$$

$$log(R_z) = -12.1 + 0.2751f_z - 2.296 \cdot 10^{-2}V_c + 1.535 \cdot 10^{-3}a_e + \\ + 1.717 \cdot 10^{-2}a_p - 7.341 \cdot 10^{-3}V_c a_e \tag{1.5}$$

The most significant terms identified for the empirical surface roughness prediction model (Eq.1.5) are: A - feed per tooth ($p-value < 2.0{\cdot}10^{-16}$), B - cutting speed ($p-value < 2.0{\cdot}10^{-16}$), D - depth of cut ($p-value < 2.0{\cdot}10^{-16}$), BC ($p-value = 3.29{\cdot}10^{-13}$). The less significant term is the factor C - cutting width ($p-value = 0.0101$).

The theoretical model (Eq.1.1) validation was performed by plotting the residuals. According to the obtained results reported in the Fig.1.6, the residuals, i.e. the difference between the theoretical (Eq.1.1) and empirical (Eq.1.5) models, is around 20.0%. Based on this result it was concluded that the proposed theoretical model is suitable for the scallop height prediction, and that it can be used to control the process quality, i.e. the surface roughness, within the framework of this research.

Table 1.2: Fractional factorial plane and average measured surface roughness R_z values: ω - spindle speed; F - feed rate

Exp.	ω, RPM	F, mm/min	A, mm/tooth	B, m/min	C, mm	D, mm	$\overline{R}_z$, μm
1	758.0	568.0	0.15	150.0	31.5	0.5	$4.223 \cdot 10^{-6}$
2	1263.0	1263.0	0.20	250.0	63.0	2.0	$7.283 \cdot 10^{-6}$
3	758.0	568.0	0.15	150.0	31.5	0.5	$4.230 \cdot 10^{-6}$
4	1263.0	947.0	0.15	250.0	31.5	2.0	$4.233 \cdot 10^{-6}$
5	758.0	568.0	0.15	150.0	63.0	2.0	$4.417 \cdot 10^{-6}$
6	758.0	568.0	0.15	150.0	63.0	2.0	$4.440 \cdot 10^{-6}$
7	1263.0	1263.0	0.20	250.0	31.5	0.5	$7.083 \cdot 10^{-6}$
8	758.0	568.0	0.15	150.0	31.5	0.5	$4.210 \cdot 10^{-6}$
9	758.0	758.0	0.20	150.0	31.5	2.0	$7.547 \cdot 10^{-6}$
10	1263.0	947.0	0.15	250.0	31.5	2.0	$4.230 \cdot 10^{-6}$
11	758.0	758.0	0.20	150.0	63.0	0.5	$7.413 \cdot 10^{-6}$
12	758.0	758.0	0.20	150.0	63.0	0.5	$7.443 \cdot 10^{-6}$
13	1263.0	947.0	0.15	250.0	63.0	0.5	$4.030 \cdot 10^{-6}$
14	1263.0	947.0	0.15	250.0	31.5	2.0	$4.240 \cdot 10^{-6}$
15	758.0	758.0	0.20	150.0	63.0	0.5	$7.473 \cdot 10^{-6}$
16	758.0	568.0	0.15	150.0	63.0	2.0	$4.467 \cdot 10^{-6}$
17	1263.0	947.0	0.15	250.0	63.0	0.5	$4.030 \cdot 10^{-6}$
18	1263.0	947.0	0.15	250.0	63.0	0.5	$4.033 \cdot 10^{-6}$
19	758.0	758.0	0.20	150.0	31.5	2.0	$7.527 \cdot 10^{-6}$
20	758.0	758.0	0.20	150.0	31.5	2.0	$7.563 \cdot 10^{-6}$
21	758.0	568.0	0.15	150.0	31.5	0.5	$4.223 \cdot 10^{-6}$
22	1263.0	1263.0	0.20	250.0	31.5	0.5	$7.103 \cdot 10^{-6}$
23	1263.0	1263.0	0.20	250.0	63.0	2.0	$7.220 \cdot 10^{-6}$
24	1263.0	1263.0	0.20	250.0	63.0	2.0	$7.270 \cdot 10^{-6}$
25	758.0	758.0	0.20	150.0	31.5	2.0	$7.573 \cdot 10^{-6}$
26	1263.0	1263.0	0.20	250.0	63.0	2.0	$7.273 \cdot 10^{-6}$
27	1263.0	1263.0	0.20	250.0	31.5	0.5	$7.077 \cdot 10^{-6}$
28	1263.0	1263.0	0.20	250.0	31.5	0.5	$7.077 \cdot 10^{-6}$
29	1263.0	947.0	0.15	250.0	31.5	2.0	$4.223 \cdot 10^{-6}$
30	758.0	758.0	0.20	150.0	63.0	0.5	$7.450 \cdot 10^{-6}$
31	1263.0	947.0	0.15	250.0	63.0	0.5	$4.037 \cdot 10^{-6}$
32	758.0	568.0	0.15	150.0	63.0	2.0	$4.443 \cdot 10^{-6}$

1.7 IMPROVEMENT OF THE EVALUATION AND PERCEPTION CONTROLLER

1.7.1 Formulation of Optimal Control Problem to Milling Process

In case of the automatic manufacturing, the OCP can be aimed at calculating the sequence of the inputs that permits a dynamical system to be controlled in an optimal way, thus allowing to maintain high productivity, quality, and low production cost. To formulate the OCP four elements have to be defined: model of the system, process controls, target functions, and set of the constraints.

In the studying system EPC, the feed rate $F(\zeta)$ and spindle speed $\omega(\zeta)$ represent the state of the machine, and they are grouped into the vector $x(\zeta)$ defined at each point of the curvilinear abscissa ζ. The process controlled variables are the linear acceleration of the axes $\dot{F}(\zeta)$ and angular acceleration of the spindle $\dot{\omega}(\zeta)$, described by the vector $u(\zeta)$. The OCP is represented as the multi-objective minimization, where the target function is defined by the weighted sum of the terms, associated to different process characteristics, such as productivity, quality, and costs. By changing the weights of the terms, the OCP can be easily applied to different applications, such as roughing and finishing operations, or hard metals processing.

The objective function associated to the process productivity (MRR) and costs (energy consumption and tool wear) is formulated as:

$$\begin{aligned} J(u(\zeta), x(\zeta)) = \int_{\zeta_i}^{Z} & \omega_{prod} J_{prod}(x(\zeta), u(\zeta)) \\ & + \omega_{energy} J_{energy}(x(\zeta), u(\zeta)) \\ & + \omega_{wear} J_{wear}(x(\zeta), u(\zeta)) d\zeta, \end{aligned} \tag{1.6}$$

where ω_{prod}, ω_{energy} and ω_{wear} are the weights associated to such terms as productivity, energy, and tool wear respectively.

The objective function $J(u(\zeta), x(\zeta))$ is integrated from the current position of the mill ζ_i to a future position Z (Fig.1.7). The element $J_{prod}(x(\zeta), u(\zeta))$ is associated to the process productivity in terms of the minimum time T_{min}, i.e. maximum MRR_{max}. The

energy consumption and tool wear are considered as $J_{energy}(x(\zeta), u(\zeta))$ and $J_{wear}(x(\zeta), u(\zeta))$ respectively. More detailed information about these terms can be found in the source [26].

On this basis, the OCP is formulated as :

$$\begin{aligned} &\text{Minimize:} \quad J \\ &\text{subject to:} \quad \begin{cases} f(\dot{x}(\zeta), x(\zeta), u(\zeta)) = 0 \\ (u(\zeta), x(\zeta)) \in C(u(\zeta), x(\zeta)) \\ B(x(\zeta_i), x(Z)) = 0, \end{cases} \end{aligned} \tag{1.7}$$

where the curvilinear abscissa ζ is the independent variable along the whole tool-path, described as a set of straight lines and arcs of circles with the interface points, where it is possible to set internal conditions according to the requirements (Fig.1.7); B is a set of the initial and final conditions on the state.

The term C in the Eq.1.7 represents a set of the constraints (limits) on the optimal cutting torque T_c, cutting power P_c, feed rate $F(\zeta)$, spindle speed $\omega(\zeta)$, feed per tooth f_z, and scallop height h:

$$C(x(\zeta)) = \begin{cases} T_c(\zeta) \leq T_{c,max} \\ P_c(\zeta) \leq P_{c,max} \\ F(\zeta)_{min} \leq F(\zeta) \leq F(\zeta)_{max} \\ \omega(\zeta)_{min} \leq \omega(\zeta) \leq \omega(\zeta)_{max} \\ f_z/f_{z,max} \leq 1, wC_{FeedLim}(\zeta) \\ h/h_{max} \leq 1, wC_{Scallop}(\zeta), \end{cases} \tag{1.8}$$

where $T_{c,max}$ and $P_{c,max}$ are the maximum torque and maximum power at the spindle respectively; $F(\zeta)_{max}$ - is the maximum feed rate; $\omega(\zeta)_{max}$ - is the maximum spindle speed of the machine; $f_{z,max}$ - is the maximum value of the feed per tooth recommended by the tool manufacturer; h_{max} - is the maximum scallop height corresponding to the technical requirements.

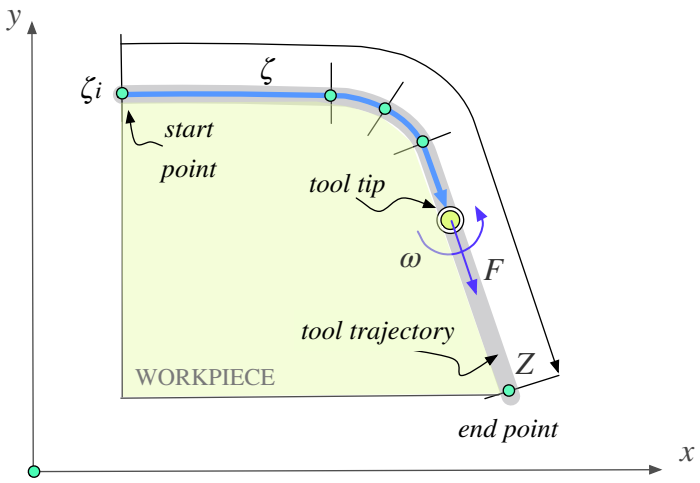

Figure 1.7: Schematic representation of the tool-path: ζ - curvilinear abscissa that defines tool tip instantaneous position; ζ_i and Z - initial and final values of ζ respectively; F - feed rate; ω - spindle speed

The maximum spindle speed, feed rate, cutting torque and power are set equal to the values reported on the data sheet by the machine manufacturer. The values $T_c(\zeta)$ and $P_c(\zeta)$ are calculated by using the approximate formula implemented into the model of the system. This formula describes the relationship between cutting power and material removal rate - the specific energy term, U_s, such as:

$$U_s = \frac{P_c}{MRR} = \frac{\omega T_c}{MRR}, \tag{1.9}$$

where

$$MRR = F(\zeta) a_p a_e \tag{1.10}$$

The spindle speed $\omega(\zeta)$ and feed rate $F(\zeta)$ values are calculated by using the following formulas:

$$\omega(\zeta) = \frac{V_c(\zeta)}{\pi D} \tag{1.11}$$

$$F(\zeta) = \omega(\zeta) f_z n, \tag{1.12}$$

where n represents the tool teeth number.

In the previous formulation of the OCP [26], the quality of the process was defined by considering the surface roughness and geometrical accuracy, which are affected by the acting cutting force and vibrations of the machine, and it was described as a term of the objective function $J(u(\zeta), x(\zeta))$ (Eq.1.6). The quality term was represented by three functions by taking into account: tool deflection, forced and self-excited vibrations.

In the present OCP formulation, what regards to the purpose of this chapter to improve the surface roughness characteristics, the quality term is no longer included into the objective function, but is described by the set of constraints $wC_{FeedLim}(\zeta)$ and $wC_{Scallop}(\zeta)$ (Eq.1.8). Such modification allows easy 'switching' of the OCP that can be applied to different cutting operations that have to be optimized. For example, the 'switching' between the normal and finishing cut can be simply done by specifying the type of the cutting operation in the G-code, and by changing the limits of the constraints in the *XOptima* while performing the offline state optimization (Fig.1.3). Moreover, this formulation provides better quality and controllability of the process, because the main term is not described as the desirable value, but as the limit which cannot be overcomed.

1.7.2 Implementation and Results

The system developed to test and evaluate the *Evaluation and Perception Controller* includes three elements: NC milling machine Alesamonti MB63 with a fixed column and movable table, measurement system, and the EPC installed on an industrial computer with a Dual Core Atom 1.6 GHz CPU (Fig.1.8 [26]).

The process state is reconstructed through the data recorded by the CNC FIDIA C20, and by a National Instruments CompactRIO 9012, which acquires the data from a triaxial accelerometer Dytran 3216M6 set on the cutting head, and 9-channels dynamometric table on which the workpiece is fixed. The dynamometric table includes three piezoelectric Kistler 9347C 3-component force links on top of which is fixed the working table. The system also includes the charge amplifier Kistler 5073 A311, used to convert the charge measured by there piezoelectric sensors into a voltage signal.

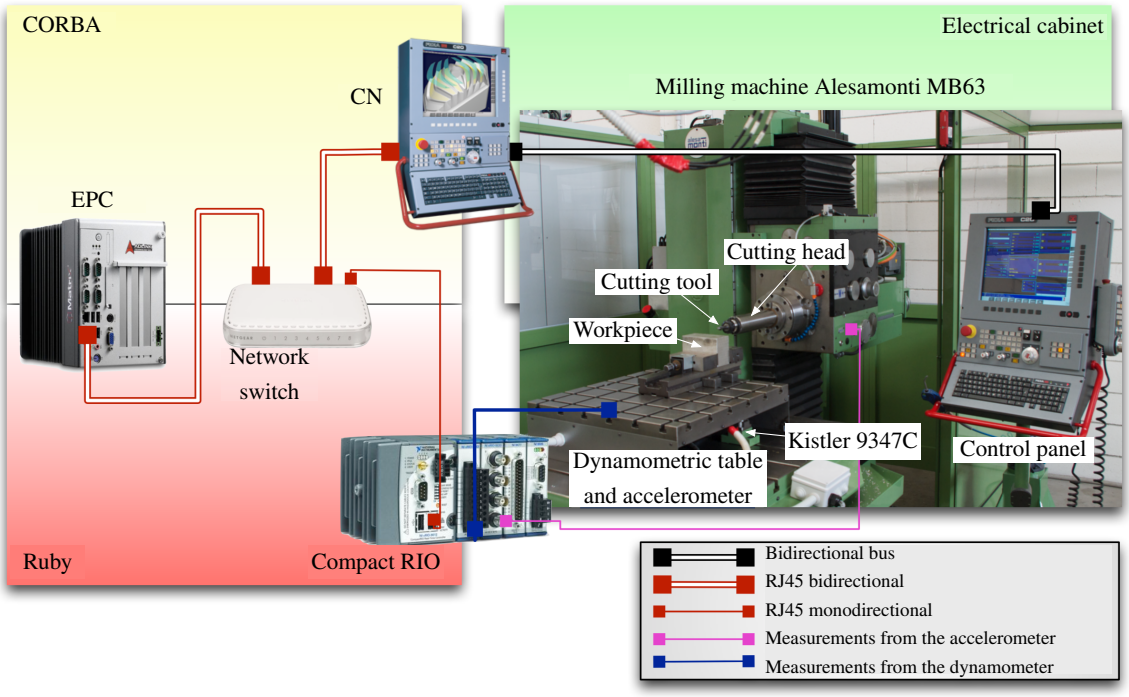

Figure 1.8: System used to evaluate the EPC [26]

The collected data is elaborated, and sent to the EPC at a low frequency (5.0 Hz) in order to have a communication that is synchronous with the optimization loop running at 5.0 Hz [26].

An experimental G-code part-program created to verify and evaluate efficiency of the proposed system with the reformulated OCP, where the scallop height is set as one of the process constraints, is shown in the Fig.1.9. As can be seen, the tool path consists of two parts: the 'first level', which is a simple face milling with 5.0 mm and 20.0 mm of the depth and width of cut respectively; and more complex 'second level' toolpath, which includes circular and angular interpolations with 4.0 mm cutting depth.

This part program was executed three times (Table 1.3): when performing a free cut (no EPC used), a cut supervised by the EPC with the target to maximize productivity ($f_{z,max}$), and a cut supervised by the EPC with limited scallop height value (h_{max}) calculated by using the proposed model (Eq.1.1).

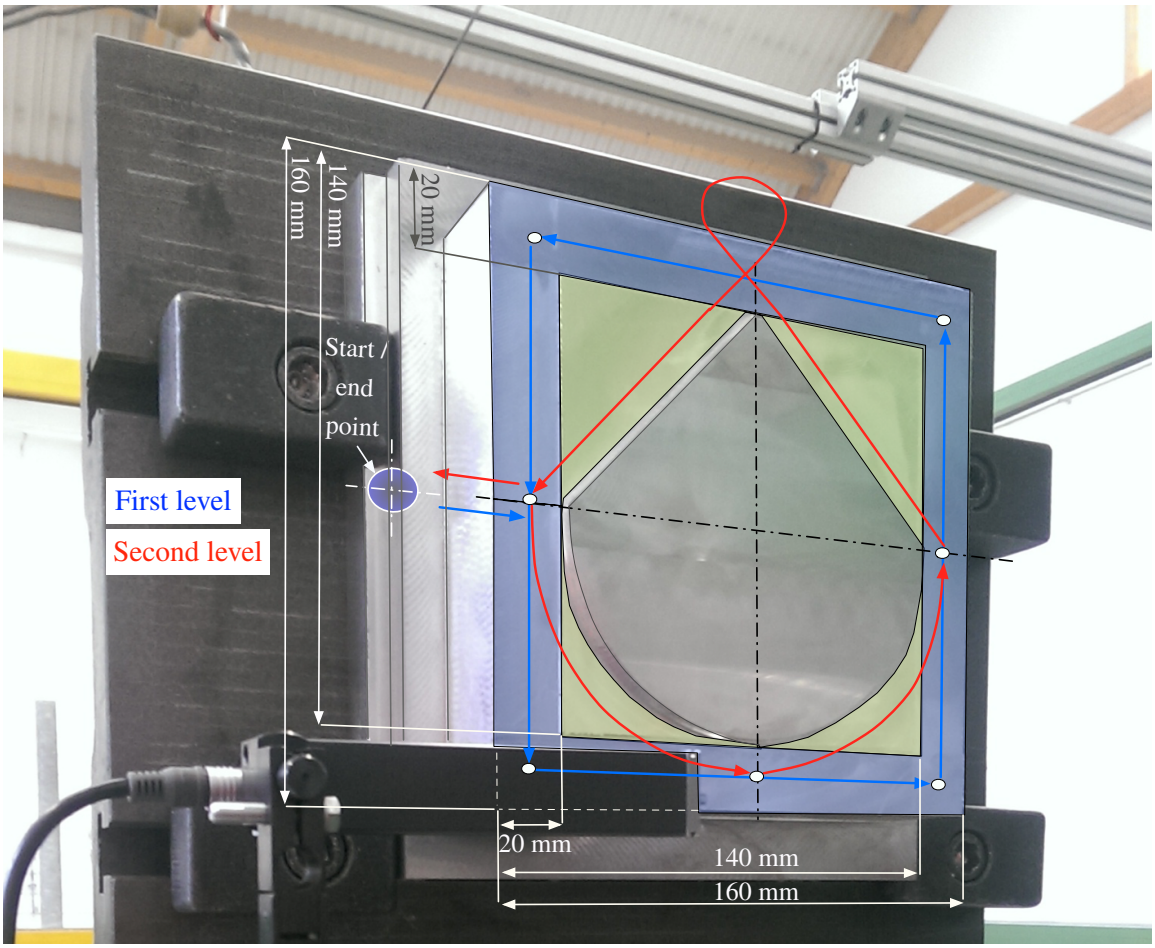

Figure 1.9: Workpiece and tool trajectory

A cubic workpiece 160.0 × 160.0 × 35.0 mm^3 made of aluminum AA 6082-T6 was used. As the cutting tool was selected a 63.0 mm diameter flat mill WIDIA M680 with five TiN-coated inserts THM XPHT-AL 160412 AL. The radius of the tool tip, R_f, is 0.8 mm. After each test, the surface roughness R_z measurements were performed. The measurement system, and the results will be discussed below in this section.

The results of the optimized process, the nominal and optimal controls, calculated in the OCP for the third milling operation (Table 1.3) are presented in the Fig. 1.10. In this figure, the nominal and optimal controls for the spindle speed $\omega(\zeta)$ and feed rate $F(\zeta)$ along the whole toolpath represented by the curvilinear abscissa are shown in *red*, *blue* and *green* respectively. The *black* line represents the cross section. As can be observed, the feed rate and spindle speed values are not kept constant along the tool path. When

Table 1.3: Experimental set-up

Operation	Limits / OCP formulation
Free	$V_c = 300.0$ m/min; $f_z = 0.2$ mm/tooth
EPC($f_{z,max}$)	$f_{z,max} = 0.25$ mm/tooth
EPC(h_{max})	$h_{max} = 4.83$ μm

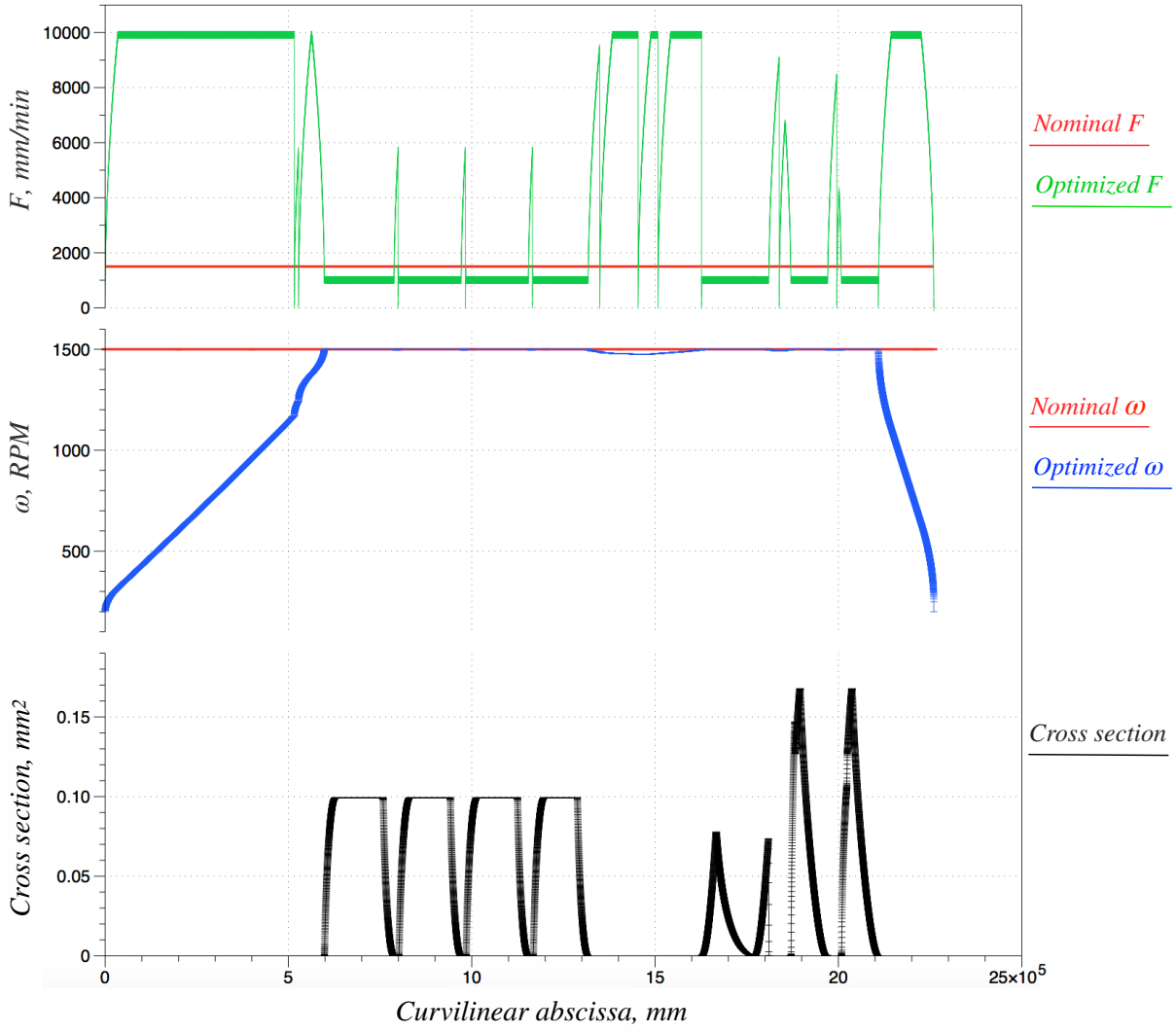

Figure 1.10: Nominal and optimal controls identified for the EPC(h_{max}) test (Table 1.3): F - feed rate; ω - spindle speed

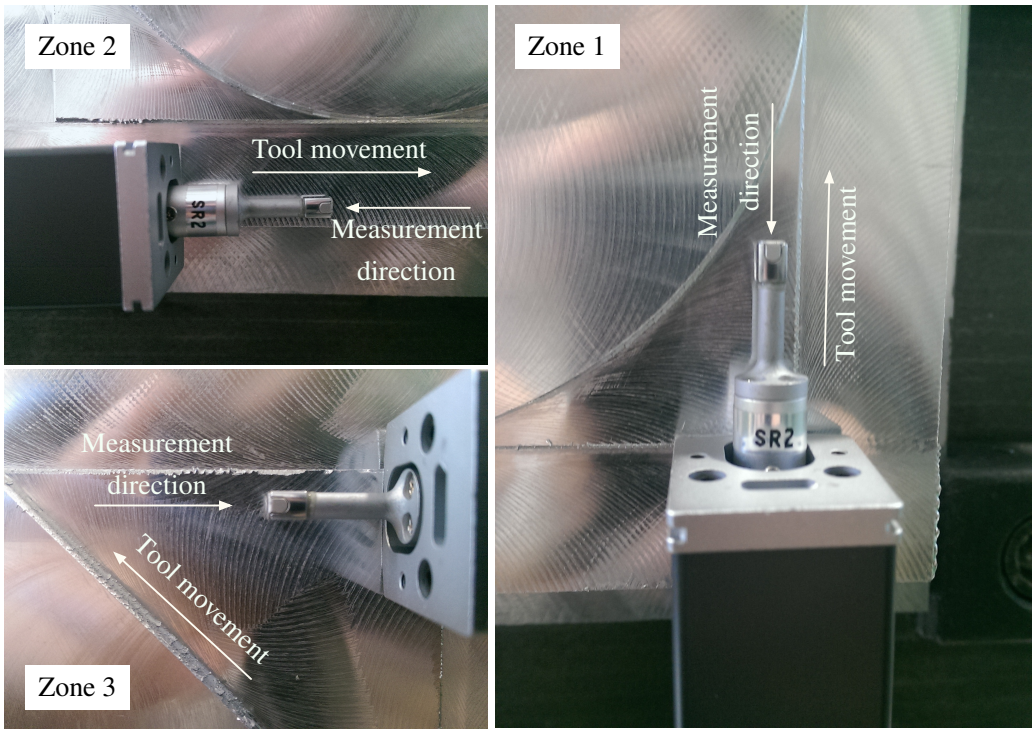

Figure 1.11: Surface roughness R_z measurements in three different cutting zones

the tool is moving in the 'in - air motion' zone, where no cut occurs, and consequently the cross section is null, the controller increases the feed rate and reduces the spindle speed, thus allowing to minimize the process time and energy consumption. Instead, in the zone where machining occurs (the cut cross section is greater than null), the cutting is governed by the opposite pair of controls - low feed rate and high spindle speed. As result, the quality characteristics can be improved due to the fact that the cutting forces tending to deflect the tool, and consequently to increase the scallop height, are reduced.

To confirm the improvement of the EPC in terms of the process quality, the surface roughness R_z measurements were performed in there different zones after each cutting test (Fig.1.11). Considering the fact that roughness is the result of the material removal rate along the curvilinear abscissa, the scallop height value is different in each cutting zone. As can be noticed in the Fig.1.11, among all three studying cutting zones, only the zone 2 corresponds to the conditions of the studying mechanism of the scallop height formation, which was reported in the Fig.1.4. Due to this fact, it is expected that the surface

Table 1.4: The average values of the surface roughness R_z plus/minus standard deviation obtained from the measurements performed after each cutting test listed in the Table 1.3

	$\overline{R}_z$ zone 1, μm	$\overline{R}_z$ zone 2, μm	$\overline{R}_z$ zone 3, μm
Free	9.69(40)	7.04(70)	6.99(30)
EPC($f_{z,max}$)	7.62(50)	5.92(70)	6.45(60)
EPC(h_{max})	7.19(40)	5.40(70)	6.14(30)

roughness R_z measurements that are performed in the zone 1 and zone 3 will be higher than the set limit equal to $h_{max} = 4.83$ μm. Nevertheless, in order to confirm the efficiency of the modified EPC it is necessary to perform the surface roughness measurements in all three cutting zones.

As shown in the Fig.1.11, the roughness R_z was measured in the opposite direction to the tool motion. The measurements were repeated three times after each cutting test, and the average values of the surface roughness R_z plus/minus standard deviation were calculated and reported in the Table 1.4.

According to the collected data, the lowest surface roughness values for all three cutting zones were achieved while performing the EPC(h_{max}) operation under the supervision of the EPC controller with constrained scallop height value (Table 1.3). As expected, the nearest value to the limit of $h_{max} = 4.83$ μm was observed in the zone 2, and it amounts 5.40(70) μm. Such results confirmed that the modification of the previous OCP formulation, where the surface roughness was represented as the element of the objective function, was successful, and that the performance characteristics of the discussed system EPC were improved.

SUMMARY

In this chapter, the state-of-the-art review of adaptive control techniques, such as adaptive control with optimization (ACO), adaptive control with constraints (ACO), and geometric adaptive compensation (GAC) applied to milling processes was discussed. It was shown that a lot of the systems proposed recently are based on such techniques as neural networks, fuzzy logic, regression models etc. used for the process model development, and that not all of them compute process control strategies by taking into account the geometry of cut, and consequently cutting forces and dynamics of the process. As result, these AC systems can be characterized as rigid and no practical.

The successful attempt to overcome these issues, the new supervision system called *Evaluation and Perception Controller* (EPC) developed by the Mechatronics group of the University of Trento and presented in the work [26], was discussed in this chapter. As mentioned previously, the developed process controller EPC is capable to simulate, optimize, monitor, and learn the milling processes. This system is based on the theoretical models used for process description, which are accurate enough to represent main phenomenons that occur in milling operations. The control strategy identification to achieve the desired targets, such as increase of productivity, decrease of energy consumption etc., is performed by involving the particular optimization technique called *Optimal Control Problem*, based on the system of *Differential Algebraic Equations* (DAE). The DAE describes the machine tool state (feed rate and spindle speed), and its dynamic characteristics (acceleration of the axes and spindle speed). As reported, the OCP strategy is aimed at the calculating the sequence of controls applied to the dynamical system, thus allowing to perform the process in the optimal way (according to the set goals, defined as a weighted sum of several contributions) along the whole tool path.

The research activities done in this chapter related to the improvement of the performance characteristics of the described system. In particular, the main goal was to improve the final quality of the product, associated to the scallop height value - one of the surface roughness characteristics. With this purpose, the state-of-the-art review of the available scallop height and surface roughness models was done. Since the main part of the found models are neural networks or fuzzy logic based, and since they require large amount of training data, the theoretical model for the scallop height prediction that takes into account tool geometry, tool tip engagement angle, and allows to estimate scallop height in any region of the engagement area was developed. The validation of the proposed model was done by comparing it against the empirical model of the surface roughness R_z, built based on the 32 experimental tests data, that was also developed in this chapter. According to the results of the validation, the difference between both models amount around 20.0%.

Based on this, the theoretical model was selected for the EPC improvement consisted in implementing this model into the *XOptima* library as one of the constraints (and not as target functions), thus allowing to control the surface roughness value close to the desired and requested limit, without the possibility to overcome it.

The efficiency of the modified system was also verified experimentally. Three different face milling operations were performed under different conditions: free cut (without control), supervised cut with the target to maximize productivity, and supervised cut with limited scallop height value. According to the collected measured data reported in the Table 1.4, the lowest surface roughness R_z was observed for the third operation with limited scallop height value, thus confirming that the improvement of the discussed system, EPC, was successful.

Chapter 2

Application of Numerical Modeling Techniques to Milling Processes

In this chapter the application of the finite element modeling (FEM) techniques to milling processes is discussed and studied. In particular, such arguments as model formulation (the Lagrangian, Eulerian, and Arbitrary Lagrangian-Eulerian), meshing techniques, friction models (the Coulomb, Tresca, and Coulomb-Tresca), chip separation, and material constitutive models (the Oxley, Johnson-Cook, and Zerilli-Armstrong) are briefly discussed. Another important arguments such as 3D FEM set-up in AdvantEdge v.7.0 by Third Wave, types of different CAD (STEP and STL) models used to describe tool geometry, techniques required to create meshes for both types of CAD models are described in detail.

The main purpose of this chapter is to evaluate the influence of CAD tool models (STEP and STL) on the accuracy of 3D FEM AdvantEdge numerical simulations of side down-milling process in terms of cutting forces and chip geometries. The research activities and selection of the arguments to study within the framework of this chapter were performed in collaboration with a production unit of Sandvik Coromant placed in Rovereto (Italy). Since STEP and STL tool models are widely used by their R&D center when designing new cutting tools, the discussed arguments and performed analysis reported in this chapter are of particular importance to this company.

A few different examples of the side down-milling process 3D FEM simulations and experimental data results are reported in this chapter. All 3D FEM simulations were performed by using the commercial software AdvantEdge v.7.0. Both, the software and CAD tool models, were provided by the production unit of Sandvik Coromant. The chapter also contains the data about the evaluation of such numerically predicted parameters as cutting forces and chip geometries compared against experimentally obtained data, collected during an experimental campaign carried out on the DMU-60T machining center, placed in Sandvik Coromant.

2.1 FINITE ELEMENT MODELING OF CUTTING PROCESSES

Cutting operations, and in particular milling, are widely used in manufacturing industry. The knowledge about process, about influence of cutting parameters on process performance (cutting forces, temperatures, tool life etc.), and consequently on product quality, is critical and very important information manufacturers have to possess in order to succeed in their field. Experimental approaches to study cutting processes behaviour are quite expensive and time-consuming, and require involving of different equipment for measurement and monitoring of studying process parameters.

In recent years FEM methods had received a lot of attention, and many tool manufacturing companies started to use them to highlight behaviour of the fundamental variables like cutting forces, temperatures, and chip shape when designing new products.

A few different commercial numerical solvers for FEM modeling of cutting processes, such as Deform, Abaqus, LS-Dyna, and AdvantEdge are available nowadays. The choice of the software is very important since assumptions and numerical techniques, and consequently solving capabilities applied in each of them are different. Due to this fact, such characteristics as robustness of the software, time-consuming, and its accuracy have to be studied and evaluated.

2.1.1 Model Formulation

There are three traditional ways of FEM formulation in metal cutting: the Lagrangian problem, the Eulerian problem, and the Arbitrary Lagrangian-Eulerian (ALE) problem.

Lagrangian formulation

The Lagrangian formulation is mainly used in solid mechanics problems. In this formulation, the finite element (FE) mesh is placed on workpiece material, and software uses a certain criteria to separate chip from workpiece. In other words, workpiece is fixed in space, and cutting tool is fed into it, thus imposing displacement boundary condition which drives plastic deformation [134].

The chip separation criteria consists in deleting elements, and is based on a geometrical distance of tool tip to closest workpiece element, plastic strain and strain energy density [114]. Since the FE mesh covers whole cutting region, this makes it highly preferable when unconstrained flow of material is involved. When applying the Lagrangian formulation, chip geometry is defined as a function of cutting parameters, plastic deformation process and material properties, and it is possible to determine chip geometry from the initial to steady state [69]. Besides, chip separation criteria can be defined to simulate processes characterized by discontinuous chips or material fracture.

In some cases, the Lagrangian formulations are used together with the mesh adaptivity and automatic remeshing techniques. When these techniques are applied, old fields of state variables are mapped to the new one, thus introducing some numerical diffusion [114].

Eulerian formulation

In the Eulerian formulation, the FE mesh is fixed in space, and material flows through the control volume. In other words, cutting tool is fixed in space, and workpiece material is treated as a fluid that flows through the volume in front of it [134].

In order to develop numerical simulation, chip shape has to be predefined (no chip separation criteria is needed), thus allowing to simulate cutting process starting from steady state, such that there is no need to integrate from the starting to stable conditions,

and to do remeshing. Such parameters as chip thickness, tool-chip contact length and contact conditions between tool-chip must be kept constant during analysis, what makes the Eulerian formulation to be inappropriate for deformation process description [14].

Since chip shape depends on many factors, it is difficult to predefine chip shape that would correspond to the exact real geometry. Due to this, the Eulerian formulation is pretty difficult, and requires advanced skills. Another disadvantage of this type of model formulation is that it cannot be easily adapted to model the unconstrained flow of material, and as a consequence it cannot be used to simulate serrated and discontinuous chip formation [114].

Arbitrary Lagrangian-Eulerian (ALE) formulation

The finite element Arbitrary Lagrangian-Eulerian (ALE) formulation was developed as an attempt to avoid and overcome the disadvantages of the Lagrangian and Eulerian formulations. The ALE formulation combines the best features of the Lagrangian formulation where mesh follows material, and the Eulerian formulation where mesh is fixed and material flows through it.

In the Arbitrary Lagrangian-Eulerian formulation, the finite element mesh is neither fixed spatially nor attached to workpiece material - it is independent of material motion. In particular, mesh follows material flow, and problem is solved for displacements in the Lagrangian step, while mesh is repositioned in cutting area around tool tip, and problem is solved for velocities in the Eulerian step. Consequently, the ALE formulation does not need a criteria to separate chip, since it occurs as a function of the plastic deformation of workpiece material [122].

Generally, the ALE formulation results to be cheaper than the Lagrangian formulation, but needs preformed chip, which puts some restriction to the ALE formulation to predict different chip shapes such as serrated and discontinuous [114].

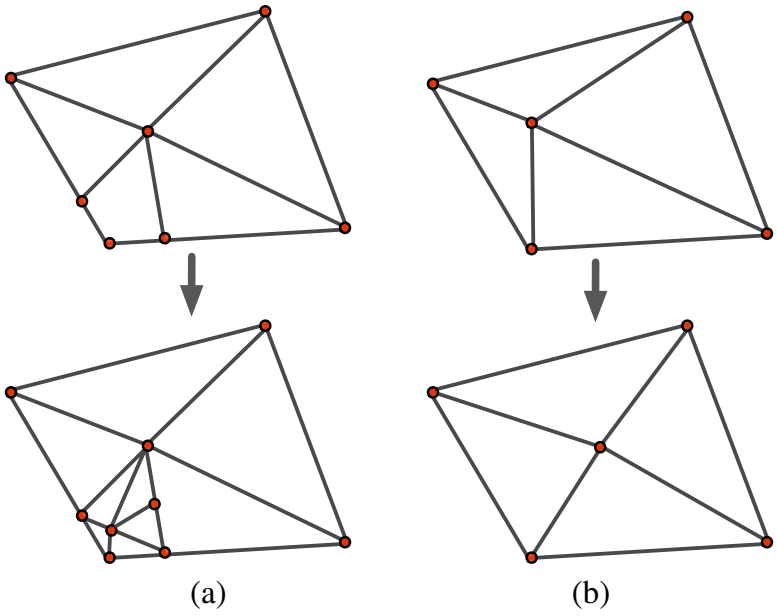

Figure 2.1: Meshing techniques: (a) - refinement; (b) - smoothing

2.1.2 Mesh Design

The very first step when performing FEM is to divide studying, i.e. solution, space into finite elementary regions, such as lines, areas or volumes, called elements. This procedure is called discretization or meshing.

In the metal cutting modeling initially designed mesh can not follow or keep its original shape, and it is distorted due to the plastic deformations that occur during cutting. This leads to the fact that distortion causes convergence rate and numerical errors, thus making the further process simulation impossible. To overcome this problem, new mesh must be generated by applying adaptive mesh procedure, thus changing its size and distribution.

Several adaptive meshing techniques are available: remeshing, smoothing, and refinement [14]. Remeshing is a technique that includes generation of a completely new FE mesh out of the existing distorted mesh. Refinement is a technique which is based on the increasing of local mesh density by reducing size of local element (Fig.2.1(a)). Finally, smoothing is a technique that uses the reallocation of individual nodes to improve local quality of the mesh (Fig.2.1(b)).

In the regions where strong gradients of variables occur, a higher mesh definition, i.e. density, is required in order to decrease solution errors. Since these gradients are unknown at the beginning, the adaptive mesh generation procedure starts with a relatively large primary mesh, and after the solution for this mesh is found, the mesh density is increased.

2.1.3 Chip Separation

Material separation is a complex phenomenon that involves many different physical processes occurring at the micromechanical level [125]. In the work [69] the author distinguishes two following methodologies to model chip separation from workpiece: to define the chip separation criteria along a predefined line, and to use the continuous remeshing technique based on the large plastic deformation. In the work [140] the authors use another classification of the chip separation criteria: the implicit Lagrange's formulation (ILF), and explicit Lagrange's formulation (ELF). In the work [32] the authors distinguish the geometrical and physical chip separation methodologies.

The first technique, the implicit Lagrange's formulation, which is also called $node - splitting$, is usually used to simulate steady-state cutting [14]. In this formulation, the chip and workpiece are described by their own meshes connected until separation, which is allowed only along a certain line lying on cutting plane parallel to workpiece surface on the height of tool tip (Fig.2.2). Each cell in mesh consists of two nodal points, and it is described by two states: no separation or separation, which depend on a certain distance between tool tip and next element along separation line. In the Fig.2.2 this distance is reported as a parameter D. Node separation occurs when this distance becomes less than a predefined critical value. When node is separated from workpiece, it becomes part of chip volume. With the progression of tool described by cutting speed V_c, workpiece continues to be deformed, and chip continues to be formed.

In this formulation, the global stiffness matrix is used in the generalized FEM model to find FEM solution, and calculation of current quantities of studying system in one time step are based on quantities calculated in previous time step.

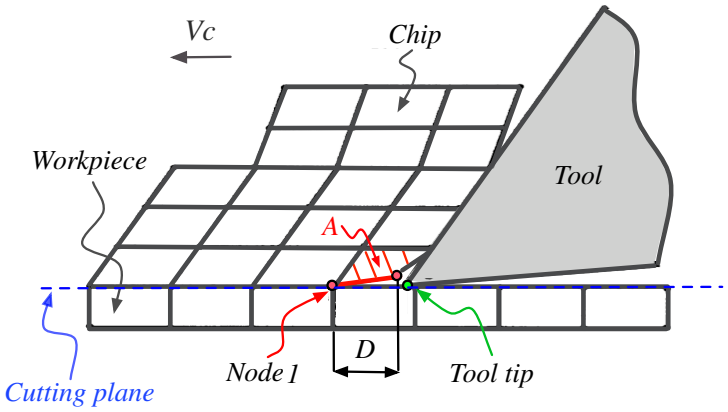

Figure 2.2: Separation of nodes based on the distance D between the tool tip and node immediately ahead

In the second physically based technique, the explicit Lagrange's formulation, the equations of motion are integrated directly (not iteratively) and explicitly, such that no stiffness matrix is used. The stresses are directly calculated in the integration from the element stresses after each single time step [140], and it is assumed that separation of two nodes takes place when the value of a predefined physical parameter, such as stress, strain or strain energy density at *Node1* or element A (Fig.2.2) achieves a predefined critical value, selected depending on workpiece material properties and cutting conditions.

According to the opinion of the authors of the works [69] and [14], the physical criteria seems to be more accurate in modeling chip separation because it is based on workpiece properties.

2.1.4 Material Constitutive Models

In cutting operations, material flow stress is an instantaneous yield stress, and it depends on such parameters as strain, strain rate, and temperature. The description of the flow stress curve is performed by using constitutive equations, i.e. material laws. Several material constitutive models are used in FEM of metal cutting, including such laws as rigid-plastic, elasto-plastic, viscoplastic, elasto-viscoplastic, etc. in order to model workpiece flow stress properly, and to obtain true results.

A wide number of different constitutive models is available nowadays. Among them, such important models as the Oxley model [102], Johnson-Cook model [62], Zerilli-Armstrong [154], Usui-Shirakashi model [143], Mechanical Threshold Stress model [19], Steinberg-Cochran-Guinan-Lund (SCGL) model [133], Preston-Tonks-Wallace model [113], Adibi-Sedeh model [7], Koppka model [73], Shi and Liu [124] are widely used to describe the workpiece flow stress [54].

In this chapter only a few constitutive equations, such as the Oxley, Johnson-Cook, Zerilli-Armstrong models will be briefly discussed.

Oxley material model

The authors Oxley et al. in their work [102] presented a material constitutive model based on the experimental observations of material deformation. As specified in the work [61], in this model the *velocity-modified temperature* concept to describe material properties as a function of strain rate and temperature is applied:

$$\sigma = \sigma_1 \mathcal{E}^n, \tag{2.1}$$

where σ and $\mathcal{E}$ are the flow stress and strain respectively; σ_1 is the material flow stress at $\mathcal{E} = 1.0$; and n is the strain hardening exponent.

The terms σ_1 and n depend on the velocity modified temperature, which is defined as:

$$T_{mod} = T\left(1 - \nu \log \frac{\dot{\mathcal{E}}}{\dot{\mathcal{E}}_0}\right), \tag{2.2}$$

where T and $\dot{\mathcal{E}}$ describe the testing temperature and strain rate respectively; ν and $\dot{\mathcal{E}}_0$ are the workpiece material constants.

Johnson-Cook material model

The Johnson-Cook is a purely empirical thermo-elasto-visco-plastic material constitutive model [62]. This model assumes that the flow stress is independently affected by strain, strain rate, and temperature independently, such as:

$$\sigma = \left(A + B\mathcal{E}^n\right)\left(1 + C\ln\frac{\dot{\mathcal{E}}}{\dot{\mathcal{E}}_0}\right)\left(1 - \left(\frac{T - T_r}{T_m - T_r}^m\right)\right), \tag{2.3}$$

where the first term $\left(A + B\mathcal{E}^n\right)$ is a elastic-plastic term, and it describes the strain hardening; the term in the second parenthesis is a viscosity term, and it shows that when the material is exposed to the high strain rates, the flow stress of the material increases; and the third term, the third parenthesis, is a temperature softening term; A, B, C, n and m are the material constants identified by material tests; T, T_r and T_m are the instantaneous temperature, room temperature and melting temperature of a given material respectively.

Zerilli-Armstrong material model

The authors Zerilli and Armstrong in the work [154] worked on the development of two microstructure-based constitutive equations. The authors used the face-centered cubic and body-centered cubic metals to analyze their temperature and high strain rate responds, and they noticed a significant difference between these materials. The presented models are physically based, and assume that the strain dependence on the flow stress in body-centered cubic structures is not affected by the strain rate and temperature, while for the face-centered cubic structures it is done the opposite assumption. The flow stress models are described by the following equations:

1. The constitutive equation to describe the flow stress for the body-centered cubic metals:

$$\sigma = C_0 + C_1\exp\left(-C_3T + C_4T\ln\frac{\dot{\mathcal{E}}}{\dot{\mathcal{E}}_0}\right) + C_5\mathcal{E}^n \tag{2.4}$$

2. The constitutive equation to describe the flow stress for the face-centered cubic metals:

$$\sigma = C_0 + C_2\mathcal{E}^{-1/2}\ \exp\left(-C_3T + C_4T\ln\frac{\dot{\mathcal{E}}}{\dot{\mathcal{E}}_0}\right) \tag{2.5}$$

In the Eq.2.4 and Eq.2.5 C_0 is a component of the stress that accounts for the dislocation density on the flow stress; C_1-C_5 and n are workpiece material constants; T is the absolute temperature.

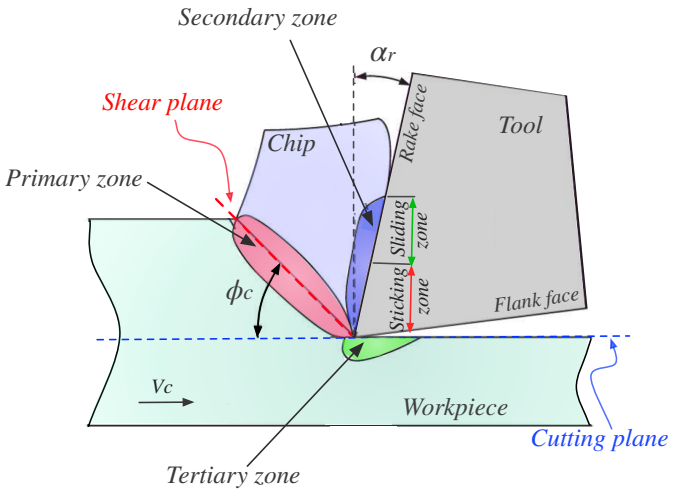

Figure 2.3: Deformation zones: V_c - cutting speed; α_r - tool rake angle; ϕ_c - shear angle

2.1.5 Deformation and Heat Generation Zones

During cutting three deformation zones occur in the tool/workpiece interaction: primary, secondary, and tertiary. As can be seen in the Fig.2.3, when the cutting edge of tool starts to penetrate into the workpiece, a part of material is sheared away over the primary zone, and chip is generated. In this zone the deformation of workpiece material is caused only by the shearing action. After the chip is generated, it starts to stick to the tool rake face (sticking region), and when the friction stress value on the tool rake face reaches the shear yield stress value of material, chip starts to slide along the secondary deformation zone (sliding region). The tertiary deformation zone occurs between the tool flank face and newly machined surface, and it is caused due to the friction between these two surfaces.

The heat is generated mainly in the primary and secondary shear zones. In the primary zone the heat is caused due to the plastic deformation of material that occurs on the shear plane. In the secondary zone the heat is caused due to the friction between cut material and tool rake face that occurs along chip-tool contact length. The highest temperature usually occurs in the sliding region [65]. Another frictional heat source can be generated in the tertiary zone, where tool flank face is in the contact with workpiece.

In the work [24] the authors reported the following equations to calculate the rate of the specific volumetric flux and of the generated heat:

1.1 The rate of the specific volumetric flux due to the plastic work:

$$\dot{q} = \frac{\zeta k \dot{W}^P}{\rho}, \tag{2.6}$$

where $\dot{W}^P$ is the plastic work rate; k is the fraction of the plastic work converted into the heat; ζ is the mechanical equivalent of the heat; ρ is the density of material to be machined.

1.2 The rate of the generated heat due to the friction:

$$\dot{Q} = F_{fr} V_r \zeta, \tag{2.7}$$

where F_{fr} is the friction force; V_r is the relative sliding velocity between tool and chip; ζ is the mechanical equivalent of the heat.

The authors also reported a formula to calculate the workpiece loses heat to the environment due to the convection:

$$q_h = h(T_w - T_0), \tag{2.8}$$

where h is the convection heat transfer coefficient of workpiece material; T_w is workpiece surface temperature; T_0 is ambient temperature.

2.1.6 Friction Models

Friction that occurs on the interaction and engaged surfaces plays an important role in prediction of such parameters as cutting forces, temperatures and tool wear in metal cutting. Friction models are used to describe contact conditions of tool/chip interactions. The accuracy of these models depends on the boundary conditions because they directly affect cutting forces and distribution of the stresses and temperatures on tool rake surface, and due to the fact that the high strain and temperatures occur in cutting region, usually

it is not so easy to identify these contact conditions experimentally. As result, frictional parameters are assumed based on experimental tests conducted on much lower strain and temperature [115].

In this section a general information about only three friction models, such as the Coulomb friction, Tresca friction, and Coulomb-Tresca friction will be reported.

Coulomb friction model

The friction law developed by Coulomb was introduced in 1773 [68], and it is valid for the elastic contact description between two surfaces. In this model, the friction coefficient is assumed to be constant over the entire rake surface, and the law says that the friction (shear) stress is proportional to the normal stress:

$$\tau = \mu\sigma_n, \tag{2.9}$$

where τ is the frictional stress; σ_n is the normal stress; μ is the friction coefficient.

Tresca friction model

The Tresca friction model, called also the shear friction model, was developed based on the assumption that the frictional stress on tool rake face is constant. In the model the low stress variation of the frictional stress and normal stress are neglected:

$$\tau = mk, \tag{2.10}$$

where τ is the frictional stress; $0 \leq m \leq 1$ is the friction factor; k is the shear flow stress of workpiece material.

Coulomb-Tresca friction model

According to the work [160], and as it has already been mentioned, there are two different zones that occur during tool/chip interaction in the secondary deformation zone: the sticking and sliding zone (Fig.2.3).

In the sticking region very high values of the normal stress occur, while the frictional stress is assumed to be equal to the equivalent shear stress limit of workpiece material,

such that no relative motion exists between tool and chip, and the Tresca model can be applied. In the sliding zone, instead, the normal stress is small, and relative sliding of chip on tool rake surface is observed, such that the Coulomb model can be applied [115].

An open question that regards the application of the Coulomb–Tresca model is to identify the length of the sticking and sliding zones. In recent years some research has been done in order to find solutions for this problem [123], [104], [5], [18], and [15].

2.2 AdvantEdge BY THIRD WAVE SYSTEMS

AdvantEdge is the Lagrangian, explicit finite element package, that was written with machining operations in mind. Thereby, the solvers applied into the software are optimized specifically for metal-cutting processes [49]. AdvantEdge has the pre-programmed modules for both 2D and 3D machining operations including turning, up-milling, down-milling, sawing, broaching, and micro-machining. The software has a very user-friendly and intuitive interface, and only several input values are needed in order to predict thermo-mechanical behaviour of machining operations.

Based on the information presented in [89], in the Fig.2.4 the author of the present work reports a generalized supplemented scheme on how the set-up of simulation in AdvantEdge is done, and which output information can be obtained. As can be seen from this figure, when FEM is applied for machining operations, the process set-up is based only on cutting parameters such as cutting speed, cutting width and depth, feed rate etc. As was mentioned by the authors in [89], it is worth noting that although every input is important, and if the cutting conditions are kept the same, the material flow stress and friction coefficient, among all inputs, are the most representative in the simulations reliability.

AdvantEdge has a very simple procedure to set up tool and workpiece geometries, and it has a built-in editor to create simple tool and workpiece geometries. In addition, such important options as the import of more complex tool and workpiece geometries, and advanced set-up of meshing parameters are also available.

Material selection for both tool and workpiece is based on the very extensive material library that contains models of many engineering metals and alloys, including several aerospace alloys. If a user has to specify a new material, the procedure is very simple since AdvantEdge provides a possibility to enter materials properties by using different models.

However, since this software is an automated program, the boundary conditions, i.e. the heat exchange with environment and velocity at contact between objects in the model [38], are hidden. To model thermal-visco plastic behavior of workpiece material, the software uses the Johnson-Cook material law. Friction behaviour is described by the Coulomb friction law.

In Third Wave AdvantEdge there is no separation criteria defined since chip formation is assumed to occur due to the plastic flow, therefore, the chip is formed by continuously remeshing the workpiece. When a simulation is running, workpiece material flows around cutting edge of tool, and remeshing takes place whenever elements from cutting edge area change their initial shape [39]. By applying this technique, automatic remeshing, modeling and simulation of milling of complex geometry workpieces can be performed.

According to the information provided in [138], the main benefits and advantages of using AdvantEdge software are:

1. Reduction of number of expensive cutting tests
2. Extension of tool life and reduction of tool breakage
3. Faster machining processes
4. Efficient productivity, increase of material removal rates and machine utilization
5. Improvement of tool geometries and chip control etc.

Nevertheless, AdvantEdge does not give the user much flexibility in configuring the controls of the solver [87]. Due to this fact, the user is restricted to the preset controls of the software.

In the present work, the commercial software AdvantEdge v.7.0 by Third Wave Systems was used as FEM environment.

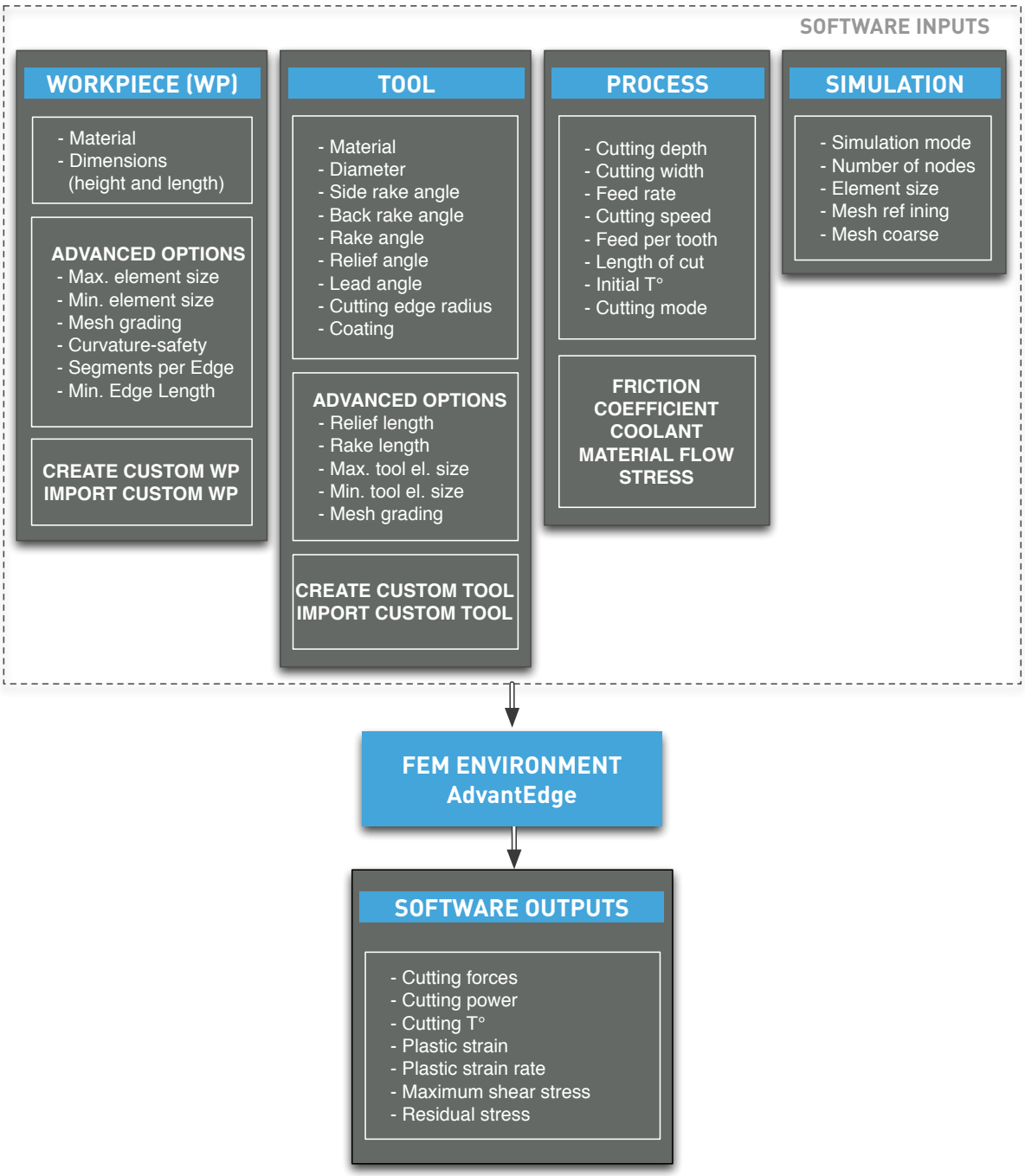

Figure 2.4: AdvantEdge machining software possible inputs and outputs

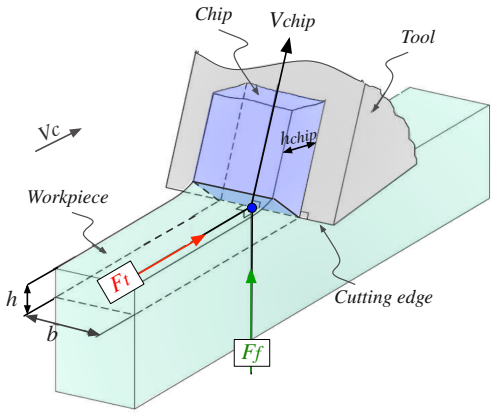

Figure 2.5: Schematic representation of orthogonal cutting process geometry: V_c - cutting speed; V_{chip} - chip velocity; h - undeformed chip thickness or feed per tooth value; h_{chip} - deformed chip thickness; F_t - tangential (cutting) force; F_f - feed force; b - cutting width

2.3 2D FEM FOR CUTTING FORCES SIMULATION

2D FEM AdvantEdge can be used for the analysis of such processes as turning, sawing, down-milling, up-milling, and broaching.

In 2D FEM of milling processes, the principles of orthogonal and oblique metal cutting are applied. In the present work only a brief description of orthogonal cutting process will be presented in this chapter.

In orthogonal cutting process, workpiece material is removed by cutting edge that is perpendicular to the direction of relative tool/workpiece motion [9]. Orthogonal cutting means cutting of a plane surface that meets the following conditions: cutting edge is normal to the main cutting motion; length of cutting edge is larger than cutting width; during process cutting speed remains constant [39].

Schematically, orthogonal cutting process can be illustrated as shown in the Fig.2.5. As can be seen, during the cut, a metal chip of the width b and depth h is sheared away from a workpiece due to the tool motion against it. Since the shearing action is assumed to be uniform along the cutting edge, orthogonal cutting represents two-dimensional or plane strain process. The forces acting on the workpiece occur in two directions: along cutting velocity and uncut chip thickness, and are called tangential F_t and feed F_f forces.

2.3.1 Literature Overview

In the past years a lot of research has been done to evaluate the effectiveness and accuracy of 2D FEM AdvantEdge in terms of cutting forces modeling, and in this section only the recent reports will be discussed.

The authors Kadirgama et al. in the work [63] used 2D FEM AdvantEdge to estimate cutting and thrust forces that occur in dry end milling process of steel AISI P20. The authors performed 29 cutting tests and process simulations by using the following cutting data: cutting speed 100.0, 140.0, 180.0 m/s; feed 0.1, 0.2, 0.3 mm/rev; axial depth of cut: 1.0, 1.5, 2.0 mm; radial depth of cut: 2.0, 3.5, 5.0 mm. All cutting tests and simulations were performed by using a square shape insert KC735M with 0.004 mm TiN coating, and with geometry represented by a back rake angle of 0°, clearance angle of 11.0°, and nose radius of 0.794 mm. The comparison of the collected data showed that for the most of the performed tests, the percentage error for the simulated cutting forces varies between 4.0% and 10.0%, and that only for five simulations the observed errors are more than 10.0%.

In the source [85] the authors Mamalis et al. presented the results of the evaluation of prediction capability of 2D FEM AdvantEdge applied to simulate high speed hard turning of AISI H-13. The authors performed 3 cutting tests and simulations by using the following parameters: cutting speed 200.0, 250.0, 300.0 m/min; feed 0.05 mm/rev; depth of cut 0.3 mm. The tool material was CBN with the rake angle of -5.0°, clearance angle of 5.0°, and 0.02 mm of the cutting edge radius. No coolant was used. The obtained experimental and simulated cutting and thrust forces were compared to each other, and the results showed that both predicted and measured values are in a very good agreement and, generally, follow the same trends. The authors also specified that the general tendency of the numerical simulation is to overestimate cutting forces.

The authors Maranhão and Davim in their work [88] studied the accuracy of 2D FEM AdvantEdge used to predict cutting and thrust forces in dry turning of stainless steel AISI 316. The authors performed a set of the cutting tests and numerical simulations under the following cutting conditions: feed rate 0.05, 0.1, 0.2 mm/rev; cutting speed 100.0 m/min; axial cutting depth 1.0 mm. All tests and simulation were performed by using a triple

layered custom cemented carbide DCMT 11T304-UM cutting tool with a chip breaker, 0.4 mm of the nose radius, 5.5 μm thickness of the coating. The meshing parameters applied to the numerical simulations were: maximum number of nodes 60000; maximum element size 0.1 mm; minimum element size 0.02 mm. As the cutting forces acquisition system a piezoelectric dynamometer was used. According to the results reported by the authors, the maximum percentage errors for the cutting and feed forces were observed for the cutting operation with 0.2 mm/rev of feed rate, and they amount 10.0% and 15.6% respectively.

In the work [145] the authors Vaz et al. presented another study of the prediction capability of 2D FEM AdvantEdge in terms of the cutting forces. The studied process, a simple orthogonal cutting, was performed by using a cutting tool with inserts TNMG 160408-QF in grade 235 produced by SANDVIK Coromant, with 6.0° rake angle and 45.0 μm edge radius. The workpiece material was SANMAC 316L. The cutting conditions used for the experimental campaign and numerical simulations were: cutting speed 120.0, 180.0, 240.0 m/min; feed rate 0.05, 0.15 mm/rev; cutting depth 3.0 mm. For the cutting forces measurements was used a Kistler dynamometer. According to the reported results of the comparison between the simulated and measured forces, the maximum observed difference amounts 14.4% for the cutting force, and 21.2% for the feed force prediction.

The authors Kandrac et al. in the work [66] worked on the estimation of the prediction accuracy of 2D FEM AdvantEdge applied to the simulation of cutting forces in two-dimensional dry orthogonal cutting of titanium Ti-6Al-4V alloy performed with uncoated carbide cutting tools WC. In the numerical simulations and cutting tests, the selected cutting tools were characterized by the clearance angle of 10.5°, rake angles of -5.0°, -10.0° and -15-0°, and by cutting edge radiuses of 20.0 μm, 50.0 μm and 80.0 μm respectively. The tool material was cemented carbide K. As the cutting conditions the authors used the following parameters: cutting speed 30.0, 90.0, 120.0 m/min; feed rate 0.05, 0.1, 0.15 mm/rev; cutting depth 1.0 mm. The comparison of the measured and simulated values showed that predicted and measured cutting forces are in a good agreement.

In the work [87] the authors studied and evaluated the accuracy of 2D FEM AdvantEdge to simulate cutting and thrust forces that occurs in dry hardened steel 55HRC turning process performed with the nixed oxide cutting inserts. The process simulations were performed by using the following parameters: nose radius 0.8 mm, rake angle 6.0°, cutting speed 90.0, 120.0, 150.0, 240.0, 350.0 m/min; feed rate 0.047, 0.1, 0.15, 0.2 mm/rev; depth of cut 0.5 mm. After having compared simulated cutting forces against measured values, the authors reported that the difference between these values does not exceed 10.0%.

Another attempt to estimate 2D FEM AdvantEdge prediction accuracy in terms of the cutting forces was performed by the authors Qian and Hossan [116]. The operation they studies was a finish hard-turning process of four different workpiece materials: AISI 52100 bearing steel, AISI H13 hot work tool steel, AISI D2 cold work steel, and AISI 4340 low alloy steel, performed by using the CBN inserts with such geometries: three different rake angle values -5.0°, -15.0°, -25.0°; four different values of edge radius 0.02, 0.06, 0.1, 0.2 mm; and relief angle of 6.0°. The conditions used to perform cutting tests and numerical simulations were: cutting speed 140.0, 180.0, 240.0 m/min; feed 0.15, 0.3, 0.45, 0.6 mm/rev; depth of cut 0.2 mm. The comparison of the predicted and measured cutting forces showed that the simulated data agree well with measured experimental values with reasonable accuracy.

Özel in the work [103] studied the cutting forces prediction accuracy of 2D FEM AdvantEdge used for the high speed cutting of hardened AISI H-13 hot work tool steel machined by using the chamfered and honed CBN tools with -5.0° rake angle and 5.0° clearance angle values. The author performed 12 different cutting tests and numerical simulations under the following conditions: cutting speed 200.0, 250.0 and 300.0 m/min; 0.05 and 0.1 mm/rev of feed rate. The cutting forces measurement system included a three-component piezoelectric force platform Kistler type 9272 dynamometer, and charge amplifiers Kistler type 5010. According to the analysis of the simulated and measured data, the good agreement between the numerical and measured cutting forces was observed for both cutting process performed by using the chamfered and honed CBN tools.

In the work [40] the authors evaluated the cutting forces prediction capability of 2D FEM AdvantEdge for the dry cutting of AA7975 aluminum performed by the TPUN 110304 (PCD) tool with 0.0° rake and 11.0° clearance angles. The following cutting conditions were used to perform numerical simulations and cutting tests: cutting speed 800.0, 1000.0, 1200.0 m/min; feed rate 0.12 mm/rev; depth of cut 12.0 mm; length of cut 15.0 mm. The meshing parameters to perform FEM were: minimum element size 0.02 mm; maximum element size 0.1 mm; maximum number of nodes 12000. A Kistler three-axis force dynamometer was used to measure the cutting forces. The comparison of the simulated and measured data showed that the maximum observed percentage error amounts 10.4% for the cutting, and 28.0% for the feed forces.

The authors Galanis and Manolakos in their work [48] presented the results of the evaluation of cutting forces prediction accuracy of 2D FEM applied for the turning of AISI 316L process simulation. The following cutting conditions were used: cutting speed 264.0, 352.0, 440.0 m/min; feed 0.06, 0.08, 0.12 mm/rev; depth of cut 0.1, 0.15, 0.2 mm. As the cutting tool was used the Carbide-General tool with 6.0° rake and 10.0° relief angles, cutting edge rounding of 0.04 mm, and with three layers of coating TiN(0.01 mm), Al_2O_3 (0.02 mm) and TiC (0.01 mm). The meshing process in 2D FEM was performed by using the following parameters: maximum number of nodes 24000, maximum element size 0.1 mm, minimum element size 0.02 mm. A Kistler dynamometer 9257A was used for the cutting forces measurements. The authors reported that the average percentage error for the cutting forces prediction that was observed during the comparison of the simulated and measured data amounts 12.0%.

Since in the literature there are many available works that study and evaluate the prediction accuracy of 2D FEM AdvantEdge applied for different cutting processes, only the latest of them were discussed in this section. According to the found data, the results in these studies showed that usually 2D FEM simulated cutting forces are in a good agreement with the experimental values. Due to this, the evaluation of 2D FEM AdvantEdge prediction capability was not studied in the present work.

2.4 3D FEM FOR CUTTING FORCES SIMULATION

3D FEM AdvantEdge can be used to study the following cutting processes: side cutting, corner cutting, face milling, ramp milling, plunge milling, and pocket milling, turning processes (oblique, facing, nose), drilling processes, grooving operations, tapping, and boring.

The side down-milling operation is used to illustrate an example of a three-dimensional process. As can be seen in the Fig.2.6, during the cut when a tool starts to rotate, one of the cutting edges 'meets' a workpiece of the height a_p, and as the penetration of the cutting edge continues, a chip sample of the thickness h_{chip}, height a_p, and width a_e is generated. Since the reported milling operation is the three-dimensional process, there are three cutting forces that occur during the cut: F_x, F_y, and F_z forces that act in the horizontal (feed), normal, and axial directions respectively.

2.4.1 Literature Overview

In the past years some work has been done in order to evaluate the effectiveness and accuracy of 3D FEM AdvantEdge in terms of the cutting forces prediction. Only the recent reports will be discussed in this section.

The authors Rao, Dandekar and Shin in the work [117] performed a study of 3D FEM AdvantEdge prediction accuracy in terms of the cutting forces for the face milling process of Ti6Al4V by using uncoated carbide cutters. As the cutting tool the authors used a standard face cutter Kennametal KDPR-4-SP4-30MB with lead angle of 30.0°, axial rake of 5.0°, and radial rake of 2.0° with uncoated carbide K313 inserts with 24.0 μm edge rounding. Both, experimental campaign and numerical simulations were performed by using the following conditions: cutting speed 76.2, 99.0, 110.6, 121.9, 152.4, 182.9 m/min; feed rate 0.05 mm/tooth; depth of cut 0.762 mm. The cutting forces measurements were done with a Kistler 9257B dynamometer. To evaluate 3D FEM AdvantEdge prediction accuracy, the authors compared simulated and measured values only for the thrust force. The authors reported that the general tendency of 3D FEM AdvantEdge is to overestimate the thrust force, and that the observed average prediction error amounts 14.0%.

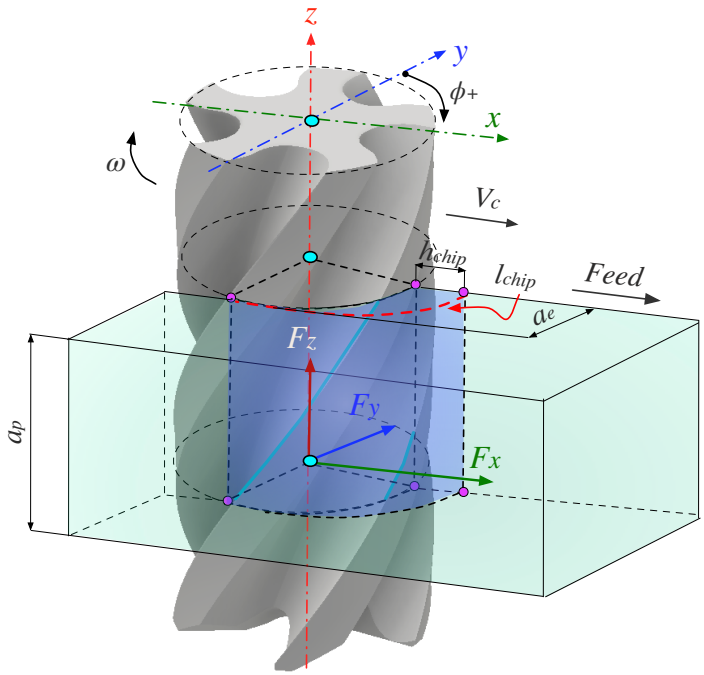

Figure 2.6: General representation of side down-milling process geometry: F_x, F_y and F_z are forces that occur during cutting process; ϕ - tool angular position; ω - tool rotation direction; V_c - cutting speed; a_p - cutting depth; a_e - cutting width; h_{chip} - deformed chip thickness

In the work [77] the authors Li and Shih performed FEM and experimental validation of 3D turning of the commercially pure titanium alloy. The experimental campaign and FEM of the studied process were performed under the following cutting conditions: cutting speed 24.4, 48.8, 97.5, 195.0 m/min; feed 0.254 and 0.381 mm/rev; depth of cut 1.02 mm. As the cutting tool was used the uncoated WC-Co tool inserts by Kennametal TPG322 with 0.8 mm nose radius, honed cutting edge, and K313 grade material. A left-handed tool holder, Kennametal CTAPL-163D, was used to hold a triangular shape insert. A Kistler 9257A 3-axis piezoelectric dynamometer was used to measure three force components in x, y, and z directions. The maximum number of the nodes in 3D FEM mesh reached 100 000 nodes. The experimental validation of FEM showed the following results. In the performed tests with the feed equal to 0.254 mm/rev, the discrepancy ranges from 15.0% at 24.4 m/min cutting speed to 12.0% at 195.0 m/min cutting speed were observed for the

F_x cutting force prediction. In the performed tests with the feed equal to 0.381 mm/rev, the observed discrepancy ranges varied between 20.0% at 24.4 m/min cutting speed and 7.6% at 195.0 m/min cutting speed. The observed discrepancy for the F_y and F_z cutting forces is less than 10.0% for all cutting tests.

The authors Man et al. in the work [86] reported the results of a study performed to evaluate 3D FEM AdvantEdge prediction accuracy in terms of the cutting forces that arise in the milling processes of Al7050-T7451 performed by using both indexable and solid tools. Unfortunately, for the sake if brevity, the authors did not reported the cutting conditions used to perform cutting tests and numerical simulations. Nevertheless, the authors presented the results of the validation of the force prediction capability of 3D FEM AdvantEdge underlining the fact that good correlations between the numerical and measured data were observed for a wide range of the cutting conditions.

In the work [90] the authors Markopoulos et al. evaluated the cutting forces prediction accuracy of 3D FEM AdvantEdge used for the turning process of AISI 1045 simulation. The following cutting parameters were used during the experimental campaign and for FEM simulations: cutting speed 300.0, 450.0, 600.0 m/min; feed 0.1, 0.2, 0.3 mm/rev; depth of cut 0.2, 0.4, 0.6 mm. As the cutting tool was used a cutter with CP500 coated grade rhombic shaped inserts. For the cutting forces measurements a Kistler 9257 dynamometer was involved. According to the results reported by the authors, the good correlation between the simulated and measured values was observed for the force F_x, while for the forces F_y and F_z the observed correlation is poorer. The authors concluded their study by establishing that the general tendency of 3D FEM AdvantEdge is to overestimate cutting forces.

Another successful attempt to estimate and evaluate the cutting forces prediction capability of 3D FEM AdvantEdge v.4.8 was performed in the work [97]. The authors studied the dry milling process of the commercially pure (CP) Titanium performed by using the WC-Co tool inserts Sandvik R216.2 with 0.8 mm nose radius, honed cutting edge, and GC 235 grade material with TiC-TiCN-TiC coating with thickness of 2.5 μm, placed on a Sandvik cutter body R216.2 - 525. The cutting tests and numerical simulations were performed by using the following cutting conditions: cutting speed 157.0 and 235.5

m/min; feed per tooth 0.1 and 0.2 mm/tooth; cutting depth of 1.0 mm. The comparison of the simulated and measured cutting forces showed the following results. It was observed that AdvantEdge FEM tool tends to underestimate all three cutting forces. For the cutting forces in x, y, and z directions the percentage errors amounted 48.0%, 17.0% and 3.0% respectively (relatively to the maximum value).

In the work [99] the authors investigated the cutting forces prediction capability of 3D FEM AdvantEdge used for the flat milling process of Ti6Al4V titanium alloy. As the cutting tool the authors used a six-flute cutter-head type H490 F90AX D050-6-22-09 with a carbon groove indexable insert type ANCX090416PDR from Iscar. The material of the selected inserts was cemented carbide H10 with 3.0 μm thickness of TiAlN coating, and 1.758 mm nose radius. The cutting conditions to perform cutting tests and FEM simulations were: cutting speed 80.0 m/min; cutting depth and cutting width of 1.0 and 10.0 mm respectively; feed per tooth 0.1 and 0.15 mm/tooth. In the experimental set-up a plate piezoelectric dynamometer Kistler 9257B with a charge amplifier module 5019B and a digital analog converter NI 6062E from National Instruments were used for the cutting forces measurements. The comparison of the predicted and simulated cutting forces indicated that the maximum percentage errors were observed for the cutting tests with feed rate of 0.1 mm/tooth, and they amount 44.0% and 60.0% for the F_x and F_y cutting forces respectively.

The authors Zhao and Guan in the work [157] presented the results of the evaluation of 3D FEM AdvantEdge cutting forces prediction accuracy for the dry pocket milling of Ti6Al4V titanium alloy performed with a prototype cemented carbide end mill. The cutting conditions to perform FEM simulations and cutting tests were: spindle speed 600.0 RPM; feed per tooth 0.08 mm/tooth; cutting depth of 2.0 mm. The cutting forces measurements were performed by using a Kistler 9253B dynamometer. The comparison of the simulated and measured data was performed for the cutting forces F_x and F_z, and it showed that the percentage error values did not exceed 15.0%.

In the work [120] the authors Roud, Sklenička and Kožmín presented the results of the evaluation of cutting forces prediction accuracy of 3D FEM AdvantEdge v.5.4 used to simulate dry drilling of AISI D3 tool steel performed with a solid carbide twist drill.

The geometry data of the selected cutting tool was not reported by the authors due to the fact that this cutting tool was a prototype. The cutting conditions used to perform cutting tests and simulations were the following: cutting speed 25.0 m/min; feed 0.08 mm/rev. During the cutting operation only the thrust force was measured by using a four-component dynamometer Kistler type 9272. The comparison of the collected experimental and simulated data showed that the thrust forces predicted by AdvantEdge tool are higher than the experimental values. The maximum difference that was observed between these values amount around 40.0%.

The authors Lui and Zhao in the work [83] evaluated 3D FEM AdvantEdge prediction accuracy in terms of the cutting forces that occur in turning of AISI 440C martensitic steel using the CBN10 grade tool diamond shape insert SECO CNGA 120408S-L0 with 0.8 mm nose radius, -6.0° rake angle, 0.0° relief angle, mounted on a right-handed tool holder Kennametal PCLNR2020K12. The experimental campaign and FEM simulations were carried out based on the following parameters: cutting speed 120.0, 150.0, 180.0 m/min, feed rate 0.1, 0.15, 0.2 mm/rev; cutting depth 0.1, 0.3, 0.5 mm. The comparison analysis of the simulated and measured cutting forces indicated that for all cutting tests the predicted cutting forces values were underestimated. The average percentage errors observed for F_x, F_y and F_z cutting forces amounted 17.2%, 18.3% and 16.7% respectively.

Another work performed to study and evaluate the cutting forces prediction capability of 3D FEM AdvantEdge was reported by the authors Lin et al. [79]. A studying cutting process was a face milling of 300M steel performed by a prototype end mill. The following cutting conditions were used to perform numerical simulations and cutting tests: spindle speed 800.0, 1100.0, 1400.0 RPM, feed rate 0.07 mm/tooth; cutting depth 2.0 mm; cutting width 4.0 mm. The results of the comparison analysis between the simulated and measured cutting forces reported by the authors indicated that the general tendency of 3D FEM AdvantEdge is to overestimate cutting forces.

In the work [98] the authors evaluated the cutting forces prediction capability of 3D FEM AdvantEdge used for the simulation of a turning process of Inconel 718 superalloy performed with the CNMG 120412-UP cutting tool inserts coated with 3.0 μm thickness of TiAlN coating produced by Kennametal. The tool geometry was described by the

following parameters: -5.0° rake angle; 5.0° clearance angle; -4.55° back rake angle value; -5.41° side rake angle; tool nose radius 1.2 mm; cutting edge radius 50.0 μm. The cutting conditions used to perform cutting tests and numerical simulations were: cutting speed 60.0, 90.0 m/min; cutting depth 0.125, 0.25, 1.0, 2.0 mm; feed 0.1 mm/rev. The experimental cutting forces measurements were performed with a Kistler 9257B piezoelectric dynamometer with a 5019B amplifier and NI 6062E National Instruments A/D multi-channel board. The comparison analysis of the simulated and measured cutting forces indicated that the prediction accuracy of 3D FEM AdvantEdge depends on the cutting depth value. The authors reported that the lower cutting depth cause the increase of the percentage error value. As instance, the authors reported that for the smaller depths of cut the maximum percentage error values that were observed amounted about 40.0% for the forces F_x and F_y, and about 20.0% for the force F_z.

As shown, a lot of studies have been performed to evaluate the cutting forces prediction capability of 3D FEM AdvantEdge. According to the data reported in the available literature, the general tendency of 3D FEM AdvantEdge is to overestimate cutting forces, and the percentage error observed for the cutting forces predictions varies between 15.0% and 40.0%. Since to the best of author's knowledge any of the available works deal with the estimation of the influence of 3D tool CAD models on the cutting forces and chip geometry prediction, these arguments will be studied within the framework of this chapter.

2.4.2 STEP and STL CAD Models

The meshing of a three-dimensional object is very important aspect in 3D FEM since it has significant impact on the accuracy of process simulations. A guided creation of the cutting tools for 3D process simulations is not always sufficient, and often the imported cutting tool geometries are required. 3D FEM AdvantEdge supports STEP, STL and VMRL tool files. In this chapter only STEP and STL file formats will be discussed.

STL (STereoLithography) is a file format native to the stereolithography CAD software created by 3D Systems, and it is supported by many CAD software packages. When a three-dimensional object is saved using STL format, only the geometry of this body is

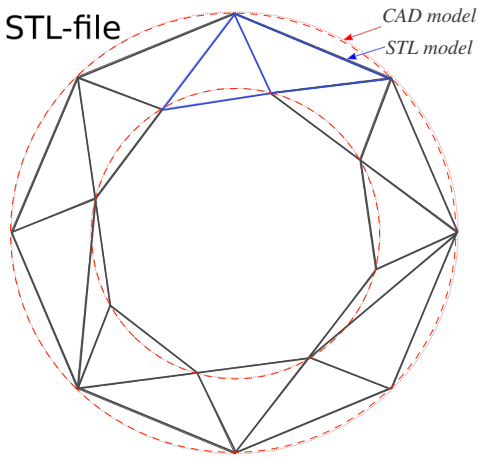

Figure 2.7: Example of STL vs CAD format [2]

described. Such characteristics of CAD attributes as representation of color or texture are not supported by STL files [37].

STL format approximates the surfaces of a solid model with triangles (Fig.2.7). A general rule says that STL file resolution can be changed by changing options such as Chord Tolerance or Angular Control. The larger STL file is, the more triangles are placed on the surface of model. For complex 3D models, STL files sizes reach 1-5 MB [1].

STEP (Standard for the Exchange of Product model data, ISO 10303-21) is another format that also allows to represent 3D objects in CAD and related information, and it is supported by many CAD tools. STEP format provides support neutral file exchange, and the standard ISO 10303-21 defines the encoding mechanism on how to correctly represent data according to a given EXPRESS schema (standard data modeling language for product data) [3].

Since the representation of three-dimensional objects is different in STEP and STL files, this fact influences the mesh development and results in FEM analysis. In this chapter such arguments as mesh development, and evaluation of the influence of these two CAD (STEP and STL) models on 3D FEM AdvantEdge prediction accuracy in terms of the cutting forces and chip geometry will be discussed.

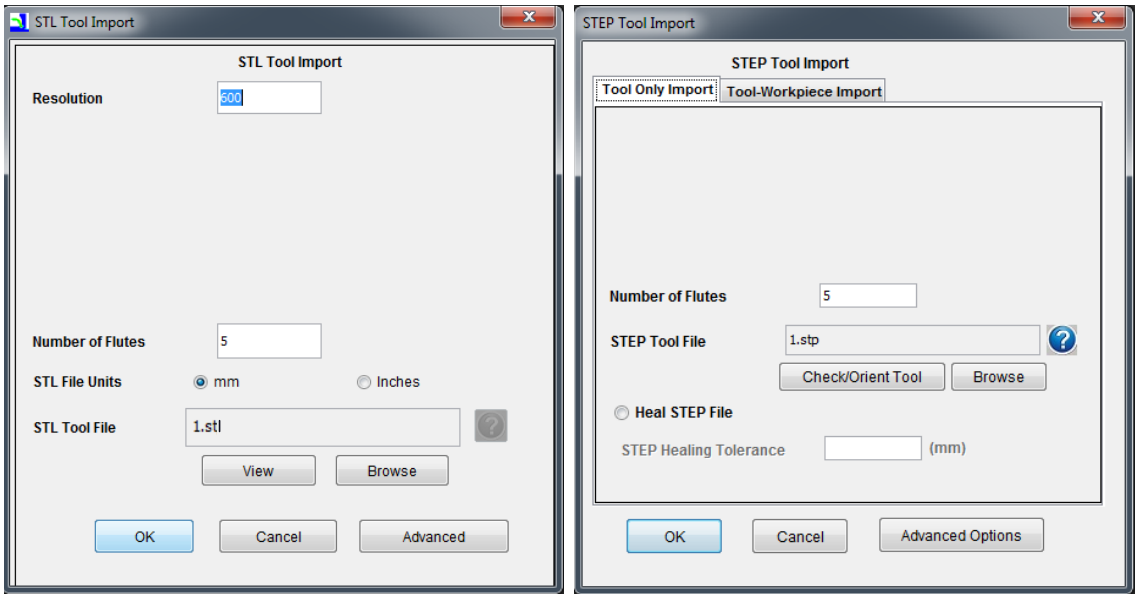

(a) (b)

Figure 2.8: Tool files import in 3D FEM AdvantEdge: (a) STL file; (b) STEP file [138]

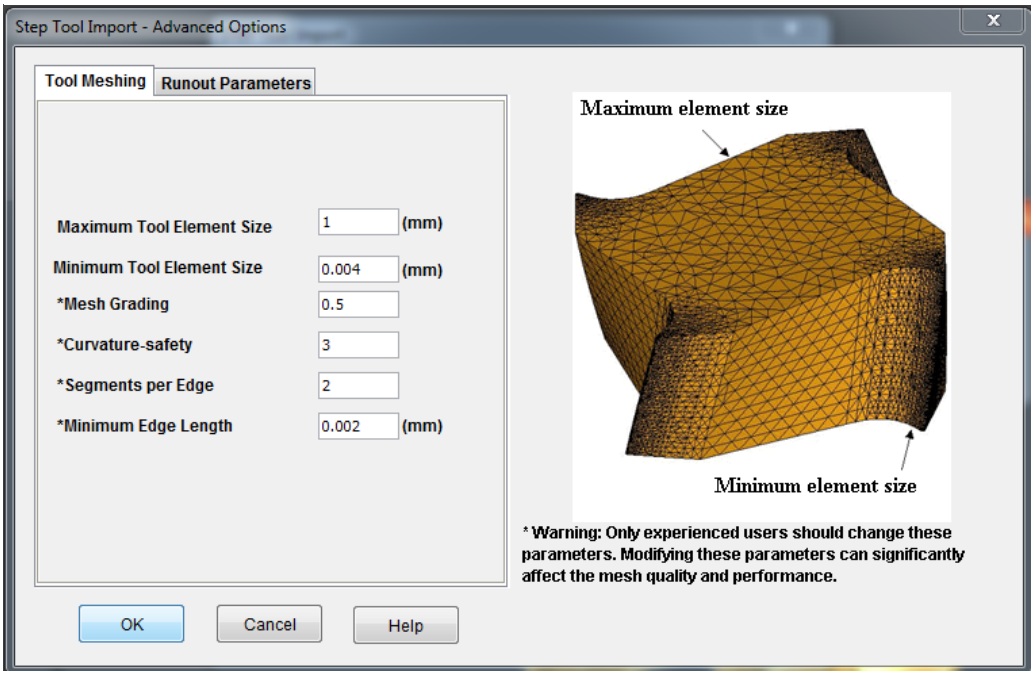

Figure 2.9: 'Advanced Options' menu for STEP files import (Fig.2.8(b)) [138]

2.4.3 3D FEM and Experimental Campaign Set-up

In 3D FEM AdvantEdge the import of the external files that contain cutting tool geometry can be done by using the following commands in the menu toolbar:

$$\text{Tool} \rightarrow \text{Import Tool} \rightarrow \text{STL / STEP Tool File}$$

As can be seen in the Fig.2.8, the meshing set-up for both file formats requires different procedures. In case when STL files have to be imported, the only one parameter - file resolution - has to be specified for meshing set-up (Fig.2.8(a)).

A more complex procedure is required to set up meshing parameters for STEP files. There are two locations to define the meshing parameters: 'Advanced Options' and 'Selective Mesh Refinement' that can be found in the 'Check/Orient Tool' menu (Fig.2.8(b)). Here, such important parameters as the maximum and minimum tool element size, mesh grading, and minimum edge length have to be specified (Fig.2.9). Another important step that has also to be performed is the 'Mesh Refinement' of the face or edge surfaces, where the minimum tool element size has to be specified (Fig.2.9).

In the present work, in order to study the influence of CAD tool models on 3D FEM AdvantEdge prediction accuracy in terms of the cutting forces and chip geometry, nine side down-milling process simulations and six cutting tests were performed. As the cutting tool two models (STEP and STL) of a five-teeth solid end mill were used. An example of the used STEP model is presented in the Fig.2.10.

The cutting conditions and tool material data are reported in the Table 2.1. Such cutting parameters as cutting speed and feed per tooth were selected equal to 80.0 m/min and 0.1 mm/tooth respectively. The parameters used to perform the meshing procedure are reported in the Table 2.3. As the workpiece material was used AISI 4140 high tensile steel. Three different tungsten-carbide (10.0% Cobalt content) with five-teeth solid end mills and 2.0 μm thickness of TiAlN coating were used to perform the cutting tests. The cutter geometry was characterized by the following parameters: variable tooth pitch, 10.0 mm diameter, 38.0° helix angle, 10.5° longitudinal rake angle, 7.0° relief angle, and three different cutting edge rounding values: sharp, 5.0 μm, and 20 μm. Both STEP and STL CAD tool models, and real end mills were provided by Sandvik Coromant.

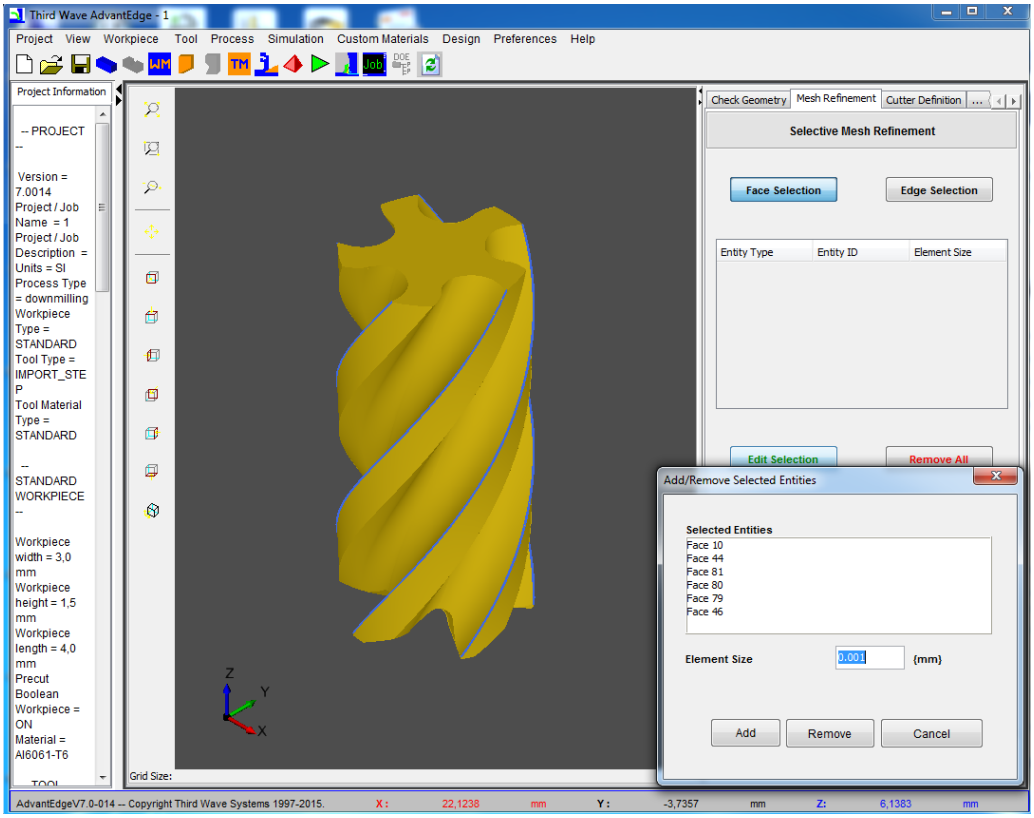

Figure 2.10: 'Mesh Refinement' option accessible from the 'Check/Orient' tool menu in STEP files import window (Fig.2.8(b)) [138]

In AdvantEdge the process parameters, friction, and coolant properties set-up menu are accessible from the main toolbar (Fig.2.11):

Process → Process Parameters

Process → Friction

Process → Coolant

All FEM simulations (Table 2.1) were performed on a personal computer Lenovo ThinkPad T420s the technical data of which is reported in the Table 2.2. The default coolant (Fig.2.11) and friction properties were applied in FEM set-up to simulate one rotation of the tool when performing side down-milling process (Fig.2.12). The post-processing of FEM data was performed by using the commercial Tecplot tool.

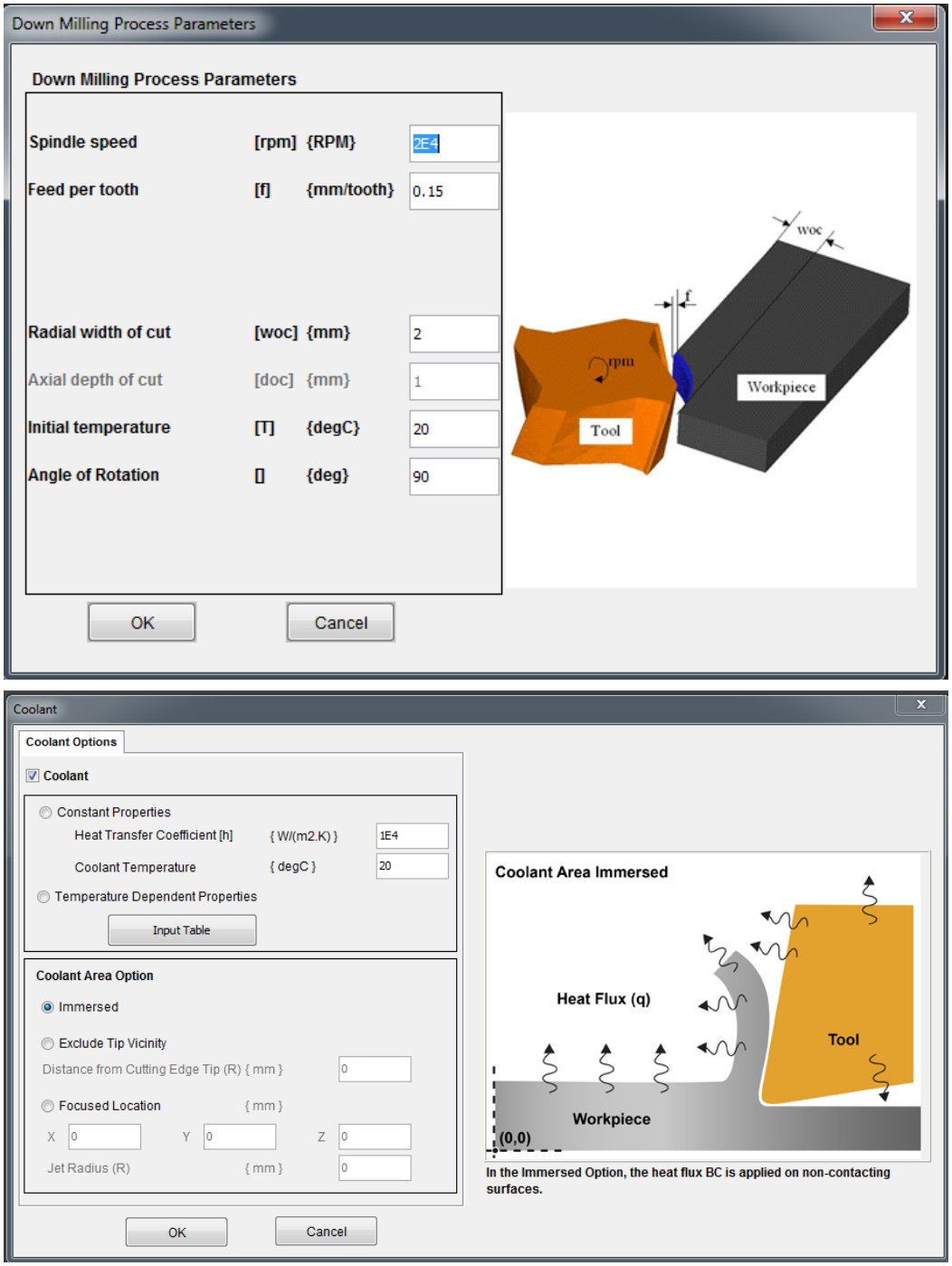

Figure 2.11: Example of the process set-up and default coolant properties in 3D FEM AdvantEdge [138]

Table 2.1: Cutting conditions used to perform 3D FEM simulations and milling tests (cutting speed V_c = 80.0 m/min; feed per tooth f_z = 0.1 mm/tooth; D - tool diameter; r_{edge} - edge radius; α_{rake} - tool rake angle; α_{rel} - tool relief angle; β - tool helix angle; C - coating TiAlN)

	D, mm	a_p, mm	r_{edge}, μm	α_{rake},°	α_{rel},°	β,°	Material	C, μm
sim 1 STEP sim 1 STL test 1 (case 1)	10.0	5.0	sharp	10.5	7.0	38.0	H10F	2.0
sim 2 STEP sim 2 STL test 2 (case 2)	10.0	5.0	20.0	10.5	7.0	38.0	H10F	2.0
sim 3 STEP sim 3 STL test 3 (case 3)	10.0	5.0	5.0	10.5	7.0	38.0	H10F	2.0
simul 4 STEP sim 4 STL test 4 (case 4)	- 10.0	- 10.0	- 5.0	- 10.5	- 7.0	- 38.0	- H10F	- 2.0
simul 5 STEP sim 5 STL test 5 (case 5)	- 10.0	- 10.0	- sharp	- 10.5	- 7.0	- 38.0	- H10F	- 2.0
simul 6 STEP sim 6 STL test 6 (case 6)	- 10.0	- 10.0	- 20.0	- 10.5	- 7.0	- 38.0	- H10F	- 2.0

Table 2.2: Characteristics of used personal computer and AdvantEdge requirements

	Lenovo ThinkPad T420s	AdvantEdge 2D	AdvantEdge 3D
Processor	Intel core i5-2520M : 2.5 GHz dual core	Intel/ADM 2.5 GHz quad core	Intel Xeon/ADM 3.0 GHz quad core
Graphic Processor	Intel(R) HD Graphics 3000	NVIDIA	NVIDIA
RAM	4.00 GB (3.88 usable)	4.00 GB	4.00 GB

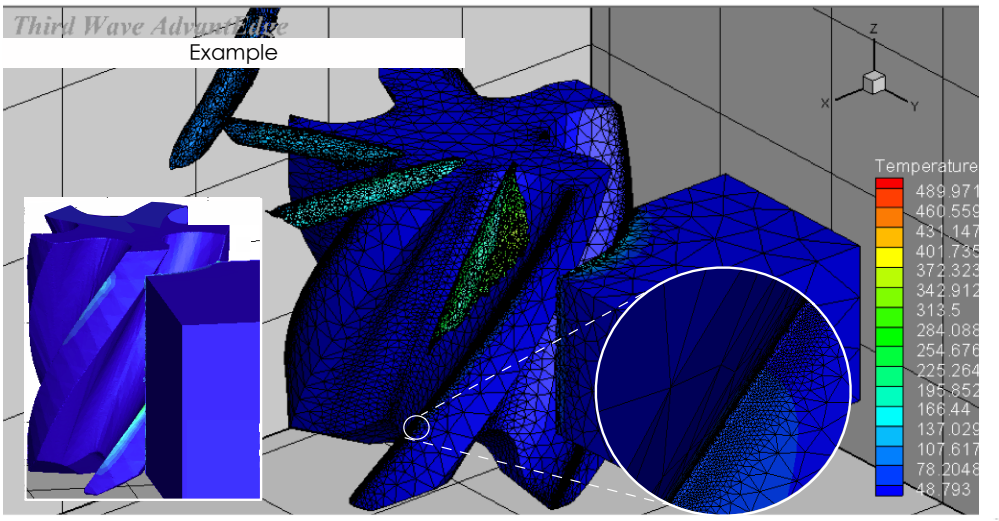

Figure 2.12: Example of the performed side down-milling process simulation in 3D FEM AdvantEdge

2.5 VALIDATION OF 3D FEM AdvantEdge RESULTS

In this section such arguments as the influence of CAD models on the tool mesh definition, and consequently on the simulated cutting forces and chip geometry are discussed. In particular, this section includes the results of the performed FEM simulations, data of the experimental campaign, and results of the evaluation of prediction accuracy of 3D FEM AdvantEdge done by means of the comparison of simulated results against experimentally measured cutting forces and collected chip samples.

Table 2.3: Mesh set-up and results: A - edge rounding; B - maximum tool element size; C - minimum tool element size; D - mesh grading; E - curvature-safety; F - segments per edge; G - minimum edge length; H - face selection function (only STEP files); I - created mesh edge rounding; J - total number of elements in the mesh; K - resolution for STL file; L - real tool edge rounding values provided by the tool manufacturer

	sim STEP	sim 2 STEP	sim 3 STEP	sim 4 STEP	sim 5 STEP	sim 6 STEP
A, μm	1.0	20.0	5.0	-	-	-
B, mm	1.0	1.0	1.0	-	-	-
C, mm	0.004	0.08	0.005	-	-	-
D	0.5	0.5	0.5	-	-	-
E	3	3	3	-	-	-
F	2	2	2	-	-	-
G, mm	0.002	0.002	0.002	-	-	-
H	0.004	0.007	0.005	-	-	-
I, mm	0.001	0.02	0.005	-	-	-
J	1 138512	597266	693431	-	-	-
	sim 1 STL	sim 2 STL	sim 3 STL	sim 4 STL	sim 5 STL	sim 6 STL
K	550	480	500	550	650	550
I, mm	0.08	0.1	0.08	0.08	0.08	0.1
J	487434	461708	382541	468380	539436	492233
L,mm	sharp	0.02	0.005	0.005	sharp	0.02

For the sake of readability, the graphical representation of the collected data (mesh geometries comparison, simulated and measured cutting forces and chip geometries) is reported only for some of the studied cases. However, the detailed information about all collected data is reported in the corresponding tables.

Finally, it has to be mentioned is that the temperature maps that can be found in the Fig.2.12 and Fig.2.13 do not have to be taken into account since they were used only for better and more clear representation of 3D FEM data.

2.5.1 Influence of CAD Tool Models on Mesh Generation

The meshing parameters reported in the Table 2.3 were selected according to the Third Wave Systems recommendations and workshops information [139], which were provided by Sandvik Coromant. The values of the meshing parameters reported in this table are the smallest possible values that permitted to build the meshes for STEP and STL tool models within the framework of this work.

It has also be noted that since in 3D AdvantEdge it is not possible to set up the edge rounding value equal to 0.0 μm for the sharp cutting edges ('sim 1 STEP' in the Table 2.1), the minimum acceptable value of 1.0 μm was used. In addition, due to the limited capacities of the used personal computer (Table 2.2) it was not possible to create mesh, and consequently, to perform 3D FEM simulations of the cutting tests with cutting depth of 10.0 mm ('sim 4 STEP', 'sim 5 STEP', and 'sim 6 STEP' reported in the Table 2.1).

As can be seen from the Table 2.1 and in the Fig.2.13, the difference between the tool mesh geometries and cells distribution created based on STEP and STL CAD models is significant, especially in the regions close to the cutting edge. In the Fig.2.13 it is clearly seen that the sizes of the mesh cells created to describe cutting edge radiuses for STL models are pretty higher than for STEP files, and in particular they are higher than the real edge rounding values reported in the Table 2.1. In addition, the mesh distributions are also different for these tool models. As can be seen in the Fig.2.13, in case of STEP files, the mesh cell sizes are not equal, and in the region close to the cutting edge the mesh cells dimensions are very small. In case of STL models, it can be observed that the mesh cells dimensions are more or less uniform for the whole tool volume.

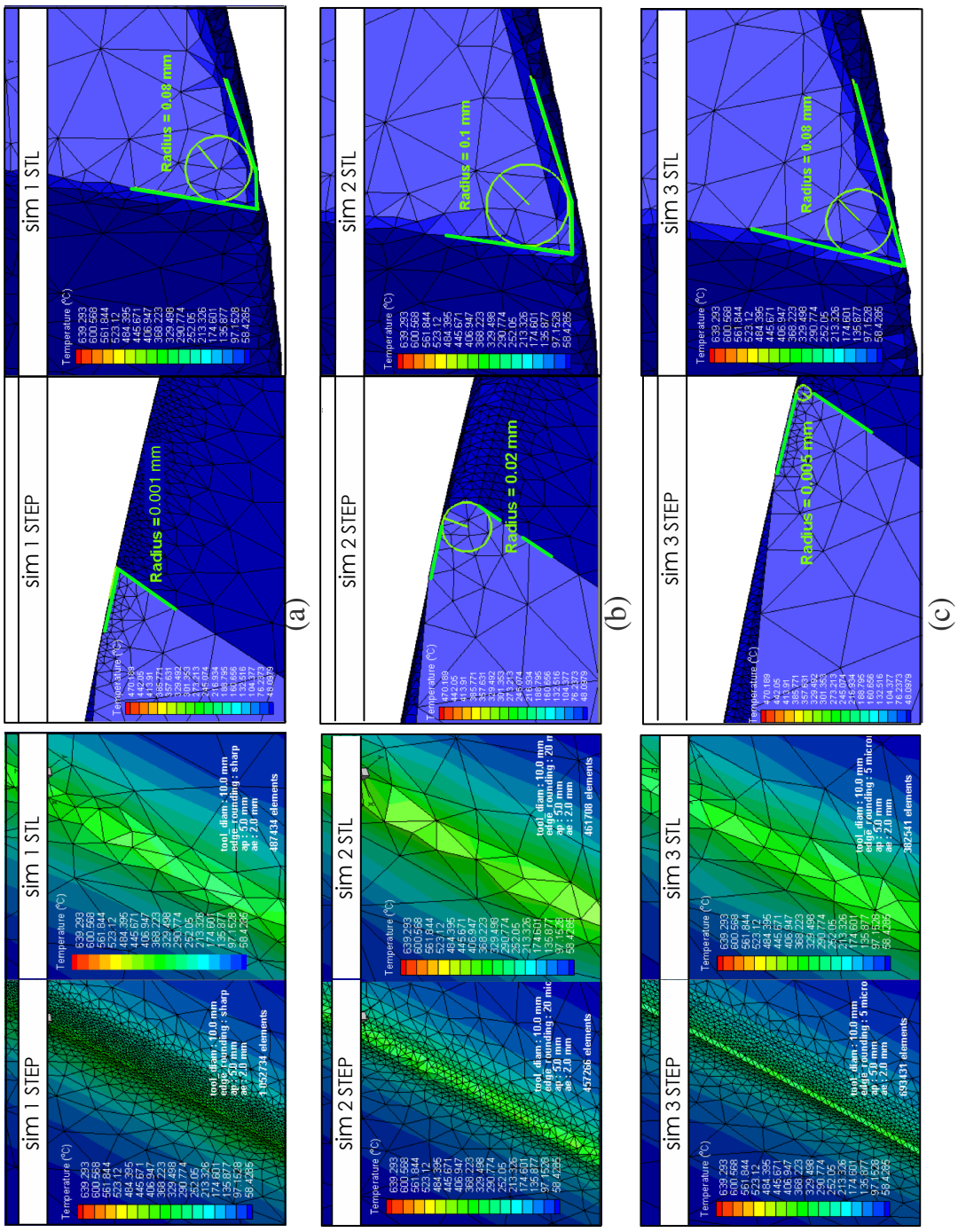

Figure 2.13: Comparison of the mesh dimensions created when using STEP and STL CAD models: (a) sim 1 STEP/STL; (b) sim 2 STEP/STL; (c) sim 3 STEP/STL reported in the Table 2.1

By measuring the cutting edge radius in Tecplot post-processing software it was observed that for the first three studying cases (Table 2.1) the following geometries were generated:

'case 1' (sharp): 1.0 μm or 0.001 (STEP) and 80.0 μm or 0.08 mm (STL);

'case 2' (20.0 μm): 20.0 μm or 0.02 mm (STEP) and 100.0 μm or 0.1 mm (STL);

'case 3' (5.0 μm): 5.0 μm or 0.005 mm (STEP) and 80.0μm or 0.08 mm (STL).

Similar results were observed for the meshes built for CAD models of the tools used to perform 'sim 4 STL', 'sim 5 STL', and 'sim 6 STL' FEM simulations:

'sim 4 STL' (5.0 μm): 80.0μm or 0.08 mm;

'sim 5 STL' (sharp): 80.0 μm or 0.08 mm;

'sim 6 STL' (20.0 μm): 100.0 μm or 0.1 mm.

By comparing the results of cutting edge radiuses generated for the corresponding STL files: 'sim 1/5 STL' (sharp cutting edge), 'sim 2/6 STL' (20.0 μm of edge radius), and 'sim 3/4 STL' (5.0 μm of edge radius), it was observed that STL file resolution value does not influence the generation of the mesh dimensions and cells distribution. Despite the fact that different values of the resolution were used, the following results were observed for the created meshes to describe cutting edges of the performed FEM simulations:

'sim 1/5 STL' (resolution 550/650): 80.0μm or 0.08 mm;

'sim 2/6 STL' (resolution 480/550): 100.0 μm or 0.1 mm;

'sim 3/4 STL' (resolution 500/550): 80.0μm or 0.08 mm.

In order to establish the influence of CAD models on the total number of mesh elements, and consequently on the time-consuming characteristics of the performed 3D FEM simulations, the data of the corresponding simulations (parameter G) reported in the Table 2.1 were compared to each other. It was observed that in cases when STEP

files were used, the total number of the mesh elements was higher than for STL files, such as:

'sim 1 STEP/STL': 1138512 and 487434 elements respectively;

'sim 2 STEP/STL': 597266 and 461708 elements respectively;

'sim 3 STEP/STL': 693431 and 382541 elements respectively.

2.5.2 Influence of CAD Tool Models on Cutting Forces Prediction

The evaluation of the influence of STEP and STL tool models on the prediction accuracy of 3D FEM AdvantEdge in terms of the cutting forces was performed by comparing average and maximum simulated values against measured data.

A Kistler 9129AA force dynamometer, mounted between the workpiece and machining table, was used to measure the instantaneous F_x, F_y, and F_z cutting forces in the workpiece reference frame (Fig.2.14). The data acquisition system was set to capture and store the cutting force data at a sampling rate of 3000.0 Hz. All cutting tests were carried out on the four-axes DMU-60T machining center (Fig.2.14).

In the Fig.2.15 an example of the measured and simulated (STL) cutting forces data is reported. It has to be noted that the simulated data reported in the Fig.2.15(b) was obtained by applying the 'Polynomial Fit' function in Tecplot post-processing tool, and that for the comparison of the data not fitted values were used.

In order to identify the average, maximum and minimum values of the F_x, F_y and F_z cutting forces, two different codes were implemented by using RUBY programming language. The obtained average, maximum, and minimum cutting forces values are reported in the Table 2.4. The percentage error values for each type of the cutting forces are reported in parentheses.

In the present work the comparison between the simulated and measured data was performed only for the average and maximum values, since these two parameters are more important for the new cutting tools development than the minimum cutting forces

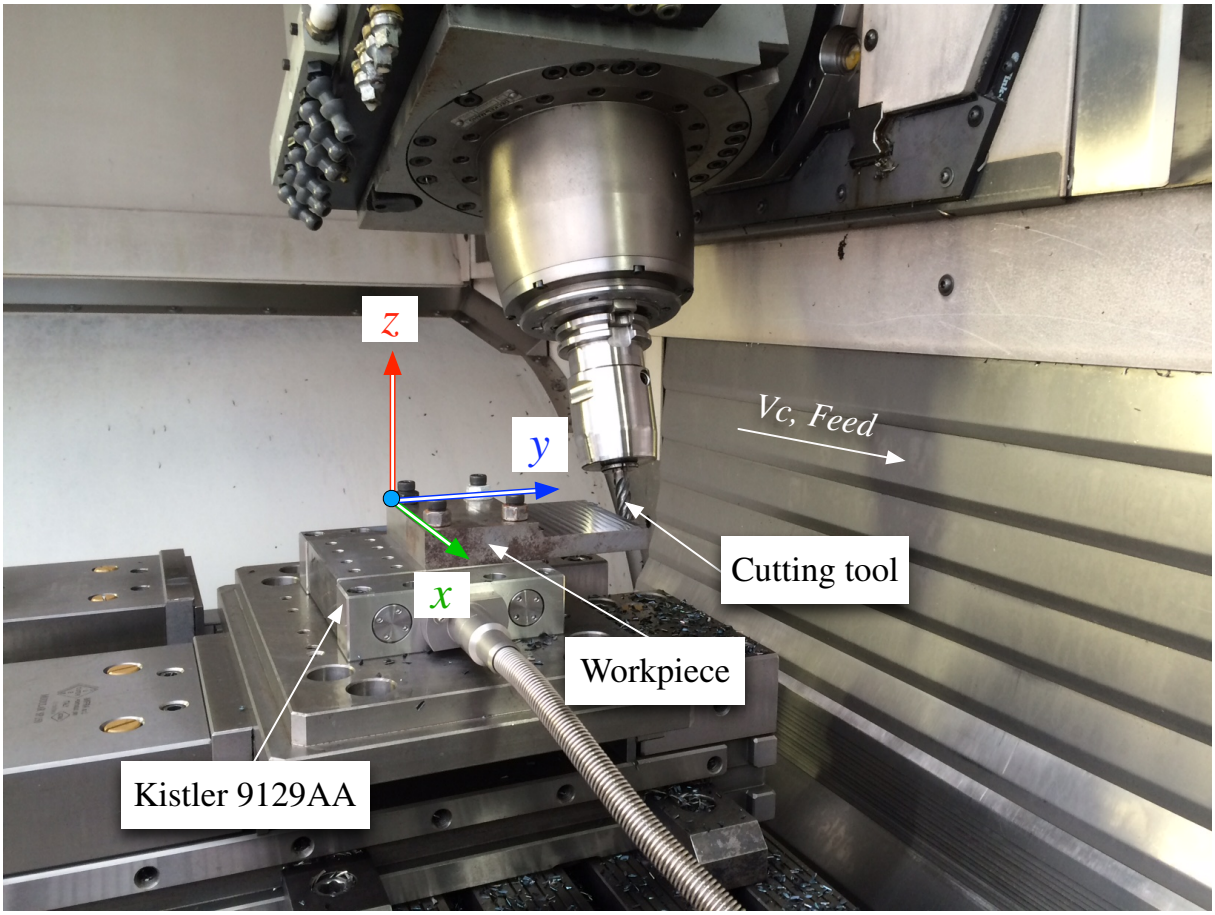

Figure 2.14: Side down-milling process performed on the DMU-60T milling center

values. Figures 2.16 and 2.17 summarize the results of the comparison reported in the Table 2.4. In these figures, the measured and simulated values are shown in the end of each column, and the percentage error values are reported in parentheses.

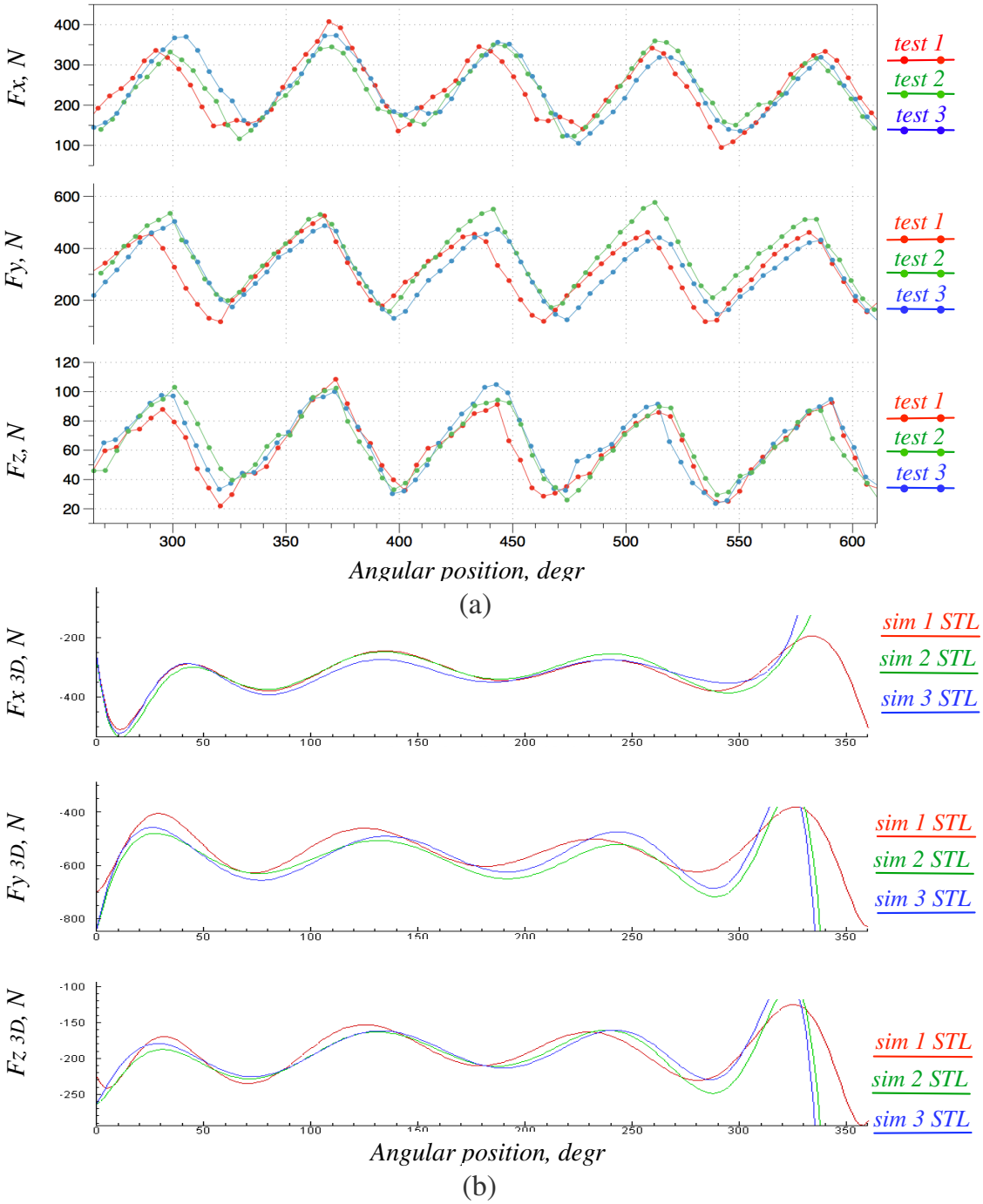

Figure 2.15: Experimental and predicted STL cutting forces F_x, F_y and F_z data of the first three cases reported in the Table 2.1: (a) experimental values; (b) 3D FEM AdvantEdge (STL) data

Table 2.4: Measured and simulated cutting forces

	sim 1 STEP	sim 1 STL	test 1	sim 2 STEP	sim 2 STL	test 2
$\overline{F}_x$, N	217.4(-8.2%)	320.4(35.5%)	236.5	146.0(-37.6%)	315.6(34.8%)	234.1
$F_{x,max}$, N	387.8(-4.5%)	430.1(6.0%)	405.9	253.8(-30.3%)	381.3(4.7%)	364.3
$F_{x,min}$, N	128.5(35.3%)	181.2(90.7%)	95.0	110.5(-3.9%)	248.7(116.0%)	115.0
$\overline{F}_y$, N	286.4(-7.0%)	564.0(83.2%)	307.9	223.8(-38.8%)	601.8(64.5%)	365.9
$F_{y,max}$, N	316.3(-39.7%)	677.6(29.2%)	524.5	265.1(-54.6%)	630.9(8.2%)	583.3
$F_{y,min}$, N	81.3(-26.8%)	237.3(113.8%)	111.0	191.2(27.4%)	317.3(111.5%)	150.0
$\overline{F}_z$, N	155.7(29.4%)	198.2(64.8%)	120.3	135.1(6.4%)	200.1(57.6%)	127.0
$F_{z,max}$, N	203.1(-5.4%)	247.9(15.4%)	214.8	192.6(-11.7%)	249.6(14.4%)	218.1
$F_{z,min}$, N	46.6(25.3%)	102.1(174.5%)	37.2	92.3(45.8%)	97.1(53.4%)	63.3
	sim 3 STEP	sim 3 STL	test 3	sim 4 STEP	sim 4 STL	test 4
$\overline{F}_x$, N	204.9(-12.8%)	327.5(39.3%)	235.1		622.9(27.2%)	489.6
$F_{x,max}$, N	365.2(-4.7%)	396.3(3.4%)	383.3		641.3(11.5%)	575.4
$F_{x,min}$, N	71.9(-32.7%)	200.1(87.4%)	106.8		551.9(43.7%)	383.6
$\overline{F}_y$, N	268.6(-12.5%)	583.4(90.0%)	307.1		1024.8(53.3%)	668.3
$F_{y,max}$, N	315.6(-38.5%)	655.9(27.8%)	513.1		1051.8(23.3%)	853.3
$F_{y,min}$, N	189.4(81.4%)	225.2(115.7%)	104.4		964.3(89.5%)	508.9
$\overline{F}_z$, N	145.3(17.6%)	198.2(60.4%)	123.6		365.3(44.3%)	253.2
$F_{z,max}$, N	204.3(-3.3%)	229.6(8.7%)	211.2		384.5(20.9%)	318.0
$F_{z,min}$, N	56.2(37.7%)	86.1(111.0%)	40.8		352.0(83.8%)	191.5
	sim 5 STEP	sim 5 STL	test 5	sim 6 STEP	sim 6 STL	test 6
$\overline{F}_x$, N		641.1(28.3%)	499.8		603.9(24.3%)	485.7
$F_{x,max}$, N		666.1(8.6%)	613.1		625.4(1.2%)	618.0
$F_{x,min}$, N		594.5(61.3%)	368.4		570.7(66.4%)	342.9
$\overline{F}_y$, N		1150.9(78.2%)	645.8		1075.9(44.3%)	745.8
$F_{y,max}$, N		1205.9(42.9%)	843.9		1125.7(16.7%)	964.8
$F_{y,min}$, N		992.8(108.6%)	475.9		958.9(70.3%)	563.2
$\overline{F}_z$, N		383.8(46.8%)	261.5		380.2(42.3%)	267.1
$F_{z,max}$, N		400.0(21.2%)	329.9		385.5(7.5%)	358.6
$F_{z,min}$, N		356.7(87.5%)	190.2		353.9(75.7%)	201.4

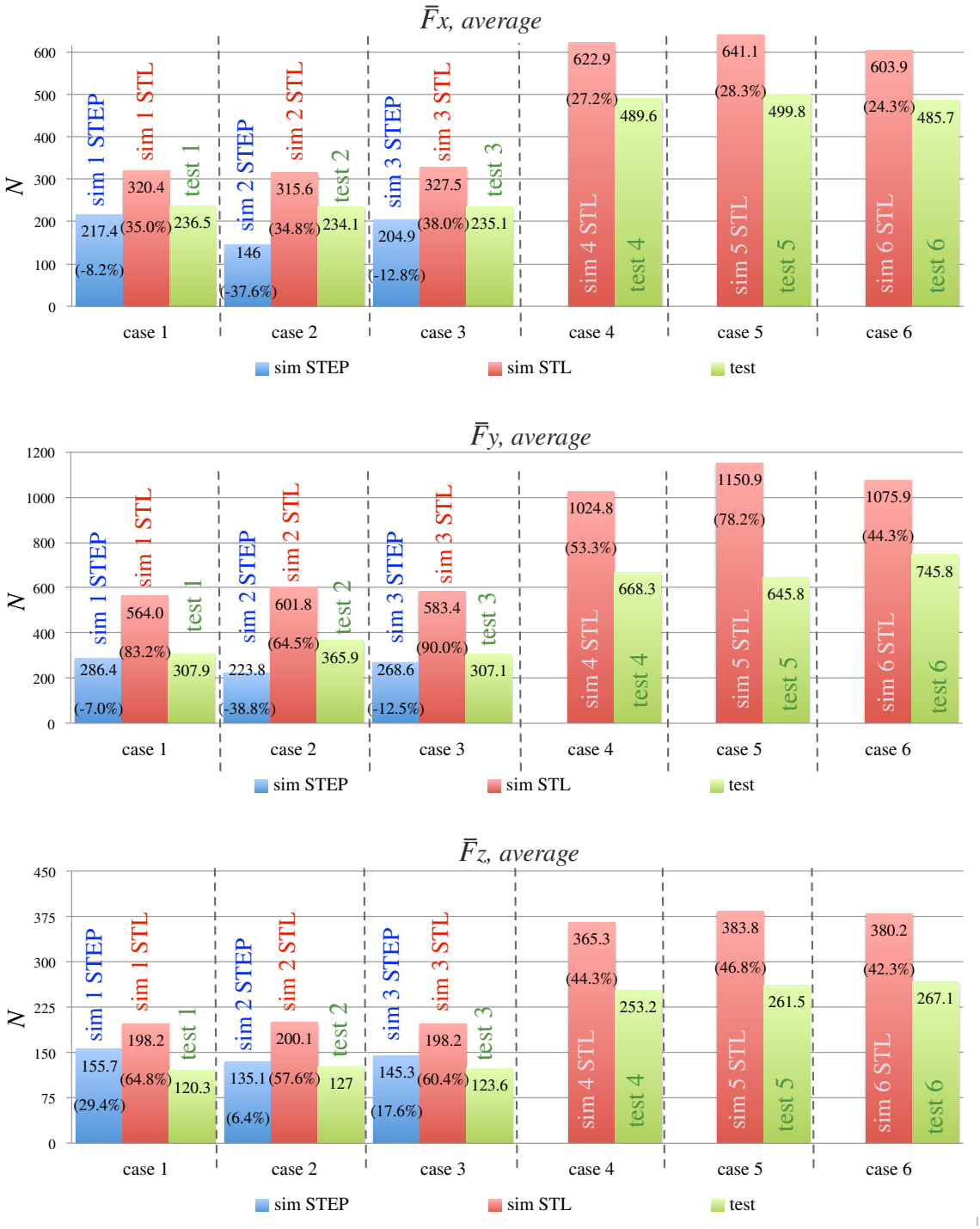

Figure 2.16: Results of the comparison between the average simulated (STEP and STL) and measured cutting forces values

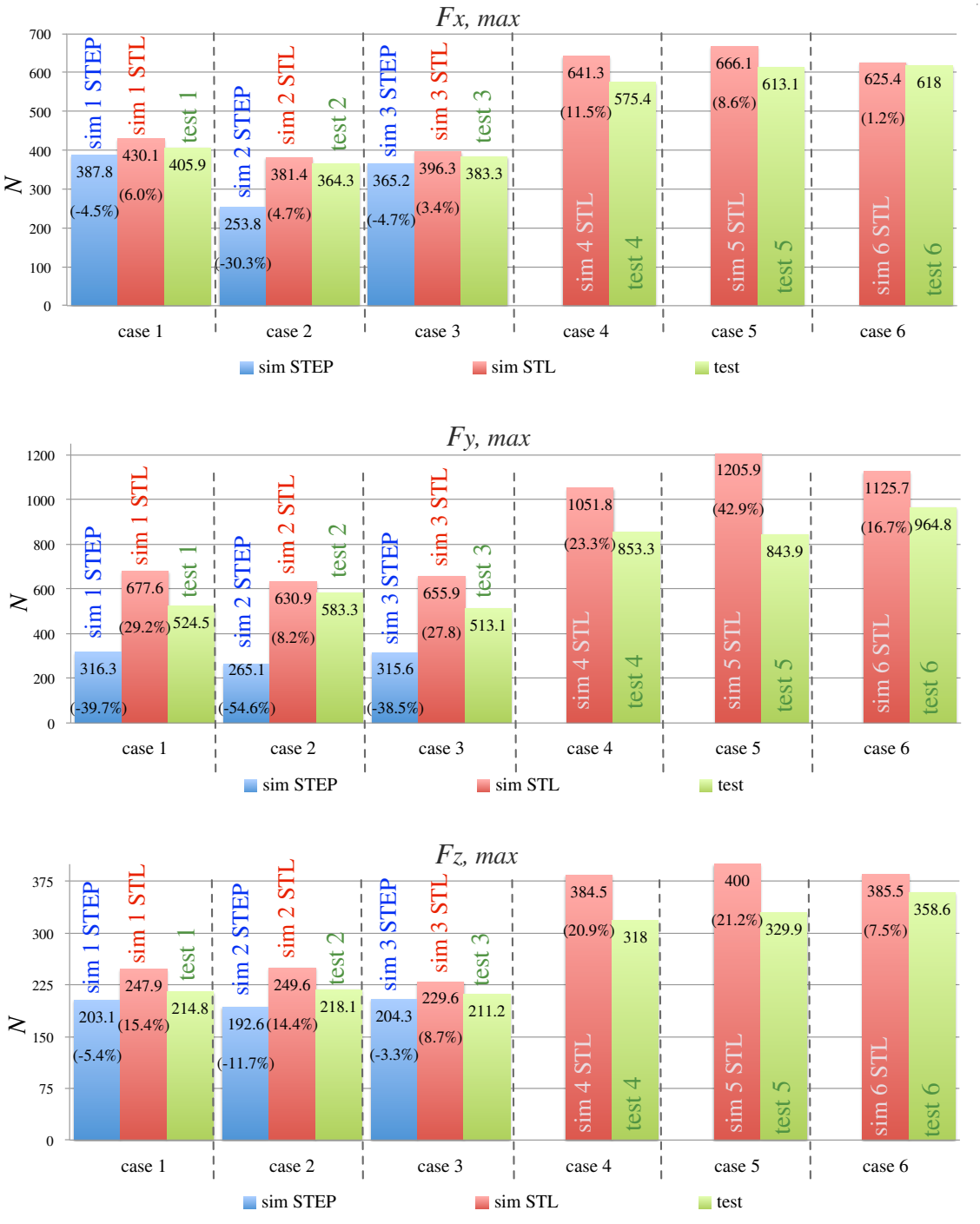

Figure 2.17: Results of the comparison between the maximum simulated (STEP and STL) and measured cutting forces values

Simulated results - the average cutting force values

Based on the results reported in the Fig.2.16, the following conclusions were done for the simulations of the average values of cutting forces $\overline{F}_x$, $\overline{F}_y$ and $\overline{F}_z$ performed in 3D FEM AdvantEdge by using STEP and STL cutting tool models:

1. For the first three studying cases with the depth of cut of 5.0 mm (Table 2.1) it was observed that the general tendency of 3D FEM simulations performed by using STEP models to represent tool geometry is to underestimate the average values of cutting forces $\overline{F}_x$ and $\overline{F}_y$, and to overestimate the average value of cutting force $\overline{F}_z$. The ranges of the percentage error values observed for the average simulated $\overline{F}_x$, $\overline{F}_y$ and $\overline{F}_z$ cutting forces simulations are (Fig.2.16):

   for the force $\overline{F}_x$: from -8.2% ('case 1') to -37.6% ('case 2');

   for the force $\overline{F}_y$: from -7.0% ('case 1') to -38.8% ('case 2');

   for the force $\overline{F}_z$: from 6.4% ('case 2') to 29.4% ('case 1').

2. The general tendency of 3D FEM AdvantEdge that was observed for the simulations performed by using STL files to represent tool geometry is to overestimate the average values of all three cutting forces.

   2.1. According to the results reported in the Fig.2.16, the ranges of the percentage errors values that were observed for the average values of simulated $\overline{F}_x$, $\overline{F}_y$ and $\overline{F}_z$ cutting forces for 5.0 mm of cutting depth tests ('case 1 - case 3' in the Table 2.1) amount:

   for the force $\overline{F}_x$: from 34.8% ('case 2') to 38.0% ('case 3');

   for the force $\overline{F}_y$: from 64.5% ('case 2') to 90.0% ('case 3');

   for the force $\overline{F}_z$: from 57.6% ('case 2') to 64.8% ('case 1').

   2.2. According to the results reported in the Fig.2.16, the ranges of the percentage errors values that were observed for the average values of simulated $\overline{F}_x$, $\overline{F}_y$ and $\overline{F}_z$ cutting forces for 10.0 mm of cutting depth tests ('case 4 - case 6' in the Table 2.1) amount:

for the force $\overline{F}_x$: from 24.3% ('case 6') to 28.3% ('case 5');

for the force $\overline{F}_y$: from 44.3% ('case 6') to 78.2% ('case 5');

for the force $\overline{F}_z$: from 42.3% ('case 6') to 46.8% ('case 5').

3. When STEP files were used to simulate the average cutting forces $\overline{F}_x$, $\overline{F}_y$ and $\overline{F}_z$, the minimum discrepancy between the simulated and measured data was obtained for the tools with sharp and 20.0 μm edge rounding (Fig.2.16), and it amounts -8.2% for the force $\overline{F}_x$ ('case 1'), -7.0% for the force $\overline{F}_y$ ('case 1'), and 6.4% for the force $\overline{F}_z$ ('case 2').

4. When STL files were used to simulate the average cutting forces $\overline{F}_x$, $\overline{F}_y$ and $\overline{F}_z$, that occur in the cutting process with 5.0 mm cutting depth, the minimum discrepancy between the simulated and measured data was obtained for the tool with 20.0 μm edge rounding ('case 2' in the Fig.2.16), and it amounts 34.8% for the force $\overline{F}_x$, 64.5% for the force $\overline{F}_y$, and 57.6% for the force $\overline{F}_z$.

5. The same result was also observed for 3D FEM simulations performed with STL models to simulate cutting tests with 10.0 mm cutting depth. The minimum discrepancy between the average values of the simulated and measured data was obtained for the 20.0 μm edge rounding ('case 6' in the Fig.2.16), and it amounts 24.3% for the force $\overline{F}_x$, 44.3% for the force $\overline{F}_y$, and 42.3% for the force $\overline{F}_z$.

Simulated results - the maximum cutting force values

The results of the maximum values of the simulated and measured cutting forces $F_{x,max}$, $F_{y,max}$ and $F_{z,max}$ are reported in the Fig.2.17 and Table 2.1.

1. For the first three studying cases, where the cutting depth value was equal to 5.0 mm (Table 2.1), it was observed that the general tendency of 3D FEM simulations performed by using STEP models to represent tool geometry is to underestimate the maximum values of all three cutting forces $F_{x,max}$, $F_{y,max}$ and $F_{z,max}$. The ranges of the percentage errors values that were observed for the maximum values of the predicted cutting forces (Fig.2.17) are:

for the force $F_{x,max}$: from -4.5% ('case 1') to -30.3% ('case 2');

for the force $F_{y,max}$: from -38.5% ('case 3') to -54.6% ('case 2');

for the force $F_{z,max}$: from -3.3% ('case 3') to -11.7% ('case 2').

2. For 3D FEM simulations performed for the milling tests with 5.0 mm cutting depth by using STL tool models it was observed that the general tendency of 3D FEM AdvantEdge is to overestimate the maximum value of all three cutting forces. The ranges of the percentage errors values that were observed for the maximum values of the predicted cutting forces are (Fig.2.17):

   for the force $F_{x,max}$: from 3.4% ('case 3') to 6.0% ('case 1');

   for the force $F_{y,max}$: from 8.2% ('case 2') to 29.2% ('case 1');

   for the force $F_{z,max}$: from 8.7% ('case 3') to 15.4% ('case 1').

3. For 3D FEM simulations performed for the milling tests with 10.0 mm cutting depth by using STL tool models it was observed that the general tendency of 3D FEM AdvantEdge is to overestimate the maximum value of all three cutting forces. The ranges of the percentage errors values that were observed for the maximum values of the predicted cutting forces are (Fig.2.17):

   for the force $F_{x,max}$: 1.2% ('case 6') and 11.5% ('case 4');

   for the force $F_{y,max}$: 16.7% ('case 6') and 42.9% ('case 5');

   for the force $F_{z,max}$: 7.5% ('case 6') and 21.2% ('case 5')

4. When STEP files were used to simulate the maximum values of cutting forces $F_{x,max}$, $F_{y,max}$ and $F_{z,max}$, the minimum discrepancy between the simulated and measured data was obtained for the tools with sharp and 5.0 μm edge rounding (Fig.2.16), and it amounts -4.5% for the force $F_{x,max}$ ('case 1'), -38.5% for the force $F_{y,max}$ ('case 3'), and -3.3% for the force $F_{z,max}$ ('case 3').

5. When STL files were used to simulate the maximum values of cutting forces $F_{x,max}$, $F_{y,max}$ and $F_{z,max}$ that occur in the cutting process with 5.0 mm cutting depth, the minimum discrepancy between the simulated and measured data was obtained for the tools with 5.0 μm and 20.0 μm edge rounding values ('case 3' and 'case 2' in the Fig.2.16 respectively), and it amounts 3.4% for the force $F_{x,max}$ ('case 3'), 8.2% for the force $F_{y,max}$ ('case 2'), and 8.7% for the force $F_{z,max}$ ('case 3').

6. For 3D FEM simulations performed by using STL models to simulate cutting tests with 10.0 mm cutting depth it was observed that the minimum discrepancy between the maximum values of the simulated and measured data was obtained for the tool with 20.0 μm edge rounding ('case 6' in the Fig.2.16), and it amounts 1.2% for the force $F_{x,max}$, 16.7% for the force $F_{y,max}$, and 7.5% for the force $F_{z,max}$.

2.5.3 Influence of CAD Tool Models on Deformed Chip Geometry

The evaluation of the influence of CAD tool models on 3D FEM AdvantEdge prediction accuracy in terms of the chip geometries (deformed chip thickness and curvature radius) was performed by comparing real and simulated chip geometries. The real chip samples were collected after having performed cutting tests reported in the Table 2.1. The chip geometries were analyzed by using a Scanning Electron Microscope (SEM) JSM-IT300LV by Jeol with 5-axis Motorized Asynchronous Stage, expanded pressure range (10-650 Pa), large specimen chamber, and embedded CCD camera with high resolution for imaging.

Three samples of each type of the collected chip types (6 studying cases) were positioned on a metal plate as shown in the Fig.2.18 to make images. An example of one taken image is reported in the Fig.2.19(a). After the images were taken, such chip geometry parameters as deformed chip thickness h_{chip}, and deformed chip curvature radius R_c were measured with respect to the scale of the image. In total, 18 samples $\times$ 2 parameters = 36 measurements were performed. The resulting average values of the deformed chip thickness and deformed chip curvature radius are reported in the Table 2.5.

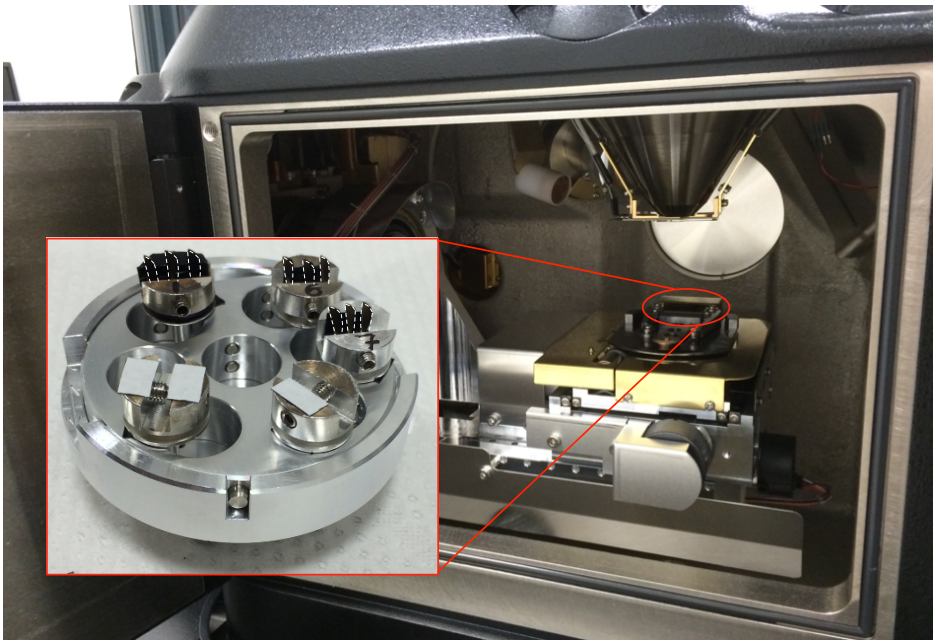

Figure 2.18: SEM JSM-IT300LV and chip samples positioning

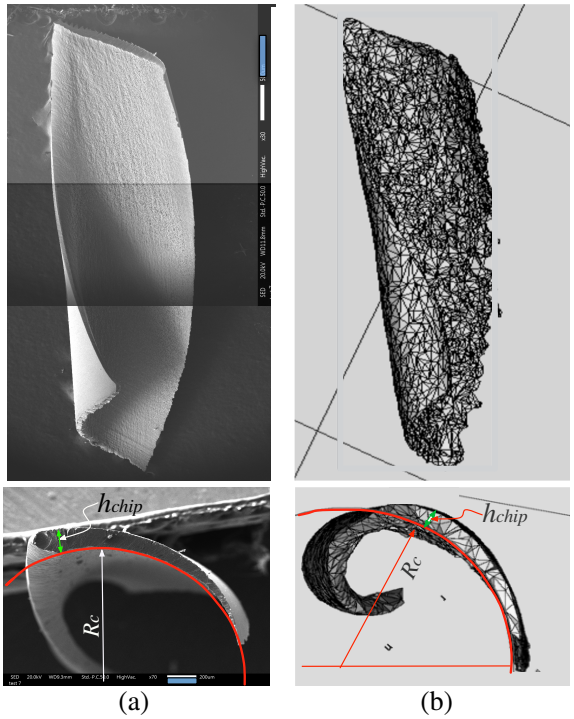

Figure 2.19: Comparison of the chip geometry: (a) collected chip samples; (b) simulated (STL) chip samples; h_{chip} - deformed chip thickness; R_c - deformed chip curvature radius

Table 2.5: Collected and simulated chip geometries

	r_{edge}, μm	n_{el}	R_{chip}, mm	h_{chip}, mm
sim 1 STEP sim 1 STL test 1	sharp	1 138512 487434	0.96 (-3.0%) 1.01 (2.0%) 0.99	0.13 (-18.8%) 0.17 (6.3%) 0.16
sim 2 STEP sim 2 STL test 2	20.0	597266 461708	0.93 (-7.0%) 1.01 (1.0%) 1.0	0.11 (-35.3%) 0.18 (5.9%) 0.17
sim 3 STEP sim 3 STL test 3	5.0	693431 382541	0.92 (-5.2%) 0.99 (2.1%) 0.97	0.14 (-6.7%) 0.17 (13.3%) 0.15
sim 4 STEP sim 4 STL test 4	5.0	- 468380	- 1.7 (3.9%) 1.03	- 0.19 (11.8%) 0.27
sim 5 STEP sim 5 STL test 5	sharp	- 539436	- 1.04 (3.0%) 1.01	- 0.18 (12.5%) 0.16
sim 6 STEP sim 6 STL test 6	20.0	- 492233	- 1.1 (3.8%) 1.06	- 0.2 (11.1%) 0.18

In order to analyze simulated chip geometries Tecplot post-processing software was used. An example of the simulated chip sample (STL), and methodology used to perform measurements of the chip geometry parameters (deformed chip thickness and deformed chip curvature radius) are shown in the Fig.2.19(b). In total, 54 measurements were performed for the simulated chip geometries (2 parameters $\times$ 9 types of simulated chip samples $\times$ 3 replications = 54 measurements). The resulting average values are reported in the Table 2.5, where in parentheses are specified the percentage error values obtained by comparing simulated geometries against real chip samples dimensions.

Figure 2.20 summarizes the results of the chip geometries comparison reported in the Table 2.5. In this figure, the real and simulated values of chip geometries are shown in the end of each column, and the percentage error values are reported in parentheses.

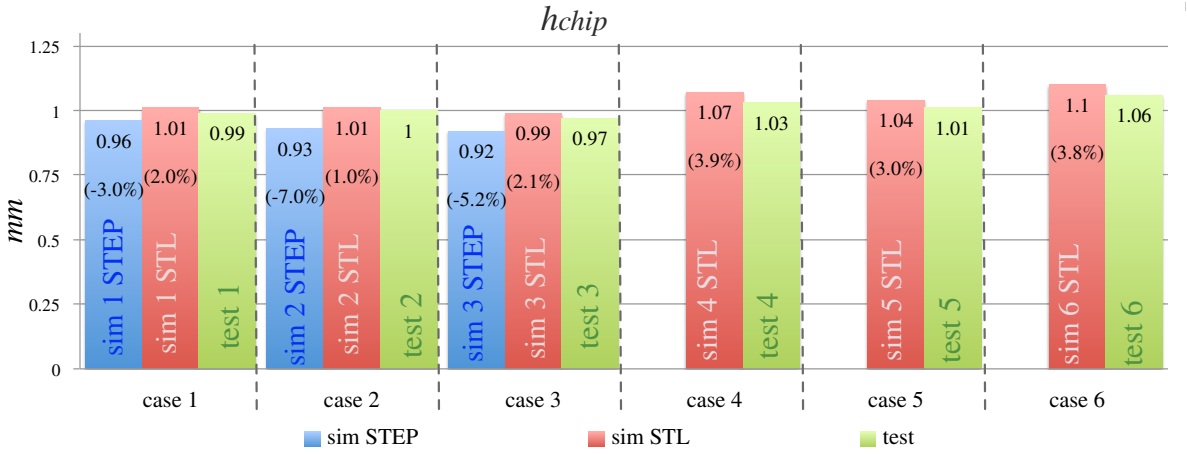

(a)

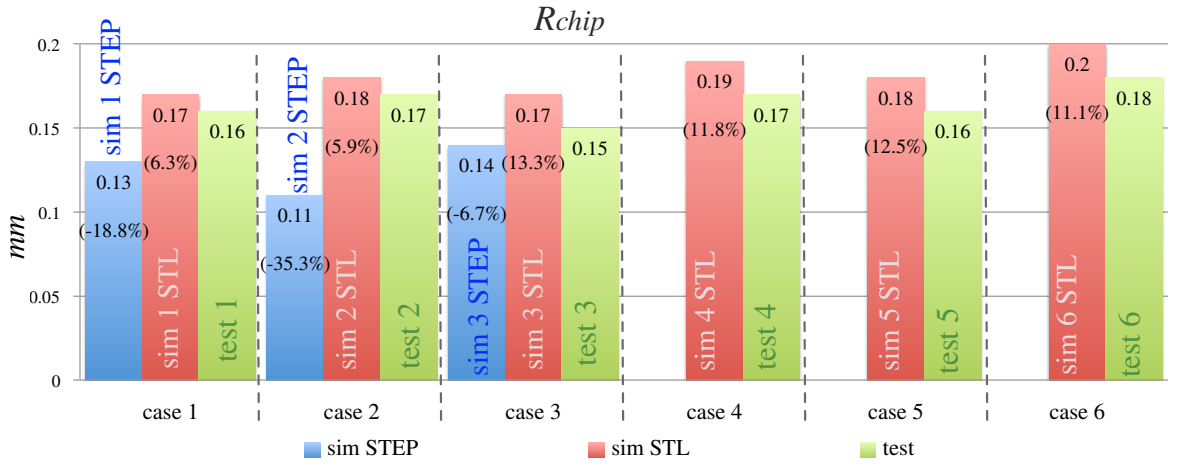

(b)

Figure 2.20: The results of comparison between the simulated (STEP and STL) and collected chip geometries: (a) deformed chip thickness; (b) deformed chip curvature radius

Simulated results - deformed chip thickness

Based on the results reported in the Fig.2.20(a) and in the Table 2.5, the following conclusions were done regarding the simulated deformed chip thickness h_{chip}:

1. For the studying cases when STEP files were used to performed milling process simulation ('case 1 - case 3' in the Table 2.5), it was observed that the general tendency of 3D FEM simulations performed in AdvantEdge is to underestimate deformed chip thickness value. According to the obtained results, the range of the percentage error values for the simulated deformed chip thickness values is (Fig.2.20(a)):

   for STEP files: from -3.0% ('case 1') to -7.0% ('case 2').

2. In cases when STL files were used to performed 3D FEM simulations, it was observed that the general tendency of the used software is to overestimate deformed chip thickness values for all six studying cases.

   2.1. As instance, when 3D FEM simulations were performed for the side down-milling process with 5.0 mm of cutting depth ('case 1 - case 3' in the Table 2.1), the following range of the percentage errors values between the simulated and real deformed chip thickness values was observed:

   for STL files: from 1.0% ('case 2') to 2.1% ('case 3').

   2.2. The results reported in the Fig.2.20(a) indicated that the percentage error value for the deformed chip thickness simulation increase with the increase of the cutting depth value. The following range of the percentage error values was observed for 3D FEM simulations performed for the side down-milling process with 10.0 mm of cutting depth ('case 4 - case 6' in the Table 2.1):

   for STL files: from 3.0% ('case 5') to 3.9% ('case 4').

Simulated results - deformed chip curvature radius

The chip curvature occurs due to the contact between the formed chip and different obstacles such as chip breaker, workpiece, face of the tool etc. During this contact, cutting forces exert on the chip, thus causing a bending moment in the chip body. As result, the chip is forced to deform elastically, and to a certain extent also plastically, by the bending moment and then to curve [46].

The following results were observed for the curvature radius R_{chip} simulations in 3D FEM AdvantEdge based on the data reported in the Fig.2.20(b) and in the Table 2.5:

1. For the studying cases when STEP files were used to performed milling process simulation ('case 1 - case 3' in the Table 2.1), it was observed that the general tendency of 3D FEM simulations performed in AdvantEdge is to underestimate deformed chip curvature radius value. According to the obtained results, the range of the percentage error values for the simulated deformed chip thickness value is (Fig.2.20(b)):

   for STEP files: from -6.7% ('case 3') to -35.3% ('case 2').

2. In cases when STL files were used to performed 3D FEM simulations, it was observed that the general tendency of AdvantEdge software is to overestimate deformed chip curvature radius value for all six studying cases.

   As instance, when 3D FEM simulations were performed for the side down-milling process with 5.0 mm and 10.0 mm of cutting depth ('case 1 - case 3' and 'case 4 - case 6' in the Table 2.1 respectively), the following ranges of the percentage errors between the simulated and measured deformed chip curvature radius values were observed:

   for STL files ($a_p = 5.0$ mm): from 5.9% ('case 2') to 13.3% ('case 3');

   for STL files ($a_p = 10.0$ mm): from 11.1% ('case 6') to 12.5% ('case 5').

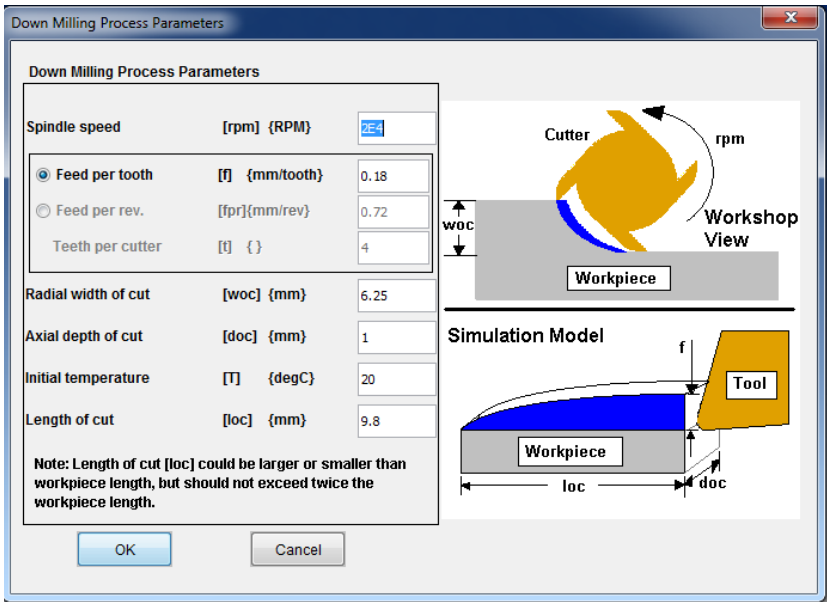

Figure 2.21: Set-up of down-milling process in 2D FEM AdvantEdge

2.6 2D FEM APPLIED TO THREE-DIMENSIONAL MILLING OPERATIONS

One of the latest strategies that manufacturing companies follow in order to speed up the pace of new product development, is to use 2D FEM instead of 3D FEM modeling as the first-step-approximation technique to study the influence of tool geometry on such process parameters as cutting forces (F_x and F_y), and cutting temperatures. Dependently on the type of studying cutting operation, 2D FEM models cannot always describe the exact geometry of cutting tool and mechanics of real three-dimensional processes, thus introducing some mismatches [127].

In case 2D FEM technique is applied to simulate side down-milling process performed by using a typical end mill with helix angle greater than *zero*, there are two important mismatches between 2D FEM approach and real cutting process. The first distinction relates to the chip shape, which in case of 2D FEM is 'straightened' (Fig.2.21), such that no curvature radius occurs and not full information about chip geometry is obtained (the chip length is neglected). The second mismatch regards to the end mill geometry. In 2D

FEM the cutter edge is assumed to be a straight fluted, and the helix angle that influences chip load and cutting forces, especially the axial force F_z, is not taken into account. Therefore, when using 2D FEM modeling for tool development, the simulated data of cutting forces cannot be directly used for real process description, understanding and analysis, unless some techniques allowing to overcome discussed differences are applied.

A two-step approach aimed to get over this problem, and to see if 2D FEM data can be used for prediction of cutting forces F_x and F_y that occur in three-dimensional processes, will be proposed in Chapter 3 of this work. The first step of this approach will consist in performing a particular tilted side down-milling operation, where the z-axial vertical force F_z is minimized, thus making this operation to appear similar to the bi-dimensional case with only F_x and F_y acting forces. Such condition will be achieved by changing orientation of the cutting tool by tilting it at an angle α against feed direction (Fig.3.13), thereby decreasing the vertical force F_z. The second step will include the tilted milling process simulation performed by applying the cutting force model, the development of which will also be discussed in Chapter 3. In order to approve or reject the possibility of 2D FEM modeling to simulate cutting forces F_x and F_y that occur in three-dimensional process side down-milling, simulations of this process will be performed by applying cutting forces coefficients identified based on 2D FEM data into the proposed cutting forces model.

SUMMARY

The research activities of this chapter deal with the application of FEM modeling techniques, and in particular of the numerical solver AdvantEdge by Third Wave System, to the cutting processes simulations, and they were performed in collaboration with the production unit of Sandvik Coromant placed in Rovereto (Italy).

Some general topics such as principles of FEM model formulation, meshing and chip separation procedures, material constitutive and friction models, and deformation and heat generation zones are briefly discussed. The state-of-the-art review regarding the results of the evaluation of prediction accuracy of AdvantEdge was done for both types of FEM modes: 2D and 3D. The available data in the literature showed that AdvantEdge numerical tool permits to predict cutting process behaviour with acceptable level of inaccuracy.

Two important arguments were discussed in this chapter. The first important study performed in this chapter was aimed at the evaluation of the influence of different CAD tool models on the prediction accuracy of 3D FEM AdvantEdge simulations in terms of the cutting forces (average and maximum values) and chip geometries. Since the R&D group of Sandvik Coromant (Rovereto, Italy) uses STEP and STL models of cutting tool prototypes to study their performance in AdvantEdge environment, these two types of models were used in this work. Regarding this topic, the application of different CAD tool models in FEM analysis in AdvantEdge, the difference between STEP and STL models, the import files and meshing set-up procedures were described in detail.

The study concluded in this chapter includes nine 3D FEM simulations of the side down-milling process (three simulations with STEP files, and six simulations with STL files) performed in 3D AdvantEdge, and the experimental campaign that consisted in six

cutting tests performed under conditions corresponding to the set-up of 3D simulations. As the cutting tools were used three different end mills with three different tool edge radiuses: sharp, 5.0 μm, and 20.0 μm provided by Sandvik Coromant.

When analyzing the mesh cells dimensions and their distribution created for both types of the tool models, STEP and STL, it was observed that the difference between these parameters is significant for two studying cases, especially in the regions close to the cutting edge. The comparison of the created mesh geometries showed that the sizes of the mesh cells created to describe cutting edge radiuses for STL models are pretty higher than for STEP files, and in particular they are higher than the real edge rounding values. The mesh comparison showed that in cases when STEP files were used, the mesh cell sizes are not equal, and in the region close to the cutting edge the mesh cells dimensions are very small. Instead, for cases when STL models were used, it was observed that the mesh cells dimensions are more or less uniform for the whole tool volume. Another important aspect that was observed for STL CAD models is that the value of the resolution that has to be specified when importing the files of this type in 3D AdvantEdge does not influence the results of mesh generation.

The analysis of the collected experimental and simulated data showed that there is a significant difference between the simulated data (the average and maximum values of the cutting forces, and values of the deformed chip thickness and curvature radius) obtained with STEP and STL CAD models of the cutting tool.

The comparison between the average values of the simulated and measured cutting forces indicated that STEP and STL influence differently the average cutting force value prediction:

1. The general tendency of 3D FEM AdvantEdge with applied STEP tool models is to underestimate the average values of cutting forces $\overline{F}_x$ and $\overline{F}_y$, and overestimate the average values of force $\overline{F}_z$.

2. The general tendency of 3D FEM AdvantEdge with applied STL tool models is to overestimate the average values of all three cutting forces $\overline{F}_x$, $\overline{F}_y$ and $\overline{F}_z$.

The comparison between the maximum values of the simulated and measured cutting forces indicated that STEP and STL influence differently the maximum cutting force value prediction:

1. The general tendency of 3D FEM AdvantEdge with applied STEP tool models is to underestimate the maximum value of all three cutting forces $F_{x,max}$, $F_{y,max}$ and $F_{z,max}$.

2. The general tendency of 3D FEM AdvantEdge with applied STL tool models is to overestimate the maximum value of all three cutting forces $F_{x,max}$, $F_{y,max}$ and $F_{z,max}$.

The comparison of the simulated and measured deformed chip thickness showed that STEP and STL influence differently the deformed chip thickness value prediction:

1. The general tendency of 3D FEM AdvantEdge with applied STEP tool models is to underestimate the deformed chip thickness value.

2. The general tendency of 3D FEM AdvantEdge with applied STL tool models is to overestimate the simulated deformed chip thickness value.

The comparison of the simulated and measured deformed chip curvature radius showed that STEP and STL influence differently the deformed chip curvature radius value prediction:

1. The general tendency of 3D FEM AdvantEdge with applied STEP tool models is to underestimate the deformed chip curvature radius value.

2. The general tendency of 3D FEM AdvantEdge with applied STL tool models is to overestimate the deformed chip curvature radius value.

The second argument discussed in this chapter is related to the problems of the application of 2D FEM modeling to simulate the influence of cutting tool geometries on cutting forces F_x and F_y that occur in three-dimensional cutting processes. The differences and mismatches between 2D FEM models and three-dimensional process geometry are discussed underlining the fact that 2D FEM modeling data cannot be directly used to study and analyze the influence of tool geometries on cutting forces F_x and F_y that act in three-dimensional systems, unless some techniques allowing to overcome discussed differences are applied. The approach to overcome mismatches between 2D FEM and real process, side down-milling operation, and results of its application will be reported in Chapter 3.

Chapter 3

Cutting Forces Modeling of Side Down-Milling Processes

In this chapter the development of a mechanistic three-dimensional model of cutting forces suitable for non-tilted and tilted side down-milling process simulations is presented. The following topics are discussed: mechanics of both non-tilted and tilted operations, and influence of the tilting angle on tool/workpiece engagement boundaries and cutting forces directions. The description of different procedures used to calculate instantaneous cutting edge engagement length and to identify the total number of edges simultaneously engaged in workpiece and their contribution to the resulting cutting force, and the approach used to identify milling force coefficients for both two- and three-dimensional systems are also discussed.

The final part of this chapter discusses the problems and issues of using 2D FEM models to study the influence of cutting tool geometries on cutting forces F_x and F_y that occur in three-dimensional milling processes, which were discussed in Chapter 2, and discusses 2D FEM simulations that were carried out for identifying the coefficients used in the proposed cutting force model. The examples of the tilted and non-tilted process simulations performed by using the developed cutting forces model, and comparison of the simulated and measured cutting forces are also reported in this chapter.

3.1 STATE-OF-THE-ART

The development of a robust and accurate approach to calculate cutting edge/workpiece interaction zone, i.e. uncut chip area, is quite critical for cutting force modeling. The instantaneous chip area associated to chip load is not constant, and changes as the cutter rotates. To calculate boundaries of this area, such parameters as instantaneous chip thickness and chip length, i.e. axial edge engagement length, have to be calculated. In recent years many attempts to develop milling process models that allow to study and analyze the effects of tool geometry and cutting conditions on cutting forces have been done.

In the work [12], the authors Altintas and Lee presented the mechanistic model for cutting forces modeling suitable for ball-end milling operations which are characterized by the small axial depth of cut and chip load. In the model, the exact positions of cutter, and consequently of acting edge, are evaluated by considering true rigid body motion and structural displacements. The cutter body is divided into a number of slices placed along tool axis direction, and by identifying angular immersion for each point on acting edge, the instantaneous chip thickness is calculated as the difference between cutting arcs generated by two successive tooth motions. The cutting forces are modeled by distinguishing shearing and edge friction components, whose coefficients are identified based on the orthogonal cutting data by using oblique transformation method presented in [30]. The experimental verification of the efficiency of the proposed modeling system showed that measured and simulated cutting forces are in good agreement.

The authors Engin and Altintas in the paper [45] presented the generalized mathematical model of tool geometry for such types of the cutters as cylindrical end mill, ball-end and bull-nose mill, taper end and taper ball-end mill, cone and rounded end mill. By applying the proposed model, the cutter geometry is modeled by helical flutes wrapped around a parametric cylinder, and the coordinates of each point on cutting edge, influenced by such parameters as tool radius, radial and axial flute immersion, are mathematically expressed. The authors also presented the chip thickness

evaluation approach, based on true kinematics of milling as well as vibration of both cutter and workpiece. For cutting forces modeling the authors applied the system described in [12] and [93]. A few simulations and real cutting processes were performed within this work in order to verify the accuracy of the proposed method. According to the obtained results, the satisfactory agreement between predicted and measured cutting forces was observed.

Another approach for cutting forces modeling and simulation in end-milling processes described in [76] is based on the predictive machining theory for cutting forces modeling in end-milling, and allows to find machining characteristic factors from the input data of fundamental workpiece material properties, tool geometry and cutting conditions. In the proposed model, each cutter edge is discretized into a number of slices along cutter axis, and cutting action of each edge is modeled as oblique cutting process with cutting edge having an inclination angle, as proposed in [102] and [11], thus allowing to take into account the edge helix angle influencing cutting forces. In order to validate the accuracy of the developed system, the authors performed nine end-milling process simulations, and compared obtained data with cutting tests performed under the same cutting conditions, stating that the maximum percentage simulation error was found to be less than 18.0%.

The authors Ikua et al. in the work [59] worked on the development of the model for cutting forces modeling in contouring and ramping operations of convex surfaces that are typically performed by using ball-end mills. The authors described a procedure to calculate chip geometry influenced by such parameters as tool/workpiece engagement geometries, cross-feed, feed rate, and depth of cut, and a procedure to calculate the trochoidal path that is followed by each point placed on the cutting edge. The cutting forces modeling is based on the rigid force model proposed in [128], into which were added two matrices to extend this model for contouring and ramping operations. The experimental verification of the efficiency of proposed modeling system showed that the measured and simulated cutting forces are in good agreement.

The authors Lamikiz et al. in the work [74] proposed the semi-mechanistic model for cutting forces modeling in sculptured surface up-milling and down-milling. In the developed system, cutting edge is discretized, thus allowing to simplify its geometry as a sequence of linear, i.e. discrete, elements. The positions of each element on cutting edge are described as a functions of spindle rotation angle, as well as their positions on tool that depends on tool radius, and are used to calculate length and width of instantaneous chip samples. In order to adapt the proposed calculation routine to the chip section identification for sculptured milling processes, the authors introduced a transformation matrix that includes two rotations and translation terms. By applying this matrix, undeformed chip thickness can be determined with respect to workpiece reference system. For instantaneous cutting forces modeling the authors applied the model proposed in the work [12], and in order to obtain resulting cutting forces that arise in sculptured milling, the authors applied another transformation matrix to project instantaneous cutting forces components into fixed tool reference system. The validation of the proposed system showed that the difference between predicted and measured cutting forces was less that 10.0% for almost all of 9 studied cases.

Another authors Azeem and Feng in [16] introduced the ball-end milling force model suitable for the modeling of cutting force arising during multi-axis ball-end milling, where non-horizontal and rotational cutting tool motions are common. The authors proposed a generalized approach to determine undeformed chip thickness, by considering individually undeformed chip thickness generated by horizontal, non-horizontal, and rotational cutting motions. In addition, the authors also discussed a procedure for cutting force coefficients calibration, specifying the fact that coefficients identified by applying traditional techniques like [30] are based on the horizontal cutting data, and cannot be used to calculate cutting forces of ball-end milling processes with non-horizontal cutting motions. The validation of the accuracy of the proposed technique was done by means of experimental campaign. It was confirmed that the developed model is suitable for cutting forces modeling in multi-axis ball-end milling.

The authors Sonawane and Joshi in their work [130] discussed the development of the analytical chip geometry model used to predict undeformed and deformed chip geometries in ball-end milling on horizontal and inclined workpieces. In addition, the authors also presented the model used to evaluate instantaneous shear angle value along any cross section as a function of chip thickness ratio and axial rake angle. As reported by the authors, the shear angle prediction is a basic step towards cutting forces modeling, which was performed as reported in another work written by one of the authors [129]. The proposed system was used to predict the instantaneous cutting forces at 0.0°, 15.0°, and 45.0° workpiece inclinations, and obtained simulated forces values were compared to measured data. According to the results, the good agreement between both types of the data was observed. Another important aspect was also highlighted by the authors. It was shown that the increase of chip dimensions, except deformed chip thickness, is directly proportional to the increase of workpiece inclination angle, what in its turn results into an easy flow of deformed chip over cutting tool flank, which leads to the higher shear angle during the cut.

In the work [44], the authors worked on the development of a cutting forces model suitable to predict cutting forces in face milling performed by using cutters with inserts. The authors developed a generalized mathematical model to describe the coordinates (locations) of cutting edges of each insert that can be differently oriented with respect to cutter body by rotating them at different lead and axial rake angles around cutter axes. In the proposed model cutting insert is divided into a number of small disk elements, and the model provides a possibility to predict chip thickness distribution along cutting zone, and consequently to predict cutting forces. In this work, the cutting force system is modeled by applying the procedure reported in [9]. The experimental validation of the developed approach showed that by solving the mechanics and dynamics of cutting at each edge point, and integrating them over contact zone, the milling process can be modeled for any inserted cutter. As instance, the authors reported the results of comparison between experimental and predicted cutting forces of slot milling tests performed with two different cutter types. According to the reported information, graphs of the cutting forces trends, the good agreement between measured and simulated values was achieved.

Lutfi et al. in the work [136] presented a general process model for cutting forces simulation in multi-axis milling. For the modeling system development the authors considered cutting tool as a revolution of an arbitrary section curve around tool axis, resulting in a volumetric tool envelope that is described by axial and radial segments. In addition, the authors also introduced the projective geometry approach to calculate tool/workpiece engagement boundaries described as a function of such parameters as cutting tool geometry, step over, cutting depth, lead, and tilt angles. By using the oblique-to-orthogonal cutting transformation presented in [30], where orthogonal cutting force parameters are derived through thermo-mechanical process model [105], the cutting forces modeling is done by applying the model proposed in [12]. The accuracy of the developed system was verified by means of six different cutting tests, and good agreement between the simulated and predicted cutting forces was observed.

The authors Huang et al. in the work [55] worked on the development of a cutting force modeling system for five-axis ball-end milling processes. The authors presented a method to calculate decoupled chip thickness by taking into account lead and tilt angles separately, and a method to calculate complex geometrical engagements that occur in five-axis ball-end milling. After the experimental validation of the proposed method was performed, where predicted and experimental chip volumes were compared, the proposed model was included into the cutting force modeling system built based on the approach presented in [12] by applying cutting force coefficients identified based on the 18 experimental tests. The validation of the cutting forces modeling approach with implemented proposed chip thickness model included 34 tests with different values of the lead and tilt angles. The results of the validation showed that the biggest deviations between the measured and simulated cutting forces that amounted around 10.0% were observed in several tests with negative tilt angles.

The authors Ozturk and Budak in the works [107] and [106] worked on the development of five-axis ball-end milling stability and cutting forces model which considers the effects of lead and tilt angles on the process. The authors introduced two types of uncut chip thickness - static and dynamic, which occur due to tool feed

movement, and due to displacements of cutting tool with respect to workpiece under the action of cutting forces respectively. In the proposed cutting forces modeling system, tool/workpiece axial engagement length is divided into the differential cutting elements to determine varying engagement boundaries. The modeling of cutting force system is done in terms of local chip thickness and width, and local cutting coefficients identified based on the procedure described in [30]. The experimental validation of the proposed cutting force model included 70 cutting tests performed under different cutting conditions and by using different lead (0.0°, 30.0°), and tilt (-40.0°, -15.0°, 50.0°) angle values. The comparison of collected experimental and predicted cutting forces data indicated that for the proposed model the maximum observed percentage error value amounted 6.2%.

The authors Taner, Ömer and Erhan in the work [136] presented a generalized cutting force modeling approach for multi-axis milling operations. In this work, the authors proposed a new methodology to describe geometry of engaged cutting tool section, where this section is considered as a revolution of an arbitrary section curve around tool axis, thus resulting in a volumetric tool envelope. In addition, the authors also presented an approach to determinate engagement region between cutting tool envelope and workpiece. This approach is based on cutting tool geometry and such process parameters as step over, cutting depth, lead, and tilt angles. To model cutting forces, the authors extended the approach presented in [12] by introducing a forces transformation matrix, and uncut chip thickness model described in terms of the normal vector to cutting edge, feed vector, and feed per tooth value. The validation of the proposed general force model was done by performing six milling tests by using standard and custom-made tools. As reported by the authors, it was observed that in general simulated cutting forces values agree well with measured data except slight discrepancies at random conditions.

The authors Baro et al. in the source [21] presented an analytical approach to predict cutting forces in face-milling operations performed by using self-propelled round insert face-milling cutters. In this work, the authors discussed the effects of geometry of inserts on undeformed chip cross-sectional area, and reported an equation to define the area of

chip cross-section. The cutting force modeling system proposed in this work is based on the model presented in the work [72], and it includes such additional terms as the effect of inclination angle of insert on the magnitude of cutting forces, effect of inserts rotation on cutting forces, and effect of friction at tool/chip interface on cutting forces. The validation of the developed cutting forces modeling system for self-propelled rotary tool face-milling operation was done by means of an experimental part that consisted in 8 cutting tests. The comparison between simulated and measured cutting forces values showed that the average error for F_x, F_y and F_z cutting forces simulation amount 10.0%, 12.0% and 17.0% respectively.

As shown, a lot of systems have been proposed to predict cutting forces for different types of milling processes. Despite this fact, to the best of author's knowledge any of them deal with such particular processes as non-tilted and tilted side down-milling performed with helical end mills. To meet the requirement, in this chapter it will be discussed and proposed the mechanistic cutting force model suitable for non-tilted and tilted side down-milling process simulations. It has to be noted that the proposed model is a rigid model since the effects of tool deflection on chip area are not taken into account.

3.2 SIDE DOWN-MILLING PROCESS

Side down-milling is a cutting operation where a cutter, i.e. end mill, rotates in the direction of feed, and a workpiece advances towards the cutter. In some particular cases, depending on the CNC machining center configuration, the position of workpiece remains fixed, and cutting action is performed by tool translation along feed direction.

As can be seen in the Fig.3.1(a), which illustrates an example of the down-milling process, the thickness of chip or chip load, h_{chip,ϕ_i}, varies periodically as a function of time-varying immersion described by the tool angular position, angle ϕ_i, and it depends on the tool/workpiece interaction zone. When the cutting edge enters into the workpiece, the chip thickness reaches maximum value, and then it gradually reaches zero at the end of cut.

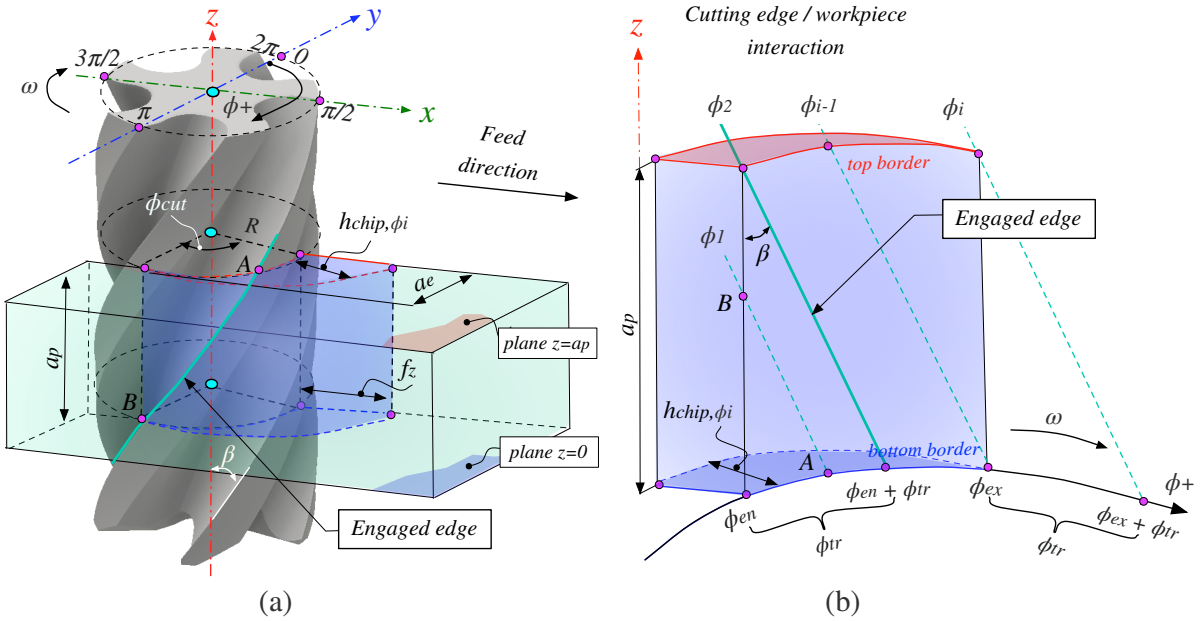

Figure 3.1: Schematic representation of: (a) side milling performed with end mill : a_p - axial cutting depth; a_e - radial cutting depth; h_{chip,ϕ_i} - instantaneous chip thickness; f_z - feed per tooth; R - tool radius; β - tool helix angle; ω - tool rotation direction; ϕ_{cut} - edge engagement angle; (b) edge/workpiece interaction phases: ϕ_{en} - edge enter angle; ϕ_{tr} - tool transient angle; ϕ_{ex} - edge exit angle; ϕ_i - instantaneous tool angular position; AB - instantaneous length of cutting edge engaged into workpiece

Figure 3.1(b) shows the engagement region between the cutting edge and workpiece. The engaged cutting edge, indicated as the inclined *straight* line, moves according to the $\phi+$ direction. The inclination of this line is described by the helix angle β value, which provides the gradually increasing chip load along this acting edge.

As can be observed in the Fig.3.1(b), the engagement region is represented by two vertical and two horizontal boundaries. The vertical limits are represented by two points, i.e. tool angular positions, called the enter ϕ_{en} and exit ϕ_{ex} angles. According to the process conditions reported in the Fig.3.1(a), in the studying system the tool rotates in the clockwise direction, and the edge exit angle ϕ_{ex} is equal to π radians. The enter angle ϕ_{en} depends on the cutting (engagement) angle ϕ_{cut} value, and can be found by using the following equations:

$$\phi_{cut} = \arccos\left[1 - \frac{a_e}{R}\right] \tag{3.1}$$

$$\phi_{en} = \phi_{ex} - \phi_{cut} \tag{3.2}$$

The horizontal boundaries of the engagement section are represented by the top and bottom limits, and they are shown in the Fig.3.1(a,b) as *blue* and *red* curves respectively. As can be seen, these boundaries are represented by the resulting surfaces of the intersection of right circular cylinder (tool body) and two parallel planes lying on the workpiece at $z = 0$ and $z = a_p$. Since these planes are perpendicular to the tool z axis, the result of this intersection are two circles. The 'footprints', i.e. projections, of these circles on the cylinder plane xz are represented by the two straight lines.

As can be seen in the Fig.3.1(b) during the cutting edge/workpiece interaction period occur three different phases that depend on the tool transient angle value ϕ_{tr}:

enter zone: $[\phi_{en}..(\phi_{en} + \phi_{tr})]$;

stable zone: $[(\phi_{en} + \phi_{tr})..\phi_{ex}]$;

exit zone: $[\phi_{ex}..(\phi_{ex} + \phi_{tr})]$.

Each angular position in the engagement interval $[\phi_1 \,..\, \phi_i]$ represents the instantaneous length of the cutting edge engaged into the workpiece, and can be used to describe the chip load behaviour. In the Fig.3.1(b) this length is shown as line AB. It must be noticed that outside of the engagement region represented by the interval $[\phi_{en}..(\phi_{ex} + \phi_{tr})]$ the chip load is not generated.

In the enter zone, the length of the edge engaged into the workpiece varies between $AB = 0$, when the point A reaches the angular $\phi_i = \phi_{en}$ position, and maximum value, $AB = a_p/\cos\beta$, reached when the point A attains the $\phi_i = \phi_{en} + \phi_{tr}$ position. The value of the transient angle ϕ_{tr} depends on the axial depth of cut, a_p, and tool geometry parameters such as tool radius R and tool helix angle β. In the present work, this angle is described as a projection of the fully engaged cutting edge on the plane xy (Fig. 3.1(a)), and is calculated by using the following formula:

$$\phi_{tr} = \frac{a_p \tan(\beta)}{R} \tag{3.3}$$

In the stable zone, limited by the $[(\phi_{en} + \phi_{tr})..\phi_{ex}]$ interval, the length of the acting edge engagement remains constant, and it is equal to the maximum possible value of $AB = a_p/\cos\beta$. Once the point A reaches the angular position $\phi_i = \phi_{ex}$, the edge engagement length starts to decrease until the cutting edge is completely outside of the cutting region, such that $AB = 0$. This is the exit phase of the edge/workpiece intersection domain, and the last position that can be reached by the point A is $\phi_i = \phi_{ex} + \phi_{tr}$.

3.2.1 Maximum Number of Engaged Cutting Edges

One of the common situations that can take place in the side milling process performed by using end mills is that there can be more than one edge cutting simultaneously. When such situation occurs, the contribution of each engaged cutting edge to the total chip load must be considered.

The maximum number of the engaged cutting edges depends on the tooth pitch angle $\psi(n)$, cutting angle ϕ_{cut}, and tool transient angle ϕ_{tr}. As discussed above, in the side milling the cutting angle (Eq.3.1) depends on the radial depth of cut a_e and tool radius R, and the transient angle (Eq.3.3) depends on the axial depth of cut a_p, tool helix angle β and radius R. The edges spacing angle $\psi(n)$ value can be constant or variable, and it depends on the total number of the tool edges. In the first case, this value can be calculated by using the Eq.3.4, and in case the cutter has variable distance between the edges, the values of the tooth spacing angles can be provided by the tool manufacturing company.

$$\psi(n) = \frac{2\pi}{n}, \tag{3.4}$$

where n is the total number of the tool edges.

In the Fig.3.2 a few examples of the possible variations of the maximum number of the simultaneously cutting edges are shown. As can be seen in the Fig.3.2(a) and Fig.3.2(b), which represent the influence of the radial cutting depth a_e on the cutting angle ϕ_{cut} value, the increase of this value (the axial cutting depth a_p is constant) causes the increase of the cutting angle value, and consequently the number of the edges cutting simultaneously. In fact, in the proposed examples the maximum number of the engaged

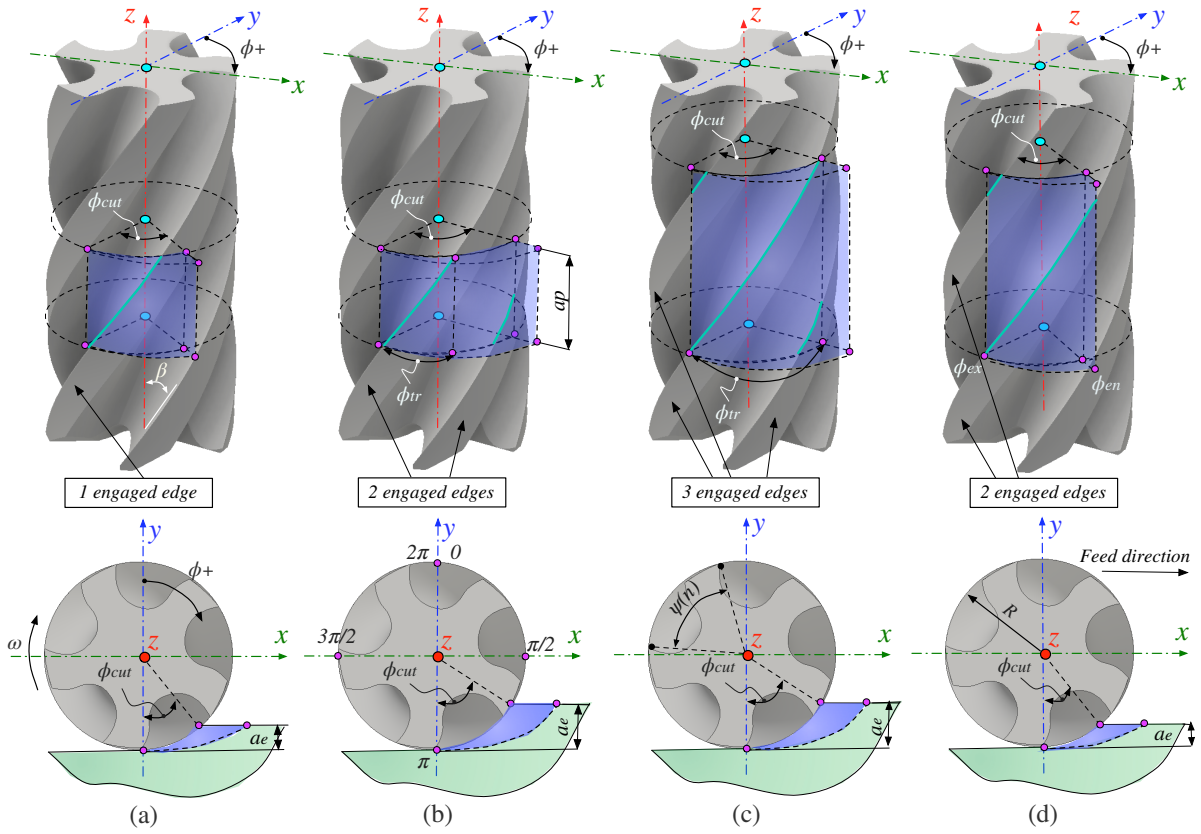

Figure 3.2: Schematic representation of possible variations of the maximum number of engaged cutting edges: $\psi(n)$ - tooth pitch angle; R - radius of the tool; β - edge helix angle; a_p - axial depth of cut; a_e - radial width of cut; ω - tool rotation direction; ϕ_{cut} - cutting (engagement) angle; ϕ - tool angular position; ϕ_{en} - edge enter angle; ϕ_{ex} - edge exit angle; ϕ_{tr} - tool transient angle; (x, y, z) - coordinate system in the workpiece reference frame that coincides with the tool coordinate system (x', y', z')

edges is one (Fig.3.2(a)) for the smaller value of the radial depth a_e, and reaches two when this depth is increased (Fig.3.2(b)). The opposite behaviour can be observed for the examples shown in the Fig.3.2(c) and Fig.3.2(d), which represent the case of the engaged edges number reduction.

In the Fig.3.2(b) and Fig.3.2(c), instead, it is shown the influence of the axial cutting depth a_p on the engaged edges number. As can be observed, the variation of this value (the radial cutting depth a_e is constant), also influences the number of the edges acting

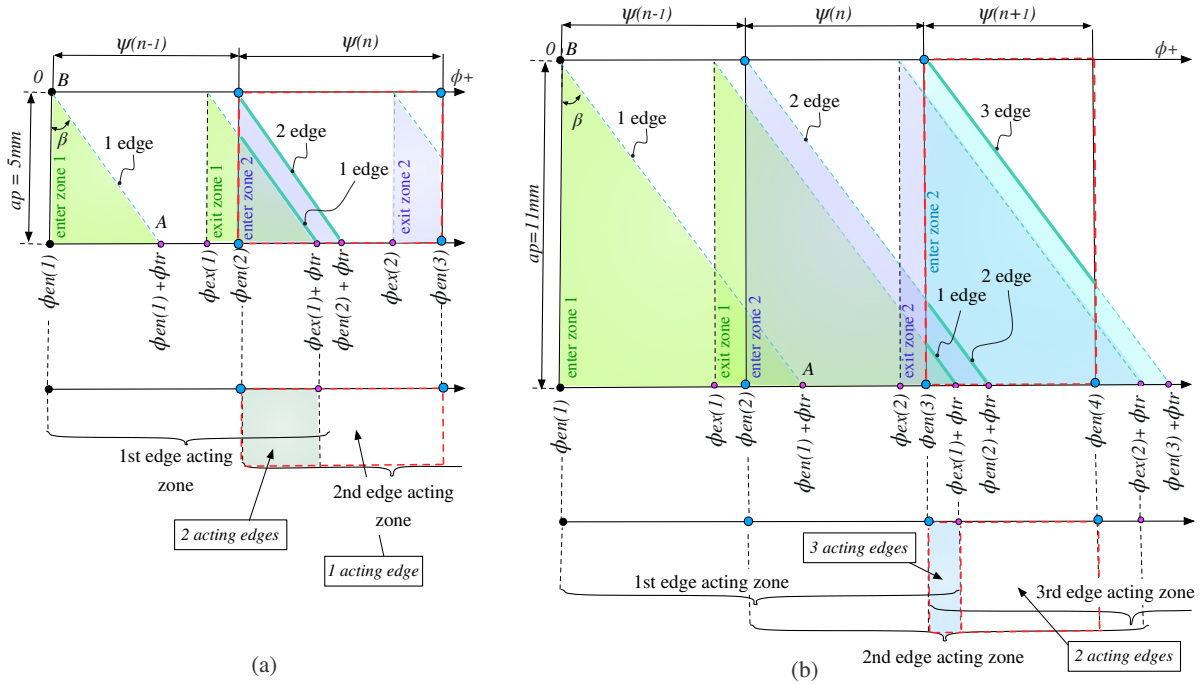

Figure 3.3: Schematic representation of the maximum engaged cutting edges number identification for n-edge end mill with variable tooth pitch angle: (a) two edges are cutting simultaneously; (b) three edges are cutting simultaneously; $\phi_{en}(n)$ and $\phi_{ex}(n)$ - enter and exit angles respectively calculated for each cutting edge of the tool; a_p - axial depth of cut; $\psi(n)$ - pitch distance between two consecutive cutting edges; ϕ - tool angular position

simultaneously. When the value of the depth a_p is increased, the maximum number of the engaged edges varies from two (Fig.3.2(b)) to three (Fig.3.2(c)).

The general approach to identify the maximum number of the engaged cutting edges is presented below. In the Fig.3.3(a) and Fig.3.3(b) the example of the identified two and three edges cutting simultaneously is shown. The approach includes the following steps:

1. The value of the constant tooth pitch angle $\psi(n)$ has to be calculated by using the Eq.3.4. Otherwise, if the tool has variable distances between edges, the values of $\psi(n)$ can be provided by tool manufacturer. In the Fig.3.3, which demonstrates the example of the tool with variable pitch angles, the positions of the angles $\psi(n)$ are shown as the *blue* dots, placed on the axis ϕ that represents tool circumference $[0..2\pi R]$.

2. The transient angle ϕ_{tr} has to be calculated by using the Eq.3.3.

3. The enter and exit angles have to be identified by using the cutting angle ϕ_{cut} value calculated with the Eq.3.1, and the process geometry parameters (Fig.3.1(a)). In case the cutting tool is characterized by the unconstant pitch angle values, the procedure has to be repeated for each cutting edge.

   For the given example in the Fig.3.3(b), these values are calculated as follows:

$$\phi_{en}(1) = 0 \tag{3.5}$$

$$\phi_{en}(2) = \psi(n-1) + \phi_{en}(1) = \psi(n-1) \tag{3.6}$$

$$\phi_{en}(3) = \psi(n) + \phi_{en}(2) = \psi(n) + \psi(n-1) \tag{3.7}$$

$$\phi_{ex}(1) = \phi_{en}(1) + \phi_{cut} = \phi_{cut} \tag{3.8}$$

$$\phi_{ex}(2) = \phi_{en}(2) + \phi_{cut} = \psi(n-1) + \phi_{cut} \tag{3.9}$$

$$\phi_{ex}(3) = \phi_{en}(3) + \phi_{cut} = \psi(n-1) + \psi(n) + \phi_{cut} \tag{3.10}$$

4. The acting zones of each cutting edge have to be calculated.

   For the studying example the following expressions are used:

$$\text{Acting zone } 1^{st} \text{ edge:} \qquad [\phi_{en}(1) \;..\; (\phi_{ex}(1) + \phi_{tr})] \tag{3.11}$$

$$\text{Acting zone } 2^{nd} \text{ edge:} \qquad [\phi_{en}(2) \;..\; (\phi_{ex}(2) + \phi_{tr})] \tag{3.12}$$

$$\text{Acting zone } 3^{rd} \text{ edge:} \qquad [\phi_{en}(3) \;..\; (\phi_{ex}(3) + \phi_{tr})] \tag{3.13}$$

5. The maximum number of the edges acting simultaneously can be identified as:

   5.1. 1^{st} case: if the sum of the exit and transient angles of the first acting edge is smaller than the pitch angle $\psi(n-1)$, i.e.

$$\Big[[\phi_{ex}(1) + \phi_{tr}] < \psi(n-1)\Big] \quad \Rightarrow \quad \text{one edge is cutting} \tag{3.14}$$

5.2. 2^{nd} case: if the sum of the exit and transient angles of the first acting edge is greater than the pitch angle $\psi(n-1)$, i.e.

$$\Big[[\phi_{ex}(1)+\phi_{tr}] > \psi(n-1)\Big] \quad \Rightarrow \quad \text{two edges are cutting (Fig.3.3(a))} \quad (3.15)$$

5.3. 3^{rd} case: if the sum of the exit and transient angles of the first acting edge is greater than the sum of the pitch angles $\psi(n-1)$ and $\psi(n)$, i.e.

$$\Big[[\phi_{ex}(1)+\phi_{tr}] > [\psi(n-1)+\psi(n)]\Big] \quad \Rightarrow \quad \text{three edges are cutting (Fig.3.3(b))} \quad (3.16)$$

3.3 TILTED SIDE DOWN-MILLING PROCESS

In the tilted milling operations the cutting parameters and edge/workpiece engagement boundaries vary with the spindle axis orientation.

Figure 3.4 illustrates an example of the tool tilting by an angle α against the feed direction. It can be seen that when the tool axes are subjected to tilting, the maximum possible axial depth of cut value, a_p, increases, and its coordinate along the fixed z axis in the workpiece reference frame (x, y, z) can be determined as $z = a_p/\cos(\alpha)$.

Since the vertical axis z' in the tool reference frame (x', y', z') is no longer perpendicular to the xy plane of the workpiece reference frame (x, y, z), the bottom and top engagement borders are now represented by two ellipses (and not circles) formed by the intersection of the 'inclined' cylinder (tool body) and two planes lying at the workpiece at $z = 0$ and $z = a_p$ (Fig.3.4).

In order to identify the z' axis coordinates of these borders in the tool reference frame (x', y', z') the following approach is proposed in the present work. The procedure is presented in the Fig.3.5(a), and includes the calculation of the tool (cylinder) and tilted ('inclined') planes intersection curves. The planes are selected with respect to the tool reference frame (x', y', z') at positions $z' = 0$ and $z' = a_p/\cos(\alpha)$. Since the tool body is assumed to be equal to the cylinder body, it is described by the equation $x'^2 + y'^2 = R^2$. The following steps have to be performed:

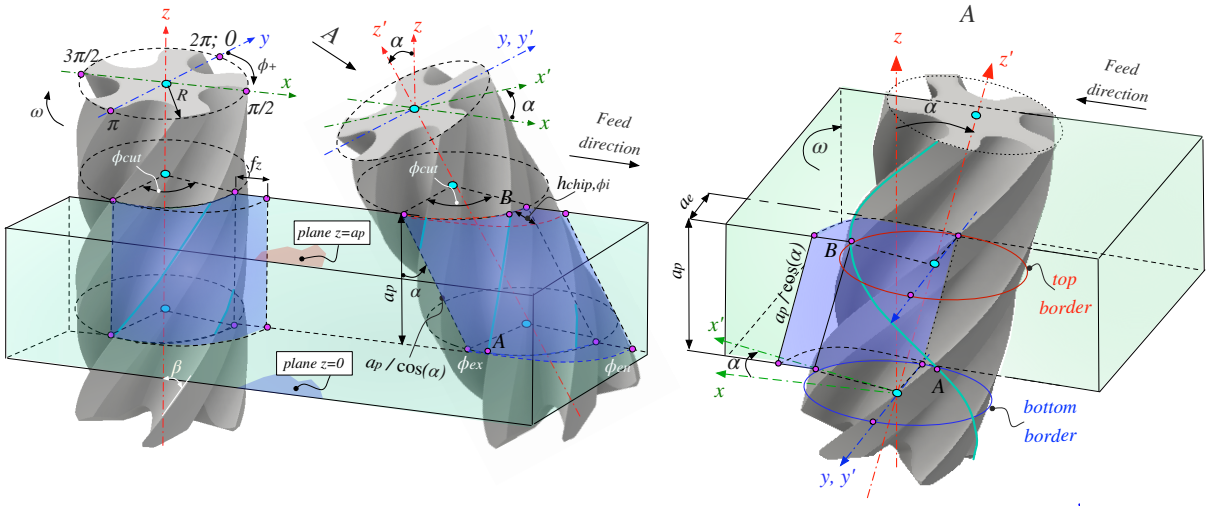

Figure 3.4: Schematic representation of the differences between the non-tilted and tilted milling: a_p - axial cutting depth; a_e - radial cutting depth; ϕ_{en} - edge enter angle; ϕ_{ex} - edge exit angle; ϕ_{cut} - tool engagement angle; α - tilting angle; AB - instantaneous engagement length of the acting edge; (x, y, z) - coordinate system in the workpiece reference frame; (x', y', z') - coordinate system in the tool reference frame; f_z - feed per tooth; h_{chip,ϕ_i} - instantaneous chip thickness; ω - tool rotation direction; ϕ - tool angular position

1. The equation of the plane passing through the point $P = [R; 0; 0]$ and perpendicular to the unit vector $\hat{n} = [\sin(\alpha); 0; \cos(\alpha)]$ has to be found. In order to do that, the general plane equation has to be rewritten by using the coordinates of the vector $\hat{n}$ and point P such as:

$$ax' + by' + cz' + d = 0 \tag{3.17}$$

   1.1. By substituting the vector $\hat{n}$ coordinates into the Eq.3.17:

$$x' \sin(\alpha) + 0 + z' \cos(\alpha) + d = 0 \tag{3.18}$$

   1.2. By substituting the coordinates of the point P into the Eq.3.18:

$$R \sin(\alpha) + d = 0 \tag{3.19}$$

   1.3. Expressing the d value from the Eq. 3.19:

$$d = -R \sin(\alpha) \tag{3.20}$$

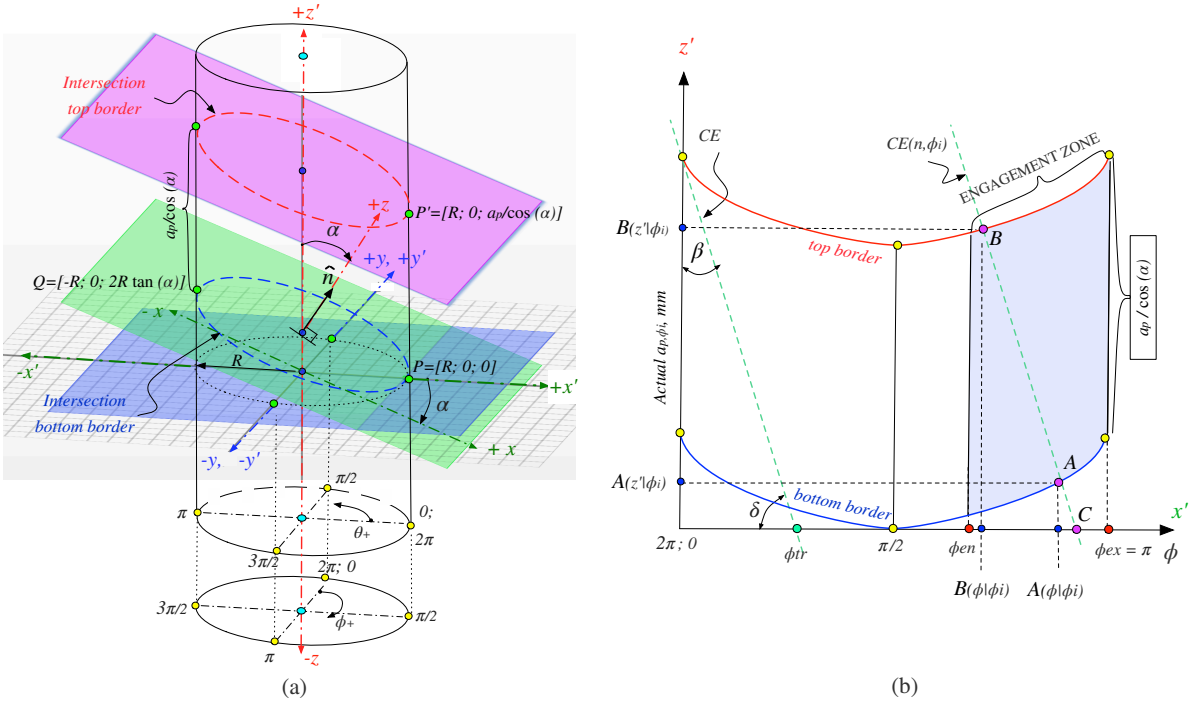

Figure 3.5: Schematic representation of the cylinder and tilted plane intersection: (a) $\hat{n}$ - unit vector; α - tilting angle; (x, y, z) - workpiece reference frame; (x', y', z') - tilted tool reference frame; P - point of intersection; $\theta = \pi - \phi$ - angle at xy plane; $\phi+$ - positive direction of the tool rotation; R - tool radius; (b) AB - engagement length of the acting edge at the instantaneous ϕ_i position; β - tool helix angle; ϕ_{tr} - tool transient angle; ϕ_{en} - edge enter angle; ϕ_{ex} - edge exit angle; $A(\phi|\phi_i)$ and $B(\phi|\phi_i)$ - projections of the points A and B on the x' axis respectively; $A(z'|\phi_i)$ and $B(z'|\phi_i)$ - projections of points A and B on the z' axis respectively; $CE(n|\phi_i)$ - actual acting edge at the instantaneous ϕ_i position; δ is the angle equal to $\delta = 180° - 90° - \beta$

Finally, the equation of the plane can be rewritten as:

$$x' \sin(\alpha) + z' \cos(\alpha) - R \sin(\alpha) = 0 \tag{3.21}$$

2. The z' axis coordinates of the curve representing the bottom border of the cylinder/tilted plane intersection in the tool reference frame (Fig.3.4) can be found by substituting the x' coordinates in the plane equation (Eq.3.21) with one of the parametric equations of the circle, such as:

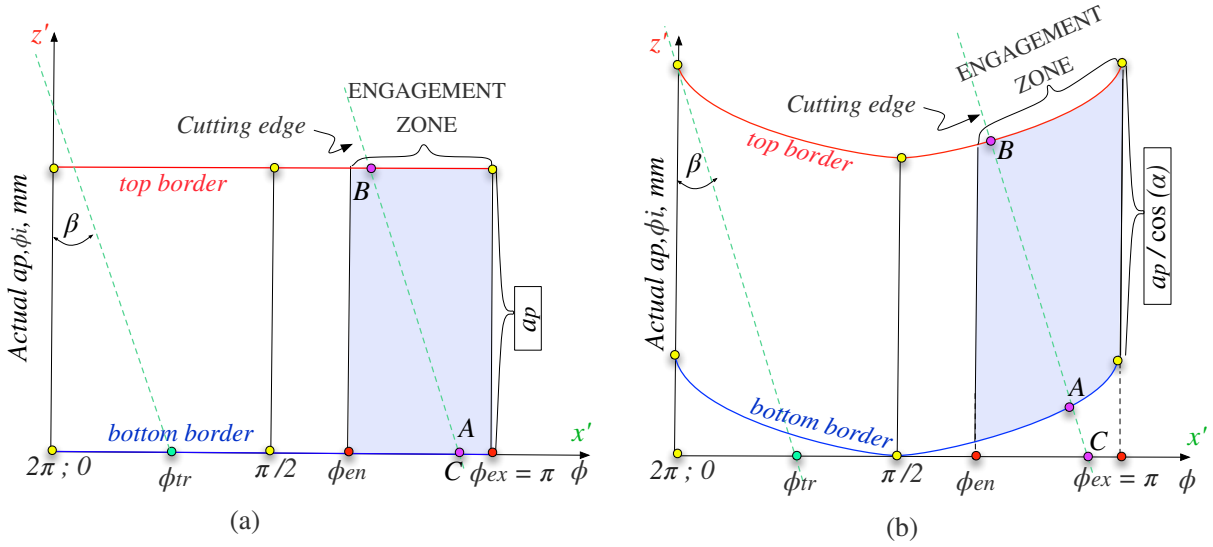

Figure 3.6: Schematic representation of the non-tilted (a) and tilted (b) engagement zones

2.1. The x' coordinates in the parametric form can be represented as (see Fig.3.5(a)):

$$x'(\phi) = R\cos(\theta) = R\cos(\pi - \phi) = R\sin(\phi) \tag{3.22}$$

2.2. By substituting the Eq.3.22 into the Eq.3.21, the following plane equation is obtained:

$$R\sin(\phi)\sin(\alpha) + z'\cos(\alpha) - R\sin(\alpha) = 0 \tag{3.23}$$

2.3. The z' coordinates can be expressed from the Eq.3.23 as:

$$z'(\phi) = \frac{R\sin(\alpha) - R\sin(\phi)\sin(\alpha)}{\cos(\alpha)} = \frac{R\sin(\alpha)\Big[1 - \sin(\phi)\Big]}{\cos(\alpha)} \tag{3.24}$$

Finally, the equation of the bottom border can be expressed as:

$$z'(\phi) = R\tan(\alpha)\Big[1 - \sin(\phi)\Big] \tag{3.25}$$

3. The z' axis coordinates of the curve representing the top border of the cylinder/tilted plane intersection (Fig.3.4) can be found by shifting vertically the equation of the bottom border (Eq.3.25) by the value $a_p/\cos(\alpha)$:

$$z'(\phi) = R\tan(\alpha)\Big[1 - \sin(\phi)\Big] + \frac{a_p}{\cos(\alpha)} \tag{3.26}$$

As can be seen from the Eq.3.25 and Eq.3.26, the profiles of the top and bottom boundaries of the tool/workpiece engagement zone vary with the tilting angle changing. In fact, this behaviour can be confirmed when analyzing the projection of the lateral surface area, i.e. 'footprint', limited by the bottom and top engagement boundaries (Fig.3.5(b) and Fig.3.6) on the tool body. The higher will be the value of the tilting angle α, more curved will be the projections of the intersection lines on the tool axis z'. In case when no tilting occurs, these projections will be represented by the straight lines like is shown in the Fig.3.6.

3.4 CUTTING FORCES MODELING

The model proposed in this chapter is the generalized cutting forces model suitable to simulate cutting forces that arise in the side down-milling operations subjected to the tool, i.e. spindle, tilting. In the proposed system, the instantaneous position of the cutting edge and geometry of the tilted cutter/workpiece engagement area are described mathematically, thus providing the accurate determination of the process behaviour - the basis for the cutting forces modeling. With respect to other available cutting force models discussed in the state-of-the-art, in the proposed model the calculation of the axial tool/workpiece engagement limits, and consequently cutting forces, is done without cutting edge discretizing into a number of the slices along the cutter axis. Instead, the instantaneous axial edge engagement length is identified by applying the Newton-Raphson algorithm, and equations of the cylinder-plane intersection that represent the top and bottom edge/workpiece engagement boundaries.

In the studying tilted milling system (Fig.3.5(b)), the point C represents, with respect to the tool angular positions ϕ, the instantaneous i-th position of the cutting edge $CE(n)$ acting in the cutting region. The instantaneous intersection of the cutting edge with the boundaries of the engagement section is shown as the segment AB, and it is used to calculate the actual length of the axial contact, a_{p,ϕ_i}, at each position of the tool. This contact length is determined as the instantaneous distance between the intersection points A and B projected on the tilted tool axis z'. The axial engagement of the tooth,

the length a_{p,ϕ_i}, has to be projected on the tool vertical axis since the model that will be utilized to calculate the cutting forces is the one proposed in [9].

3.4.1 Flute Engagement Length

An approach to identify the instantaneous positions of the intersection points A and B, and the instantaneous value of the axial cutting edge engagement length a_{p,ϕ_i} for a given mill position ϕ_i in the engagement region $[\phi_{en}..(\phi_{ex} + \phi_{tr})]$ is presented below (see also the Fig.3.5(b)). The following steps have to be performed:

1. The engagement boundaries, both vertical and horizontal, have to be identified by using the equations discussed previously (Eq.3.2, Eq.3.25, Eq.3.26):

$$f_{left}(\phi) = \phi_{en} \tag{3.27}$$

$$f_{right}(\phi) = \phi_{ex} \tag{3.28}$$

$$f_{top}(\phi) = R\tan(\alpha)\Big[1 - \sin(\phi)\Big] + \frac{a_p}{\cos(\alpha)} \tag{3.29}$$

$$f_{bottom}(\phi) = R\tan(\alpha)\Big[1 - \sin(\phi)\Big] \tag{3.30}$$

2. The equations to represent the cutting edge $CE(n)$ and its instantaneous positions have to be defined. In order to do that, the cutting edge can be represented by the linear function $z' = mx' + q$, where as the x' independent parameter is used the tool angular position ϕ (Fig.3.7(a)). The instantaneous position ϕ_i of the cutting edge in the engagement region ϕ can be determined by the horizontal translation of the linear function to the right.

   2.1. In order to represent the CE line with negative slope the following equation can be used:

$$m = -\frac{dz'}{Rd\phi} = -R\tan(\delta), \tag{3.31}$$

   where R is the tool radius; δ is the angle equal to $\delta = 180° - 90° - \beta$ or $\delta = \pi - \pi/2 - \beta$.

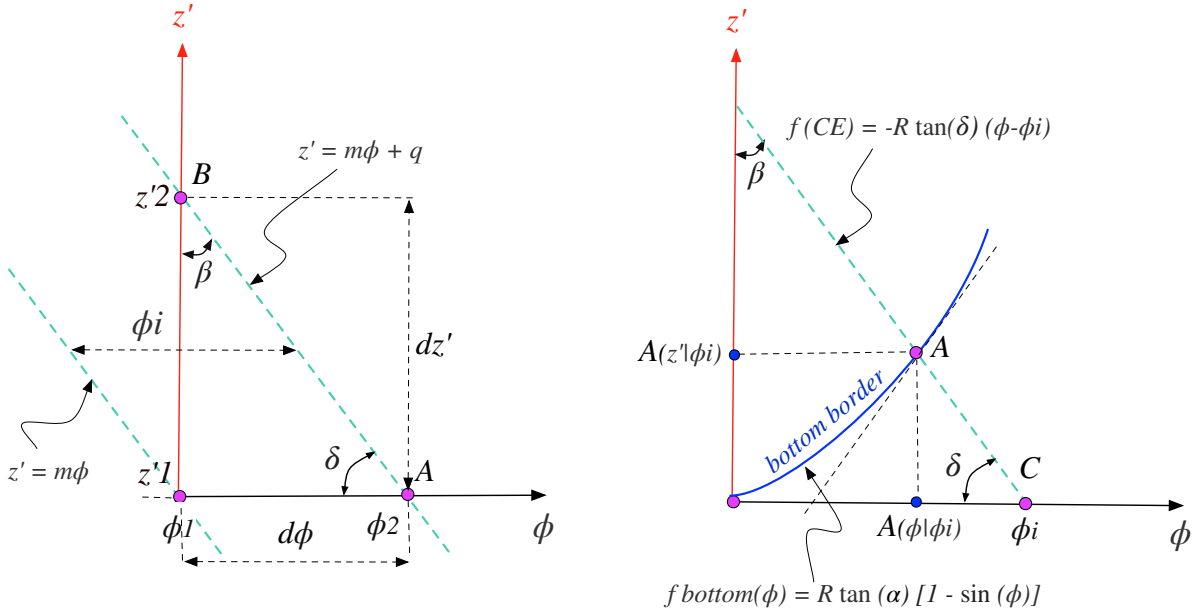

Figure 3.7: Schematic representation: (a) of the linear function translation approach, where m - slope of the line segment AB; q - point where the line AB crosses the z' axis, called $z'-intercept$; ϕ - tool angular position; ϕ_i - actual position of the line segment AB; δ - angle that is equal to $\delta = 180° - 90° - \beta$ or $\delta = \pi - \pi/2 - \beta$; β - tool helix angle; (b) of the Newton-Raphson algorithm used to calculate the abscissas of the intersection points A and B

2.2. At each instantaneous position ϕ_i along the cutting region ϕ the cutting edge line can be represented by the function:

$$f_{CE}(\phi|\phi_i) = m\phi + q = -R\tan(\delta)\phi + q \tag{3.32}$$

The identification of the instantaneous position of the cutting edge $CE(n)$ described by the translation of the function $f_{CE}(\phi|\phi_i)$ can be done as:

$$f_{CE}(\phi|\phi_i) = -R\tan(\delta)(\phi - \phi_i), \tag{3.33}$$

where the term $(\phi - \phi_i)$ is selected according to the function transformations rules.

3. The abscissas of the points A and B, which are described by the $A(\phi|\phi_i)$ and $B(\phi|\phi_i)$ values respectively, can be defined by solving the following equations, as instance with the Newton-Raphson algorithm.

   3.1. The general formula of the Newton-Raphson method is:

$$x_{n+1} = x_n - \frac{f(x_n)}{f'(x_n)}, \tag{3.34}$$

   where $f(x_n)$ is a function defined over the x axis; $f'(x_n)$ is a derivative of the function; x_n is an initial guess for a root of the function $f(x_n)$; x_{n+1} is the next approximation of the position of the intersection point between the tangent line of the graph at the position x_n and x axis.

   For the system proposed in this work, which is schematically illustrated in the Fig.3.7(b), the Newton-Raphson method can be written as:

$$\phi_{i+1} = \phi_i - \frac{f(\phi_i)}{f'(\phi_i)} \tag{3.35}$$

   3.2. The abscissae $A(\phi|\phi_i)$ and $B(\phi|\phi_i)$ of the points A and B respectively can be calculated by following procedure:

      3.2.1. The abscissa of the point A can be found as:

$$\begin{aligned} f(A)(\phi|\phi_i) &= f_{bottom}(\phi|\phi_i) - f_{CE}(\phi|\phi_i) \\ &= R\tan(\alpha)[1-\sin(\phi)] + R\tan(\delta)(\phi-\phi_i) \end{aligned} \tag{3.36}$$

$$\begin{aligned} f'(A)(\phi|\phi_i) &= f'_{bottom}(\phi|\phi_i) - f'_{CE}(\phi|\phi_i) \\ &= -R\tan(\alpha)\cos(\phi) + R\tan(\delta) \end{aligned} \tag{3.37}$$

$$A(\phi|\phi_i) = \phi_i - \frac{f(A)(\phi|\phi_i)}{f'(A)(\phi|\phi_i)} \tag{3.38}$$

3.2.2. The abscissa of the point B can be found as:

$$f(B)(\phi|\phi_i) = f_{top}(\phi|\phi_i) - f_{CE}(\phi|\phi_i) = \left[R\tan(\alpha)[1-\sin(\phi)] + \frac{a_p}{\cos(\alpha)}\right] + R\tan(\delta)(\phi-\phi_i) \quad (3.39)$$

$$f'(B)(\phi|\phi_i) = f'_{top}(\phi|\phi_i) - f'_{CE}(\phi|\phi_i) = -R\tan(\alpha)\cos(\phi) + R\tan(\delta) \quad (3.40)$$

$$B(\phi|\phi_i) = \phi_i - \frac{f(B)(\phi|\phi_i)}{f'(B)(\phi|\phi_i)} \quad (3.41)$$

3.3. When the abscissae are identified, it has to be verified that:

3.3.1. the maximum value of the $A(\phi|\phi_i)$ has to be $\leq \phi_{ex}$ position

$$A(\phi) = \min(\phi_{ex}, A(\phi|\phi_i)) \quad (3.42)$$

3.3.2. the minimum value of the $B(\phi|\phi_i)$ has to be $\geq \phi_{en}$ position

$$B(\phi) = \max(\phi_{en}, B(\phi|\phi_i)) \quad (3.43)$$

4. The ordinates of the points A and B, which are described by the $A(z'|\phi_i)$ and $B(z'|\phi_i)$ values, can be defined by solving the following equations:

$$A(z'|\phi_i) = f_{CE}(A(\phi|\phi_i)) = -R\tan(\delta)[A(\phi)-\phi_i] \quad (3.44)$$

$$B(z'|\phi_i) = f_{CE}(B(\phi|\phi_i)) = -R\tan(\delta)[B(\phi)-\phi_i] \quad (3.45)$$

5. Finally, the instantaneous value of the edge axial engagement length, a_{p,ϕ_i}, can be calculated by using the following formula:

$$a_{p,\phi_i} = |B(z'|\phi_i) - A(z'|\phi_i)| \quad (3.46)$$

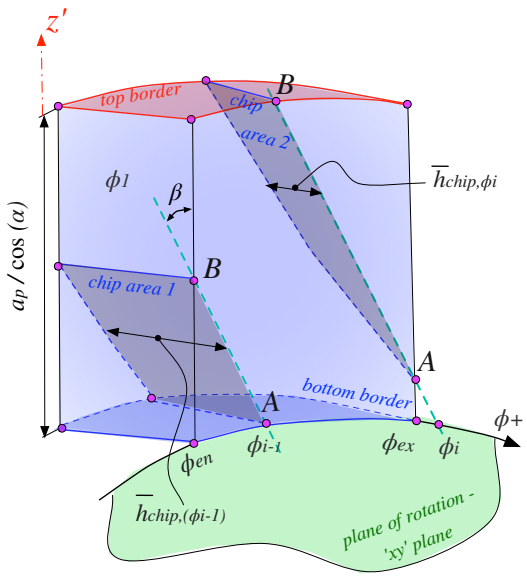

Figure 3.8: Schematic representation of a single engagement area that occur during the non-tilted cut: ϕ - tool angular position; ϕ_i - tool instantaneous position; $\phi+$ - tool rotation direction; ϕ_{en} - edge enter angle; ϕ_{ex} - edge exit angle; AB - engagement length of the acting edge at ϕ_i position; $\overline{h}_{chip,\phi_i}$ - instantaneous average chip thickness

3.4.2 Chip Thickness

In side milling process, the uncut chip area varies as the cut progresses in the $\phi+$ direction (Fig.3.8). Consequently, the value of the uncut chip thickness, h_{chip,ϕ_i}, has to be evaluated for each instantaneous edge position ϕ_i in the engagement region. Due to this, in order to facilitate the cutting forces modeling, it is convenient to specify the mean instantaneous chip thickness, $\overline{h}_{chip,\phi_i}$, that can be computed by taking the mean over the single angular position:

$$\overline{h}_{chip,\phi_i} = \begin{cases} -f_z \cos(\alpha) \left[\frac{\cos(A(\phi)) - \cos(B(\phi))}{A(\phi) - B(\phi)} \right], & \text{if } A(\phi) - B(\phi) > 0 \\ 0, & \text{otherwise} \end{cases} \tag{3.47}$$

3.4.3 Cutting Forces

Cutting forces depend on such parameters as tool geometry, cutting conditions, and workpiece material. The side milling process performed by using end mills is characterized by three cutting forces that act in the x, y and z axes directions. In the present work these forces are distinguished as the forces that act along the workpiece reference frame axes, $[F_{x,\phi_i}, F_{y,\phi_i}, F_{z,\phi_i}]$, and the forces that act along the tool reference frame axes, $[F'_{x,\phi_i}, F'_{y,\phi_i}, F'_{z,\phi_i}]$. Since the cutting forces are associated to the tool or workpiece, their directions depend on the position of the tool and workpiece with respect to each other.

In the Fig.3.9 it is illustrated the influence of the tool position on the directions of the forces $[F'_{x,\phi_i}, F'_{y,\phi_i}, F'_{z,\phi_i}]$. When no tilting of the tool occurs, the tool reference frame (x', y', z') coincides with the workpiece frame (x, y, z), and the directions of the cutting forces $[F'_{x,\phi_i}, F'_{y,\phi_i}, F'_{z,\phi_i}]$ coincide with the directions of the axes in the workpiece reference frame. Instead, when the tool is subjected to tilting, the tool reference frame is 'rotated' by the tilting angle value (angle α in the Fig.3.9) with respect to the workpiece frame, such that the directions of the forces $[F'_{x,\phi_i}, F'_{y,\phi_i}, F'_{z,\phi_i}]$ in the tool reference frame no longer coincide with the workpiece reference frame.

From the Fig.3.9 it can be also noticed that tilting of the tool influences the angle γ, which is the angle between the axis z in the workpiece reference frame and helix angle β of the cutting edge. Thus, when the tilting occurs, the value of the angle γ is decreased, and one of the total force components, the vertical force F_{z,ϕ_i}, is minimized. As result, since this third component does not contribute to the total cutting force, the cutting operation appears similar to the two-dimensional case with only two acting forces F_{x,ϕ_i} and F_{y,ϕ_i}.

The tangential F'_{t,ϕ_i}, radial F'_{r,ϕ_i}, and axial F'_{a,ϕ_i} forces act on the engaged n-th cutting edge at each instantaneous tool angular position ϕ_i. If no tool tilting occurs, the tangential and radial cutting forces lie on the workpiece plane xy, which is perpendicular to the tool z' axis. Instead, in case of the tool tilting, as shown in the Fig.3.10(a) and Fig.3.10(b), the tool axis z' is no longer perpendicular to the xy plane of the workpiece reference frame, and the forces $[F'_{t,\phi_i}, F'_{r,\phi_i}, F'_{a,\phi_i}]$ do not coincide with the workpiece coordinate system.

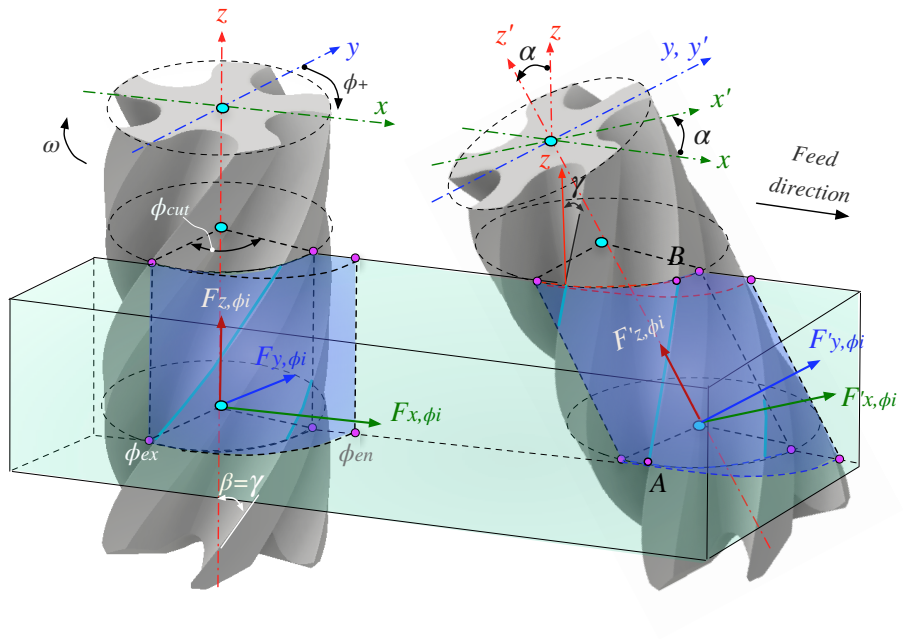

Figure 3.9: Schematic representation of the cutting forces acting along the workpiece and tool reference frame axes: ϕ - tool angular position; ω - tool rotation direction; ϕ_{en} - edge enter angle; ϕ_{ex} - edge exit angle; γ - angle between the axis z in the workpiece frame and edge; β - helix angle; α - tilting angle; $[F_{x,\phi_i}, F_{y,\phi_i}, F_{z,\phi_i}]$ and $[F'_{x,\phi_i}, F'_{y,\phi_i}, F'_{z,\phi_i}]$ are cutting forces that act in the workpiece and tool reference frames respectively

The tangential F'_{t,ϕ_i}, radial F'_{r,ϕ_i}, and axial F'_{a,ϕ_i} forces can be expressed as a function of such time-varying engagement parameters as instantaneous uncut chip area and instantaneous edge axial engagement length [9]. The following formula can be used:

$$\begin{bmatrix} F'_{r,\phi_i} \\ F'_{t,\phi_i} \\ F'_{a,\phi_i} \end{bmatrix} = a_{p,\phi_i}\overline{h}_{chip,\phi_i}K'_c + a_{p,\phi_i}K'_e$$

$$= a_{p,\phi_i}\overline{h}_{chip,\phi_i}\begin{bmatrix} K'_{rc} \\ K'_{tc} \\ K'_{ac} \end{bmatrix} + a_{p,\phi_i}\begin{bmatrix} K'_{re} \\ K'_{te} \\ K'_{ae} \end{bmatrix}, \tag{3.48}$$

where $a_{p,\phi_i}\overline{h}_{chip,\phi_i}$ is a term that represents the instantaneous undeformed chip

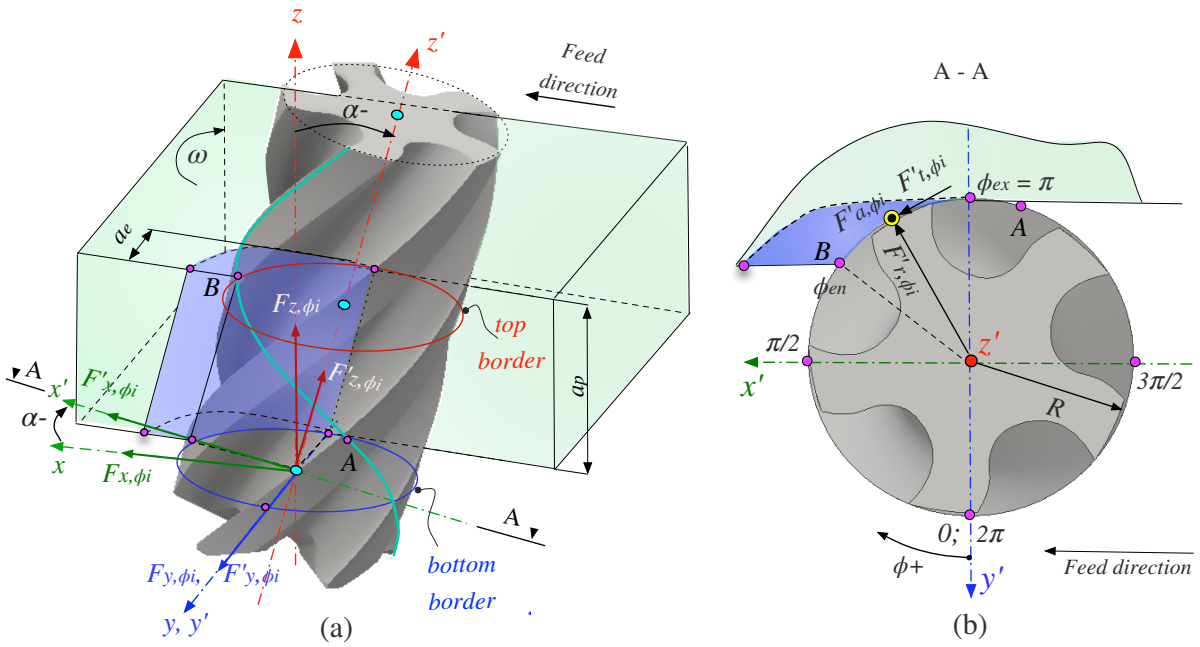

Figure 3.10: Schematic representation of the cutting forces acting on the n-th edge: (a) ω - tool rotation direction; ϕ_{en} - edge enter angle; ϕ_{ex} - edge exit angle; ϕ_i - instantaneous tool angular position; α - tilting angle; a_e - cutting width; a_p - cutting depth; (b) ϕ - tool angular position; $[F_{x,\phi_i}, F_{y,\phi_i}, F_{z,\phi_i}]$ and $[F'_{x,\phi_i}, F'_{y,\phi_i}, F'_{z,\phi_i}]$ are cutting forces that act in the workpiece and tool reference frames respectively; $[F'_{t,\phi_i}, F'_{r,\phi_i}, F'_{a,\phi_i}]$ - tangential, radial, and axial cutting forces respectively that act in the tool reference frame

area; K'_c is a vector that represents the tilted cutting forces coefficients $[K'_{rc}, K'_{tc}, K'_{ac}]$ contributed by the shearing action in the radial, tangential, and axial directions respectively; K'_e is a vector that represents the tilted cutting edge constants $[K'_{re}, K'_{te}, K'_{ae}]$.

The cutting forces coefficients can be evaluated mechanistically from milling tests or from the data obtained with FEM simulations. Both procedures will be discussed in one of the following sections of this chapter.

Once the instantaneous cutting forces in the tool reference frame $[F'_{r,\phi_i}, F'_{t,\phi_i}, F'_{a,\phi_i}]$ are computed, it is possible to find the instantaneous forces $[F_{x,\phi_i}, F_{y,\phi_i}, F_{z,\phi_i}]$ acting in the workpiece reference frame. In order to do that, the equilibrium diagram, i.e. the rotation matrix M'_z along z' axis (Fig.3.10(a) and Fig.3.10(b)), is used to calculate the axial forces

$[F'_{x,\phi_i}, F'_{y,\phi_i}, F'_{z,\phi_i}]$ acting in the tilted tool reference frame (x', y', z'). When these forces are computed, they are projected on the workpiece reference frame by applying the rotation matrix along the y axis, thus allowing to compute the cutting forces $[F_{x,\phi_i}, F_{y,\phi_i}, F_{z,\phi_i}]$. The resulting transformation matrix is:

$$V_{xyz,\phi_i} = M'_z(\phi) M_y(\alpha) V'_{rta,\phi_i} \tag{3.49}$$

$$\begin{bmatrix} F_{x,\phi_i} \\ F_{y,\phi_i} \\ F_{z,\phi_i} \end{bmatrix} = \begin{bmatrix} -\sin(-\phi) & -\cos(-\phi) & 0 \\ \cos(-\phi) & -\sin(-\phi) & 0 \\ 0 & 0 & 1 \end{bmatrix} \begin{bmatrix} \sin(\alpha) & 0 & -\cos(\alpha) \\ 0 & 1 & 0 \\ \cos(\alpha) & 0 & \sin(\alpha) \end{bmatrix} \begin{bmatrix} F'_{a,\phi_i} \\ F'_{t,\phi_i} \\ F'_{r,\phi_i} \end{bmatrix}$$

$$= \begin{bmatrix} \sin(\phi)\ \sin(\alpha)\ F'_{a,\phi_i} - \cos(\phi)\ F'_{t,\phi_i} - \sin(\phi)\ \cos(\alpha)\ F'_{r,\phi_i} \\ \cos(\phi)\ \sin(\alpha)\ F'_{a,\phi_i} + \sin(\phi)\ F'_{t,\phi_i} - \cos(\phi)\ \cos(\alpha)\ F'_{r,\phi_i} \\ \cos(\alpha)\ F'_{a,\phi_i} - \sin(\alpha)\ F'_{r,\phi_i} \end{bmatrix} \tag{3.50}$$

where $M_y(\alpha)$ and $M'_z(\phi)$ are the rotation matrices along y and z' axes in the workpiece and tool reference frames respectively; V_{xyz,ϕ_i} is a vector that represents the forces $[F_{x,\phi_i}, F_{y,\phi_i}, F_{z,\phi_i}]$ acting in the workpiece reference frame; V'_{rta,ϕ_i} is a vector that represents the forces $[F'_{r,\phi_i}, F'_{t,\phi_i}, F'_{a,\phi_i}]$ acting in the tool reference frame. The matrices $M_y(\alpha)$ and $M_z(\phi)'$ are selected with respect to the procedure described in [44] by taking into account the differences in the directions of the rotation ϕ and tilting α angles used in the present work and in the system proposed by another authors.

As mentioned previously, the chip load, and consequently the cutting forces $[F_{x,\phi_i}, F_{y,\phi_i}, F_{z,\phi_i}]$ are produced only when the cutting edge is acting in the engagement zone $[\phi_{en}..(\phi_{ex} + \phi_{tr})]$. When the single cutting edge is outside of this zone, the cutting forces are equal to zero:

$$[F_{x,\phi_i}, F_{y,\phi_i}, F_{z,\phi_i}] > 0 \quad \text{if} \quad \phi_i \in [\phi_{en}..(\phi_{ex} + \phi_{tr})] \tag{3.51}$$

The total number of the cutting edges simultaneously engaged into the workpiece can be identified by following the procedure discussed in one of the previous sections. If there is more than one cutting edge engaged into the workpiece, the contribution of each edge to the total tangential, radial, and axial forces, and consequently to the total $F_{x,\phi_i}^{TOT}, F_{y,\phi_i}^{TOT}, F_{z,\phi_i}^{TOT}$ forces must be taken into consideration when performing the milling process simulation. As highlighted previously, each n-th cutting edge of the tool is distant from its two neighboring edges $(n-1)$ and $(n+1)$ by the amount of the pitch angles $\psi(n-1)$ and $\psi(n+1)$, which can be equal to each other (constant tooth pitch angle) or can have different values (variable tooth pitch angle). If the tool is characterized by the variable pitch angle values, each cutting edge will enter and exit from the engagement zone at different angular positions. Due to this, the value of the instantaneous uncut chip thickness removed by each of the engaged edges will be different. The total cutting forces can be calculated by using the following equation:

$$\begin{aligned} F_{x,\phi_i}^{TOT} &= \sum_{1}^{N} F_{x,\phi_i}(n) \\ F_{y,\phi_i}^{TOT} &= \sum_{1}^{N} F_{y,\phi_i}(n) \\ F_{z,\phi_i}^{TOT} &= \sum_{1}^{N} F_{z,\phi_i}(n), \end{aligned} \tag{3.52}$$

where $F_{x,\phi_i}(n)$, $F_{y,\phi_i}(n)$ and $F_{z,\phi_i}(n)$ are the cutting forces contributed by a single engaged cutting edge; N is the total number of the engaged edges; F_{x,ϕ_i}^{TOT}, F_{y,ϕ_i}^{TOT} and F_{z,ϕ_i}^{TOT} are the total cutting forces contributed by all engaged edges.

3.5 CUTTING FORCE COEFFICIENTS

Cutting coefficients are empirical values, and they can be determined experimentally or theoretically. The experimental identification of these values can be done by means of cutting tests, and the theoretical identification, instead, can be done by using cutting forces data from FEM simulations. Both procedures must include the execution or

simulation of milling operations performed with different feed per tooth values (or feed values in case of the turning process), and constant values of the axial and radial depths of cut.

In case the cutting forces coefficients have to be used to simulate cutting forces of the tilted milling operation, the most convenient approach according to the author's opinion is to identify these coefficients for the non-tilted process, and then to correct them by applying the rotation matrix around the y axis (if the tool tilting is done with respect to the xy plane in the workpiece reference frame).

3.5.1 Identification of Cutting Constants for Two-dimensional Systems

The cutting force coefficients can be identified by using the cutting forces data obtained from different 2D FEM simulations or from orthogonal cutting tests that represent two-dimensional systems. According to the procedures presented in [9], [51] and [6], the cutting force coefficients can be expressed as the coefficients of the linear equations that relate the average forces to the feed per tooth or feed values used to obtain the cutting data, such that:

$$\overline{F}_x = K_{tc}\ a_p\ f_z + K_{te}\ a_p \tag{3.53}$$

$$\overline{F}_y = K_{rc}\ a_p\ f_z + K_{re}\ a_p, \tag{3.54}$$

where K_{tc} and K_{rc} are the cutting coefficients contributed by the shearing action, $[N/mm^2]$; K_{te} and K_{re} are the cutting edge coefficients, $[N/mm]$; a_p is the axial depth of cut value, $[mm]$; f_z is the feed per tooth value, $[mm/tooth]$; $\overline{F}_x$ and $\overline{F}_y$, $[N]$ are the average tangential and feed cutting forces respectively estimated by the linear regression of 2D FEM or measured cutting forces data.

It is clear to see that since the orthogonal cutting tests or 2D FEM provide the information about only two cutting forces acting on the xy plane, the identified four cutting force coefficients can be used only for the simulation of the F_x and F_y forces arising during the milling processes.

3.5.2 Identification of Cutting Constants for Three-dimensional Systems

In case of the three-dimensional cutting force system, 3D FEM modeling or experimental cutting forces data can be used to identify all six cutting force coefficients, and consequently all three cutting forces F_x, F_y and F_z can be predicted in order to study the system behaviour. The work [30] contains very detailed explanation of the procedure for the cutting force coefficients identification for the full-immersion milling operations, where the enter ϕ_{en} and exit ϕ_{ex} angles are equal *zero* and π respectively. Since the process studied in this work is characterized by the partial tool/workpiece engagement, which is different from the case discussed in [30], a procedure suitable for the cutting forces coefficients identification for this particular operation will be discussed below.

According to the approach presented in [9], by equating the average cutting forces $\overline{F}_x$, $\overline{F}_y$ and $\overline{F}_z$ (obtained experimentally or by modeling in 3D FEM) to the analytically derived average forces, it is possible to identify cutting force coefficients. The average cutting forces have to be integrated along the whole cutting edge/workpiece engagement period $[\phi_{en}..(\phi_{ex}+\phi_{tr})]$ such as:

$$\begin{aligned}\overline{F}_x =&\Big\{P\Big[K_{tc}\cos(2\phi) - K_{rc}[2\phi - \sin(2\phi)]\Big] \\ &- G\Big[K_{te}\sin(\phi) - K_{re}\cos(\phi)\Big]\Big\}_{\phi_{en}}^{(\phi_{ex}+\phi_{tr})}\end{aligned} \tag{3.55}$$

$$\begin{aligned}\overline{F}_y =&\Big\{P\Big[K_{tc}[2\phi - \sin(2\phi)] + K_{rc}\cos(2\phi)\Big] \\ &- G\Big[K_{te}\cos(\phi) + K_{re}\sin(\phi)\Big]\Big\}_{\phi_{en}}^{(\phi_{ex}+\phi_{tr})}\end{aligned} \tag{3.56}$$

$$\overline{F}_z =\Big\{G\Big[- K_{ac}f_z\cos(\phi) + K_{ae}\,\phi\Big]\Big\}_{\phi_{en}}^{(\phi_{ex}+\phi_{tr})} \tag{3.57}$$

$$P = \frac{a_p f_z n}{8\pi} \tag{3.58}$$

$$G = \frac{a_p n}{2\pi} \tag{3.59}$$

where a_p - axial depth of cut; f_z - feed per tooth; n - number of the tool edges.

1. By expressing the average forces by the linear functions of the feed per tooth value and offset contributed by the edge forces, the following equations are obtained:

$$\overline{F}_x = \overline{F}_{xc} f_z + \overline{F}_{xe} \tag{3.60}$$

$$\overline{F}_y = \overline{F}_{yc} f_z + \overline{F}_{ye} \tag{3.61}$$

$$\overline{F}_z = \overline{F}_{zc} f_z + \overline{F}_{ze} \tag{3.62}$$

Thus, the expressions describing the average cutting forces can be rewritten as:

$$\begin{aligned} \overline{F}_{xc} f_z + \overline{F}_{xe} = & \Big\{ P\Big[K_{tc}\cos(2\phi) - K_{rc}(2\phi - \sin(2\phi))\Big] \\ & - G\Big[K_{te}\sin(\phi) - K_{re}\cos(\phi)\Big] \Big\}_{\phi_{en}}^{(\phi_{ex}+\phi_{tr})} \end{aligned} \tag{3.63}$$

$$\begin{aligned} \overline{F}_{yc} f_z + \overline{F}_{ye} = & \Big\{ P\Big[K_{tc}(2\phi - \sin(2\phi)) + K_{rc}\cos(2\phi)\Big] \\ & - G\Big[K_{te}\cos(\phi) + K_{re}\sin(\phi)\Big] \Big\}_{\phi_{en}}^{(\phi_{ex}+\phi_{tr})} \end{aligned} \tag{3.64}$$

$$\overline{F}_{zc} f_z + \overline{F}_{ze} = \Big\{ G\Big[- K_{ac} f_z \cos(\phi) + K_{ae}\,\phi\Big] \Big\}_{\phi_{en}}^{(\phi_{ex}+\phi_{tr})} \tag{3.65}$$

By integrating the equations Eq.3.63, Eq.3.64 and Eq.3.65 presented above, and evaluating the results at the points ϕ_{en} and ϕ_{ex}, it is possible to express the equations for the cutting force coefficients evaluation.

2. The average values of the shearing forces $\overline{F}_{xc}$, $\overline{F}_{yc}$ and $\overline{F}_{zc}$ acting in tangential, radial and axial direction respectively can be calculated as:

2.1. The average shearing force $\overline{F}_{xc}$ acting in tangential direction:

$$\begin{aligned} \overline{F}_{xc} f_z = & P\Big[K_{tc}\cos(2\phi_{ex}) - K_{rc}[2\phi_{ex} - \sin(2\phi_{ex})] \\ & - K_{tc}\cos(2\phi_{en}) + K_{rc}[2\phi_{en} - \sin(2\phi_{en})]\Big] \\ = & P\Big[\cos(2\phi_{ex}) - \cos(2\phi_{en})\Big] K_{tc} \\ & - P\Big[2\phi_{ex} - \sin(2\phi_{ex}) - 2\phi_{en} + \sin(2\phi_{en})\Big] K_{rc} \end{aligned} \tag{3.66}$$

From the Eq.3.66 the force $\overline{F}_{xc}$ can be expressed as:

$$\overline{F}_{xc} f_z = TK_{tc} - EK_{rc}, \tag{3.67}$$

where terms T and E are:

$$T = P\Big[\cos(2\phi_{ex}) - \cos(2\phi_{en})\Big] \tag{3.68}$$

$$E = P\Big[2\phi_{ex} - \sin(2\phi_{ex}) - 2\phi_{en} + \sin(2\phi_{en})\Big] \tag{3.69}$$

2.2. The average shearing force $\overline{F}_{yc}$ acting in radial direction:

$$\begin{aligned}\overline{F}_{yc} f_z &= P\Big[K_{tc}[2\phi_{ex} - \sin(2\phi_{ex})] + K_{rc}\cos(2\phi_{ex}) \\ &\quad - K_{tc}[2\phi_{en} - \sin(2\phi_{en})] - K_{rc}\cos(2\phi_{en})\Big] \\ &= P\Big[2\phi_{ex} - \sin(2\phi_{ex}) - 2\phi_{en} + \sin(2\phi_{en})\Big]K_{tc} \\ &\quad + P\Big[\cos(2\phi_{ex}) - \cos(2\phi_{en})\Big]K_{rc}\end{aligned} \tag{3.70}$$

From the Eq.3.70 the force $\overline{F}_{yc}$ can be expressed as:

$$\overline{F}_{yc} f_z = EK_{tc} + TK_{rc} \tag{3.71}$$

2.3. The average value of the shearing force $\overline{F}_{zc}$ acting in axial direction:

$$\begin{aligned}\overline{F}_{zc} f_z &= G\Big[-K_{ac}\, f_z\, \cos(\phi_{ex}) + K_{ac}\, f_z\, \cos(\phi_{en})\Big] \\ &= G\Big[-\cos(\phi_{ex}) + \cos(\phi_{en})\Big]K_{ac} f_z\end{aligned} \tag{3.72}$$

From the Eq.3.72 the force $\overline{F}_{zc}$ can be expressed as:

$$\overline{F}_{zc} f_z = SK_{ac} f_z, \tag{3.73}$$

where

$$S = G\Big[-\cos(\phi_{ex}) + \cos(\phi_{en})\Big] \tag{3.74}$$

3. The cutting force coefficients K_{tc}, K_{rc} and K_{ac} contributed by the shearing action can be found from the Eq.3.67, Eq.3.71 and Eq.3.73 such as:

   3.1. The coefficient K_{rc} can be expressed from the Eq.3.67 as:

$$\overline{F}_{xc} f_z = T K_{tc} - E K_{rc} \quad \Rightarrow \quad K_{rc} = \frac{-\overline{F}_{xc} f_z + T K_{tc}}{E} \tag{3.75}$$

   3.2. By substituting the expression of the term K_{rc} into the Eq.3.71, it is possible to find the equation for the coefficient K_{tc} evaluation:

$$\begin{aligned} \overline{F}_{yc} f_z &= E K_{tc} + T\Big[\frac{-\overline{F}_{xc} f_z + T K_{tc}}{E}\Big] \\ &= \frac{K_{tc}}{E}\left(E^2 + T^2\right) - \frac{T}{E}\left(\overline{F}_{xc} f_z\right) \end{aligned} \tag{3.76}$$

   The coefficient $K_{tc}, [N/mm^2]$ can be expressed as:

$$\frac{K_{tc}\left(E^2 + T^2\right)}{E} = \frac{\overline{F}_{yc} f_z E}{E} + \frac{T\overline{F}_{xc} f_z}{E} \quad \Rightarrow \quad K_{tc} = \frac{f_z\left(\overline{F}_{yc} E + T\overline{F}_{xc}\right)}{\left(E^2 + T^2\right)} \tag{3.77}$$

   3.3. The expression for the coefficient $K_{rc}, [N/mm^2]$ can be found by replacing the Eq.3.77 into the Eq.3.75:

$$\begin{aligned} K_{rc} &= \frac{1}{E}\left[-\overline{F}_{xc} f_z + T\Big(\frac{f_z\left(\overline{F}_{yc} E + T\overline{F}_{xc}\right)}{E^2 + T^2}\Big)\right] \\ &= -\frac{\overline{F}_{xc} f_z}{E} + \frac{T f_z}{E\left(E^2 + T^2\right)}\left[E\overline{F}_{yc} + T\overline{F}_{xc}\right] \end{aligned} \tag{3.78}$$

   3.4. The coefficient $K_{ac}, [N/mm^2]$ can be expressed from the Eq.3.73 as:

$$\overline{F}_{zc} f_z = S K_{ac} f_z \qquad \Rightarrow \qquad K_{ac} = \frac{\overline{F}_{zc}}{S} \tag{3.79}$$

4. The average edge forces $\overline{F}_{xe}$, $\overline{F}_{ye}$ and $\overline{F}_{ze}$ acting in tangential, radial and axial direction respectively, can be found from the Eq.3.63, Eq.3.64 and Eq.3.65 such as:

   4.1. The edge force $\overline{F}_{xe}$ acting in tangential direction:

$$\begin{aligned}\overline{F}_{xe} &= -G\Big[K_{te}\sin(\phi_{ex}) - K_{re}\cos(\phi_{ex}) - K_{te}\sin(\phi_{en}) + K_{re}\cos(\phi_{en})\Big] \\ &= \quad G\Big[-\sin(\phi_{ex}) + \sin(\phi_{en})\Big]K_{te} + G\Big[\cos(\phi_{ex}) - \cos(\phi_{en})\Big]K_{re} \end{aligned} \tag{3.80}$$

   From the Eq.3.80 the edge force $\overline{F}_{xe}$ can be expressed as:

$$\overline{F}_{xe} = AK_{te} + BK_{re}, \tag{3.81}$$

   where

$$A = G\Big[-\sin(\phi_{ex}) + \sin(\phi_{en})\Big] \tag{3.82}$$

$$B = G\Big[\cos(\phi_{ex}) - \cos(\phi_{en})\Big] \tag{3.83}$$

   4.2. The average value of the edge force $\overline{F}_{ye}$ acting in radial direction:

$$\begin{aligned}\overline{F}_{ye} &= -G\Big[K_{te}\cos(\phi_{ex}) + K_{re}\sin(\phi_{ex}) - K_{te}\cos(\phi_{en}) - K_{re}\sin(\phi_{en})\Big] \\ &= -G\Big[\cos(\phi_{ex}) - \cos(\phi_{en})\Big]K_{te} + G\Big[-\sin(\phi_{ex}) + \sin(\phi_{en})\Big]K_{re} \end{aligned} \tag{3.84}$$

   From the Eq.3.84 the edge force $\overline{F}_{ye}$ can be expressed as:

$$\overline{F}_{ye} = -BK_{te} + AK_{re}, \tag{3.85}$$

   4.3. The edge force $\overline{F}_{ze}$ acting in axial direction can be found as:

$$\overline{F}_{ze} = G\Big[K_{ae}\,\phi_{ex} - K_{ae}\,\phi_{en}\Big] = G\Big[\phi_{ex} - \phi_{en}\Big]K_{ae} \tag{3.86}$$

   From the Eq.3.86 the edge force $\overline{F}_{ze}$ can be expressed as:

$$\overline{F}_{ze} = QK_{ae}, \tag{3.87}$$

   where

$$Q = G\Big[\phi_{ex} - \phi_{en}\Big] \tag{3.88}$$

5. The cutting force coefficients K_{te}, K_{re} and K_{ae} contributed by the edge forces can be found from the Eq.3.81, Eq.3.85 and Eq.3.87 such as:

   5.1. The coefficient K_{te} can be expressed from the Eq.3.81 as:

$$\overline{F}_{xe} = AK_{te} + BK_{re} \quad \Rightarrow \quad K_{te} = \frac{\overline{F}_{xe} - BK_{re}}{A} \tag{3.89}$$

   5.2. By substituting the expression of the coefficient K_{te} into the Eq. 3.85, it is possible to find the equation for the coefficient K_{re} evaluation:

$$\begin{aligned} \overline{F}_{ye} &= -B\left[\frac{\overline{F}_{xe} - B\,K_{re}}{A}\right] + AK_{re} \\ &= -\frac{B\overline{F}_{xe}}{A} + \frac{K_{re}}{A}\left(A^2 + B^2\right) \end{aligned} \tag{3.90}$$

   The coefficient $K_{re}, [N/mm]$ can be expressed as:

$$K_{re}\left(A^2 + B^2\right) = A\left[\frac{\overline{F}_{ye}\,A + \overline{F}_{xe}B}{A}\right] \quad \Rightarrow \quad K_{re} = \frac{\overline{F}_{ye}A + \overline{F}_{xe}B}{(A^2 + B^2)} \tag{3.91}$$

   5.3. The expression for the coefficient $K_{te}, [N/mm]$ can be found by replacing the Eq.3.91 into the Eq.3.89:

$$\begin{aligned} K_{te} &= \frac{1}{A}\left[\overline{F}_{xe} - B\Big(\frac{\overline{F}_{ye}A + \overline{F}_{xe}B}{(A^2 + B^2)}\Big)\right] \\ &= \frac{\overline{F}_{xe}}{A} - \frac{B}{A\,(A^2 + B^2)}\Big[\overline{F}_{ye}A + \overline{F}_{xe}B\Big] \end{aligned} \tag{3.92}$$

   5.4. The coefficient $K_{ae}, [N/mm]$ can be expressed from the Eq.3.87 as:

$$\overline{F}_{ze} = Q \cdot K_{ae} \qquad \Rightarrow \qquad K_{ae} = \frac{\overline{F}_{ze}}{Q} \tag{3.93}$$

3.5.3 Cutting Force Coefficients Transformation for Tilted Milling

The development of the procedure to identify cutting force coefficients $K_c = [K_{rc}, K_{tc}, K_{ac}]$ and $K_e = [K_{re}, K_{te}, K_{ae}]$ for two-dimensional and three-dimensional systems, which is described above, was done by following the approach presented in [9], where it is assumed that no tool tilting occurs, and that the tool z' axis is perpendicular to the feed rate and xy plane in the workpiece reference frame. Such assumption is not satisfied when the tool is tilted by the angle α against the feed direction since in this case the tool and workpiece reference frames do not coincide (Fig.3.10). Due to this, the identified milling coefficients (Eq.3.77, Eq.3.78, Eq.3.79, Eq.3.91, Eq.3.92 and Eq.3.93) correspond to the forces, the directions of which are not aligned with the axes of the tilted tool coordinate system, and the found values of these cutting constants have to be corrected. Since the coefficients K_{tc}, K_{rc}, K_{ac}, and K_{te}, K_{re}, K_{ae} are associated to the shearing action and to the edge constants respectively, they can be interpreted as forces (except for the constants). Therefore, for the studying system shown in the Fig.3.10 the cutting constants can be corrected by rotating them around the y axis such as:

$$M_y = \begin{bmatrix} \cos(\alpha) & 0 & \sin(\alpha) \\ 0 & 1 & 0 \\ -\sin(\alpha) & 0 & \cos(\alpha) \end{bmatrix} \tag{3.94}$$

$$K'_c = \begin{bmatrix} K'_{rc} \\ K'_{tc} \\ K'_{ac} \end{bmatrix} = M_y \begin{bmatrix} K_{rc} \\ K_{tc} \\ K_{ac} \end{bmatrix} = \begin{bmatrix} K_{rc}\cos(\alpha) + K_{ac}\sin(\alpha) \\ K_{tc} \\ -K_{rc}\sin(\alpha) + K_{ac}\cos(\alpha) \end{bmatrix} \tag{3.95}$$

$$K'_e = \begin{bmatrix} K'_{re} \\ K'_{te} \\ K'_{ae} \end{bmatrix} = M_y \begin{bmatrix} K_{re} \\ K_{te} \\ K_{ae} \end{bmatrix} = \begin{bmatrix} K_{re}\cos(\alpha) + K_{ae}\sin(\alpha) \\ K_{te} \\ -K_{re}\sin(\alpha) + K_{ae}\cos(\alpha) \end{bmatrix}, \tag{3.96}$$

where K_{tc}, K_{rc}, K_{ac}, K_{te}, K_{re}, K_{ae} are the cutting forces coefficients identified by using the approach described in the previous section; K'_{tc}, K'_{rc}, K'_{ac}, K'_{te}, K'_{re}, K'_{ae} are the corrected coefficients; α is the tilting angle; M_y is the rotation matrix along y axis.

3.6 APPLICATION AND EXPERIMENTAL VALIDATION OF THE PROPOSED MODEL

In this section the approach aimed to overcome the problems that relate to the application of 2D FEM to predict cutting forces in three-dimensional cutting processes, that were discussed in Chapter 2, is presented.

The approach includes the following steps. At first, a few 2D FEM simulations are performed to simulate cutting forces, and the obtained data are used to identify the milling constants according to the procedure described above in this chapter. After that, the found values of the cutting force coefficients are applied in the proposed cutting forces model in order to perform several tilted and non-tilted milling process simulations. Finally, the predicted forces are compared to the cutting data obtained experimentally.

The main purpose of this section is to verify the suitability of the proposed cutting force model to predict cutting forces behaviour in side down-milling processes performed under different cutting conditions, and also to investigate the application of 2D FEM data for simulating cutting forces F_x and F_y that occur in three-dimensional systems.

3.6.1 2D FEM Setup, Results, and Identified Cutting Constants

In order to identify the cutting forces coefficients K_{tc}, K_{te}, K_{rc} and K_{rc}, three different simulations of the turning process were performed by using Third Wave AdvantEdge v7.0 (Fig.3.11).

The data of the tool geometry used to set up these simulations were: 10.5° longitudinal rake angle, 7.0° relief angle, cutting edge with 20.0 μm rounding. As the tool material was selected H10F carbide with 2.0 μm thickness of TiAlN coating. The tool meshing procedure in FEM was done under the following settings (Fig.3.12): maximum element size = 0.1 mm, minimum element size = 0.007 mm, mesh grading = 0.4, maximum number of nodes 100000. No coolant was used. The steel AISI 4140 was selected as the workpiece material.

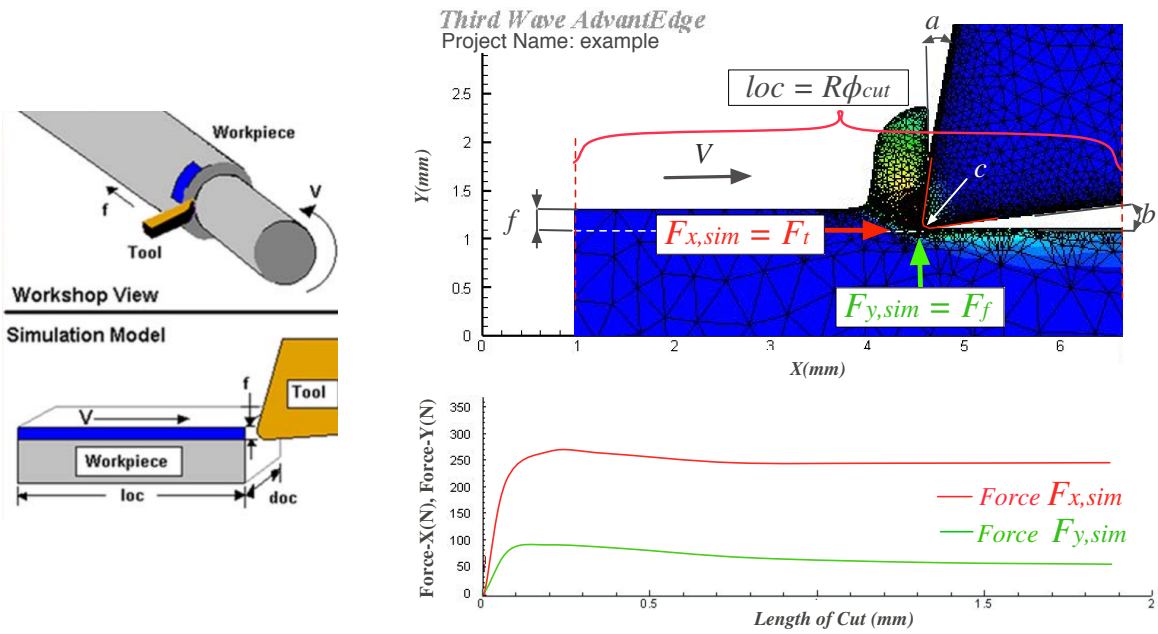

Figure 3.11: 2D FEM of turning in AdvantEdge v7.0 (note that in this figure it is illustrated an example of the performed 2D FEM modeling, and that the temperature map does not have to be taken into account): $F_{x,sim} = F_t$ and $F_{y,sim} = F_f$ are the simulated tangential and feed cutting forces respectively; *loc* - length of cut; *doc* - depth of cut, f - feed; V - cutting speed; a - longitudinal rake angle; b - relief angle; c - edge rounding

Table 3.1: 2D FEM simulations: set-up and results

	V_c, m/min	f, mm/rev	$doc = d$, mm	$loc = l$, mm	$\overline{F}_{x,sim}$, N	$\overline{F}_{y,sim}$, N
simul 1	80.0	0.05	1.0	2.0	137.6	64.6
simul 2	80.0	0.1	1.0	2.0	243.9	96.0
simul 3	80.0	0.15	1.0	2.0	347.0	128.0

The workpiece geometry, cutting parameters used to perform 2D FEM, and the average values of the simulated cutting forces $\overline{F}_{x,sim}$ and $\overline{F}_{y,sim}$ are reported in the Table 3.1. All numerical simulations were performed on the personal computer with the characteristics already reported in Chapter 2 (Table 2.2).

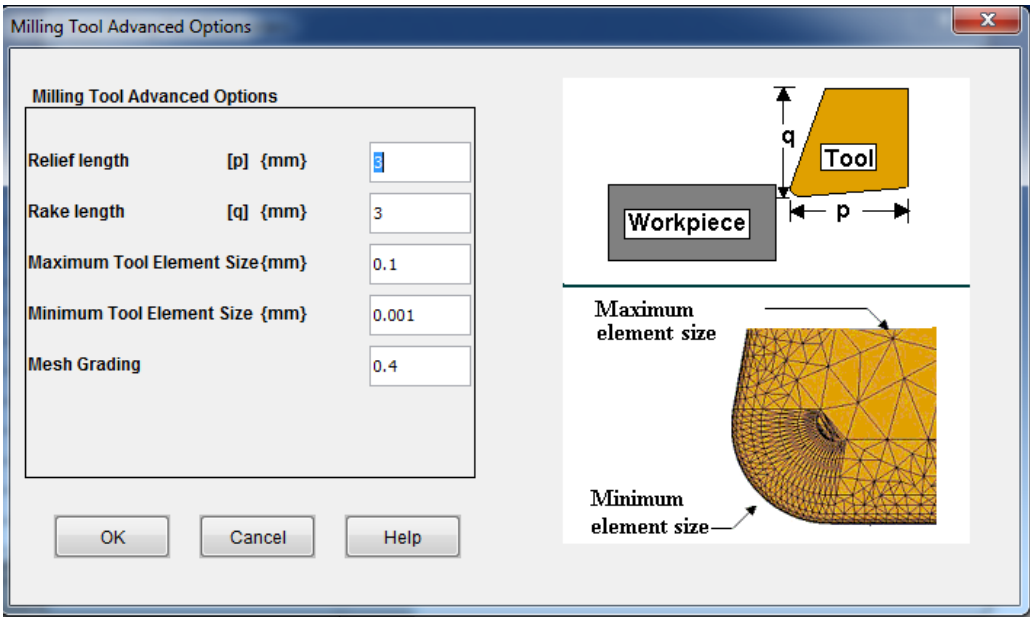

Figure 3.12: Meshing set-up in 2D FEM of turning in AdvantEdge v7.0

By using the exported results of the performed 2D FEM simulations, the average values of the tangential $\overline{F}_{x,sim}$ and feed $\overline{F}_{y,sim}$ forces were identified by applying an algorithm written in RUBY language. Based on the obtained cutting forces values, the cutting forces coefficients were identified by applying the linear regression analysis technique according to the approach explained previously in this chapter. The algorithm for these calculations was implemented in Maple 18. The obtained linear models and identified cutting constants are:

$$\overline{F}_{x,sim} = K_{tc}\, d\, f + K_{te}\, d \quad = \quad 2093.8 f + 33.5 \tag{3.97}$$

$$\overline{F}_{y,sim} = K_{rc}\, d\, f + K_{re}\, d \quad = \quad 634.0 f + 32.8 \tag{3.98}$$

As mentioned previously, if the simulations of tilted milling process have to be performed, the identified cutting constants must corrected by using the Eq.3.95 and Eq.3.96. The results of this transformation for each tilted process simulation will be reported in one of the following sections that reports the comparison of the predicted and measured cutting forces.

Table 3.2: Experimental conditions

	V_c, m/min	f_z, mm/tooth	a_p, mm	a_e, mm	α,°
test 1	80.0	0.1	5.0	2.0	0.0°
test 2	80.0	0.1	5.0	2.0	19.0°
test 3	80.0	0.1	5.0	2.0	22.0°
test 4	80.0	0.1	5.0	2.0	27.8°
test 5	80.0	0.1	10.0	1.0	21.4°
test 6	80.0	0.1	10.0	2.0	0.0°
test 7	80.0	0.1	10.0	2.0	19.0°
test 8	80.0	0.1	12.0	2.0	21.0°
test 9	80.0	0.1	12.0	2.0	27.8°

3.6.2 Experimental Setup

The information about the experimental campaign performed to obtain real cutting forces data is described below. All cutting tests were carried out on the four-axes DMU-60T machining center (Fig.3.13). The cutting conditions, such as cutting speed V_c, feed per tooth f_z, tilting angle α, axial a_p and radial a_e depths of cut are listed in the Table 3.2. No coolant was used during the tests. A tungsten-carbide (10% Cobalt content) five-teeth solid end mill with 2.0 μm of TiAlN coating provided by Sandvik Coromant was used as the cutting tool. The cutter geometry is characterized by the following parameters: variable tooth pitch angle, 10.0 mm diameter, 38.0° helix angle, 10.5° longitudinal rake angle, 7.0° relief angle, and cutting edge with 20.0 μm rounding. In the performed tests, three AISI 4140 steel blocks with different thickness values of 5.0 mm, 10.0 mm and 12.0 mm were used as the workpieces.

A Kistler 9129AA force dynamometer, mounted between the workpiece and machining table, was used to measure the instantaneous F_x, F_y, and F_z cutting forces in the workpiece reference frame (x, y, z). The data acquisition system DynoWare Type 5697 was set to capture and store the cutting force data at a sampling rate of 3000.0 Hz. The multichannel charge amplifier Kistler Type 5070 was used to convert the charge measured by the force dynamometer into a voltage signal.

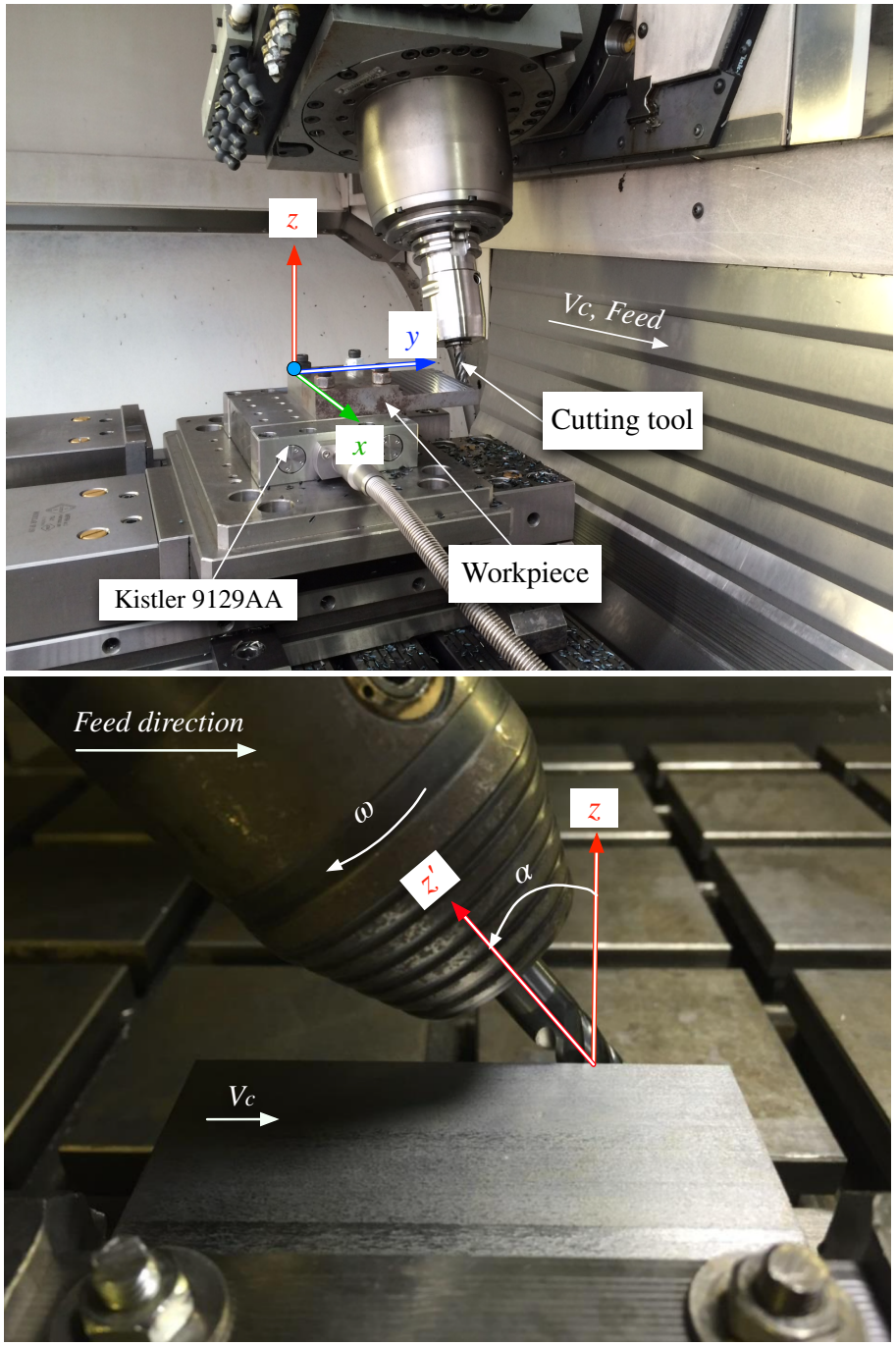

Figure 3.13: Side down-milling performed with tool tilting by the angle α against the feed direction: ω - tool rotation direction; V_c - cutting speed; (x, y, z) - workpiece reference frame

Table 3.3: Conditions used to perform milling process simulations and milling tests: f_z = 0.1 mm/tooth; [K'_{tc}, K'_{rc}, K'_{ac}] =N/mm^2 and [K'_{te}, K'_{re}, K'_{ae}] =N/mm are the corrected cutting forces coefficients that were used to perform milling process simulations

	α, $^\circ$	a_p, mm	a_e, mm	K'_{tc}	K'_{te}	K'_{rc}	K'_{re}	K'_{ac}	K'_{ae}
test 1 model 1	0.0	5.0	2.0	2093.8	33.5	634.0	32.8	0.0	0.0
test 2 model 2	19.0	5.0	2.0	2093.8	33.5	599.5	31.0	-206.4	-10.7
test 3 model 3	22.0	5.0	2.0	2093.8	33.5	587.8	30.4	-237.5	-12.3
test 4 model 4	27.8	5.0	2.0	2093.8	33.5	560.8	29.0	-295.7	-15.3
test 5 model 5	21.4	10.0	1.0	2093.8	33.5	590.3	30.5	-231.3	-11.9
test 6 model 6	0.0	10.0	2.0	2093.8	33.5	634.0	32.8	0.0	0.0
test 7 model 7	19.0	10.0	2.0	2093.8	33.5	599.5	31.0	-206.4	-10.7
test 8 model 8	21.0	12.0	2.0	2093.8	33.5	591.9	30.6	-227.2	-11.8
test 9 model 9	27.8	12.0	2.0	2093.8	33.5	560.8	29.0	-295.7	-15.3

3.6.3 Predicted and Measured Cutting Forces

The proposed model for the cutting forces simulation was implemented as a numerical algorithm written in RUBY. Several non-tilted and tilted milling process simulations were performed by using the identified cutting force coefficients (Eq.3.97 and Eq.3.98). The cutting conditions used to perform these simulations correspond to the experimental tests, and are listed in the Table 3.3. The results of the performed milling process simulations and experimental data - the average, minimum and maximum values of the forces F_x, F_y and F_z observed for one cutting tool rotation, and percentage error values are reported below in the Table 3.4 - Table 3.12, and in the Fig.3.14 - Fig.3.22.

It has to be noted that since the cutting force coefficients used to simulate the milling processes listed in the Table 3.3 were identified by using 2D FEM data, which provides the information about only two cutting forces acting on the xy plane, the coefficients K_{ac} and K_{ae}, and consequently the predicted force F_z will be always equal to $zero$, and the percentage error for this parameter will be always equal to 100.0%. Despite the fact that the measured values of all three cutting forces are reported in this chapter, the comparison between the simulated and measured forces F_z was not performed in this work. The measured data of the cutting force F_z was reported in order to demonstrate the influence of the tool tilting on this parameter.

Table 3.4: Predicted and experimental values of the cutting forces F_x, F_y and F_z corresponding to the test 1 conditions (Fig.3.14): $a_p = 5.0$ mm; $a_e = 2.0$ mm; $f_z = 0.1$ mm/tooth; $\alpha = 0.0°$

	test 1	model 1	% error
$\overline{F}_x$, N	234.1	279.1	19.2
$F_{x,max}$, N	364.3	442.9	21.6
$F_{x,min}$, N	115.0	146.3	27.2
$\overline{F}_y$, N	365.9	412.3	12.7
$F_{y,max}$, N	583.3	645.6	10.7
$F_{y,min}$, N	150.0	148.7	-0.9
$\overline{F}_z$, N	127.0	0.0	100.0
$F_{z,max}$, N	218.1	0.0	100.0
$F_{z,min}$, N	43.3	0.0	100.0

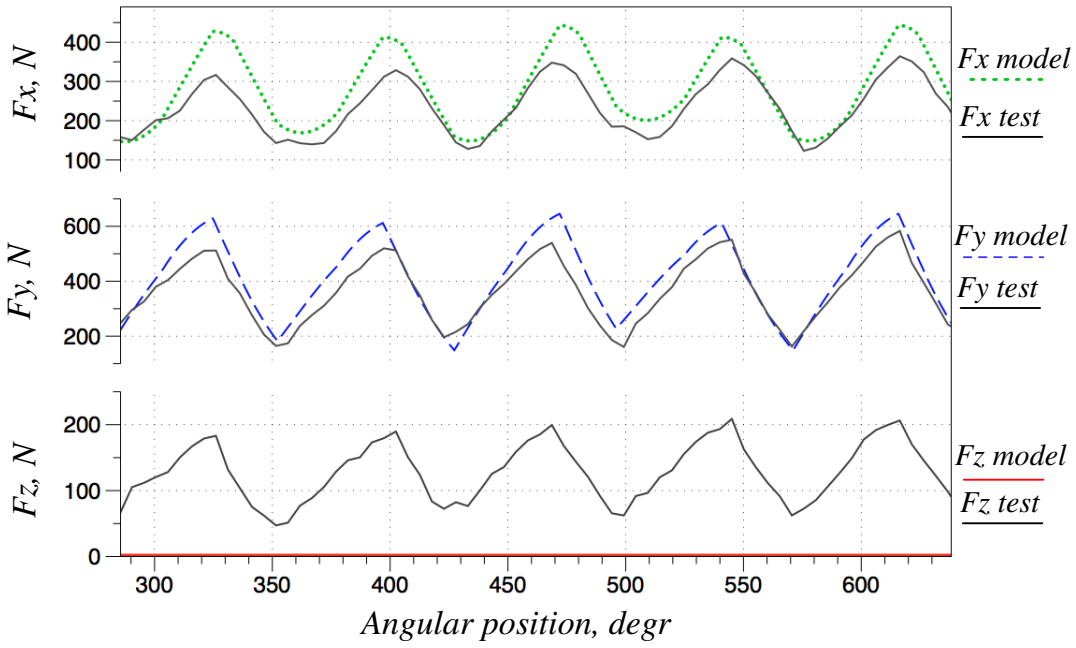

Figure 3.14: Predicted vs. experimental forces: test 1 / model 1

Table 3.5: Predicted and experimental values of the cutting forces F_x, F_y and F_z corresponding to the test 2 conditions (Fig.3.15): $a_p = 5.0$ mm; $a_e = 2.0$ mm; $f_z = 0.1$ mm/tooth; $\alpha = 19.0°$

	test 2	model 2	% error
$\overline{F}_x$, N	270.0	276.8	2.52
$F_{x,max}$, N	360.9	366.2	1.47
$F_{x,min}$, N	184.02	204.4	11.1
$\overline{F}_y$, N	380.7	421.5	10.7
$F_{y,max}$, N	542.1	591.9	9.2
$F_{y,min}$, N	235.9	228.5	-3.14
$\overline{F}_z$, N	49.4	0.0	100.0
$F_{z,max}$, N	82.2	0.0	100.0
$F_{z,min}$, N	12.0	0.0	100.0

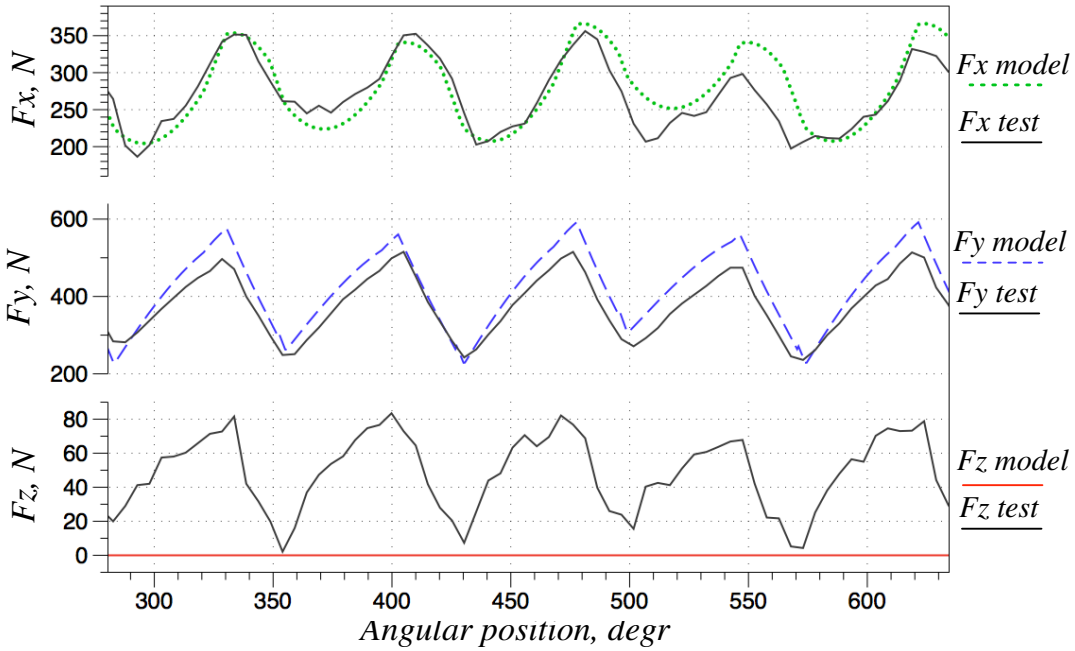

Figure 3.15: Predicted vs. experimental forces: test 2 / model 2

Table 3.6: Predicted and experimental values of the cutting forces F_x, F_y and F_z corresponding to the test 3 conditions (Fig.3.16): $a_p = 5.0$ mm; $a_e = 2.0$ mm; $f_z = 0.1$ mm/tooth; $\alpha = 22.0°$

	test 3	model 3	% error
$\overline{F}_x$, N	259.0	277.4	7.10
$F_{x,max}$, N	332.6	355.9	7.01
$F_{x,min}$, N	184.7	213.8	15.8
$\overline{F}_y$, N	381.5	424.7	11.32
$F_{y,max}$, N	516.5	579.9	12.3
$F_{y,min}$, N	235.7	243.1	3.14
$\overline{F}_z$, N	24.9	0.0	100.0
$F_{z,max}$, N	51.2	0.0	100.0
$F_{z,min}$, N	-14.0	0.0	100.0

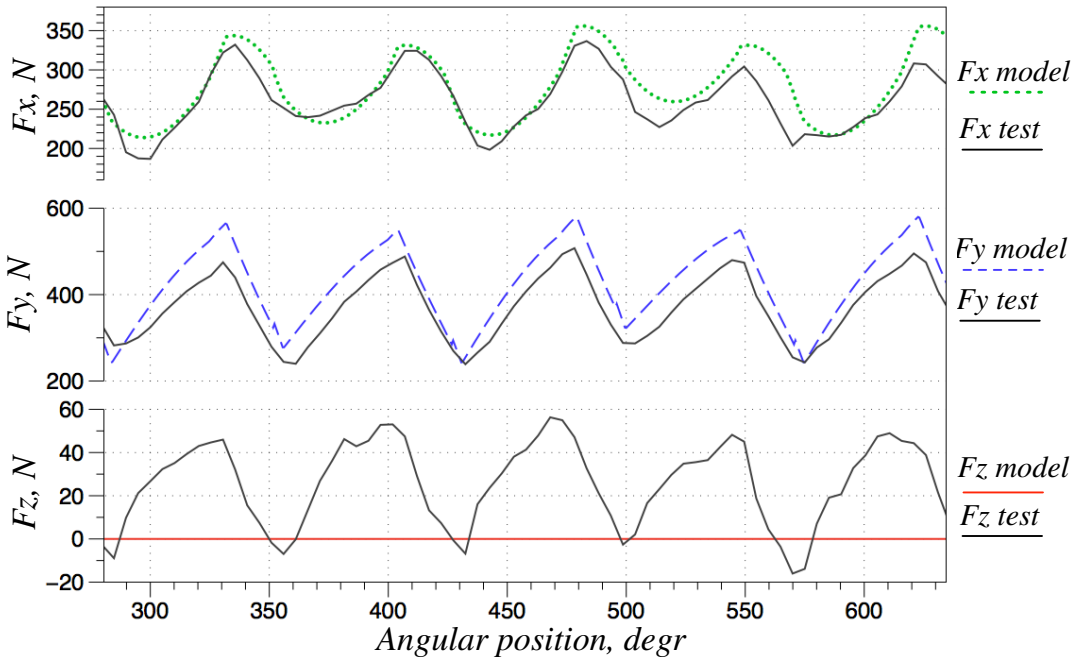

Figure 3.16: Predicted vs. experimental forces: test 3 / model 3

Table 3.7: Predicted and experimental values of the cutting forces F_x, F_y and F_z corresponding to the test 4 conditions (Fig.3.17): $a_p = 5.0$ mm; $a_e = 2.0$ mm; $f_z = 0.1$ mm/tooth; $\alpha = 27.8°$

	test 4	model 4	% error
$\overline{F}_x$, N	262.4	279.5	6.52
$F_{x,max}$, N	317.0	337.0	6.31
$F_{x,min}$, N	199.0	231.9	16.3
$\overline{F}_y$, N	390.0	432.7	10.9
$F_{y,max}$, N	503.9	560.0	11.1
$F_{y,min}$, N	276.2	274.8	-0.51
$\overline{F}_z$, N	0.27	0.0	100.0
$F_{z,max}$, N	24.4	0.0	100.0
$F_{z,min}$, N	-29.0	0.0	100.0

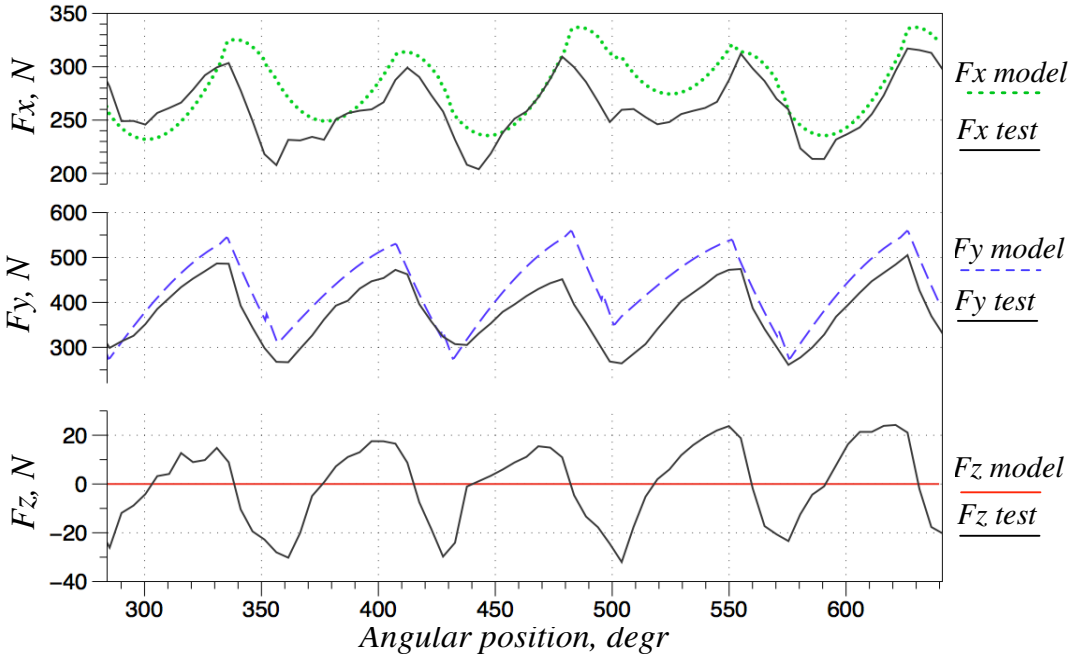

Figure 3.17: Predicted vs. experimental forces: test 4 / model 4

Table 3.8: Predicted and experimental values of the cutting forces F_x, F_y and F_z corresponding to the test 5 conditions (Fig.3.18): $a_p = 10.0$ mm; $a_e = 1.0$ mm; $f_z = 0.1$ mm/tooth; $\alpha = 21.4°$

	test 5	model 5	% error
$\overline{F}_x$, N	366.3	387.8	5.84
$F_{x,max}$, N	462.6	497.5	7.54
$F_{x,min}$, N	277.6	292.2	5.26
$\overline{F}_y$, N	422.5	430.4	1.87
$F_{y,max}$, N	561.3	574.5	2.35
$F_{y,min}$, N	306.2	316.7	3.43
$\overline{F}_z$, N	0.13	0.0	100.0
$F_{z,max}$, N	20.9	0.0	100.0
$F_{z,min}$, N	-17.6	0.0	100.0

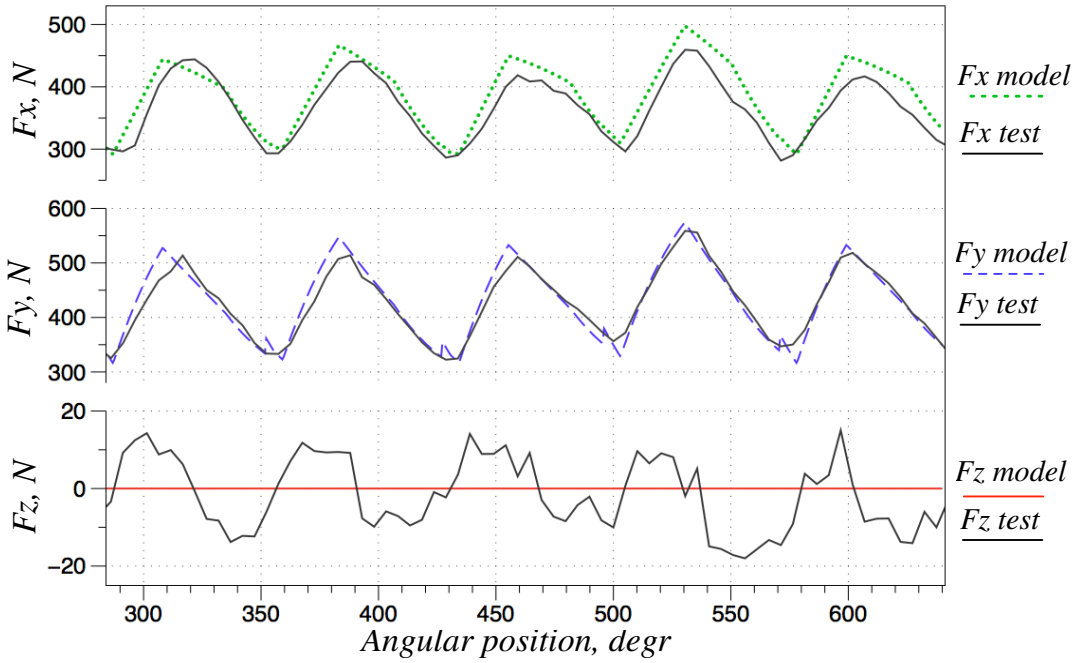

Figure 3.18: Predicted vs. experimental forces: test 5 / model 5

Table 3.9: Predicted and experimental values of the cutting forces F_x, F_y and F_z corresponding to the test 6 conditions (Fig.3.19): $a_p = 10.0$ mm; $a_e = 2.0$ mm; $f_z = 0.1$ mm/tooth; $\alpha = 0.0°$

	test 6	model 6	% error
$\overline{F}_x$, N	485.7	579.8	19.4
$F_{x,max}$, N	618.0	685.9	11.0
$F_{x,min}$, N	342.9	480.6	40.2
$\overline{F}_y$, N	745.8	804.5	7.87
$F_{y,max}$, N	964.8	1053.6	9.20
$F_{y,min}$, N	563.2	631.8	12.18
$\overline{F}_z$, N	267.1	0.0	100.0
$F_{z,max}$, N	358.6	0.0	100.0
$F_{z,min}$, N	201.4	0.0	100.0

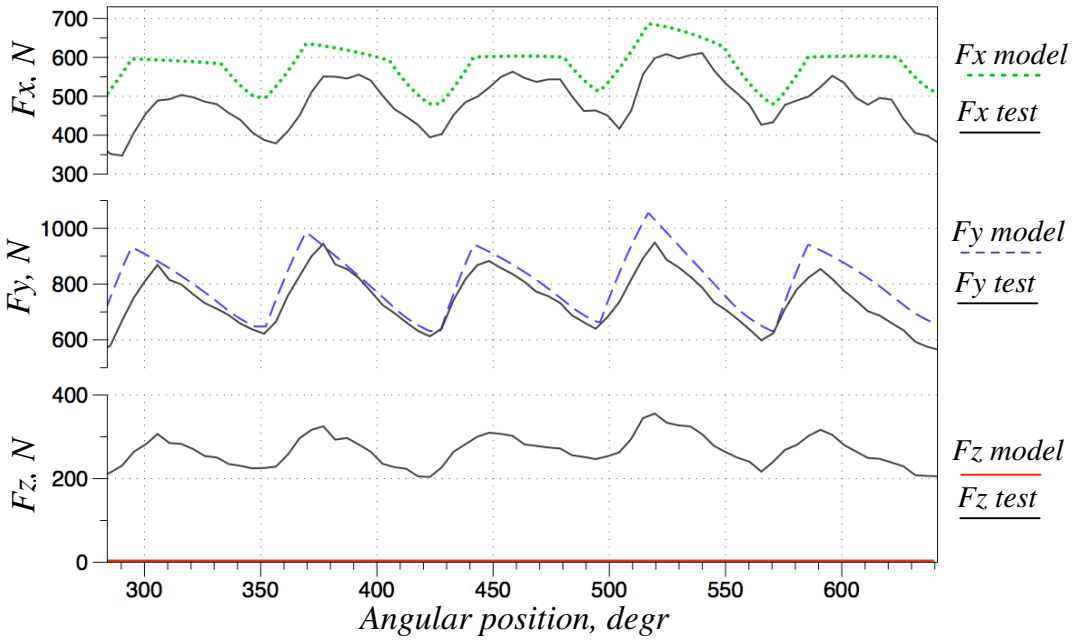

Figure 3.19: Predicted vs. experimental forces: test 6 / model 6

Table 3.10: Predicted and experimental values of the cutting forces F_x, F_y and F_z corresponding to the test 7 conditions (Fig.3.20): $a_p = 10.0$ mm; $a_e = 2.0$ mm; $f_z = 0.1$ mm/tooth; $\alpha = 19.0°$

	test 7	model 7	% error
$\overline{F}_x$, N	544.9	581.4	6.7
$F_{x,max}$, N	650.9	662.3	1.75
$F_{x,min}$, N	432.7	513.3	18.6
$\overline{F}_y$, N	778.9	825.4	5.97
$F_{y,max}$, N	945.5	1028.9	8.82
$F_{y,min}$, N	647.5	662.0	2.24
$\overline{F}_z$, N	85.6	0.0	100.0
$F_{z,max}$, N	123.6	0.0	100.0
$F_{z,min}$, N	47.7	0.0	100.0

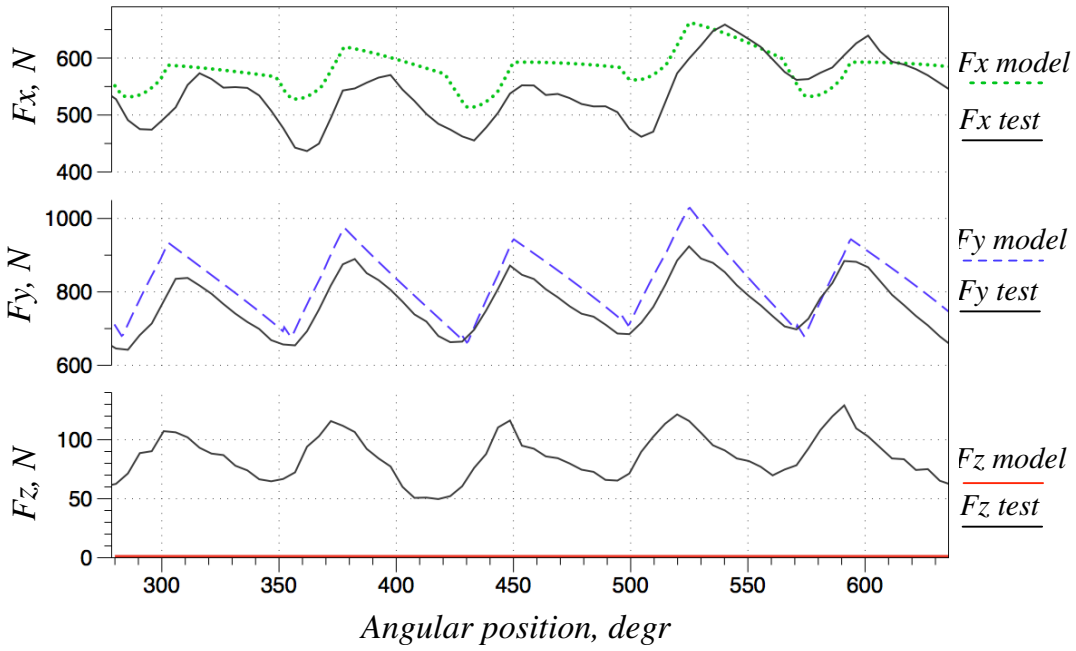

Figure 3.20: Predicted vs. experimental forces: test 7 / model 7

Table 3.11: Predicted and experimental values of the cutting forces F_x, F_y and F_z corresponding to the test 8 conditions (Fig.3.21): $a_p = 12.0$ mm; $a_e = 2.0$ mm; $f_z = 0.1$ mm/tooth; $\alpha = 21.0°$

	test 8	model 8	% error
$\overline{F}_x$, N	662.8	706.8	6.64
$F_{x,max}$, N	744.5	807.1	8.41
$F_{x,min}$, N	568.2	636.7	12.06
$\overline{F}_y$, N	917.5	994.5	8.39
$F_{y,max}$, N	1099.9	1181.7	7.44
$F_{y,min}$, N	767.1	798.2	4.05
$\overline{F}_z$, N	78.5	0.0	100.0
$F_{z,max}$, N	120.1	0.0	100.0
$F_{z,min}$, N	31.3	0.0	100.0

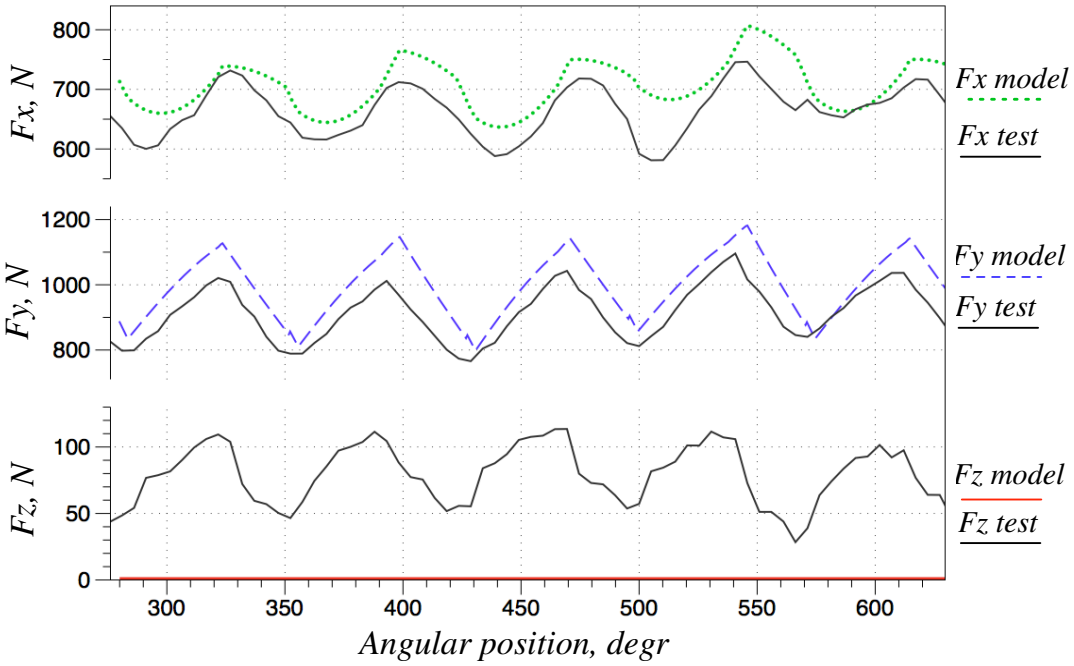

Figure 3.21: Predicted vs. experimental forces: test 8 / model 8

Table 3.12: Predicted and experimental values of the cutting forces F_x, F_y and F_z corresponding to the test 9 conditions (Fig.3.22): $a_p = 12.0$ mm; $a_e = 2.0$ mm; $f_z = 0.1$ mm/tooth; $\alpha = 27.8°$

	test 9	model 9	% error
$\overline{F}_x$, N	656.9	714.8	8.81
$F_{x,max}$, N	714.1	790.5	10.7
$F_{x,min}$, N	576.0	665.9	15.6
$\overline{F}_y$, N	925.6	1018.6	10.1
$F_{y,max}$, N	1041.5	1157.9	11.2
$F_{y,min}$, N	804.3	855.6	6.38
$\overline{F}_z$, N	-0.5	0.0	100.0
$F_{z,max}$, N	26.0	0.0	100.0
$F_{z,min}$, N	-41.5	0.0	100.0

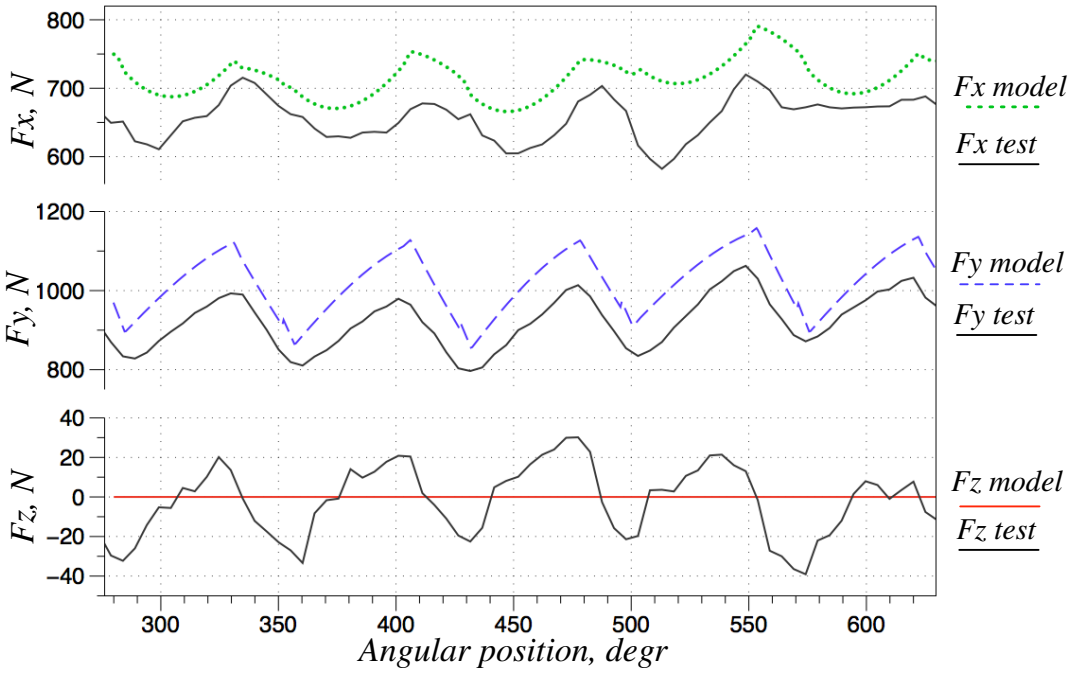

Figure 3.22: Predicted vs. experimental forces: test 9 / model 9

3.6.4 Comparison of Predicted and Measured Cutting Forces

The comparison between the predicted and measured cutting forces F_x and F_y was done for the average and maximum values, while the minimum simulated force value was neglected due to the fact that this parameter is not of particular interest to the purpose of this work. As can be seen from the Fig.3.14 - Fig. 3.22, which report the measured and simulated forces trends, despite the results show the general tendency of the proposed model to overestimate cutting forces F_x and F_y, the good agreement between the trends of the simulated and experimental forces can be observed. The overestimation of the cutting forces can be explained by the fact that the cutting forces coefficients implemented into the proposed model were identified based on 2D FEM results obtained in AdvantEdge, which, as has already been reported in Chapter 2, tends to overvalue these parameters.

Figure 3.23 reports the summarized data about the percentage error values observed between the average and maximum values of the simulated and measured cutting forces. From this figure it can be observed that:

1. The maximum percentage error values observed between the predicted and measured average values of the cutting forces are:

   19.4% for the force $\overline{F}_x$ (test 6);

   12.7% for the force $\overline{F}_y$ (test 1).

2. The maximum percentage error values observed between the predicted and measured maximum values of the cutting forces are:

   21.6% for the force $F_{x,max}$ (test 1);

   12.3% for the force $F_{y,max}$ (test 3)

Figure 3.24 reports the percentage error values of the average and maximum values of the cutting forces simulated under the conditions of the test 1, test 2, test 4, test 6, test 7, and test 9 (Table 3.2). From this figure it can be observed that in case the tilting angle value is kept constant, the percentage deviations between the average and maximum values of the simulated and measured cutting forces are sensitive to the cutting depth value. The following tendencies were observed:

1. The dependence of the percentage error of the $\overline{F}_x$ average value is directly proportional to the cutting depth increase, such as:

   $\overline{F}_x$ % error at $\alpha = 0.0°$:

   19.2% (test 1, $a_p = 5.0$ mm) and 19.4% (test 6, $a_p = 10.0$ mm);

   $\overline{F}_x$ % error at $\alpha = 19.0°$:

   2.52% (test 2, $a_p = 5.0$ mm) and 6.7% (test 7, $a_p = 10.0$ mm);

   $\overline{F}_x$ % error at $\alpha = 27.8°$:

   6.52% (test 4, $a_p = 5.0$ mm) and 8.81% (test 9, $a_p = 12.0$ mm).

2. The dependence of the percentage error of the $\overline{F}_y$ average value is inversely proportional to the cutting depth increase, such as:

   $\overline{F}_y$ % error at $\alpha = 0.0°$:

   12.7% (test 1, $a_p = 5.0$ mm) and 7.87% (test 6, $a_p = 10.0$ mm);

   $\overline{F}_y$ % error at $\alpha = 19.0°$:

   10.9% (test 2, $a_p = 5.0$ mm) and 5.97% (test 7, $a_p = 10.0$ mm);

   $\overline{F}_y$ % error at $\alpha = 27.8°$:

   10.9% (test 4, $a_p = 5.0$ mm) and 10.1% (test 9, a_p =12.0 mm).

3. The dependence of the percentage error of the $F_{x,max}$ maximum value is neither directly nor inversely proportional to the cutting depth increase. The following results were observed:

   $F_{x,max}$ % error at $\alpha = 0.0°$:

   21.6% (test 1, $a_p = 5.0$ mm) and 11.0% (test 6, $a_p = 10.0$ mm);

   $F_{x,max}$ % error at $\alpha = 19.0°$:

   1.47% (test 2, $a_p = 5.0$ mm) and 1.75% (test 7, $a_p = 10.0$ mm);

   $F_{x,max}$ % error at $\alpha = 27.8°$:

   6.31% (test 4, $a_p = 5.0$ mm) and 10.7% (test 9, a_p =12.0 mm).

4. The dependence of the percentage error of the $F_{y,max}$ maximum value is neither directly nor inversely proportional to the cutting depth increase. The following results were observed:

   $F_{y,max}$ % error at $\alpha = 0.0°$:

   10.7% (test 1, $a_p = 5.0$ mm) and 9.2% (test 6, $a_p = 10.0$ mm);

   $F_{y,max}$ % error at $\alpha = 19.0°$:

   9.2% (test 2, $a_p = 5.0$ mm) and 8.8% (test 7, $a_p = 10.0$ mm);

   $F_{y,max}$ % error at $\alpha = 27.8°$:

   11.1% (test 4, $a_p = 5.0$ mm) and 11.2% (test 9, $a_p = 12.0$ mm).

Another important phenomenon that shows the influence of the tilting angle on the percentage error value was also observed when comparing the results of predicted and measured average and maximum values of cutting forces for the cases with 5.0 mm axial cutting depth value (test 1, test 2, test 4 in the Fig.3.24). It was observed that:

1. The percentage error values for the average $\overline{F}_x$ cutting force are:

   19.2% (test 1, $\alpha = 0.0°$);

   2.52% (test 2, $\alpha = 19.0°$);

   6.52 % (test 4, $\alpha = 27.8°$).

2. The percentage error values for the average $\overline{F}_y$ cutting force are:

   12.7% (test 1, $\alpha = 0.0°$);

   10.7% (test 2, $\alpha = 19.0°$);

   10.9 % (test 4, $\alpha = 27.8°$)

3. The percentage error values for the maximum $F_{x,max}$ cutting force are:

   21.6% (test 1, $\alpha = 0.0°$);

   1.47% (test 2, $\alpha = 19.0°$);

   6.31 % (test 4, $\alpha = 27.8°$).

4. The percentage error values for the maximum $F_{y,max}$ cutting force are:

   10.7% (test 1, $\alpha = 0.0°$);

   9.2% (test 2, $\alpha = 19.0°$);

   11.1 % (test 4, $\alpha = 27.8°$).

These obtained results indicate that the minimum discrepancy for both the average and maximum values of simulated and measured cutting forces F_x and F_y occurs when predicting these cutting forces for the tilted side down-milling with $\alpha = 19.0°$ (test 2).

Instead, the maximum discrepancy between the simulated and measured values of the average F_x and F_y, and maximum F_x cutting forces occurs when simulating the non-tilted process with $\alpha = 0.0°$ (test 1), which is three-dimensional case. The maximum discrepancy between the simulated and measured values of the maximum F_y cutting force occurs when predicting this value for the tilted process with $\alpha = 27.8°$ (test 4).

Such results demonstrate that in case the cutting forces modeling is made on the basis of the cutting forces coefficients identified by using 2D FEM data, the percentage error values will be higher for the processes with the smaller tilting angle values (except for the maximum value of the force F_y), since the mechanics of these processes is not similar to the mechanics of the bi-dimensional operations.

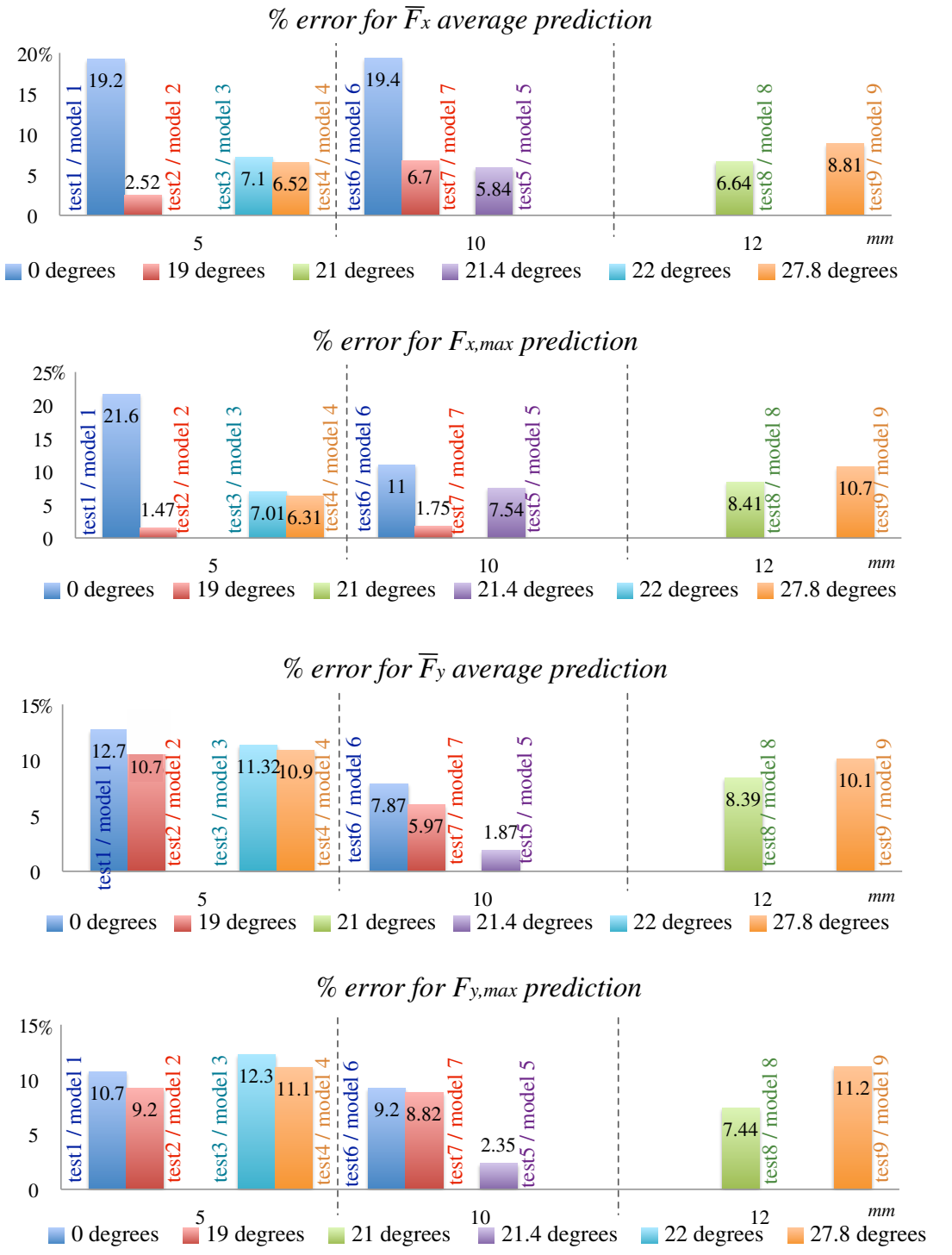

Figure 3.23: The percentage errors of the simulated average and maximum cutting forces values

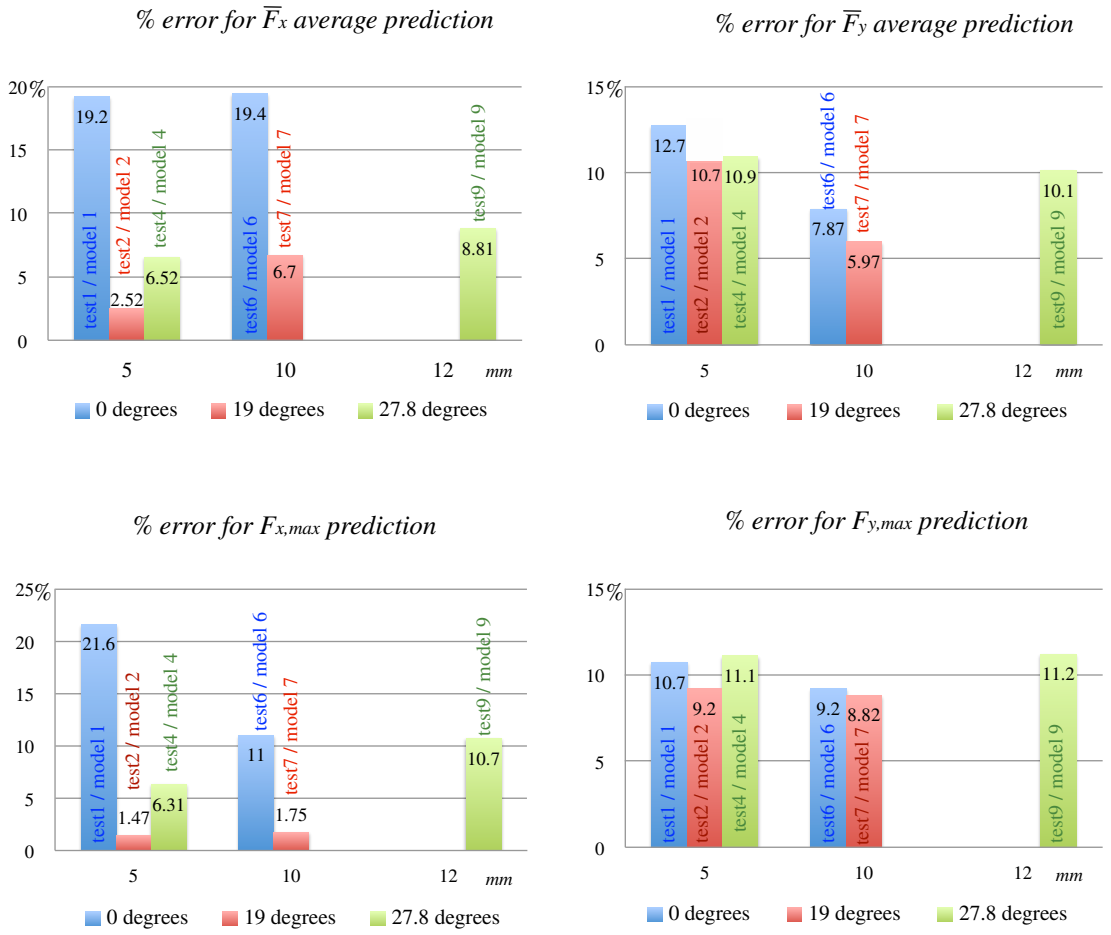

Figure 3.24: The percentage error of the cutting average and maximum forces F_x and F_y simulations compared to the measured data of the milling tests 1, 2, 4, 6, 7, 9 listed in the Tables 3.4, 3.5, 3.7, 3.9, 3.10 and 3.12 respectively

3.6.5 2D FEM accuracy evaluation

Since all of the milling process simulations were performed by applying cutting force coefficients identified based on 2D FEM cutting forces data (Table 3.3), it is possible to evaluate the prediction accuracy of this numerical modeling technique.

By looking at the results of the test 4 ($a_p = 5.0$mm, $a_e = 2.0$mm, $\alpha = 27.8°$), test 5 ($a_p = 10.0$mm, $a_e = 1.0$mm, $\alpha = 21.4°$) and test 9 ($a_p = 12.0$mm, $a_e = 2.0$mm, $\alpha = 27.8°$) reported in the Table 3.7, Table 3.8, Table 3.12 and in the Fig.3.17, Fig.3.18, Fig.3.22 respectively, which are considered to be similar to the bi-dimensional processes since the average values of the measured force F_z are close to *zero*, it can be seen that:

1. The observed range of the percentage error values for the average $\overline{F}_x$ cutting force simulation is:

   for $\overline{F}_x$ force: from 5.84% (test 5) to 8.81% (test 9)

2. The observed range of the percentage error values for the average $\overline{F}_y$ cutting force simulation is:

   for $\overline{F}_y$ force: from 1.87% (test 5) to 10.9% (test 4)

3. The observed range of the percentage error values for the maximum $F_{x,max}$ cutting force simulation is:

   for $F_{x,max}$ force: from 6.31% (test 4) to 10.7% (test 9)

4. The observed range of the percentage error values for the maximum $F_{y,max}$ cutting force simulation is:

   for $F_{y,max}$ force: from 2.35% (test 5) to 11.2% (test 9)

As can be seen from the reported results, the ranges of the percentage errors for both the average and maximum cutting forces F_x and F_y modeling are observed to have the acceptable level of inaccuracy, such confirming that the data of 2D FEM numerical simulations can be used as the first-step-approximation technique for the modeling of cutting forces that occur in three-dimensional systems.

SUMMARY

In this chapter, the state-of-the-art review of the available cutting forces modeling methods for different types of milling processes was done. Despite a lot of methods have been proposed, to the best of author's knowledge any of them deal with such particular processes as non-tilted and tilted side down-milling performed by using end mills with the helix angle value greater than *zero*. To meet the requirements, the development of a mechanistic model suitable for the modeling of the cutting forces that occur in non-tilted and tilted side down-milling operations was proposed in this chapter. In addition, such arguments as the mechanics of the tilted and non-tilted processes, methodologies to identify the maximum number of the edges cutting simultaneously, the edge/workpiece engagement boundaries, the instantaneous engagement length and chip thickness values, and the methodology to identify cutting forces constants were also discussed.

The validation of the proposed model was done by means of the experimental campaign, consisted in 9 milling tests performed with different non-tilted and tilted tool positions, and with different values of the axial and radial depths of cut. The cutting forces simulations corresponding to the experimental campaign tests were done by using the proposed cutting forces model with applied cutting forces coefficients identified based on 2D FEM data obtained by using the commercial software AdvantEdge v.7.0.

The analysis of the collected data reported in the Fig.3.23 showed that the proposed cutting forces model is accurate and suitable for both non-tilted and tilted cutting forces prediction. The following results were observed:

1. The minimum and maximum percentage error values that were observed for the average force $\overline{F}_x$ modeling amount 2.52% (test 2) and 19.4% (test 6) respectively.

2. The minimum and maximum percentage error values that were observed for the average force $\overline{F}_y$ modeling 1.87% (test 5) and 12.7% (test 1) respectively.

3. The minimum and maximum percentage error values that were observed for the maximum force $F_{x,max}$ modeling amount 1.47% (test 2) and 21.6% (test 1) respectively.

4. The minimum and maximum percentage error values that were observed for the maximum force $F_{y,max}$ modeling amount 2.35% (test 5) and 11.2% (test 9) respectively.

The analysis of the collected predicted and measured cutting forces also demonstrated that 2D FEM numerical simulations can be used as the first-step-approximation technique for the modeling of cutting forces that occur in three-dimensional systems. It has to be taken into account that in case the cutting forces modeling is done based on the cutting forces coefficients identified by using 2D FEM data, the percentage error values will be higher for the processes with the smaller tilting angle values (except for the maximum value of the force F_y), since the mechanics of these processes is not similar to the mechanics of the bi-dimensional operations.

Chapter 4

Achievements and Future Work

The research activities of the present PhD thesis relate to the study, application and improvement of the milling process modeling, optimization and control techniques, such as FEM numerical tools and adaptive control systems.

The first part of this thesis deals with the paradigm of *Intelligent Manufacturing Systems* that was implemented into the artificial operator called *Evaluation and Perception Controller* (EPC) based on the theoretical models, and capable to simulate, optimize, monitor, and learn the milling processes. In particular, it was studied the possibility of the improvement of this system in terms of the product final quality, associated to the scallop height value - one of the surface roughness characteristics. With this purpose, the theoretical model that represents the scallop height formation mechanism was developed. This model, after having been compared against the empirical model of the surface roughness R_z, was implemented into the *XOptima* library as one of the constraints (and not as target functions), thus allowing to reformulate the OCP problem, and to represent and control surface roughness value as desired and requested limit. The experimental activities showed that the proposed improvement of the EPC system was successful, and that it is possible to control the surface quality of the product by applying the discussed technique.

The second part of this work deals with the application of FEM techniques to study milling processes. In particular, the research was focused on evaluating the influence of STEP and STL CAD models, used to represent prototype tool geometries, on the cutting forces and deformed chip geometries prediction accuracy of 3D AdvantEdge by Third Wave Systems. The choice of the arguments to discuss, and experimental and modeling activities were performed in collaboration with the production unit of Sandvik Coromant placed in Rovereto (Italy). Since STEP and STL tool models are widely used by their R&D center when designing new products, the discussed arguments and performed analysis reported in this study were of particular importance to this company. It was shown that the applications of STEP and STL CAD files have a great and different impact on the cutting forces and deformed chip geometry modeling.

The third important argument discussed in this thesis is dedicated to the development of a cutting forces modeling system suitable for the non-tilted and tilted side down-milling process simulations. The development of such model had two purposes. First of all, this model can be implemented into the EPC, thus extending the field of the possible applications of this system. The second purpose relates to the problem of the application of 2D FEM modeling to study the influence of prototype cutting tool geometries on cutting forces F_x and F_y that occur in three-dimensional cutting processes. The experimental campaign carried out to study the accuracy of the proposed cutting forces model demonstrated that the model is accurate and suitable for both non-tilted and tilted cutting forces prediction. It was also shown that by implementing the cutting forces coefficients identified based on 2D FEM data into the proposed cutting forces model, it is possible to simulate cutting forces F_x and F_y that occur in three-dimensional systems, but it has to be taken into account the fact that the percentage error values in this case will be higher for the processes with the smaller tilting angle values (except for the maximum value of the force F_y), since the mechanics of these processes is not similar to the mechanics of bi-dimensional operations.

As the future works related to this study the author would like to specify the following important arguments: the study of the prediction accuracy of the proposed cutting forces modeling system that has to be performed by implementing into it cutting forces coefficients identified experimentally, the application of the proposed cutting forces modeling system into the EPC system, and the study of the influence of 2D and 3D (performed by using STEP and STL CAD tool models) AdvantEdge numerical approaches on temperature modeling.

The implementation of the cutting forces system model into the EPC system can be done by including this model into the process simulator, which performs the tool path analysis, and calculates the material removal rate (MRR), cutting force vector, and stability lobes diagrams (SLD). The importance of this step is related to the fact that such improvement of the EPC will allow to increase the level of its performance characteristics, and to expand of the field of its applicability and functionality.

The second argument that relates to the study of AdvantEdge prediction accuracy in terms of cutting temperatures has also importance for the tool manufacturing companies since this information can provide better understanding and research in such fields as tool coating and lubrication application.

An attempt to perform this study has already been done in the present PhD thesis, but due to the lack of time and difficulties with the experimental set-up and available equipment to reconstruct the representation of FEM modeling, and with analysis of the collected the data, this study was not concluded, and it was not reported in this work.

The activities performed to collect the data, simulated and real temperatures, included different 2D and 3D simulations performed in AdvantEdge v.7.0, and registration of the videos of cutting tests performed by using the FLIR ThermoVision A230 temperature measurement infrared camera. In particular, the problems with the experimental set-up related to the position of the FLIR A320 camera with respect to the cutting zone, where the temperature had to be measured. As can be seen in the Fig.4.1, from the location where the thermal camera was positioned it was not possible to catch cutting region, and to register data describing tool behaviour in this zone. Due to this, the experimental temperatures were registered only for the tool at the end of cutting operation.

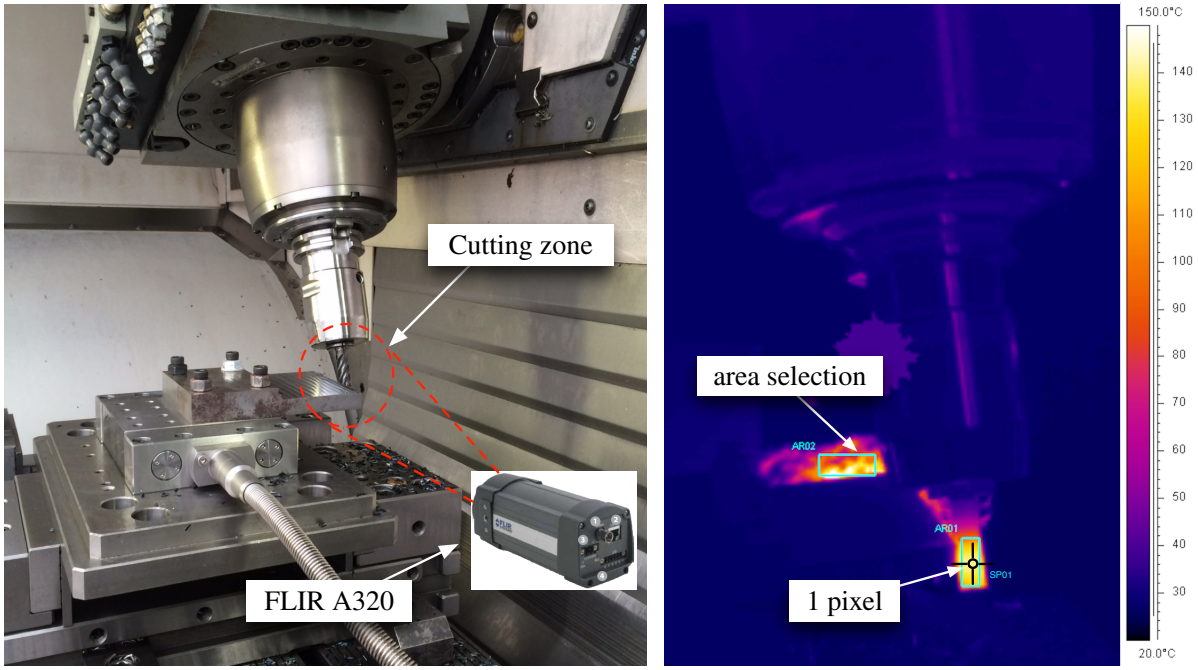

Figure 4.1: Temperature measurements set-up, field of view, and example of the types of measurement tools in ThermaCAM dialog window ('area-selection' and 'single-point-selection' that is able to capture the area of 1 pixel)

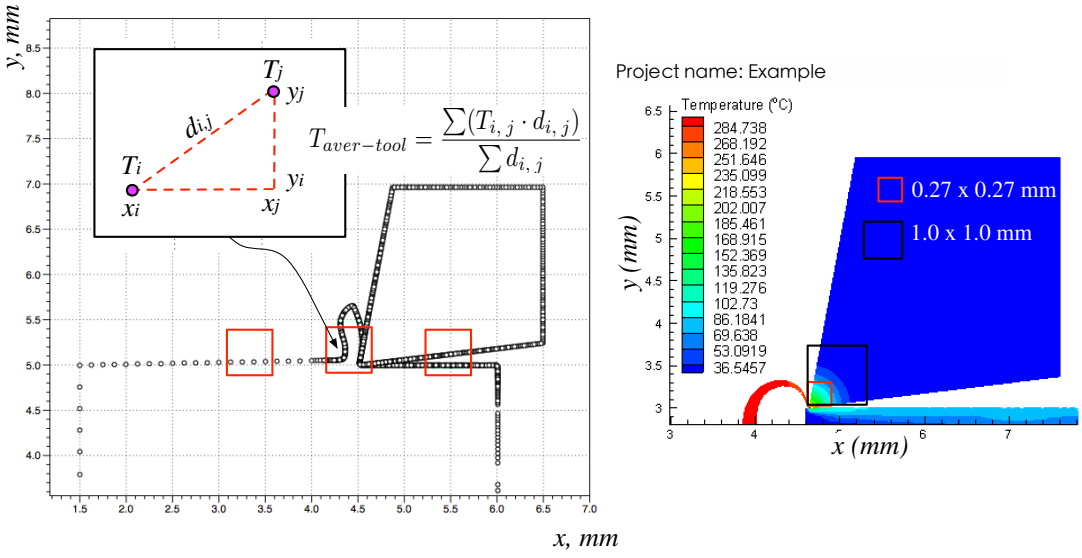

(a) (b)

Figure 4.2: (a) Schematic representation of the algorithm used to calculate temperature as a volume-weighted average value on the area equal to 1 pixel; (b) Example of 2D FEM AdvantEdge

Another difficulty that was faced related to the temperature measurements performed by using the commercial software ThermaCAM. Since it was necessary to measure the temperature of the tool at the end of the cutting operation, while the tool was exiting from the workpiece, the registered videos were stopped at the moment corresponding to this condition. To perform video-processing in ThermaCAM such tools as 'area-selection' and 'single-point-selection' were used to detect the highest value of the temperature registered in one of the pixels of this single image.

In order to adapt 2D FEM data to the experimental campaign conditions, and to able to identify simulated temperatures on the same area as it was done by using ThermaCAM tool, it was written an algorithm in RUBY that is based on the exported AdvantEdge data containing the x and y coordinates of the nodes representing the bounds of studying system, and the temperature values of each node (Fig.4.2(a)). In this algorithm, the temperature is calculated as a volume-weighted average value on the area that can be equal or to 1 pixel area that is caught by the 'single-point-selection' tool, or to area caught by the 'area-selection' tool (Fig.4.2(b)) of ThermaCAM software.

In this work, since the registered temperatures corresponded to the stable cutting conditions, it was also done an attempt to simulate these steady-state conditions in 2D and 3D FEM AdvantEdge.

Two different 2D numerical simulations were performed. The first case that was represented included the simulation of five rotations of one-tooth tool with only one single chip sample to cut during each rotation (Fig.4.3(a)). The second case included the simulation of a single rotation of falsely-five-teeth tool, where five chip samples had to be cut by the same tooth. Unfortunately, it was observed that the steady-state conditions were not reached for any of two performed 2D FEM simulations. As can be seen in the Fig.4.3(a, b), the area of the cutting tooth that was simulated as heated up is incomparably small with respect to the registered heated area of the cutting tool (Fig.4.1). Due to these reasons the comparison between the simulated in 2D and measured temperatures was not possible to perform.

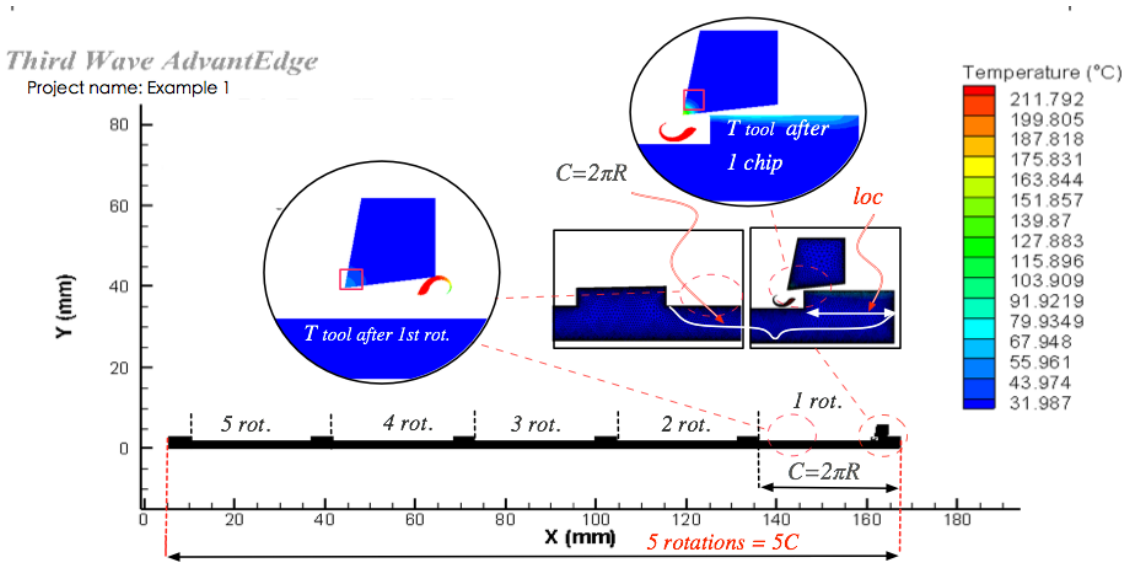

(a)

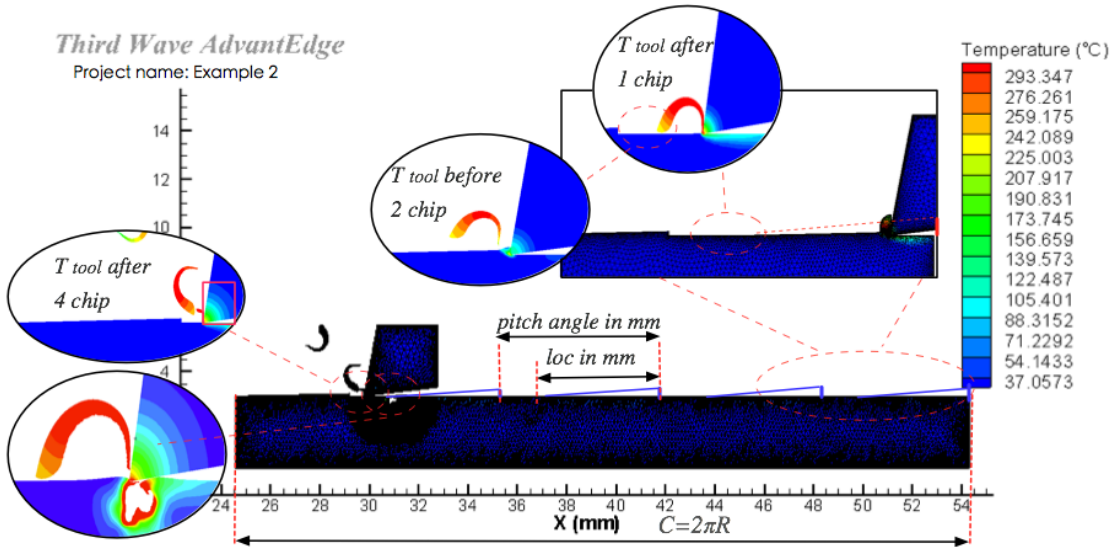

(b)

Figure 4.3: Performed 2D FEM AdvantEdge to reach steady-state conditions: (a) simulation of five rotations of the tool, where only single chip sample is cut during one rotation; (b) simulation of one rotation of the tool with five chip samples to cut

In case of 3D FEM simulations performed in AdvantEdge it was also demonstrated that the steady-state conditions are not easy to reach. In the Fig.2.12, that has already been reported in Chapter 2, it is well seen that after one rotation of the tool was simulated, the area of the cutting edge that was heated up is also incomparably small if compared to the registered heated area of the cutting tool (Fig.4.1).

In theory, the steady-state conditions can be reached by increasing the length of the workpiece (2D FEM) or by increasing the number of the tool rotations (3D FEM) when performing simulation set-up, but the increase of these parameters would dramatically affect time-consuming characteristics of this modeling technique, thus making it inapplicable and ineffective.

With respect to the information reported regarding the problems of the application of 2D and 3D FEM AdvantEdge to study cutting temperatures, the author would like to underline the fact that the study of this argument is very important and crucial, and that the fast, easy and efficient methods have to be built in case this modeling technique has to be applied to study temperatures when designing and developing new cutting tools.

Bibliography

[1] 3D Systems. https://www.3dsystems.com/quickparts/learning-center/what-is-stl-file, .

[2] Wikipedia. https://en.wikipedia.org/wiki/STL_(file_format), .

[3] Wikipedia. https://en.wikipedia.org/wiki/ISO_10303-21.

[4] R. G. Abraham. Westinghouse progress in adaptive control. *Westinghouse Machine Tool Forum*, 1973.

[5] N. A. Abukhshim, P. T. Mativenga, and M. A. Sheikh. An investigation of the tool-chip contact length and wear in high-speed turning of EN19 steel. *Proceedings of the Institution of Mechanical Engineers*, 118: 889–903, 2004.

[6] O. Adetoro and P. Wen. Prediction of mechanistic cutting force coefficients using ALE formulation. *The International Journal of Advanced Manufacturing Technology*, 46:79–90, 2010. doi: 10.1007/s00170-009-2079-7.

[7] A. H. Adibi-Sedeh, M. Vaziri, V. Pednekar, V. Madhavan, and R. Ivester. Investigation of the effect of using different material models on finite element simulations of metal cutting. *8th CIRP International Workshop on Modeling of Machining Operations*, 2005.

[8] Y. Altintas. Direct adaptive control of end milling process. *International Journal of Machine Tools Manufacturing*, 34:461–472, 1994.

[9] Y. Altintas. *Manufacturing Automation: Metal Cutting Mechanics, Machine Tool Vibrations, and CNC Design*. Cambridge university press, 2012.

[10] Y. Altintas and N. A. Erol. Open architecture modular tool kit for motion and machining process control. *Manufacturing Technology*, 47:295–300, 1998.

[11] Y. Altintas and P. Lee. A general mechanics and dynamics model for helical end mills. *CIRP Annals - Manufacturing Technology*, 45:59–64, 1996.

[12] Y. Altintas and P. Lee. Mechanics and dynamics of ball end milling. *Journal of Manufacturing Science and Engineering*, 120:684–692, 1998.

[13] G. Amitay, S. Malkin, and Y. Koren. Adaptive control optimization of grinding. *Journal of Engineering for Industry*, 103:103–108, 1981.

[14] V. P. Astakhov and J. C. Outeiro. Metal cutting mechanics, Finite Element Modelling. *Machining: fundamentals and recent advances*, pages 1–27, 2008.

[15] T. Atkins. Prediction of sticking and sliding lengths on the rake faces of tools using cutting forces. *International Journal of Mechanical Sciences*, 91:33–45, 2015.

[16] A. Azeem and H.-Y. Feng. Cutting force prediction for ball-end mills with non-horizontal and rotational cutting motions. *International Journal of Advanced Manufacturing Technologies*, 67:1833–1845, 2013. doi: 10.1007/s00170-012-4612-3.

[17] D. K. Baek, T. J. Ko, and H. S. Kim. A dynamic surface roughness model for face milling. *Precision Engineering*, 20:171–178, 1997.

[18] S. Bahi, M. Nouari, A. Moufki, M. E. Mansori, and A. Molinari. A new friction law for sticking and sliding contacts in machining. *Tribology International*, 44:764–771, 2011.

[19] B. Banerjee. The mechanical threshold stress model for various tempers of AISI 4340 steel. *International Journal of Solids and Structures*, 44:834–859, 2007.

[20] R. Baptista and J. F. A. Simões. Three and five axes milling of sculptured surfaces. *Journal of Materials Processing Technology*, 103:398–403, 2000.

[21] P. K. Baro, S. Joshia, and S. Kapoor. Modeling of cutting forces in a face-milling operation with self-propelled round insert milling cutter. *International Journal of Machine Tools and Manufacture*, 45:831–839, 2005.

[22] S. Bedi, F. Ismail, M. Mahjoob, and Y. Chen. Toroidal versus ball nose and flat bottom end mills. *International Journal of Advanced Manufacturing Technology*, 13:326–332, 1997.

[23] P. Benardos and G. C. Vosniakos. Prediction of surface roughness in CNC face milling using neural networks and Taguchi's design of experiments. *Robotics and Computer-Integrated Manufacturing*, pages 343–354, 2002.

[24] H. Bil, S. E. Kiliç, and A. E. Tekkaya. A comparison of orthogonal cutting data from experiments with three different finite element models. *International Journal of Machine Tools and Manufacture*, 44:933–944, 2004.

[25] F. Biral, P. Bosetti, R. Oboe, and F. Tondini. A new direct deformation sensor for active compensation of positioning errors in large milling machines. *Advanced Motion Control*, pages 126–131, 2006.

[26] C. M. G. Bort. *On application of optimal control to Intelligent Manufacturing*. Phd thesis, University of Trento, 2013.

[27] P. Bosetti and F. Biral. Rapid development of a CNC software within manufacturing automation courses. *International Mechanical Engineering Congress and Exposition*, pages 1–10, 2008.

[28] P. Bosetti and F. Biral. Application of optimal control theory to milling process. *Institute of Electrical and Elecronics Engineering*, 14:4896–4901, 2014.

[29] E. Budak and L. Kops. Improving productivity and part quality in milling of Titanium based impellers by chatter suppression and force control. *Manufacturing Technology*, 49:31–36, 2000.

[30] E. Budak, Y. Altintas, and E. J. A. Armarego. Prediction of milling force coefficients from orthogonal cutting data. *Journal of Manufacturing Science and Engineering*, 118:216–224, 1994.

[31] D. Carpenter. Adaptive control. *Proceedings of the Machine Tool Task Force Conference*, 4:31–40, 1980.

[32] J. T. Carroll and J. S. Strenkowski. Finite element models of orthogonal cutting with application to single point diamond turning. *International Journal of Mechanical Sciences*, 30:899–920, 1988.

[33] R. M. Centner and J. M. Idelsohn. Adaptive controller for a metal cutting process. *Proceedings of IEEE ASME Joint Automatic Control Conference*, pages 154–161, 1964.

[34] J.-S. Chen, Y.-K. Huang, and M.-S. Chen. A study of the surface scallop generating mechanism in the ball-end milling process. *International Journal of Machine Tools and Manufacture*, 45:1077–1084, 2005.

[35] X. Chen, J. Zhao, Y. Dong, S. Han, A. Li, and D. Wang. Effects of inclination angles on geometrical features of machined surface in five-axis milling. *International Journal of Advanced Manufacturing Technology*, 65: 1721–1733, 2013.

[36] S.-T. Chiang, D.-I. Liu, A.-C. Lee, and W.-H. Chieng. Adaptive control optimization in end milling using neural networks. *International Journal of Machining Tools Manufacturing*, 34:637–660, 1995.

[37] C. K. Chua, K. F. Leong, and C. S. Lim. *Rapid prototyping: principles and applications*. World Scientific Publishing, 2003.

[38] C. Constantin, S.-M. Croitoru, G. Constantin, and E. Strajescu. 3D FEM analysis of cutting processes. *Proceedings of the 3rd WSEAS international conference on Visualization, imaging and simulation*, pages 41–46, 2010.

[39] C. Constantin, S.-M. Croitoru, G. Constantin, and E. Strajescu. FEM Tool for cutting process modelling and simulation. *Mechanical Engineering*, 74:149–162, 2012.

[40] J. P. Davim, P. Reis, C. Maranhão, and J. Gracio. Finite element simulation and experimental analysis of orthogonal cutting of an aluminium alloy using Polycrystalline Diamond tools. *International Journal of Materials and Product Technology*, 37:46–59, 2010.

[41] B. Denkena, H.-C. Moehring, and J. C. Will. Tool deflection compensation with an adaptronic milling spindle. 46, 2015.

[42] A. Duroobi, H. X. Zhong, and C. Wenliang. Feed-interval scallop height estimation using multi-axis CNC milling machine. *Anbar Journal for Engineering Science*, 5:51–63, 2012.

[43] M. A. A. Elbestawi. *A study of an adaptive control constraint system for milling.* Phd thesis, McMaster University, 1980.

[44] S. Engin and Y. Altintas. Generalized modeling of milling mechanics and dynamics: Part 2 - inserted cutters.

[45] S. Engin and Y. Altintas. Mechanics and dynamics of general milling cutters: Part 1: helical end mills. *International Journal of Machine Tools and Manufacture*, 41:2195–2212, 2001.

[46] Y. Fang. *Theoretical modelling and animation of the chip curling process in 3D metal cutting.* Phd thesis, University of Wollongong, 1998.

[47] K.-H. Fuh and C.-F. Wu. A proposed statistical model for surface quality prediction in end-milling of Al alloy. *International Journal of Machine Tools and Manufacture*, 35:1187–1200, 1995.

[48] N. I. Galanis and D. E. Manolakos. Finite element analysis of the cutting forces in turning of femoral heads from AISI 316L stainless steel. *Proceeding of the World Congress on Engineering*, 2, 2014.

[49] J. D. Gardner, A. Vijayaraghavan, and D. A. Donrfeld. Comparative study of finite element simulation software. *Consortium on Deburring and Edge Finishing*, 74, 2005.

[50] A. Ghasempoor, J. Jeswiet, and T. N. Moore. Automatic adjustment of cutting conditions in rough turning. *Engineering Manufacture*, 217:1393–1400, 1999.

[51] O. Gonzalo, H. Jauregi, L. G. Uriarte, and L. N. López de Lacalle. Prediction of specific force coefficients from a FEM cutting model. *International Journal of Advanced Manufacturing Technology*, 43:348–356, 2009.

[52] A. V. Gopal and P. V. Rao. Selection of optimum conditions for maximum material removal rate with surface finish and damage as constraints in SiC grinding. *International Journal of Machine Tools and Manufacture*, 43:1327–1336, 2003.

[53] M. Groover and E. Zimmers. *CAD/CAM: Computer-Aided Design and manufacturing.* Technology and Engineering, 1983.

[54] S. Hoppe. *Experimental and numerical analysis of chip formation in metal cutting.* Master thesis, 2003.

[55] T. Huang, X. Zhang, and H. Ding. Decoupled chip thickness calculation model for cutting force prediction in five-axis ball-end milling. *International Journal of Advanced Manufacturing Technology*, 69:1203–1217, 2013.

[56] J. Huber and R. Centner. *Test results with an adaptively controlled milling machine.* Dearborn (Mich.) : American Society of Tool and Manufacturing Engineers, 1968.

[57] S. Ibaraki, T. Shimizu, and A. Matsubara. A long-term control scheme of cutting forces to regulate tool life in end milling processes. *Precision Engineering*, 34:675–682, 2010.

[58] F. Ijaz, N. Mehmood, M. Jamil, and Y. Ayaz. Developments in adaptive control techniques for machine tools. *International Conference on Robotics and Emerging Allied Technologies in Engineering*, pages 186–190, 2014.

[59] B. W. Ikua, H. Tanaka, F. Obata, and S. Sakamoto. Prediction of cutting forces and machining error in ball end milling of curved surfaces - I theoretical analysis. *Journal of the International Societies for Precision Engineering and Nanotechnology*, 25:266–273, 2001.

[60] V. S. Jatti, R. Sekhar, and R. K. Patil. Study of ball nose end milling of LM6 Al alloy: surface roughness optimisation using Genetic Algorithm. *International Journal of Engineering and Technology*, 5:2859–2865, 2013.

[61] V. Jivishov and E. Rzayev. Influence of material models used in finite element modeling on cutting forces in machining. *Materials Science and Engineering*, 142:1–9, 2016.

[62] G. R. Johnson and W. H. Cook. A constitutive model and data for metals subjected to large strains, high strain rates and high temperatures. *Proceedings of 7th International Symposium Ball*, 30:541–547, 1983.

[63] K. Kadirgama, M. M. Noor, N. M. Zuki, and M. R. M. R. abd Bb Mohammad. Prediction of cutting force by numerical solution and statistic method in end-milling operation. *2nd International Conference on Science and Technology, Applications in Industry and Education (ICSTIE)*, pages 466–472, 2008.

[64] Y. Kakino, H. Ohtsuka, H. Nakagawa, T. Yirogaki, and M. Sasaki. A study on end milling of Hardened Steel (1st Report). Simplified prediction model for cutting forces and control for constant cutting foces using this model. *Journal of the Japan Society for Precision Engineering*, 66:730–734, 2000.

[65] V. Kalhori. *Modeling and simulations of mechanical cutting.* Phd thesis, Lulea Tekniska Universitet, 2001.

[66] L. Kandrac, I. Maňková, M. Vrabel, and J. Beňo. Finite element simulation of cutting forces in orthogonal machining of titanium alloy Ti-6Al-4V. *Applied Mechanics and Materials*, 474:192–199, 2014.

[67] R. L. Kegg. Production experience with adaptive controls. *3rd NC Robot Automation Conference*, 1978.

[68] K. Kendall, N. J. Shang, and I. Staffell. Application of Coulomb's friction law to define energy consumption of new drive-trains. *Hybrid and Electric Vehicles Conference*, pages 1–5, 2013.

[69] C. Kiliçaslan. *Modeling and simulation of metal cutting by finite element method.* Master thesis, Graduate School of Engineering and Sciences of Izmir Institute of Technology, 2009.

[70] B. H. Kim and C. N. Chu. Texture prediction of milled surfaces using texture superposition method. *Computer-Aided Design*, 31:485–494, 1999.

[71] D. Kim and D. Jeon. Fuzzy-logic control of cutting forces in CNC milling processes using motor currents as indirect force sensors. *Precision Engineering*, 35:143–152, 2011.

[72] H. S. Kim and K. Ehmann. A cutting force model for face-milling operation. *International of Journal of Machine Tool Manufacture*, 33:651–673, 1993.

[73] F. Koppka, H. Sahlan, P. Sartkulvanich, and T. Altan. Experimental determination of flow stress data for FEM simulation of machining operations. *ERC Report*, 2001.

[74] A. Lamikiz, L. N. López de Lacalle, J. A. Sánchez, and M. A. Salgad. Cutting force estimation in sculptured surface milling. *International Journal of Machine Tools and Manufacture*, 44:1511–1526, 2004.

[75] Y. Landon, S. Segonds, P. Lascoumes, and P. Lagarrigue. Tool positioning error (TPE) characterization in milling. *International Journal of Machine Tools and Manufacture*, 20:457–464, 2004.

[76] H. Li, W. Zhang, and X. Li. Modelling of cutting forces in helical end milling using a predictive machining theory. *International Journal of Mechanical Sciences*, 43:1711–1730, 2001.

[77] R. Li and A. J. Shih. Finite element modeling of 3D turning of titanium. *International Journal of Advanced Manufacturing Technology*, 29, 2005.

[78] S. Y. Liang, R. L. Hecker, and R. G. Landers. Machining process monitoring and control: the state-of-the-art. *ASME International Mechanical Engineering Congress and Exposition*, pages 1–8, 2002.

[79] S. Lin, F. Peng, Y. Liu, S. Yang, and R. Yan. Finite element research on cutting force and temperature in milling 300M steel. *6th International Conference on Intelligent Robotics and Applications*, pages 481–490, 2013.

[80] H. Liu, T. Wang, and D. Wang. Constant cutting force control for CNC machining using dynamic characteristic-based fuzzy controller. *Shock and Vibration*, 2015, 2015.

[81] Y. Liu and C. Wang. Neural Network based adaptive control and optimisation in the milling process. *International Journal of Advanced Manufacturing Technology*, 15:791–795, 1999.

[82] Y. Liu, L. Zuo, and C. Wang. Intelligent adaptive control in milling processes. *International Journal of Computer Integrated Manufacturing*, 12:453–460, 1999.

[83] Z. Q. Liu and P. F. Zhao. An experimental and numerical analyses of hard turning AISI 440C martensitic steel. *Materials Processing Science and Technology*, 1:39–52, 2010.

[84] Z.-C. Luo, F.-Y. Peng, X.-B. Chen, and L.-F. Wei. Prediction and simulation of surface topomorphy in ultraprecision milling for optical freeform surface. *Journal of Vacuum Science and Technology*, 27:1230–1237, 2009.

[85] A. G. Mamalis, J. Kundrák, A. Markopoulos, and D. E. Manolakos. On the finite element modelling of high speed hard turning. *International Journal of Advanced Manufacturing Technology*, 38:441–446, 2008.

[86] X. Man, D. Ren, S. Usui, C. Johnson, and T. D. Marusich. Validation of finite element cutting force prediction for end milling. *Procedia CIRP*, 1:663–668, 2012.

[87] I. Maňková, P. Kovac, J. Kundrak, and J. Beňo. Finite element analysis of hardened steel cutting. *Journal of Production Engineering*, 14:7–10, 2003.

[88] C. Maranhão and J. P. Davim. Finite element modelling of machining of AISI 316 steel: numerical simulation and experimental validation. *Simulation Modelling Practice and Theory*, 18:139–156, 2010.

[89] C. Maranhão and J. P. Davim. An overview on commercial software's in FEM analysis machining. *International Journal of Engineering*, 74:137–139, 2012.

[90] A. P. Markopoulos, K. Kantzavelos, N. I. Gakanis, and D. E. Manolakos. 3D finite element modeling of high speed machining. *Dynamic Methods and Process Advancements in Mechanical, Manufacturing, and Materials Engineering*, pages 178–195, 2012.

[91] R. A. Mathias. Adaptive control of the milling process. *Proceedings of the IEEE National Machine Tools Industry Conference*, 1967.

[92] R. A. Mathias, W. Boock, and A. Welch. Adaptive control: monitoring and control of metal-cutting processes. *Proceedings of the Machine Tool Task Force Conference*, 4, 1980.

[93] S. D. Merdol and Y. Altintas. Virtual cutting and optimization of three-axis milling processes. *International Journal of Machine Tools and Manufacture*, 48:1063–1071, 2008.

[94] B. Mikó, J. Beňo, and I. Maňková. Experimental verification of cusp heights when 3D milling rounded surfaces. *Acta Polytechnica Hungarica*, 9:101–116, 2012.

[95] M. Milfelner, J. Kopac, F. Čuš, and U. Župerl. Genetic equation for the cutting force in ball-end milling. *Journal of Materials Processing Technology*, 164:1554–1560, 2005.

[96] A. Molina, C. A. Rodriguez, H. Ahuett, J. A. Cortés, M. Ramírez, G. Jiménez, and S. Martinez. Next-generation manufacturing systems: key research issues in developing and integrating reconfigurable and intelligent machines. *International Journal of Computer Integrated Manufacturing*, 18:525–536, 2005.

[97] M. Monno, G. M. Pittalà, and F. Linares. 3D finite element modeling of milling of titanium. 2015.

[98] P. Nieslony, W. Grzesik, K. Zak, and P. Laskowsli. 3D FEM simualtions and experimental studies of the turning process of Inconel 718 superalloy. *Journal of Machine Engineering*, 14:39–52, 2014.

[99] P. Nieslony, W. Grzesik, and W. Habrat. Experimental and simualtion investigations of face milling process of Ti-6AL-4V titanium alloy. *Advances in Manufacturing Science and Technology*, 39:39–52, 2015.

[100] M. V. Nojedeh, M. Habibi, and B. Arezoo. Tool path accuracy enhancement through geometrical error compensation. *International Journal of Machine Tools and Manufacture*, 51:471–482, 2011.

[101] F. T. Ordubadi. *Adaptive control of the milling process.* Phd thesis, Faculty of the Mechanical Engineering, The university of British Columbia, 1989.

[102] P. L. B. Oxley. *The mechanics of machining : an analytical approach to assessing machinability.* Chichester, England, 1989.

[103] T. Özel. Modeling of hard part machining: effect of insert edge preparation in CBN cutting tools. *Journal of Materials Processing Technology*, 141:284–293, 2003.

[104] T. Özel and E. Zeren. Finite element modelling of the influence of edge roundness on the stress and temperature fields induced by high speed machining. *International Journal of Advanced Manufacturing Technology*, 35:255–267, 2007.

[105] E. Özlü, E. Budak, and A. Molinari. Thermomechanical modeling of orthogonal cutting including the effect of stick-slide regions on the rake face. *10th International Workshop on Modeling of Machining Operations*, 2007.

[106] E. Ozturk and E. Budak. Modeling of 5 axis milling processes. *Machining Science and Technology*, 11: 287–311, 2007.

[107] E. Ozturk and E. Budak. Dynamics and stability of five-axis ball-end milling. *Journal of Manufacturing Science and Engineering*, 132:021003–1–021003–13, 2010. doi: 10.1115/1.4001038.

[108] H. J. Pahk and S. W. Lee. Thermal error measurement and real time compensation system for the CNC machine tools incorporating the spindle thermal error and the feed axis thermal error. *International Journal of Advanced Manufacturing Technology*, 20:487–494, 2002.

[109] J. G. Parmar and A. Makwana. Prediction of surface roughness for end milling process using Artificial Neural Network. *International Journal of Modern Engineering Research*, 2:1006–1013, 2012.

[110] J. Peklenik. Analysis of the adaptive control of manufacturing systems - a critical assessment. *CIRP Fourth International Seminar on Optimization of Manufacturing Systems*, 1972.

[111] B. Porter and R. D. M. J. Summers. Adaptive machine-tool control - the State of the Art. *Machinery.*

[112] B. S. Prasad, D. S. Prasad, A. Sandeep, and G. Veeraiah. Condition monitoring of CNC machining using adaptive control. *International Journal of Automation and Computing*, 10:202–209, 2013. doi: 10.1007/s11633-013-0713-1.

[113] D. L. Preston and D. L. T. ans Dd Cc Wallace. Model of plastic deformation for extreme loading conditions. *Journal of Applied Physics*, 93:849–857, 2003.

[114] J. M. R. Prieto. *Numerical modeling of metal cutting processes using the Particle finite element method.* Master thesis, University of Catalonia, 2013.

[115] A. Priyadarshini, S. K. Pal, and A. K. Samantaray. Influence of the Johnson-Cook material model parameters and friction models on simulation of orthogonal cutting process. *Journal of Machining and Forming Technologies*, 4:59–83.

[116] L. Qian and M. R. Hossan. Effect on cutting force in turning hardened tool steels with cubic boron nitride inserts. *Journal of Materials Processing Technology*, 191:274–278, 2007.

[117] B. Rao, C. R. Dandekar, and Y. C. Shin. An experimental and numerical study on the face milling of Ti-6Al-4V alloy: tool performance and surface integrity. *Journal of Materials Processing Technology*, 211: 294–304, 2011.

[118] V. S. Rao and P. V. M. Rao. Modelling of tooth trajectory and process geometry in peripheral milling of curved surfaces. *International Journal of Machine Tools and Manufacture*, 45:617–630, 2005.

[119] V. S. Rao and P. V. M. Rao. Tool deflection compensation in peripheral milling of curved geometries. *International Journal of Machine Tools and Manufacture*, 46:2036–2043, 2006.

[120] P. Roud, J. Sklenička, and P. Kožmín. Using FEM in prediction of chip shape and cutting force when drilling materials with difficul machinability. *Advances in Manufacturing Science and Technology*, 35:39–52, 2011.

[121] Y. Sahin and A. R. Motorcu. Surface roughness model for machining mild steel with coated carbide tool. *Materials and Design*, 26:321–326, 2005.

[122] N. Sawarkar and G. Boob. Finite element based simulation of orthogonal cutting process to determine residual stress induced. *International Journal of Computer Applications*, pages 33–38, 2014.

[123] M. Shatla, C. Kerk, and T. Altan. Process modelling in machining. Part II: validation and applications of the determined flow stress data. *International Journal of Tools and Manufacturing*, 41:1659–1680, 2001.

[124] J. Shi and C. R. Liu. The influence of material models on finite element simulation of machining. *Journal Manufacturing Science and Engineering*, 126:849–857, 2004.

[125] Y. C. Shin and C. Dandekar. Mechanics and modeling of chip formation in machining of MMC. *Machining of Metal Matrix Composites*, pages 1–50, 2012.

[126] K. Skrypka and P. Bosetti. Application of optimal control problem for surface roughness improvement in milling. *Key Engineering Materials*, pages 1217–1222, 2015.

[127] K. Skrypka and G. Pittalà. A methodology for 2D cutting process simulation of solid end mill. *20th International ESAFORM Conference on Material Forming*, 2017.

[128] S. Smith and J. Tlusty. An overview of modeling and simulation of the milling process. *Journal of Engineering for Industry*, 113:169–175, 1991.

[129] H. Sonawane. *Modeling of tool-work interaction mechanics in ball-end milling of superalloy.* Phd thesis, Indian Institute of Technology, 2013.

[130] H. Sonawane and S. Joshi. Analytical modeling of chip geometry in high-speed ball-end milling on inclined Inconel-718 workpieces. *Journal of Manufacturing Science and Engineering*, pages 011005–1–011005–12, 2015. doi: 10.1115/1.4028635.

[131] J. Stahovec, J. Beňo, and M. Vrabel. Investigation of the cusp height when ball-end milling form shaped surfaces. *Mechanika*, 85:187–196, 2013.

[132] P. Stavropoulos, D. Chantzis, C. Doukas, A. Papacharalampopoulos, and G. Chryssolouris. Monitoring and control of manufacturing processes: a review. *Procedia CIRP*, 8:421–425, 2013.

[133] D. J. Steinberg, S. G. Cochran, and V. Guinan. A constitutive model for metals applicable at high-strain rate. *Journal of Applied Physics*, 51, 1980.

[134] D. A. Stephenson and J. S. Agapiou. *Metal cutting theory and practice.* CRC Press, 2006.

[135] A. Talyan, A. Manglik, R. Hussain, A. Singh, T. Varshney, and B. K. Jha. Error compensation and accuracy improvement in five-axis CNC machine tool. *International Journal of Advanced Mechanical Engineering*, 4: 129–138, 2014.

[136] T. L. Taner, Ö. Ömer, and E. Budak. Generalized cutting force model in multi-axis milling using a new engagement boundary determination approach. *International Journal of Advanced Manufacturing Technologies*, 77:341–355, 2015.

[137] Y. Tang, C. Xu, and M. Jackson. Geometrical adaptive controller for tool deflection compensation in helical end milling processes. *International Manufacturing Science and Engineering Conference*, pages 377–383, 2009.

[138] Third Wave Systems. *AdvantEdge 7.0 user's manual.* 2015.

[139] Third Wave Systems. *AdvantEfge FEM tech node. 3D tool meshing strategy.* Third Wave Systems, 2015.

[140] H. K. Toenshoff and B. Denkena. *Basics of cutting and abrasive processes.* Springer-Verlag Berlin Heidelberg, 2013.

[141] A. Ulsoy and Y. Koren. Control of machining process. *Transaction of the ASME*, 115.

[142] A. G. Ulsoy. *Condition monitoring and control for Intelligent Manufacturing*. Springer, 2006.

[143] E. Usui and T. Shirakashi. Mechanics of machining - from descriptive to predictive theory. On the art of cutting metals – 75 Years Later. *ASME Pressure Equipment Directive*, 7:13–55, 1982.

[144] A. M. Vasiloni and M. V. Dragoi. Smart adaptive CNC machining - State of the Art. *Applied Mechanics and Materials*, 657:859–863, 2014.

[145] M. Vaz, D. R. J. Owen, V. Kalhori, M. Lundblad, and L. E. Lindgren. Modelling and simulation of machining processes. *Archives of Computational Methods in Engineering*, 14:173–204, 2007.

[146] X.-J. Wan, L. Hua, X.-F. Wang, Q.-Z. Peng, and X.-P. Qin. An error control approach to tool path adjustment conforming to the deformation of thin-walled workpiece. *International Journal of Machine Tools and Manufacture*, 51:221–229, 2011.

[147] M.-Y. Wang and H.-Y. Chang. Experimental study of surface roughness in slot end milling AL2014-T6. *International Journal of Machine Tools and Manufacture*, 44:51–57, 2004.

[148] S. Wang, X. Lu, and W. Li. Sustainable process planning for customized production optimization. *Advances in Manufacturing Technology*, pages 387–392, 2016.

[149] C. Wick. Automatic adaptive control of machine tools. *Manufacturing Engineering*, 4:38–45, 1977.

[150] C. Xu and Y. C. Shin. Design of a multi-level fuzzy controller for nonlinear systems and stability analysis. *IEEE Transactions on Fuzzy Systems*, 13:761–778, 2005.

[151] C. Xu and Y. C. Shin. An adaptive fuzzy controller for constant cutting force in end-milling process. *Journal of Manufacturing Science and Engineering*, 130:031001–1–031001–10, 2008.

[152] S. Yang, J. Yuan, and J. Ni. The improvement of thermal error modelling and compensation on machine tools by CMAC neural network. *International Journal of Machine Tools and Manufacture*, 36:527–537, 1996.

[153] M. Young and J. Lee. Measurement and prediction of thermal errors of a CNC machining center using two spherical balls. *Journal of Materials Processing Technology*, 75:180–189, 1998.

[154] F. J. Zerilli and R. W. Armstrong. Dislocation-mechanics-based constitutive relations for material dynamics calculations. *Journal of Applied Physics*, 61:1816–1825, 1987.

[155] J. Z. Zhang, J. C. Chen, and E. D. Kirby. Surface roughness optimization in an end-milling operation using the Taguchi design method. *Journal of Materials Processing Technology*, 184:233–239, 2007.

[156] Y. Zhang, D. H. Zhang, and B. H. Wu. An adaptive approach to error compensation by on-machine measurement for precision machining of thin-walled blade. *IEEE International Conference on Advanced Intelligent Mechatronics (AIM)*, pages 1356–1360, 2015.

[157] C. Zhao and Y. Guan. The experiments and simulation of titanium cutting based on AdvantEdge software. *Applied Mechanics and Materials*, 159:371–375, 2012.

[158] J. Zhu. *Robust thermal error modeling and compensation for CNC machine tools*. Phd thesis, University Of Michigan, 2008.

[159] Y. Zhu, P. Shum, C. Lu, M. B. Lacquet, P. L. Swart, A. A. Chtcherbakov, and S. J. Spammer. Temperature insensitive measurements of static displacements using a fiber Bragg grating. *Optics Express*, 11:1918–1924, 2003.

[160] N. N. Zorev. Inter-relationship between shear processes occurring along the tool face and shear plane in metal cutting. *International Research in Production Enginerring ASME*, pages 42–49, 1963.

[161] X. Zuo, B. Li, J. Yang, and X. Jiang. Integrated geometric error compensation of machining processes on CNC machine tool. *14th CIRP Conference on Modeling of Machining Operations*, 8:135–140, 2013.

[162] U. Župerl and F. Čuš. Tool cutting force modeling in ball-end milling using multilevel perception. *Journal of Materials Processing Technology*, 153:268–275, 2004.

[163] U. Župerl, F. Čuš, and M. Milfelner. Fuzzy control strategy for an adaptive force control in end-milling. *Journal of Materials Processing Technology*, 164-165:1472–1478, 2005.

[164] U. Župerl, F. Čuš, and V. Gecevska. Optimization of the characteristic parameters in milling using the PSO evolution technique. *Strojniski Vestnik*, 53:354–368, 2007.

[165] U. Župerl, F. Čuš, and M. Reibenschuh. Neural control strategy of constant cutting force system in end milling. *Robotics and Computer-Integrated Manufacturing*, 27:485–493, 2011.

[166] U. Župerl, F. Čuš, and M. Reibenschuh. Modeling and adaptive force control of milling by using artificial techniques. *Journal of Intelligent Manufacturing*, 23:1805–1815, 2012.